Synthesis, characterization, and use of accessible π-conjugated structures for organic electronics

Tatiana Ghanem

COLLEGE DOCTORAL PAYS DE LA LOIRE
ED MATIERE, MOLECULES MATERIAUX ET GEOSCIENCES

université angers

THESE DE DOCTORAT

DE
L'UNIVERSITÉ D'ANGERS

SOUS LE SCEAU DE

LA COMUE ANGERS – LE MANS

ECOLE DOCTORALE N° 596
Matière, Molécules, Matériaux et Géosciences
Spécialité : *Chimie Organique*

Par
Tatiana GHANEM

Synthesis, Characterization, and Use of Accessible π-conjugated Structures for Organic Electronics

Thèse présentée et soutenue à Angers, le 24 Novembre 2023

Unité de recherche : Laboratoire MOLTECH-Anjou – CNRS UMR 6200

Rapporteurs avant soutenance :

Christine Lartigau-Dagron, Maître de Conférences HDR, Université de Pau et des Pays de l'Adour
Zacharias Amara, Maître de Conférences HDR, CNAM Paris

Composition du Jury :

Examinateurs :	Julien Boixel, Chargé de Recherche CNRS, Université de Rennes Piétrick Hudhomme, Professeur, Université d'Angers
Directeur de thèse :	Clément Cabanetos, Directeur de recherche CNRS, Université d'Angers
Co-directeur de thèse :	Philippe Blanchard, Directeur de recherche CNRS, Université d'Angers
Invité :	Yann Pellegrin, Directeur de recherche CNRS, Université de Nantes

Acknowledgments

Here I am, after three years, finishing my thesis manuscript. None of this work would have been possible without the contribution, help, and support of the following people.

Firstly, I would like to express my deepest gratitude to my two supervisors Clément Cabanetos and Philippe Blanchard for everything they have taught me. Thank you Clément for never running out of ideas, for the weekly Zoom meetings, for always pushing me to challenge myself, and for your generosity. Philippe, thank you for all the scientific discussions, your constant support, your infinite kindness, and always finding time in your busy schedule. I am grateful to both of you.

I want to thank all the jury members, in particular, Christine Lartigau-Dagron and Zacharias Amara for accepting to be reviewers of this PhD thesis and Julien Boixel, Piétrick Hudhomme, and Yann Pellegrin for their participation as examiners of this work.

I would also like to acknowledge all the collaborators on different parts of this work. Thank you to Jong Hyeok Park and Jung Hwan Lee (Yonsei University) for testing some molecules in perovskite solar cells. Thanks to Eunkyoung Kim and Kwang Keat Leong (Yonsei University) for the light-emitting electrochemical devices fabrication. In addition, I would also like to thank the above-mentioned people for their warm welcome and fruitful discussions during my two-week visit to Seoul. I also want to thank Gregory Welch and Akpeko Gasonoo (University of Calgary) for incorporating the emissive molecules in organic light-emitting diodes. I definitely want to thank Dominik Lungerich and Pablo Simon Marqués for the theoretical calculations detailed in this manuscript.

I wish to express my sincere appreciation to all the SFR Matrix colleagues, especially Ingrid Freuze for the mass spectra, Magali Allain for the X-ray analysis, Sylvie Dabos Seignon for the AFM images, and Benjamin Siegler for the NMR characterization. Thank you Cécile Mézière for helping with all the shipping packages. Also a big thanks to the administrative personnel for always doing their best.

A special thanks to all of the SCL team members, especially Lionel Sanguinet, Pierre Frère, and Frédéric Gohier for all the advice during the group meetings.

Not to forget the Master students who worked with me during internships, Tony Vincendeau and Alexis Hardouin, thank you for your investment and work.

Here comes the part of expressing the deepest gratitude to all the “non-permanent” people of MOLTECH-Anjou laboratory.

I would like to begin by thanking the wonderful lab mates who shared K108 with me. Ali Yassin, thank you so much for all the help, great pieces of advice, discussions, and support. Thank you for always listening to me and making me question things. To Pierre Josse, “le bouilloire”, thanks for the laughs, the good ambiance you always brought, and all your help. Despite you making fun of me, it was a pleasure working with you. Korentin Morice, even with all your mess, I will always be happy to teach you new Lebanese words. To the one who plays the best Spanish music, Dario Javier Sanchez, thank you for being so helpful. Keep it up for your last year!

To all my Lebanese colleagues who made it home away from home, Jennifer, Rana, Melissa, Khaled, Jihad, Youssef… from the heart, thank you. Especially Aline, Soussana, and Elie, you were family to me. Thank you for always being there, without you I would not have been able to deal with all the ups and downs of this PhD thesis. Grateful for all the love, good moments, and happy memories.

To Adèle, thanks for all the “pause café/thé” and all the discussions and gossip. Glad I got to know you. To the “little” ones, les trois mousquetaires, Louis, Romain, and Axel, thank you for all the food and drinks and best of luck for the rest of your PhDs.

Thank you to all of MOLTECH members, Federica, Nataliya, Yohan, Chloé, Maurizio, Sana, Hayley, Arthur… who supported or helped me in any way.

My warmest gratitude goes to my lifelong friends back home, Elissa, Maria, Julia, and Carine, for always knowing how to cheer me up and motivate me when visiting Lebanon.

To my life partner, Majd, so grateful for you always being by my side and supporting me. Thank you for handling all my mood swings, especially in this writing phase. Cheers to more achievements, together.

Last but definitely not least, I want to finish by thanking my family for their infinite support during all of this period. Among all of them, my deepest appreciation goes of course to my parents, Mom and Dad, thank you for everything; and to my little brother, Charly, who is growing up with me being far away. I certainly would not be here without you. Hope I made you proud. أحبكم

Table of Contents

TABLE OF CONTENTS

TABLE OF CONTENTS

List of abbreviations and symbols

A	Electron-accepting block/material
ACQ	Aggregation caused quenching
AFM	Atomic force microscopy
BDT	Benzodithiophene
BHJ	Bulk heterojunction
BT2F	5,6-difluoro-2,1,3-benzothiadiazole
BTI	2-(alkyl)-1*H*-thioxantheno[2,1,9-*def*]isoquinoline-1,3(2*H*)-dione
BzT	Benzo[*c*][1,2,5]thiadiazole
CE	Current efficiency (cd/A)
CIE	Chromaticity coordinates of the “Comission Internationale de l’Eclairage”
CV	Cyclic voltammetry
CT	Charge-transfer
D	Electron-donating block/material
DCV	Dicyanovinyl
DFT	Density functional theory
DHA	Direct heteroarylation
DMA	*N*,*N*-dimethylacetamide
DMF	*N*,*N*-dimethylformamide
DPP	Diketopyrrolopyrrole
DSSCs	Dye-sensitized solar cells
E_{ox}	Oxidation potential (V)
E_{red}	Reduction potential (V)
EL	Electroluminescence
EML	Emissive layer
ETL	Electron transporting layer
ETM	Electron transporting material
EQE	External quantum efficiency
Et_3N	Triethylamine
FA	Formamidinium
Fc/Fc^+	Ferrocene/ferrocenium redox couple
FF	Fill factor
FRET	Forster resonance energy transfer
HOMO	Highest occupied molecular orbital
HRMS	High-resolution mass spectrometry
HTL	Hole-transporting layer
HTM	Hole-transporting material

LIST OF ABBREVIATIONS AND SYMBOLS

IC	Internal conversion
ICT	Internal charge transfer
ISC	Inter-system crossing
ITO	Indium tin oxide
IQE	Internal quantum efficiency
J	Current density (mA cm^{-2})
J_{max}	Maximum current density (mA cm^{-2})
J_{sc}	Short-circuit current density (mA cm^{-2})
L	Luminance (cd/m^2)
LEC	Light-emitting electrochemical cell
Li-TFSI	Lithium bis(trifluoromethanesulfonyl)imide
LUMO	Lowest unoccupied molecular orbital
MA	Methylammonium
MALDI	Matrix-assisted laser desorption/ionization
MAPI	methylammonium lead triiodide
ML	Multi-layer
MS	Mass spectrometry
NDI	Naphthalenediimide
NFA	Non-fullerene acceptor
NMR	Nuclear magnetic resonance
OFET	Organic field-effect transistor
OLED	Organic light-emitting diode
OPV	Organic photovoltaics
OSC	Organic solar cells
OTFT	Organic thin-film transistor
P3HT	Poly(3-hexylthiophene-2,5-diyl)
$PC_{61}BM$	[6,6]-phenyl-C_{61}-butyric acid methyl ester
$PC_{71}BM$	[6,6]-phenyl-C_{71}-butyric acid methyl ester
PCE	Power conversion efficiency (%)
PDI	Perylenediimide
PE	Power efficiency (lm/W)
PEDOT	Poly(3,4-ethylenedioxythiophene)
PESA	Photoelectron spectroscopy in air
PHJ	Bilayer/planar heterojunction
P_i	Irradiating power (mW cm^{-2})
P_{max}	Maximum power (mW cm^{-2})
PSC	Perovskite solar cells
PV	Photovoltaics
R2R	Roll-to-roll
RISC	Reverse intersystem crossing

LIST OF ABBREVIATIONS AND SYMBOLS

RMS	Root mean square roughness
RPM	Revolutions per minute
SL	Single-layer
T	Thiophene
TADF	Thermally activated delayed fluorescence
$TBAPF_6$	Tetrabutylammonium hexafluorophosphate
tBP	Tert-butylpyridine
TD-DFT	Time-dependent density functional theory
THF	Tetrahydrofuran
TMS	Trimethylsilyl
TOF	Time-of-flight
TPA	Triphenylamine
TPA-BP	4,4'-diphenyltriphenylamine
TPA-OMe	4,4'-dimethoxytriphenylamine
UV	Ultraviolet
V	Voltage (V)
VR	Vibrational relaxation
V_{max}	Maximum voltage (V)
V_{oc}	Open circuit voltage (V)
V_{on}	Turn-on voltage (V)
E_g^{opt}	Optical band gap (eV)
ε	Molar absorptivity ($M^{-1} cm^{-1}$)
λ	Wavelength (nm)
μ_e	Electron mobility ($cm^2 V^{-1} s^{-1}$)
μ_h	Hole mobility ($cm^2 V^{-1} s^{-1}$)
QY	Fluorescence quantum yield

CHAPTER 1

CHAPTER 1

CHAPTER 1

CHAPTER 1

CHAPTER 1

CHAPTER 1

Chapter 1:

General Introduction

CHAPTER 1

Carbon is a ubiquitous, though unique, element that can form different covalent bonds with other carbon atoms, as well as with a variety of other elements such as hydrogen, oxygen, nitrogen, sulfur, *etc*. The chemistry of carbon is fundamental to life on Earth, since all living organisms are composed of organic-based structures. The latter, such as carbohydrates, lipids, proteins, and nucleic acids indeed play crucial roles in biological processes including energy production, cell structure and function, and genetic storage information and expression. This ability to generate molecules from the simplest to the most complex form (methane vs DNA), defines the vast and almost endless array of organic compounds found in nature but also in laboratories. Major focus of attention since the dawn of modern chemistry, the synthesis of such materials entitled “organic chemistry” encompasses a wide range of subcategories and topics, including the study of properties and reactivity of organic compounds, elucidation of their reaction mechanisms, and synthesis of new compounds with desired properties for specific applications. Consequently, this field of research plays a vital role in many areas of science and technology, including medicine, materials science, and energy research: in other words, in our daily modern lives.

1.1 Organic electronics

The term "Organic Electronics" refers to a broad area based on the synthesis and use of π-conjugated structures characterized by conducting or semiconducting properties. In contrast to most conventional inorganic materials like silicon, the popularity of organic-based devices came along with their flexibility, lightweight, large-area, and low-cost manufacturing since potentially compatible with printing techniques. Hence, organic light-emitting diodes (OLEDs) [1-2], organic field-effect transistors (OFETs),[3-6] organic photovoltaics (OPVs),[7-9] electrochromic devices (ECDs),[10-11] and photodetectors [12] have attracted considerable attention over the last few decades.

From a molecular/chemical point of view, anthracene was amongst the very first organic compounds studied, in the late 50s, for its semiconducting properties.[13-15] However, the field really took off in the 70s-80s with the synthesis and characterization of conductive polymers such as polypyrrole,[16-17] polyaniline,[18] and polyacetylene [19-20] (Figure 1.1). From these discoveries, several years went by before the first reported example of organic-based devices with the demonstration, in 1987, of an organic light-emitting diode (OLED) by Ching Wan Tang and Steven Van Slyke, the two OLED pioneers, from Eastman Kodak.[21-23] This

innovation paved the way for modern organic-based displays that are currently widely embedded in smartphones and televisions.

In parallel, the development of organic field-effect transistors (OFETs), in the 1990s, demonstrated the potential use of organic materials in electrical circuits.[24-25] As a result, organic thin-film transistors (OTFTs) [26] are nowadays used in several applications, such as flexible screens, sensors,[27-28] and electronic papers.[29]

Another striking example, the first bulk heterojunction solar cell was reported in 1995 and was based on purely organic compounds. This breakthrough initiated more than two decades of intensive research and development resulting in the demonstration of materials and devices now competing, in terms of efficiencies, with silicon-based solar technologies.[30-33]

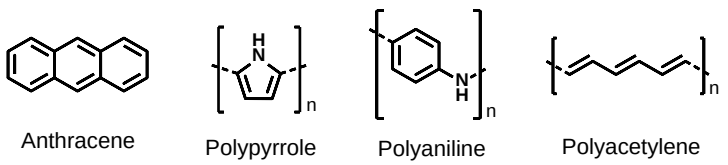

Figure 1.1 Structures of the first organic compounds used in organic electronics.

Stemming from this intensive research, the development of electro-active inks from organic materials opened doors to low-cost printing processes such as screen-printing, blade coating, inkjet printing, rotogravure printing, aerosol spray coating, and slot-die coating. Most of these methods target large areas and automated roll-to-roll (R2R) production, where substrate reels are continually involved in procedures used in the graphic/advertising printing sector (*ie*, coating, drying, laminating, and cutting procedures). Simple electronic devices, such as sensors, logic circuits, and more complex such solar cells can be produced through these methods in a quicker and cheaper way than that of conventional inorganic-based electronic components. For instance, two companies, namely "Armor" [34] (France) and "Heliatek" [35] (Germany) already supplied large-area, flexible, and lightweight organic-based solar panels (see example in Figure 1.2), using R2R production from solutions or by evaporation techniques respectively.

On the niche side, the capacity to print onto a range of substrates creates prospects for the integration of electronics into paper-, textile- and plastic-based items and thus potential new applications (such as smart packaging, *etc*.).[36] In addition, organic-based electronic

components can be (semi)transparent or in a range of precisely tuned colors providing motivational and innovative integration of the latter devices in places that were not considered for conventional electronics (architectures, sails, etc.). For instance, LG [37] recently supplied large-area, flexible, and lightweight transparent OLED walls installed at Incheon International Airport (Figure 1.2).

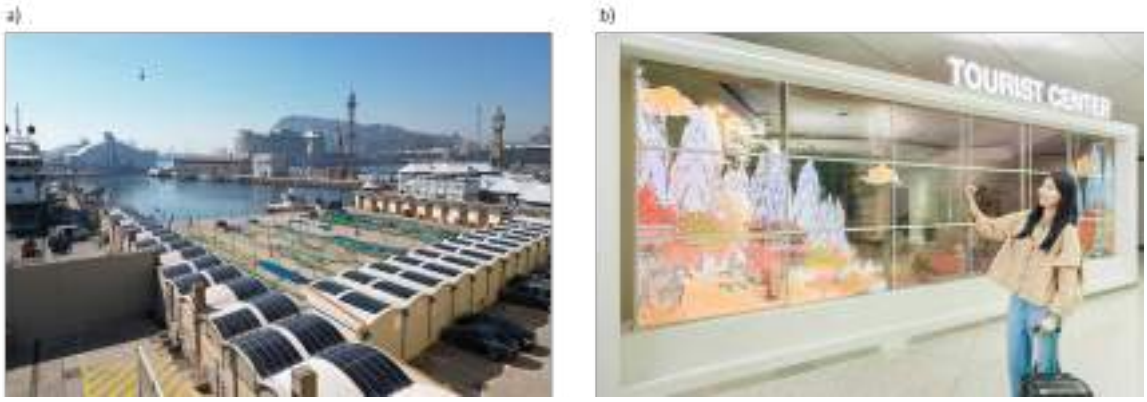

Figure 1.2 a) OPV installation on undulating rooftops in the Port of Barcelona, by Heliatek; b) Transparent OLED display at Korea's Incheon International Airport, by LG.

Finally, the potential biocompatibility of organic-based devices also provides new prospects to probe, monitor or communicate with living systems. Hence, research and development in organic electronics offer the advantage of features that are/were not possible/accessible with conventional inorganic materials rather than just improving performances to, somehow, replace the existing technologies.

1.2 Organic semiconductors

The semiconducting properties of organic materials are the foundation of organic electronics. This feature results from the ability to transport charge carriers, namely electrons and/or holes, within the backbone and the stacks (materials) of small molecules and polymers. As chemists, it is important to understand (1) the working principle of such categories of active compounds and (2) how chemical modifications can affect their electronic and photophysical properties to target specific applications through an optimized rationalization of the structure-property relationships.

1.2.1 π-conjugated materials

π-conjugated materials, whether molecular or polymeric, are usually constituted of alternated single and double bonds that create a plane of sp^2 hybridized orbitals with $2p_z$ orbitals left perpendicular to that plane. The overlap of these $2p_z$ orbitals forming a network of π bonds allows the delocalization of electrons across the conjugated system.

One of the key design principles of π-conjugated materials relies on the commonly referred "*energy gap engineering*". The energy gap of an organic semiconductor can be defined as the difference, in energy, between its highest occupied molecular orbital (HOMO) and lowest unoccupied molecular orbital (LUMO). Hence, when considering molecular design, a fine-tuning of these frontier orbitals can be achieved by (1) extending the conjugation of the π-system, (2) incorporating electron-donating or -withdrawing groups, (3) using the intramolecular Donor-Acceptor (D-A) strategy, *ie*, alternating electron-rich and poor moieties, and finally (4) rigidifying/bridging the π-conjugated system.

(1) In general, the extension of the conjugation length of a material, leads to a decrease in the energy difference between the HOMO and LUMO levels as a result of the linear combination of molecular orbitals.[38] Varying the length of the π-conjugated backbone from ethylene through butadiene, octatetraene, and then longer polyenes, increases the number of overlapping $2p_z$ orbitals resulting in the concomitant stabilization of the LUMO level and destabilization of the HOMO levels, hence changing the properties from insulators to semiconductors (Figure 1.3).

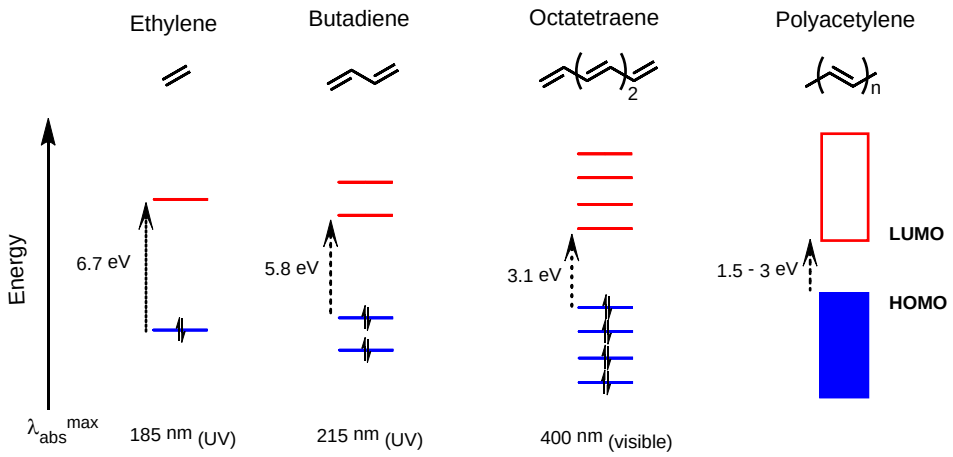

Figure 1.3 Diagram showing the effect of increasing the conjugation length on the energetic gap between HOMO and LUMO levels.

Moreover, this reduction of the band gap also has a direct impact on the optical properties, since it gradually shifts the absorption wavelength of these materials towards lower energies.

Theoretically, extending the conjugation to some extent would result in a negligible bandgap between the HOMO and LUMO levels affording metal-like behaving organic conductors. However, the narrowing of the energy gap *via* this approach is somehow limited by the instability of a quasi-one-dimensional structure of sp^2 hybridized C-C bonds. This will lead to a distortion of the chain, known as Peierl's distortion, to provide stabilization through a lower energy arrangement. The physical effect of this stabilization is seen through bond-length alternation (BLA) of shorter and longer bonds, thus preventing organic conjugated materials from achieving the zero-energy bandgap seen in conducting metals. [39]

(2) The incorporation of electron-donating or electron-withdrawing substituents, inductive or mesomeric, is known to be an efficient strategy to fine-tune the HOMO/LUMO gap of a π-conjugated material. [40] Convenient from an organic chemistry point of view, this approach is thus frequently and complementarily used with the previously discussed π-extension of the backbone. Hence, electron-donating groups will decrease the ionization potential of the material, thus, destabilizing the HOMO energy level, while electron-withdrawing groups will increase the electron affinity of the material, and therefore stabilize the LUMO energy level.

(3) The intramolecular Donor-Acceptor (D-A) concept results from the alternation of electron-rich, donor (D), and electron-poor, acceptor (A) units within the same π-conjugated framework, leading to new HOMO and LUMO energy levels, wherein the energy gap is narrowed by forming a higher-lying HOMO and a lower-lying LUMO from the new hybridized orbitals (Figure 1.4). This approach introduces "push-pull" driving forces through internal charge transfers that facilitate electron delocalization, an effect that cannot be achieved by simply repeating the same unit. [41-42]

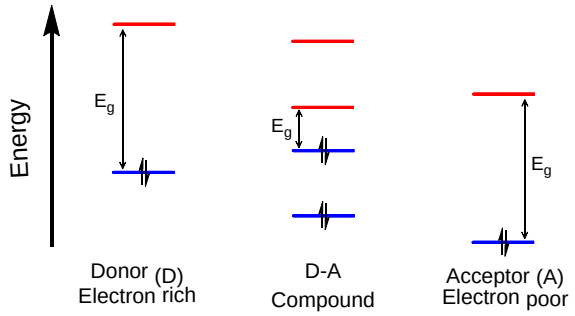

Figure 1.4 Diagram showing the D-A approach.

(4) The planarity of the conjugated backbone also plays a crucial role in all of these energy gap-engineering strategies. Planarizing a structure indeed enables a more effective π-orbital overlap resulting in an easier delocalization of the π-electrons and therefore reduction of the gap. The effect of the covalent rigidification of the π-conjugated system on the energy band gap is illustrated with practical examples in Figure 1.5. [43] As a result, this geometric variation can also be a useful tool to tune the energy gap of a particular material.

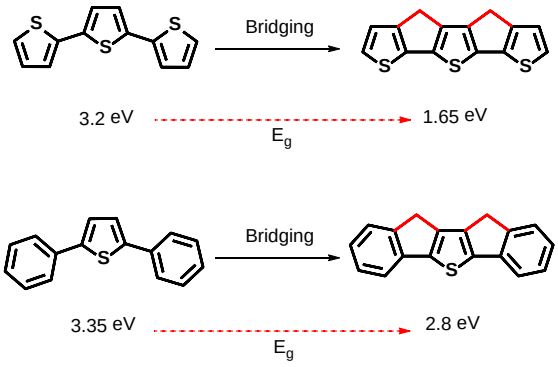

Figure 1.5 Effect of the rigidification on the HOMO-LUMO energy gap of π-conjugated systems.

1.2.2 Molecular *vs.* polymeric organic semiconductors

By applying the above-mentioned strategies, two types of organic semiconductors are usually synthesized namely the polymers and the "well-defined" molecular structures. Both types of architectures have been massively investigated within the organic electronics community since both are characterized by peculiar advantages but also drawbacks.[44]

As mentioned, polyacetylene [19-20] was amongst the first reported and one of the most studied conjugated polymers. However, its relative instability to air and tedious processability (limited solubility) motivated researchers to develop functionalization strategies and new materials. The second generation of semiconducting polymers indeed relies on aromatic and polycyclic structures. Several key examples are illustrated in (Figure 1.6) such as the poly(p-phenylenevinylene) (PPV) that was used in the 90s for the preparation of light-emitting demonstrators. [45] Stemming from this simple structure, a large library of semiconducting polymers has been synthesized and investigated, particularly those incorporating heterocycles with five-membered rings (pyrrole, thiophene, *etc.*).

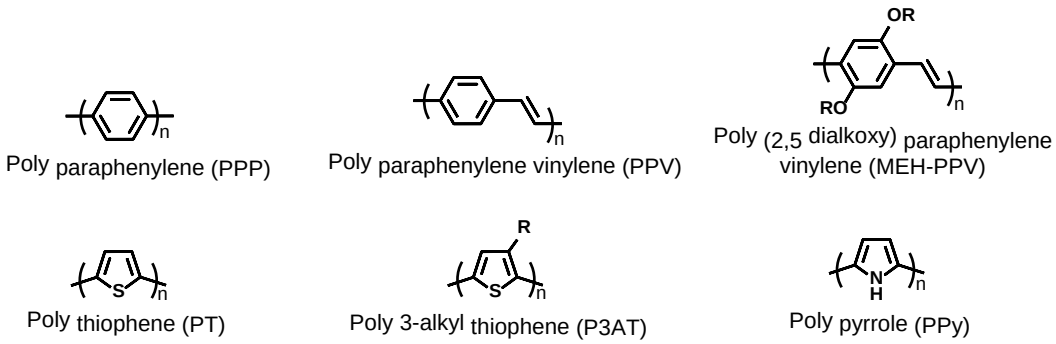

Figure 1.6 Molecular structures of some important heterocyclic polymers (second generation).

Nevertheless, this second generation of semiconducting polymers also suffers from significant drawbacks such as limited solubility and usually wide band gaps thus limiting, for instance, their sunlight-harvesting ability, a key parameter in organic solar cells.[46-47]

From these statements, the third generation of semiconducting polymers emerged in the 2000s. The latter have more complex molecular structures with different atoms in the repeating units with either heterocycles or benzene rings. Organic chemists have developed and combined tremendous amounts of building blocks, such as fluorine,[48-49] carbazole,[50-51] thiophene and its fused derivatives,[52-55] benzothiadiazole and (hetero)variations,[56-59] indacenodithiophene,[60-61] rylene diimides,[62-64] isoindigo [65] and diketopyrrolopyrrole,[66-69] *etc.* (see structures in Figure 1.7). Indeed, beyond conventional homopolymers, D-A alternated copolymers have attracted considerable research attention, since a straightforward strategy to decrease and fine-tune the band gap, solubility, and self-assembling properties. [70] With almost an endless combination of the D-A units, with different lengths and natures of the side chains, myriads of structures have

thus been reported leading to important breakthroughs in their respective fields.[9, 71-77] Some examples are depicted in Figure 1.2.5.

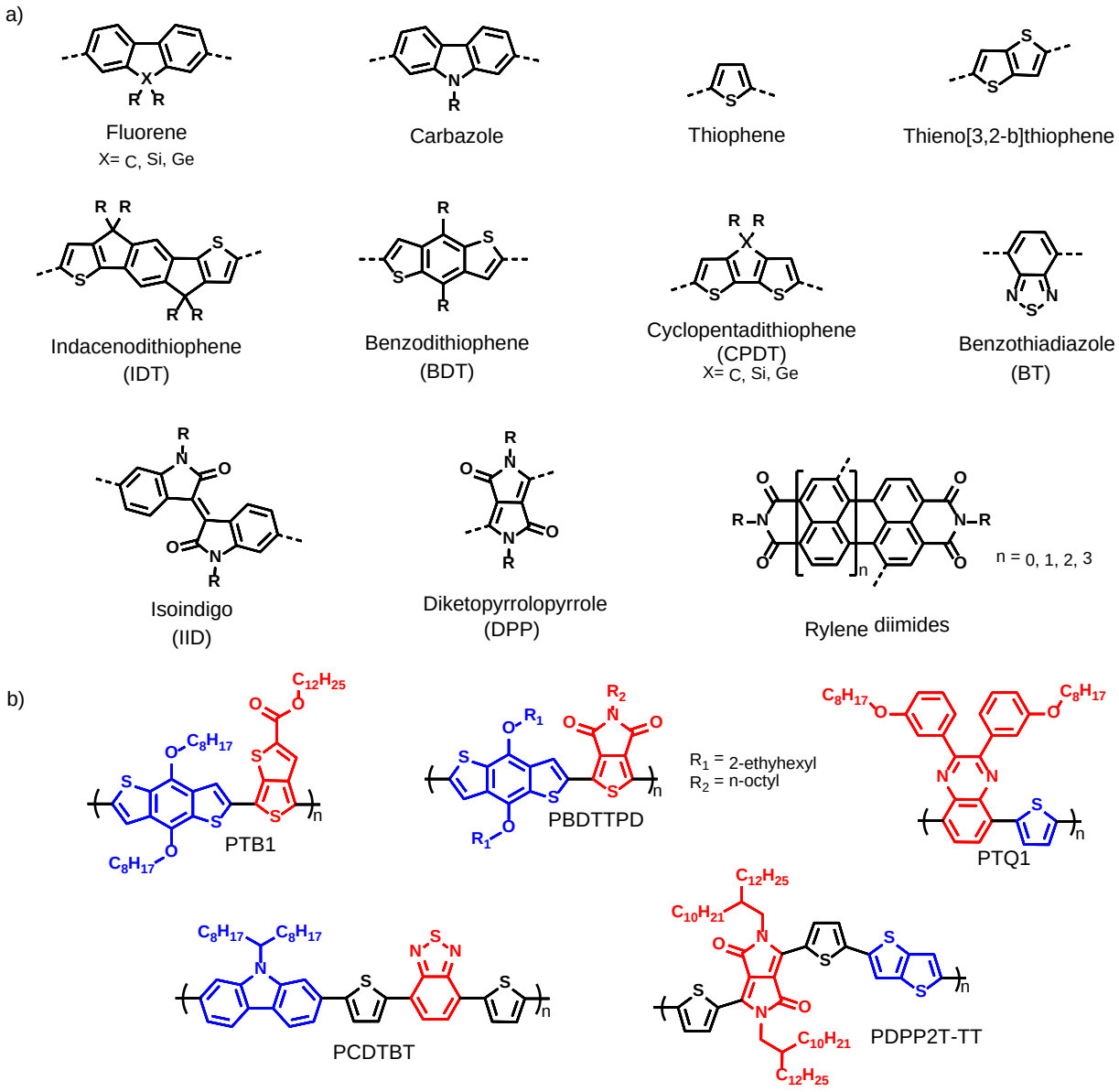

Figure 1.7 a) Example of typical building blocks for conjugated processable polymers; b) Illustration of some low band-gap (D-A) polymers.

Despite remarkable optoelectronic and, above all, processing/film-forming properties, semiconducting polymers nonetheless suffer from several drawbacks. First, regarding their synthesis, polymeric materials, by nature, always have an intrinsic degree of dispersity affecting both the reproducibility (batch-to-batch variation) and purification (mainly limited to

precipitation, Soxhlet extraction, and/or size exclusion chromatography). Consequently, researchers have focused, in parallel, their attention on small organic molecules [62, 78-81] (Figure 1.8). The latter are indeed monodispersed and can be purified by traditional workups, *ie*, column chromatography, distillation, and/or sublimation. These features make them ideal candidates for mass production at an industrial scale. However, to increase charge mobility, densely packed crystalline morphologies are expected while on the other hand, such self-assembling properties impact their processability, particularly from inks (strong aggregation). Even if several systems were used to achieve highly efficient vacuum deposited devices,[42, 82-83] this technique limits the design to small and robust molecular systems while their crystallinity was found to affect their use in flexible electronics.

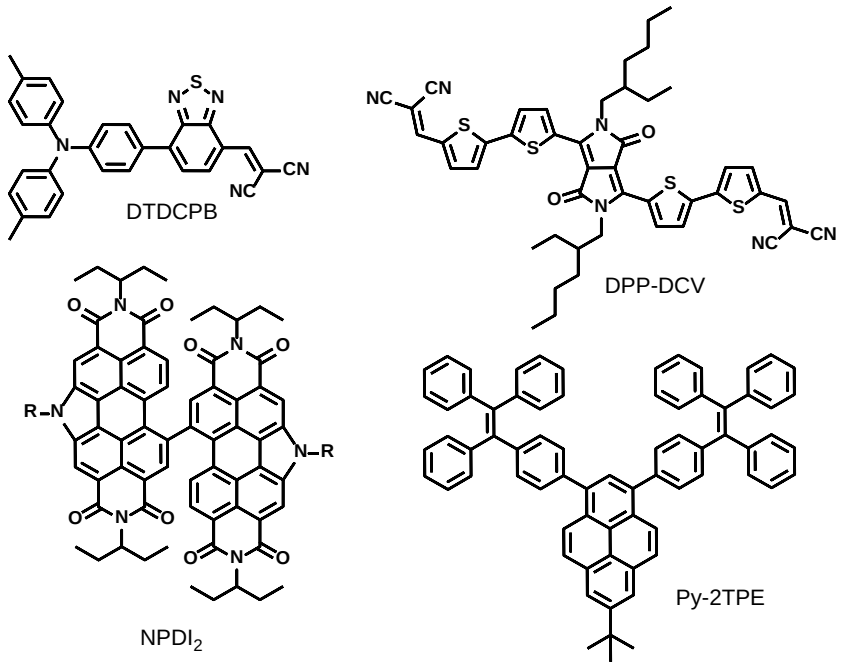

Figure 1.8 Structure of some small organic molecules used in organic electronics.

Consequently, to overcome these limitations and also gain in efficiency and processability, larger architectures decorated with various aliphatic solubilizing chains were reported (see examples in Figure 1.9). [84-86]

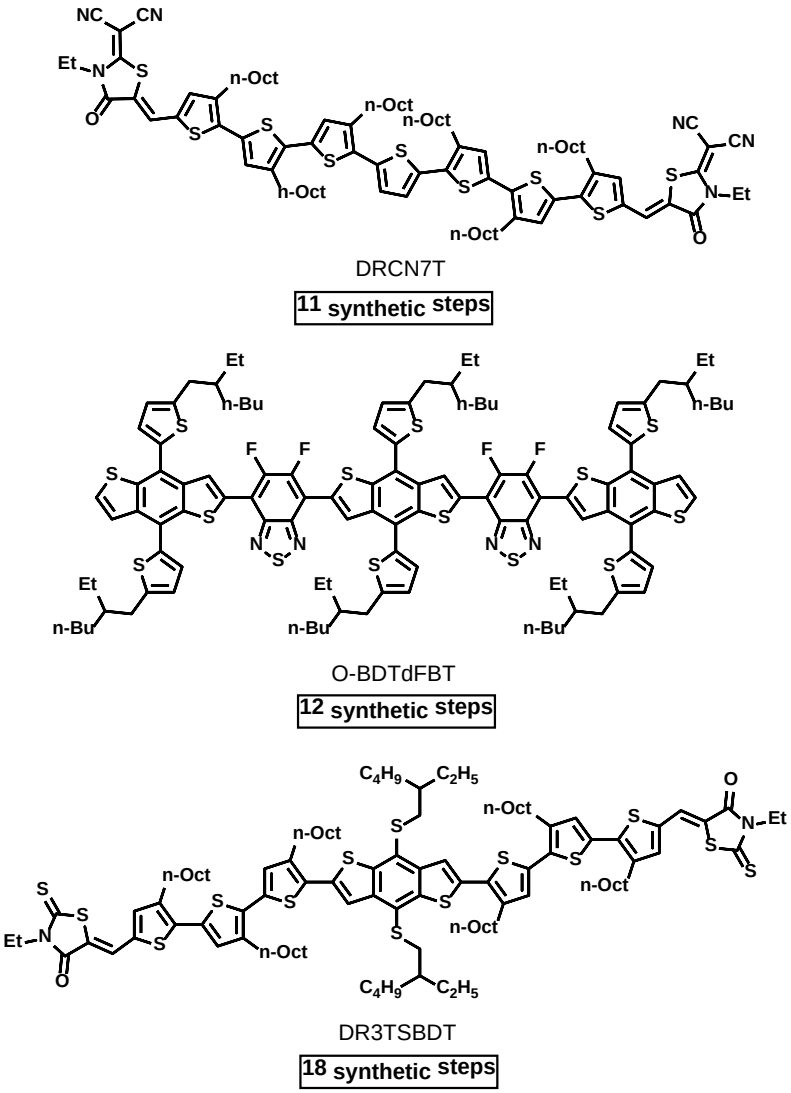

Figure 1.9 Structure of large architecture molecular donors for OSCs.

However, this would lead to an increase in the complexity of the reported designs, marking a starting point of formal divergence with the concept of organic electronics which is the cost-effectiveness, affordability, and accessibility of these technologies. [87]

Indeed, the latter architectures require a significant number of synthetic and purification steps, drastically impacting the cost of the final products.

This complexification is also found in polymeric materials. Considering the evolution from P3HT to PM6 (for example) not complex enough, from a synthetic and costly point of view, chemists push the concept of complexification beyond side chain "engineering" in macromolecular architectures by, for instance, incorporating a third monomer resulting in ternary random copolymers (Figure 1.10).[88-89]

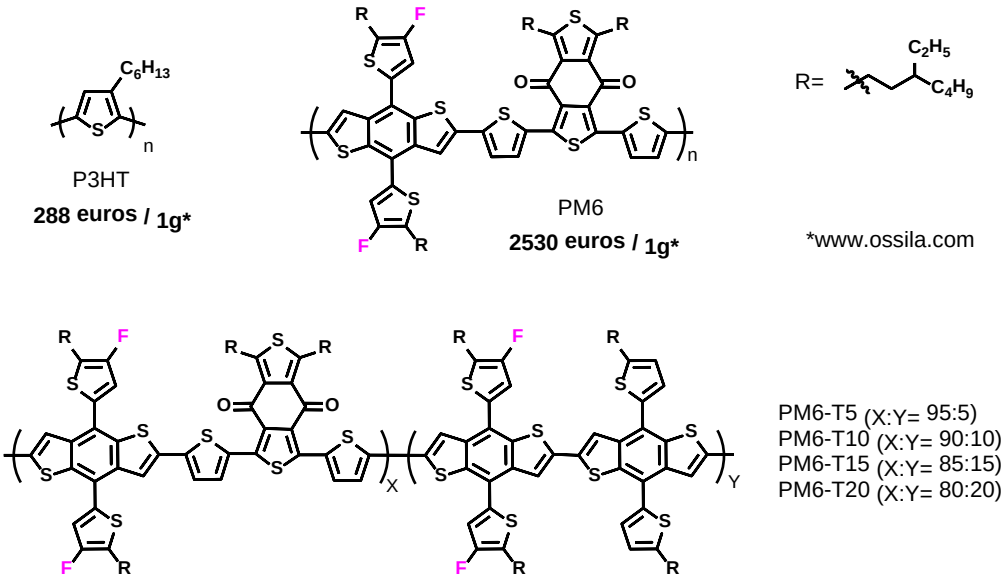

Figure 1.10 Structure of efficient donor polymers.

High-performance materials developed in the laboratory do not (yet) meet the specifications of potential industrialization due to excessively long synthetic routes, the use of dangerous reagents, costly purifications, limited recyclability, and the generation of large quantities of (chemical) waste.

In this context, the objective of this thesis is to afford simple and accessible active materials to "make organic electronics simple again". Beyond the design of target materials with specific properties, synthetic tools to limit the number of synthetic steps and waste will be carefully selected.

1.2.3 Simplification from a synthetic point of view: Objective of the thesis

Carbon-carbon bond formation plays a major role in the design and synthesis of organic building blocks during the preparation of target organic π-conjugated materials. With a few exceptions, these processes usually rely on transition-metal-catalyzed C–C cross-coupling reactions (Stille and Suzuki). [90-91] This strategy requires the halogenation and functionalization of complementary building blocks by organometallic functional groups, that can be highly

toxic (*e.g.* organotin), and challenging to prepare and purify when applied to large-scale syntheses (Figure 1.11). [92]

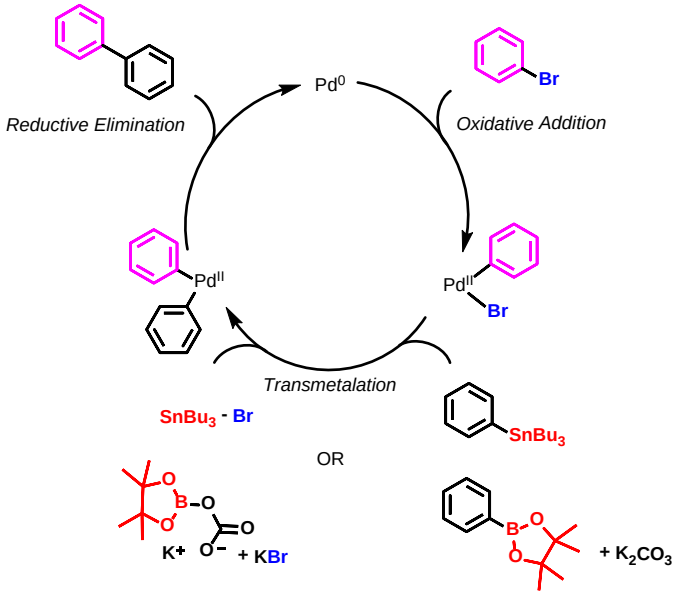

Figure 1.11 Proposed mechanism of the Stille and Suzuki coupling reactions (Ligands are omitted from the Pd-metal center for clarity reasons).

Therefore, the direct functionalization of C-H bonds appears to be the optimal cross-coupling technique, since this procedure does not require organometallic derivatives, simplifying the synthetic pathways and improving the general safety of the experimentalist's environment. In recent years, the direct arylation of C–H-activated aromatic or heteroaromatic moieties has emerged, as an efficient atom-economical alternative method to conventional organometallic-based cross-coupling reactions.[93-95] The direct heteroarylation (DHA) approach has demonstrated its potential, huge versatility, and compatibility with a wide range of blocks resulting in myriads π-conjugated polymers and molecular materials prepared under very mild conditions. [96-98] In the typical processes illustrated in figure (Figure 1.12), DHA enables the coupling of an aryl bromide with a thiophene heterocycle's activated C-H bond at the 2-position to create a carbon-carbon single bond.

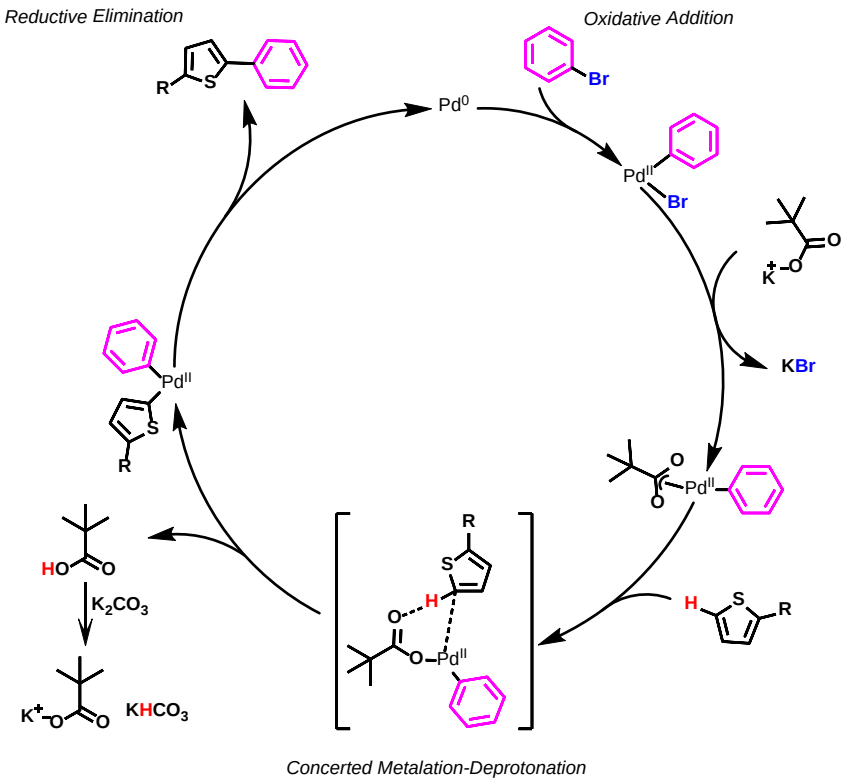

Figure 1.12 Proposed mechanism cycle for a Pd-catalyzed direct heteroarylation coupling reaction (Ligands are omitted from the Pd-metal center for clarity reasons).

This bonding results from a concerted metalation-deprotonation process that uses a carbonate base and carboxylic acid as the proton shuttle. It has been demonstrated that potassium carbonate and pivalic acid work synergistically in a proper stoichiometry to produce, *in situ*, potassium pivalate that will subsequently coordinate the metal center thus expelling the halide from Pd(II). The pivalate ligand can deprotonate an acidic hydrogen from the second substrate allowing its coordination to the metal center and the dissociation of pivalic acid. Reductive elimination is subsequently executed to generate the target product while regenerating the catalyst (Pd(0)).

The use of DHA has met with some success since a broad range and variety of employed organic building blocks, including functionalized thiophenes, furans, and thiazoles using a variety of aryl halides have been successfully applied. [78, 99-100] However this reaction is not universal and sometimes requires a drastic optimization of the reaction conditions to reach and defeat the conventional Stille and Suzuki couplings in terms of conversion and thus synthetic yields. This is mostly due to the lack of selectivity without proper directing groups, resulting in undesirable isomers and/or cross-linked materials during polymerization operations.

Moreover, homocoupling side reactions can occur between aryl bromides and also the activated C-H moieties. [99, 101-103]

However, these limitations can be overcome by carefully adjusting the reaction parameters such as the choice of the carboxylic acid, the phosphine-based ligand, the temperature, and the reaction time. [104-107] Even if such careful optimization is required, DHA still remains an amazing tool and method to afford new materials in a more eco-friendly way while limiting the number of synthetic steps. Consequently, most of the target compounds considered during this doctorate were prepared by applying this cross-coupling reaction.

Divided into two parts, this thesis manuscript will report and discuss novel materials designed and prepared by eco-friendly synthetic routes for photovoltaics (chapter 2) and light-emitting devices (chapter 3).

Bibliography

[1] J. Bauri, R. B. Choudhary and G. Mandal, Journal of Materials Science 2021, 56, 18837-18866.
[2] G. Hong, X. Gan, C. Leonhardt, Z. Zhang, J. Seibert, J. M. Busch and S. Bräse, Advanced Materials 2021, 33, 2005630.
[3] G. Horowitz, Advanced Materials 1998, 10, 365-377.
[4] M. Muccini, Nature Materials 2006, 5, 605-613.
[5] D. Braga and G. Horowitz, Advanced Materials 2009, 21, 1473-1486.
[6] G. S. Lee, H.-j. Kwon, T. K. An and Y.-H. Kim, Chemical Communications 2023, 59, 4995-5015.
[7] J. Panidi, D. G. Georgiadou, T. Schoetz and T. Prodromakis, Advanced Functional Materials 2022, 32, 2200694.
[8] W. Xu, Y. Chang, X. Zhu, Z. Wei, X. Zhang, X. Sun, K. Lu and Z. Wei, Chinese Chemical Letters 2022, 33, 123-132.
[9] A. G. S. Al-Azzawi, S. B. Aziz, E. M. A. Dannoun, A. Iraqi, M. M. Nofal, A. R. Murad and A. M. Hussein, Polymers 2023, 15, 164.
[10] P. M. Beaujuge and J. R. Reynolds, Chemical Reviews 2010, 110, 268-320.
[11] A. M. Österholm, L. Nhon, D. E. Shen, A. M. Dejneka, A. L. Tomlinson and J. R. Reynolds, Materials Horizons 2022, 9, 252-260.
[12] J. H. Kim, T. Schembri, D. Bialas, M. Stolte and F. Würthner, Advanced Materials 2022, 34, 2104678.
[13] R. G. Kepler, Physical Review 1960, 119, 1226-1229.
[14] O. H. LeBlanc, Jr., The Journal of Chemical Physics 1960, 33, 626-626.
[15] O. H. LeBlanc, Jr., The Journal of Chemical Physics 1961, 35, 1275-1280.
[16] J. McGinness, P. Corry and P. Proctor, Science 1974, 183, 853-855.
[17] B. Bolto, R. McNeill and D. Weiss, Australian Journal of Chemistry 1963, 16, 1090-1103.
[18] S. C. Rasmussen, Substantia 2017, 1, 99-109.
[19] C. K. Chiang, C. R. Fincher, Y. W. Park, A. J. Heeger, H. Shirakawa, E. J. Louis, S. C. Gau and A. G. MacDiarmid, Physical Review Letters 1977, 39, 1098-1101.
[20] H. Shirakawa, E. J. Louis, A. G. MacDiarmid, C. K. Chiang and A. J. Heeger, Journal of the Chemical Society, Chemical Communications 1977, 578-580.
[21] C. W. Tang and S. A. VanSlyke, Applied Physics Letters 1987, 51, 913-915.
[22] C. W. Tang, S. A. VanSlyke and C. H. Chen, Journal of Applied Physics 1989, 65, 3610-3616.
[23] S. A. Van Slyke, C. H. Chen and C. W. Tang, Applied Physics Letters 1996, 69, 2160-2162.
[24] A. Tsumura, H. Koezuka and T. Ando, Applied Physics Letters 1986, 49, 1210-1212.
[25] H. Koezuka, A. Tsumura and T. Ando, Synthetic Metals 1987, 18, 699-704.
[26] A. Sharma, C. Madhu and J. Singh, Int. J. Comput. Appl 2014, 89, 36-40.
[27] X. Ma, H. Chen, P. Zhang, M. C. Hartel, X. Cao, S. E. Diltemiz, Q. Zhang, J. Iqbal, N. R. d. Barros, L. Liu and H. Liu, IEEE Sensors Journal 2022, 22, 11405-11414.
[28] D. Elkington, N. Cooling, W. Belcher, P. C. Dastoor and X. Zhou, Electronics 2014, 3, 234-254.
[29] X. Yin, J. Yang and H. Wang, Advanced Functional Materials 2022, 32, 2202071.
[30] C. W. Tang, Applied Physics Letters 1986, 48, 183-185.
[31] G. Yu, J. Gao, J. C. Hummelen, F. Wudl and A. J. Heeger, Science 1995, 270, 1789-1791.
[32] A. J. Heeger, Advanced Materials 2014, 26, 10-28.

[33] J. J. M. Halls, C. A. Walsh, N. C. Greenham, E. A. Marseglia, R. H. Friend, S. C. Moratti and A. B. Holmes, Nature 1995, 376, 498-500.
[34] Armor Web page.
[35] Heliatek Web page.
[36] H. Liu, D. Liu, J. Yang, H. Gao and Y. Wu, Small 2023, 19, 2206938.
[37] in LG Web page, Vol.
[38] U. Salzner, J. B. Lagowski, P. G. Pickup and R. A. Poirier, Synthetic Metals 1998, 96, 177-189.
[39] M. Kertesz, C. H. Choi and S. Yang, Chemical Reviews 2005, 105, 3448-3481.
[40] J. Roncali, Chemical Reviews 1997, 97, 173-206.
[41] A. Labrunie, Y. Jiang, F. Baert, A. Leliège, J. Roncali, C. Cabanetos and P. Blanchard, RSC Advances 2015, 5, 102550-102554.
[42] P. Simón Marqués, J. M. A. Castán, B. A. L. Raul, G. Londi, I. Ramirez, M. S. Pshenichnikov, D. Beljonne, K. Walzer, M. Blais, M. Allain, C. Cabanetos and P. Blanchard, Chemistry – A European Journal 2020, 26, 16422-16433.
[43] J. Roncali and C. Thobie-Gautier, Advanced Materials 1994, 6, 846-848.
[44] I. Osaka, S. Shinamura, T. Abe and K. Takimiya, Journal of Materials Chemistry C 2013, 1, 1297-1304.
[45] J. H. Burroughes, D. D. C. Bradley, A. R. Brown, R. N. Marks, K. Mackay, R. H. Friend, P. L. Burns and A. B. Holmes, Nature 1990, 347, 539-541.
[46] A. J. Heeger, Chemical Society Reviews 2010, 39, 2354-2371.
[47] A. J. Heeger, Angewandte Chemie International Edition 2001, 40, 2591-2611.
[48] J. U. Wallace and S. H. Chen in Fluorene-Based Conjugated Oligomers for Organic Photonics and Electronics, Eds.: U. Scherf and D. Neher), Springer Berlin Heidelberg, Berlin, Heidelberg, 2008, pp. 145-186.
[49] I. V. Kurdyukova and A. A. Ishchenko, Russian Chemical Reviews 2012, 81, 258.
[50] J. V. Grazulevicius, P. Strohriegl, J. Pielichowski and K. Pielichowski, Progress in Polymer Science 2003, 28, 1297-1353.
[51] J. Li and A. C. Grimsdale, Chemical Society Reviews 2010, 39, 2399-2410.
[52] A. D'Orazio-Colman, D. H. Son, R. F. Binti Nasrun and J. H. Kim, Journal of Power Sources 2022, 542, 231737.
[53] B. Amna, H. M. Siddiqi, A. Hassan and T. Ozturk, RSC Advances 2020, 10, 4322-4396.
[54] Z. Xue, S. Chen, N. Gao, Y. Xue, B. Lu, O. A. Watson, L. Zang and J. Xu, Polymer Reviews 2020, 60, 318-358.
[55] S. H. Park, J.-S. Ahn, N. Y. Kwon, C. H. Diem, A. K. Harit, H. Y. Woo, M. J. Cho and D. H. Choi, Macromolecular Research 2021, 29, 435-442.
[56] S.-i. Kato, T. Furuya, A. Kobayashi, M. Nitani, Y. Ie, Y. Aso, T. Yoshihara, S. Tobita and Y. Nakamura, The Journal of Organic Chemistry 2012, 77, 7595-7606.
[57] J. Yuan, Y. Zhang, L. Zhou, C. Zhang, T.-K. Lau, G. Zhang, X. Lu, H.-L. Yip, S. K. So, S. Beaupré, M. Mainville, P. A. Johnson, M. Leclerc, H. Chen, H. Peng, Y. Li and Y. Zou, Advanced Materials 2019, 31, 1807577.
[58] H. Yu, M. Pan, R. Sun, I. Agunawela, J. Zhang, Y. Li, Z. Qi, H. Han, X. Zou, W. Zhou, S. Chen, J. Y. L. Lai, S. Luo, Z. Luo, D. Zhao, X. Lu, H. Ade, F. Huang, J. Min and H. Yan, Angewandte Chemie International Edition 2021, 60, 10137-10146.
[59] T. Wang, R. Sun, W. Wang, H. Li, Y. Wu and J. Min, Chemistry of Materials 2021, 33, 761-773.
[60] Y. Li, M. Gu, Z. Pan, B. Zhang, X. Yang, J. Gu and Y. Chen, Journal of Materials Chemistry A 2017, 5, 10798-10814.

[61] I. McCulloch, R. S. Ashraf, L. Biniek, H. Bronstein, C. Combe, J. E. Donaghey, D. I. James, C. B. Nielsen, B. C. Schroeder and W. Zhang, Accounts of Chemical Research 2012, 45, 714-722.
[62] A. Laventure, S. Stanzel, A.-J. Payne, B. H. Lessard and G. C. Welch, Journal of Chemical Technology & Biotechnology 2022, 97, 844-851.
[63] A. C, D. K. Dubey, M. Pahlevani and G. C. Welch, Advanced Materials Technologies 2021, 6, 2100264.
[64] S. V. Dayneko, E. Cieplechowicz, S. S. Bhojgude, J. F. Van Humbeck, M. Pahlevani and G. C. Welch, Materials Advances 2021, 2, 933-936.
[65] R. Stalder, J. Mei, K. R. Graham, L. A. Estrada and J. R. Reynolds, Chemistry of Materials 2014, 26, 664-678.
[66] L. Fu, W. Fu, P. Cheng, Z. Xie, C. Fan, M. Shi, J. Ling, J. Hou, X. Zhan and H. Chen, Journal of Materials Chemistry A 2014, 2, 6589-6597.
[67] C.-W. Ge, C.-Y. Mei, J. Ling, F.-G. Zhao, H.-J. Li, L. Liang, J.-T. Wang, J.-C. Yu, W. Shao, Y.-S. Xie and W.-S. Li, Journal of Polymer Science Part A: Polymer Chemistry 2014, 52, 2356-2366.
[68] O. Wallquist and R. Lenz, Macromolecular Symposia 2002, 187, 617-630.
[69] S. Ghosh, R. Raveendran, A. Saeki, S. Seki, M. Namboothiry and A. Ajayaghosh, ACS Applied Materials & Interfaces 2019, 11, 1088-1095.
[70] T. Xu and L. Yu, Materials Today 2014, 17, 11-15.
[71] X. Guo, M. Baumgarten and K. Müllen, Progress in Polymer Science 2013, 38, 1832-1908.
[72] S. B. Mdluli, M. E. Ramoroka, S. T. Yussuf, K. D. Modibane, V. S. John-Denk and E. I. Iwuoha, Polymers 2022, 14, 716.
[73] L. Lu, T. Zheng, Q. Wu, A. M. Schneider, D. Zhao and L. Yu, Chemical Reviews 2015, 115, 12666-12731.
[74] R. S. Kularatne, F. J. Taenzler, H. D. Magurudeniya, J. Du, J. W. Murphy, E. E. Sheina, B. E. Gnade, M. C. Biewer and M. C. Stefan, Journal of Materials Chemistry A 2013, 1, 15535-15543.
[75] C. Cabanetos, A. El Labban, J. A. Bartelt, J. D. Douglas, W. R. Mateker, J. M. J. Fréchet, M. D. McGehee and P. M. Beaujuge, Journal of the American Chemical Society 2013, 135, 4656-4659.
[76] W. Li, K. H. Hendriks, M. M. Wienk and R. A. J. Janssen, Accounts of Chemical Research 2016, 49, 78-85.
[77] E. Wang, L. Hou, Z. Wang, S. Hellström, F. Zhang, O. Inganäs and M. R. Andersson, Advanced Materials 2010, 22, 5240-5244.
[78] J. Kudrjasova, J. Kesters, P. Verstappen, J. Brebels, T. Vangerven, I. Cardinaletti, J. Drijkoningen, H. Penxten, J. Manca, L. Lutsen, D. Vanderzande and W. Maes, Journal of Materials Chemistry A 2016, 4, 791-795.
[79] Y.-H. Chen, L.-Y. Lin, C.-W. Lu, F. Lin, Z.-Y. Huang, H.-W. Lin, P.-H. Wang, Y.-H. Liu, K.-T. Wong, J. Wen, D. J. Miller and S. B. Darling, Journal of the American Chemical Society 2012, 134, 13616-13623.
[80] J. Zeng, N. Qiu, J. Zhang, X. Wang, C. Redshaw, X. Feng, J. W. Y. Lam, Z. Zhao and B. Z. Tang, Advanced Optical Materials 2022, 10, 2200917.
[81] J. Roncali, Accounts of Chemical Research 2009, 42, 1719-1730.
[82] Z. Zhang and Y. Lin, ACS Omega 2020, 5, 24994-24999.
[83] F. C. Krebs, Organic Electronics 2009, 10, 761-768.
[84] Y. Li, Science China Chemistry 2015, 58, 191-191.

[85] B. Kan, Q. Zhang, M. Li, X. Wan, W. Ni, G. Long, Y. Wang, X. Yang, H. Feng and Y. Chen, Journal of the American Chemical Society 2014, 136, 15529-15532.
[86] L. Yuan, Y. Zhao, J. Zhang, Y. Zhang, L. Zhu, K. Lu, W. Yan and Z. Wei, Advanced Materials 2015, 27, 4229-4233.
[87] R. Po and J. Roncali, Journal of Materials Chemistry C 2016, 4, 3677-3685.
[88] P. Bi, C. An, T. Zhang, Z. Chen, Y. Xu, Y. Cui, J. Wang, J. Li, Y. Wang, J. Ren, X. Hao, S. Zhang and J. Hou, Journal of Materials Chemistry A 2023, 11, 983-991.
[89] S. Tu, L. Zhang, X. Lin, L. Xiao, W. Wang and Q. Ling, Journal of Materials Chemistry C 2022, 10, 2026-2033.
[90] B. Carsten, F. He, H. J. Son, T. Xu and L. Yu, Chemical Reviews 2011, 111, 1493-1528.
[91] P. Espinet and A. M. Echavarren, Angewandte Chemie International Edition 2004, 43, 4704-4734.
[92] I. Maluenda and O. Navarro, Molecules 2015, 20, 7528-7557.
[93] D. J. Schipper and K. Fagnou, Chemistry of Materials 2011, 23, 1594-1600.
[94] J. Zhang, D.-Y. Kang, S. Barlow and S. R. Marder, Journal of Materials Chemistry 2012, 22, 21392-21394.
[95] P. Berrouard, A. Najari, A. Pron, D. Gendron, P.-O. Morin, J.-R. Pouliot, J. Veilleux and M. Leclerc, Angewandte Chemie International Edition 2012, 51, 2068-2071.
[96] J.-R. Pouliot, F. Grenier, J. T. Blaskovits, S. Beaupré and M. Leclerc, Chemical Reviews 2016, 116, 14225-14274.
[97] L. G. Mercier and M. Leclerc, Accounts of Chemical Research 2013, 46, 1597-1605.
[98] R. Matsidik, H. Komber and M. Sommer, ACS Macro Letters 2015, 4, 1346-1350.
[99] T. Bura, S. Beaupré, M.-A. Légaré, J. Quinn, E. Rochette, J. T. Blaskovits, F.-G. Fontaine, A. Pron, Y. Li and M. Leclerc, Chemical Science 2017, 8, 3913-3925.
[100] P. Chávez, C. Ngov, P. d. Frémont, P. Lévêque and N. Leclerc, The Journal of Organic Chemistry 2014, 79, 10179-10188.
[101] P. Josse, S. Dayneko, Y. Zhang, S. Dabos-Seignon, S. Zhang, P. Blanchard, G. C. Welch and C. Cabanetos, Molecules 2018, 23, 962.
[102] F. Lombeck, H. Komber, S. I. Gorelsky and M. Sommer, ACS Macro Letters 2014, 3, 819-823.
[103] W. B. Breukelaar, S. M. McAfee and G. C. Welch, New Journal of Chemistry 2018, 42, 1617-1621.
[104] R. Matsidik, H. Komber, A. Luzio, M. Caironi and M. Sommer, Journal of the American Chemical Society 2015, 137, 6705-6711.
[105] R. Matsidik, J. Martin, S. Schmidt, J. Obermayer, F. Lombeck, F. Nübling, H. Komber, D. Fazzi and M. Sommer, The Journal of Organic Chemistry 2015, 80, 980-987.
[106] F. Grenier, K. Goudreau and M. Leclerc, Journal of the American Chemical Society 2017, 139, 2816-2824.
[107] S.-L. Suraru, J. A. Lee and C. K. Luscombe, ACS Macro Letters 2016, 5, 724-729.

CHAPTER 2
CHAPTER 2
CHAPTER 2
CHAPTER 2
CHAPTER 2

Chapter 2:

Preparation of active compounds by DHA for solar cells applications

CHAPTER 2

The Photovoltaic Effect

Discovered in 1839 by Alexandre Edmond Becquerel, the photovoltaic effect corresponds to the generation of electric current and voltage from a material when exposed to light.[1-2] He indeed showed that a photon absorbed by a semi-conducting material brings the requested energy to promote the formation of a hole-electron pair, named exciton, which, once dissociated into two different charges, leads to the generation of an electric current.

However, it was not until 1954 that the first solar cell prototype was demonstrated, out of crystalline silicon, thus kick-starting the era of the first generation of solar cells.[3] Couple of years later, this technology is now totally viable since commercially available and accessible to *the man on the street*. As a matter of fact, silicon-based PV currently produces 95% of the photo generated electricity.[4] However, it suffers from several drawbacks such as limited recyclability, high weight and rigidity (architectural constraints), high energy-demanding fabrication, and weak indoor efficiencies or simply under diffused light.

In this context, a second generation of solar cells was developed in the early 70's, based on crystalline inorganic materials such as GaAs (gallium arsenide), CIGS (copper indium gallium diselenide) or CdTe (cadmium telluride).[5-7] Their improved optical properties (in comparison to the first generation) allow the use of thinner layers, decreasing the required weight and even enabling their deposition on flexible substrates. Nevertheless, the rarity and/or toxicity of some of the constituting active materials represent(s) significant obstacles to a potential large-scale commercialization and dissemination.

Hence, to overcome these major issues, the third and current generation was introduced which is based on the use of organic active components. This generation is divided into three different subfamilies, namely, the Dye-Sensitized Solar Cells (DSSCs),[8-10] the Organic Solar Cells (OSCs), and the Perovskite Solar Cells (PSCs).

Directly related to these last two types of devices, new accessible active compounds prepared by direct (hetero) arylation within the frame of this PhD thesis, will thus be discussed in the remainder of this chapter.

2.1 Organic Photovoltaics (OPVs)

2.1.1 A Brief History of OPVs

The first example of solar cells using organic materials as the active layer was reported in 1958.[11] From an architectural point of view, it consisted of a superposition of magnesium phthalocyanine (MgPh) and tetramethyl *p*-phenylenediamine (TMPD) layers coated between two electrodes. Even though the efficiency of this cell was extremely low, the authors had already discovered the primordial concept of using electron donor (D) and electron acceptor (A) materials in the active layer. Then, in the following years, the so-called Schottky cells were mainly developed, consisting in the use of a single organic semiconductor sandwiched between two metal electrodes characterized by different work functions.[12] Various dyes were thus embedded such as magnesium phthalocyanine,[13] chlorophyll a,[14] squaraine derivatives,[15] or even merocyanines[16-17] (structures in Figure 2.1).

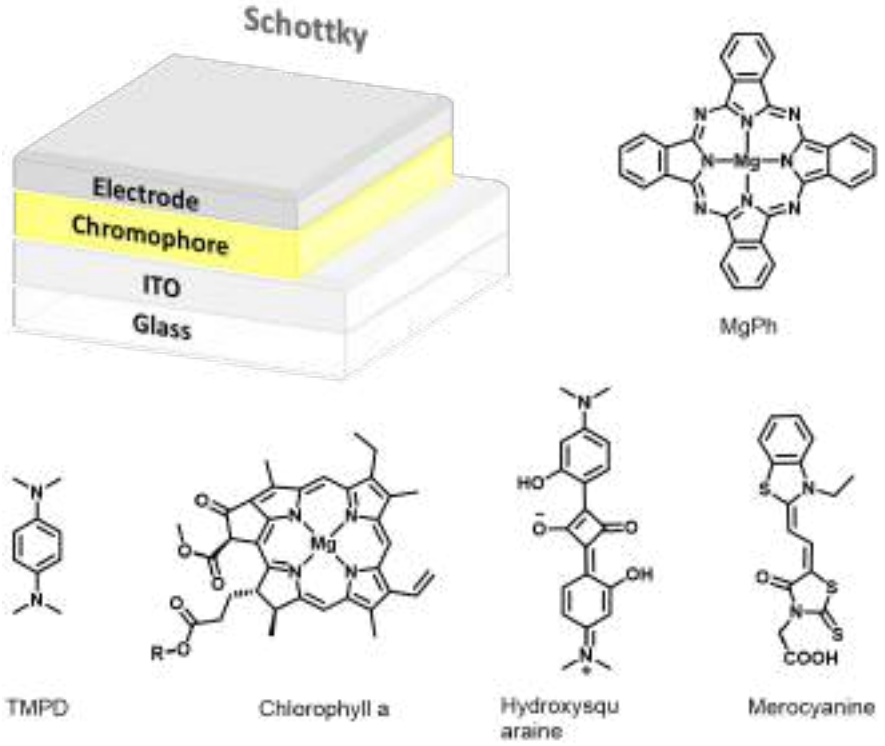

Figure 2.1 Structure of a Schottky device and example of chromophores used as active compounds.

The photovoltaic conversions of these single-material devices were notably inefficient (< 1%). The electric field generated by the electrodes remains insufficient, not allowing an effective dissociation of the charges thus favoring a high rate of recombination within the material and exciton quenching at the organic material/metallic electrode interface.

It took several years to see the donor-acceptor concept reconsidered and revived by Tang.[18] Indeed, a bilayer structure (so-called bilayer or planar heterojunction (PHJ) solar cell) with two organic materials with different electron-affinity and ionization potentials, was reported in 1986 by combining an electron-donating compound, the copper phthalocyanine (CuPc) and an electron-accepting material, the perylenebisbenzimidazole (PTCBI) (Figure 2.2).

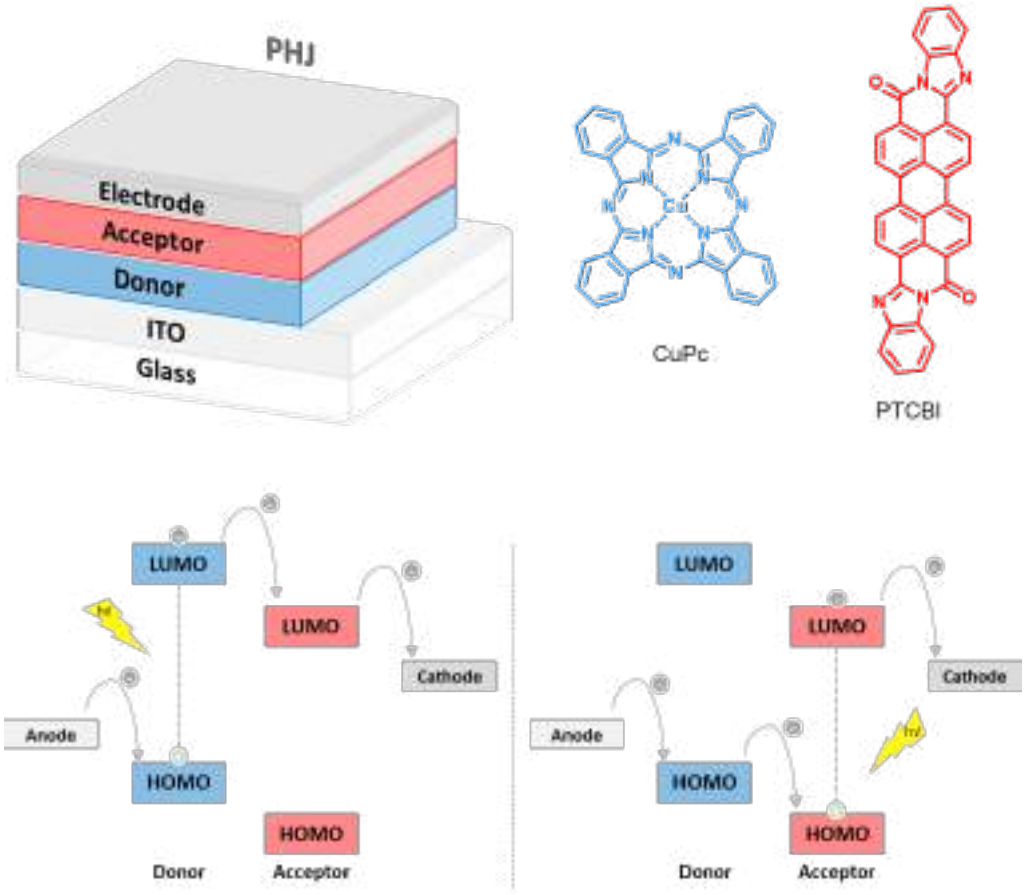

Figure 2.2 Architecture of the bilayer cell reported by Tang in 1986 with the chemical structures of the donor and acceptor molecules used to create the planar heterojunction and its working principle.

In this planar heterojunction, the photocurrent results from four specific steps that are:

(1) Photon absorption: The photon absorbed by one of the semiconducting materials of the active layer leads to the excitation of an electron from the HOMO to the LUMO level, creating an electron-hole pair, the so-called exciton.

(2) Exciton diffusion: The exciton obtained migrates to the D/A interface.

(3) Exciton dissociation: With optimized energy levels, the exciton generates free charge carriers, dissociating into positive charges (holes) and negative charges (electrons).

(4) Charges collection: The electron goes through the acceptor toward the cathode and the hole through the donor towards the anode, thus creating an electrical current.

Hence with a promising power conversion efficiency of 1% demonstrated, this architecture was rapidly adopted by the OSC community and is still used to assess the potential of new organic materials. However, the short exciton lifetime in organic semiconductors (< 1 ns), limits the diffusion length to 20 nm approximatively, thus impacting the thickness of the layers, the light absorption, and subsequently the efficiency of the device.[19]

To tackle these limitations, the concept of bulk heterojunction (BHJ) was then introduced in 1995.[20-21] In this architecture, both components of the active layer are mixed together before deposition, instead of processed separately, leading to phase-separated nanodomains of donors and acceptors favoring the exciton dissociation (Figure 2.3).[22]

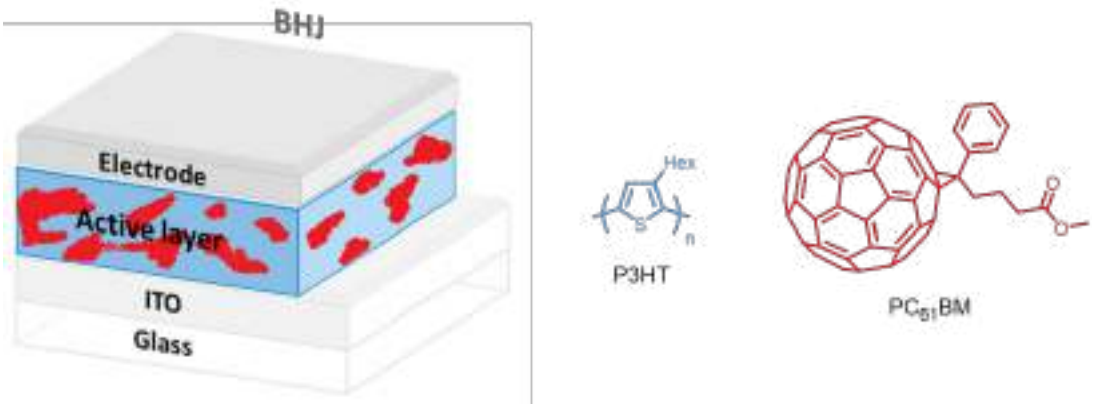

Figure 2.3 Architecture of the bulk heterojunction device with the structures of the most-studied photoactive layer.

Since the seminal report of this concept, one of the most-studied photoactive layer in BHJ OSCs was undoubtedly based on poly(3-hexylthiophene-2,5-diyl) (P3HT) blended with [6,6]-phenyl-C_{61}-butyric acid methyl ester ($PC_{61}BM$), as electron-donor and electron-acceptor, respectively.[23]

2.1.2 The active layer

In current state-of-the-art devices, the active layer is still composed of a blend of an electron-donor (D) and an electron-acceptor (A) materials. In addition to significant device optimization to mainly control the morphology and adapt the interlayers for a better charge discrimination/extraction,[24-25] remarkable work has been achieved by chemists in providing original and compatible D and A structures.

2.1.2.1 Acceptor materials

Since their discovery in 1985,[26] fullerene derivatives have been widely used as acceptor materials in OSCs. Their long reign can be directly related to their i) great electron-withdrawing capability, ii) ability to reversibly accept up to six electrons, iii) outstanding electron mobility, and iv) isotropic charge transport.[27-28] In comparison to the most studied acceptor semiconductor namely the C_{60} characterized by an almost negligible absorption in the visible spectrum, the more expensive C_{70}, shows additional electronic transitions resulting in an improved absorbance between 400-600 nm and subsequently improved photoconversion.[29] Deposited by *vacuum*-process due to their low solubility in common organic solvents, cyclopropanation reactions were developed to afford soluble fullerene analogs namely $PC_{61}BM$ and $PC_{71}BM$, thus opening doors to solution-processed OSCs (Figure 2.4).[30]

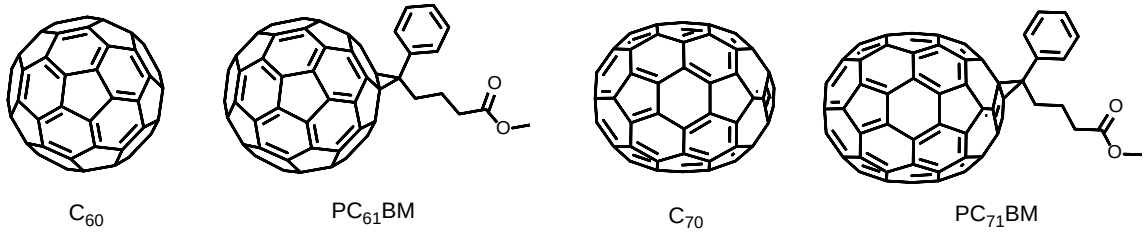

Figure 2.4 Chemical structures of fullerene acceptors.

However, the limited range of chemical modifications to tune their energy levels, their low absorption properties in the visible range and modest stabilities of the resulting devices (crystallinity, dimerization, *etc.*) pushed chemists to consider and develop alternatives, paving the way to the current generation of Non-Fullerene Acceptors (NFA).[31-34]

Historically used (cf Tang's bilayer), and one of the most commonly investigated families of compounds as NFAs undoubtedly is the rylene family,[35] and more precisely the perylene diimide (PDI) molecule.[36-38] The latter is indeed available at low cost and shows great absorption coefficient, good mobility, and electron-affinity, in addition to excellent thermal and chemical stabilities. The evolution of PDI-based acceptors, in the last decade, is strongly correlated to the development of multimer architectures by attaching a number of PDI units to a central core resulting in a geometrical distortion of the molecules inhibiting the strong propensity to self-aggregate [39-42] (see some structures in Figure 2.5).

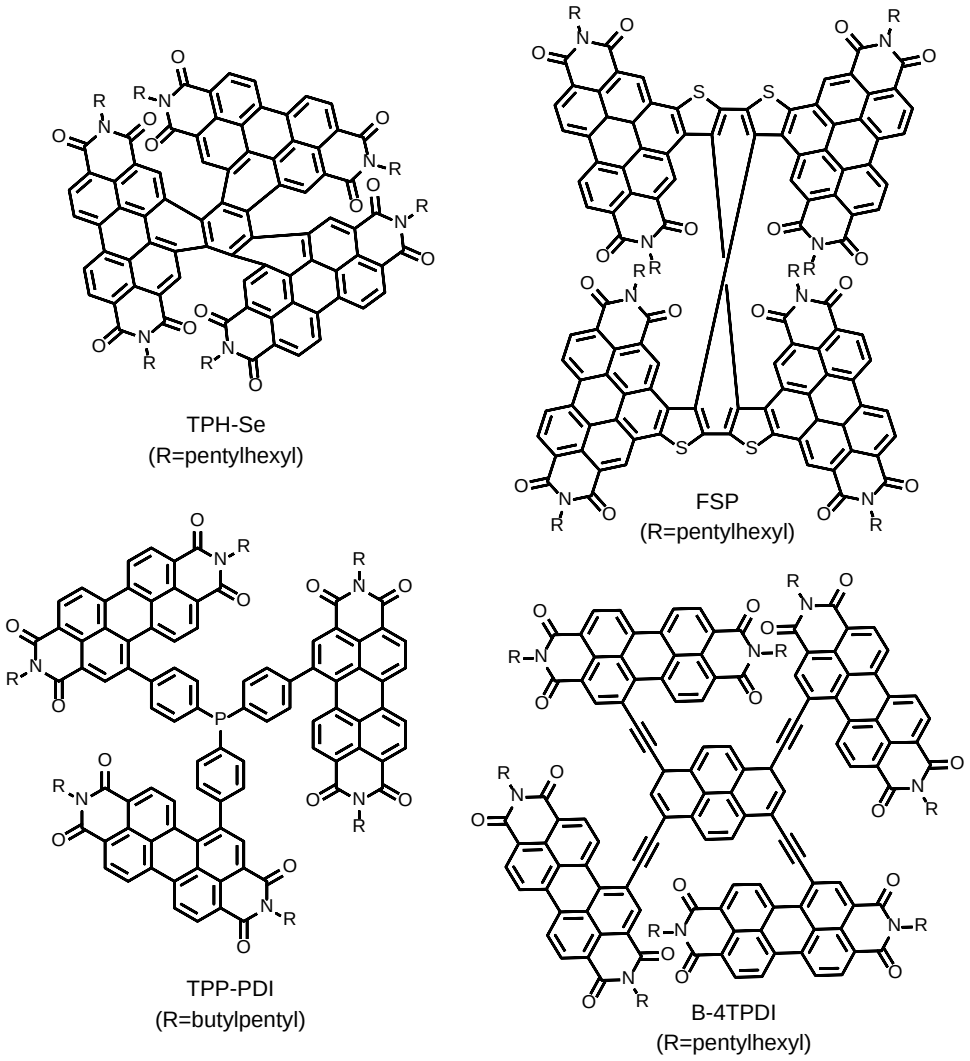

Figure 2.5 Examples of some PDI derivatives used as NFAs in OPV.

Recently, OSCs based on PDI-type NFAs have surpassed 11% of efficiencies once combined with a mid/low band gap donor polymer (P3TEA or PM6).[43-45] However, this PCE does not come free of charge since the synthetic complexity of these molecules appears to be significantly improved compared to the simple monomeric PDIs.

In recent years, another type of NFAs has been reported and built on A-D-A or A-DA'D-A molecular configuration. The most famous and most studied families are based on ITIC and Y6 key building blocks (see Figure 2.6). With impressive efficiencies, swiftly surpassing those of the fullerene, hundreds of molecules/analogs have been designed, synthesized, evaluated, and reported.[46-48] For instance, the Y-series NFAs are capable to achieve more red-shifted

absorption bands than those of ITIC-type NFAs,[49] increasing the J_{SC} values with relatively low V_{OC} losses reaching PCEs over 18% and becoming the current state-of-the-art family. Both ITIC and Y6 are now "*commercially*" available (from middle-scale companies), but their complex synthetic procedures impact their prices (> 2000 euros for 1 g of Y6).

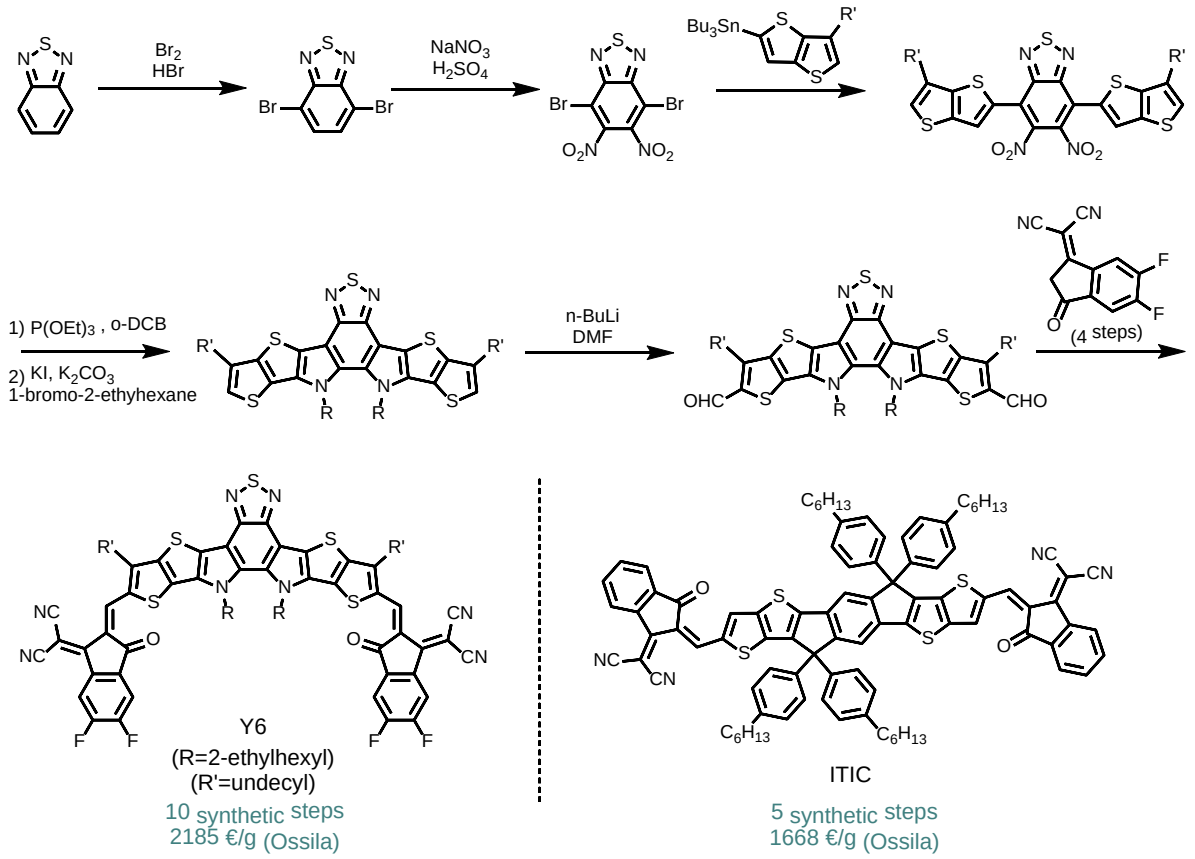

Figure 2.6 Representation of the synthetic path towards Y6 molecule and chemical structure of the ITIC NFA.

But instead of devoting efforts to simplifying the synthetic route, researchers tend to design even more complicated structures to keep improving the efficiencies and therefore publish these results in high-impact factor journals. An obvious example is the trimer acceptor named TYT (Figure 2.7), consisting of three "small" molecular acceptor units linked by two electron-donating thiophene spacers. Despite an obvious synthetic challenge, this molecule in combination with the PM6 polymer donor, was able to reach a high PCE of 18.15% but above

all, a good operational stability under 1-sun illumination with a retention of 80% of this value after 8454 hours.[50]

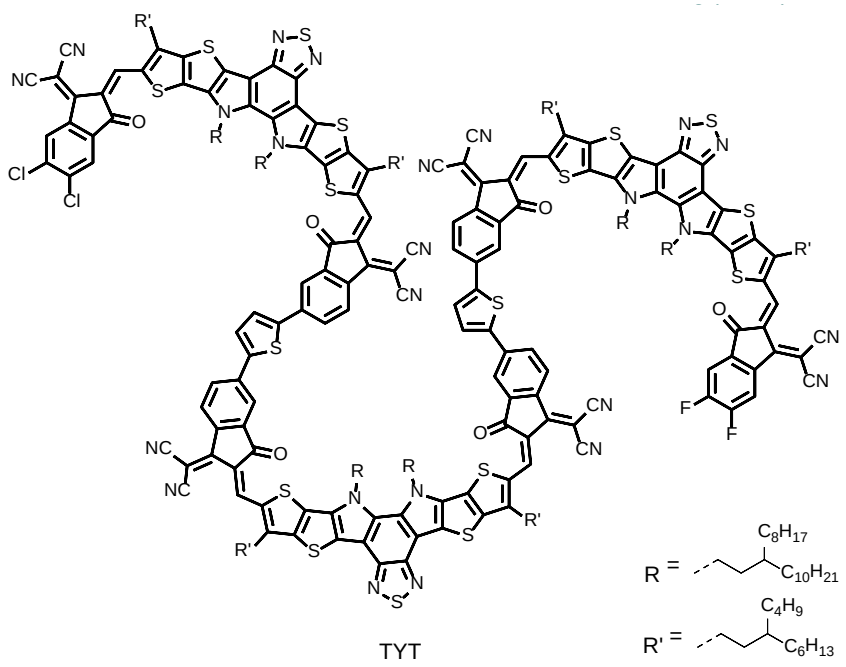

Figure 2.7 Structure of the high-performance TYT NFA molecule.

2.1.2.2 Donor materials

With almost two decades of reign of fullerene-based acceptors, myriads of donor materials were reported to target an optimized complementarity from both energetic and morphological points of view. Briefly introduced in Chapter 1, this paragraph will mostly focus on the synthetic pathways, number of steps, and costs of some selected high performing donor materials.[51]

Usually prepared by altering electron-poor and electron-rich building blocks/monomers, almost endless combinations can be easily considered.[52] From the literature, the benzodithiophene (BDT) appears as a key and major unit for the preparation of both high performing molecules[53-55] and polymers.[56-58] Used as monomer, the latter was co-polymerized with different electron-poor blocks to afford, for instance the PBDB-T, also known as PCE12, corresponding to its performance when blended with $PC_{71}BM$ (polymerization with the co-monomer BDD, Figure 2.8).

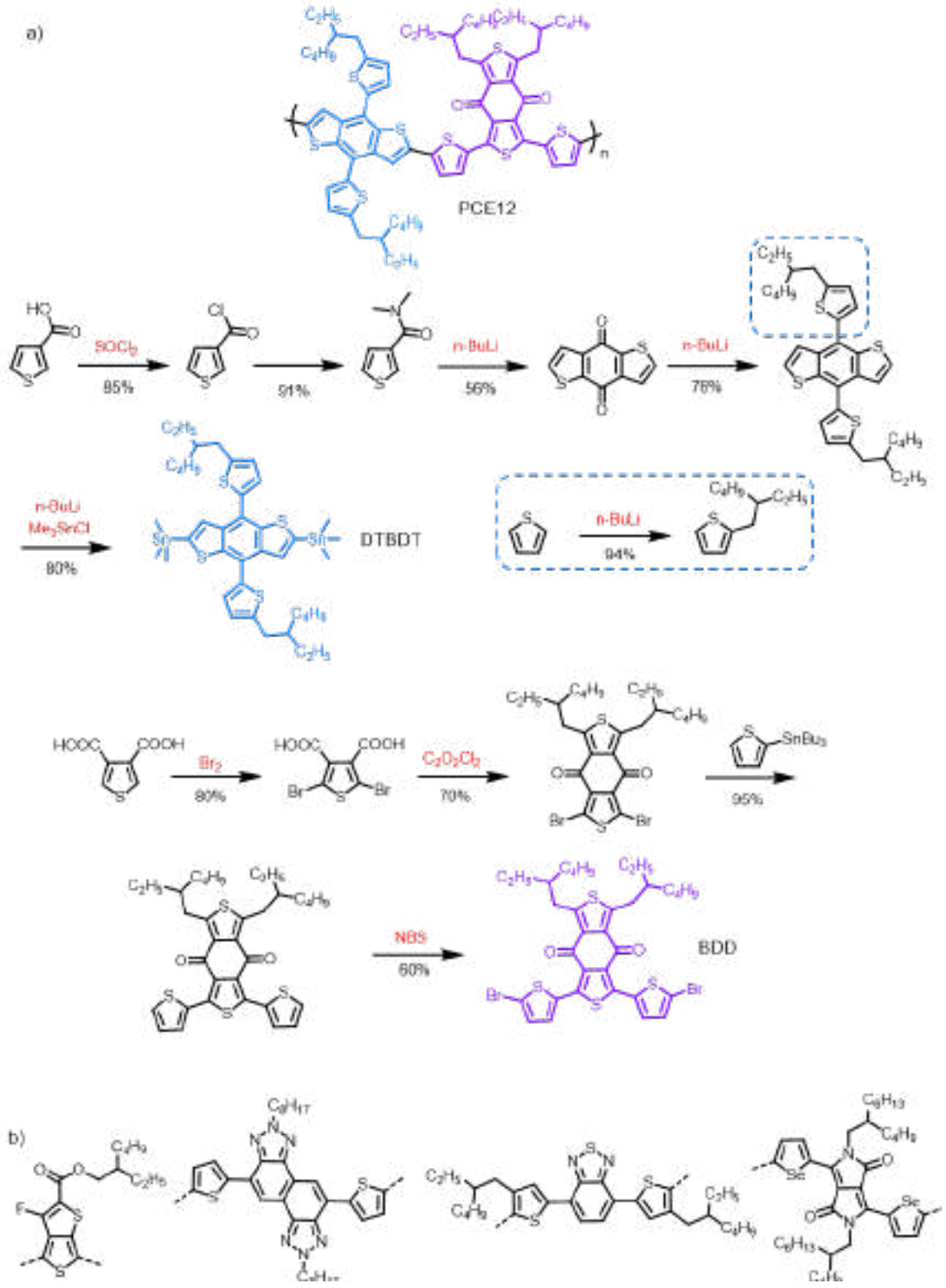

Figure 2.8 a) Synthetic procedures to obtain DTBDT and BDD, monomers of the PCE12 polymer; b) Structures of some other electron-poor monomers polymerized with DTBDT.

In parallel, the BDT was also used to prepare the O-BDTdFBT large molecular donor (see synthesis and structure in Scheme 2.1) that was able to achieve a PCE > 8% in 2015 when, once again, combined with $PC_{71}BM$.[53]

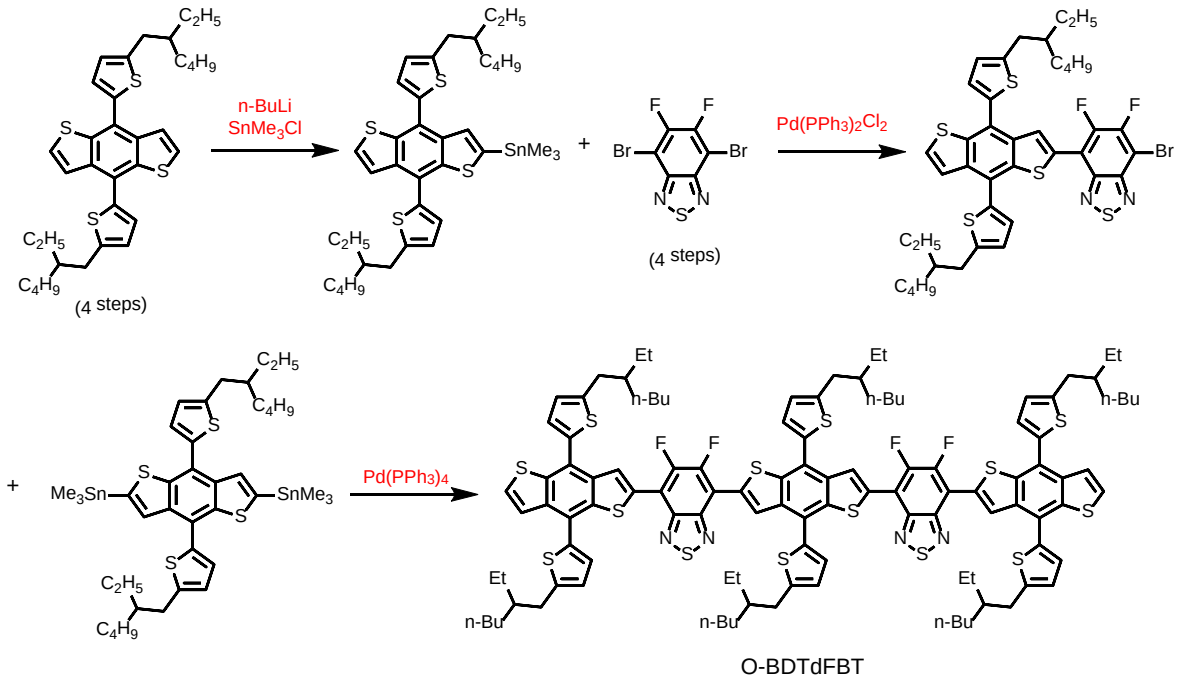

Scheme 2.1 Synthesis and chemical structure of the O-BDTdFBT molecular donor.

Though highly efficient, particularly when now associated with the new generation of non-fullerene acceptors, their time consuming multi steps syntheses hinder their potential large scale and commercial preparation. In this context, Sun C. *et al.* designed in 2018 a low cost and high performance polymer donor material, namely the PTQ10 that was demonstrated to achieve PCEs around 12.70% when used with IDIC acceptor [59] (see structures in Figure 2.9). Recently, this promising donor was combined to the T2EH acceptor (Figure 2.9), functionalized with alkylthienyl outer sidechains, and an outstanding PCE above 18% was recorded.[60]

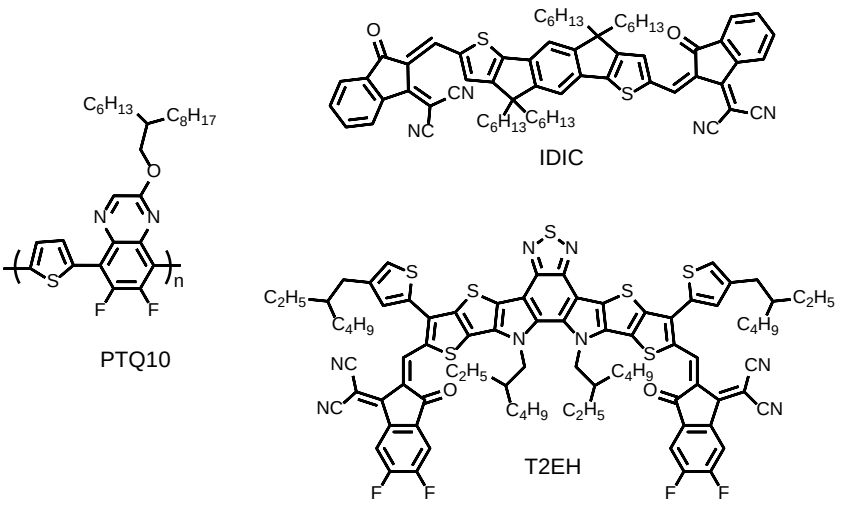

Figure 2.9 Structures of PTQ10 donor polymer, IDIC and T2EH NFAs.

Beyond this efficiency, half issue remains considering the synthetic accessibility of the acceptor. Moreover, PTQ10 as a polymer, still presents a major drawback which is its inherent polydispersity, known to affect the batch-to-batch reproducibility. Consequently, discrete conjugated molecules[61] appears to be an ideal and appealing alternative. And several examples of simple structure such as push-pull type molecules (i.e. presenting an internal charge transfer) have attracted considerable research attention due to their ease of synthesis, tunability, suitable absorption in the visible spectrum [62-64] and potential compatibility with both solution and vacuum deposition processes. For instance, the DTDCPB derivative (Scheme 2.2), prepared in 5 steps, is a good example since impressive efficiencies of 9.8% and 15% were demonstrated when combined with C_{70} in single- and multi-junction stacks, respectively.[65]

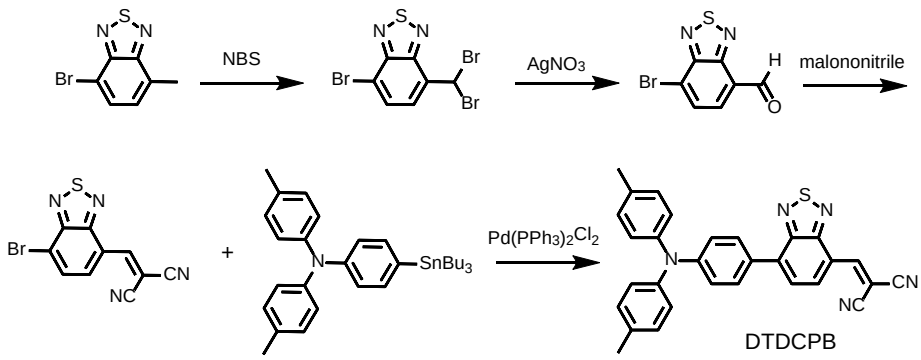

Scheme 2.2 Synthesis and structure of DTDCPB.

2.1.3 Making it Simple: the signature look of Angers for the past 17 years

Major actor in the development of simple and accessible active compounds for OSCs, the SCL "Systèmes Conjugués Linéaires" group of MOLTECH-Anjou laboratory has spent more than 17 years on arylamine-based push-pull molecules,[66] initiated by the groundbreaking on a star-shaped triphenylamine (TPA), published in 2006.[67] This electron-rich block indeed demonstrates strong hole transport properties and a high degree of versatility since minor chemical changes can induce significant impact on the optical, electrochemical, self-assembling, and therefore, photovoltaic performances.[68]

Flagship of the group, the TPA-T-DCV compound,[69] obtained by coupling a TPA donor block[70] to a dicyanovinyl (DCV) acceptor unit through a thiophene spacer, constitutes the archetype of this family (Figure 2.10).

Initially synthesized in three steps, the latter allowed for achieving photoconversion yields of 2.5% in a PHJ cell with C_{60}. The PCE was then raised to 3.7% with C_{70}[71] and 4.0% in co-evaporated BHJ-based solar cells, thanks to device engineering and optimization.[72]

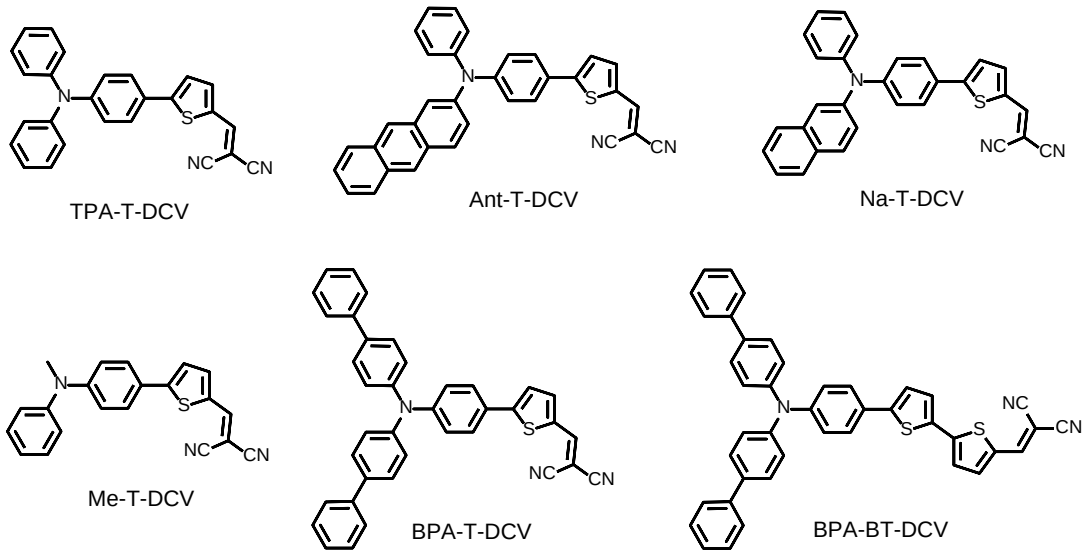

Figure 2.10 Chemical structures of arylamine-based push-pull small molecular donors from Angers.

In parallel, various chemical modifications were considered and carried out over the years. For instance, substituting one of the outer phenyls of the TPA unit with an anthryl (Ant-T-DCV) or a naphthyl (Na-T-DCV) was shown to improve the hole-mobilities (by three and five times respectively).[73-74] In addition, the replacement of an outer phenyl group by a simple methyl (Me-T-DCV) results in an unexpected gap reduction in the thin film along with a marked improvement in the hole-transport characteristics (ca. 5.0×10^{-4} $cm^2V^{-1}s^{-1}$ vs. 1.0×10^{-5} $cm^2V^{-1}s^{-1}$ for TPA-T-DCV), leading to a higher power conversion efficiency (3.3% vs. 2.5% for TPA-T-DCV).[75] Last but not least, the preparation of biphenylamine-based push-pull derivatives (BPA-T-DCV and BPA-BT-DCV) yielded remarkable hole mobilities (of *ca.* 1.0×10^{-3} $cm^2V^{-1}s^{-1}$) and FFs values among the highest published so far with small molecular donors (> 73%).[76]

Considering that the lower production cost is still one of the major advantages of OPVs claim by the community over conventional silicon or inorganic photovoltaic technologies, efforts should be devoted to reduce/limit the synthetic steps, complexity and chemical waste generated during the synthesis of active compounds.[77-78] Based on the know-how of the group, promising results already published, it is in this context that the new TPA based derivatives were designed, synthesized and evaluated.

2.2 Triarylamine-difluorobenzothiadiazole based push-pull molecular donors for Organic Photovoltaics

2.2.1 Context and molecular design

Recently, the synthesis of the triarylamine based push–pull TPA-T-DCV, (Figure 2.1.9) flagship of our group, was simplified by using the trendy direct (hetero)arylation cross-coupling reaction.[79] Accessible now at gram-scale in only two steps from cheap commercially available starting materials, these results opened doors to new potential chemical variations accessible with difficulties with conventional coupling reactions. Hence, considering the impressive efficiencies achieved by Wong and coworkers with their DTDCPB, the insertion of electron-deficient (hetero)aromatic namely the benzothiadiazole (BzT) represents a particularly interesting approach to fine-tune the ground- and excited-state characteristics of the D–A system.[80] However, as depicted in Scheme 2.2, the use of the BzT building block generally requires harsh electrophilic halogenation conditions leading to moderate yields, mixtures of products, and/or unstable intermediates.[81] In this context, the direct (hetero)-arylation appears to be a method of choice to overcome these synthetic problems, particularly with 5,6-difluoro-2,1,3-benzothiadiazole (BT2F) where only two positions are reactive. Moreover, it is important to note that the latter can be prepared in only one step from a cheap and commercially available starting block, *vs* four for its dibromo analog (Scheme 2.3).

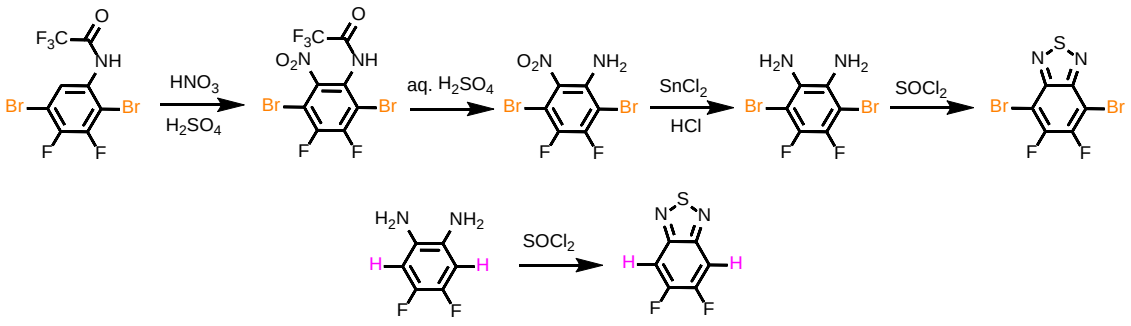

Scheme 2.3 Comparison of the synthetic route to 5,6-difluoro-2,1,3-benzothiadiazole compared to its dibromo counterpart.

However, very limited examples of BT2F-based molecular systems were found in the literature and to date none of them were embedded in devices.[82] With this in mind and from the experience

of the group, the two target molecular push–pull derivatives, which structures are illustrated in Figure 2.11, were designed.

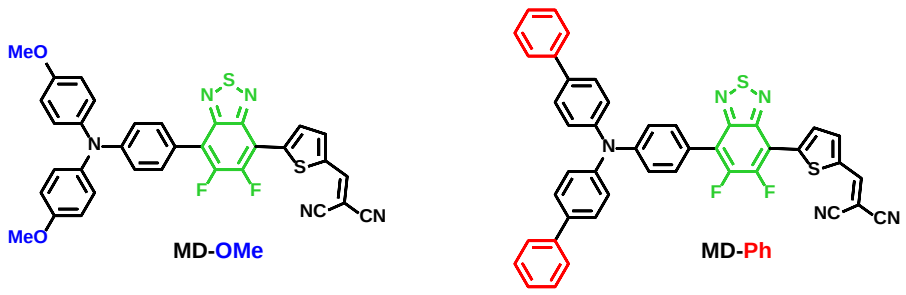

Figure 2.11 Chemical structures of the target push-pull derivatives.

Two different triphenylamine blocks were thus considered to rationalize their impact on the electronic, charge transport and therefore their photovoltaic properties. While the methoxy groups of MD-OMe are expected to increase the donor strength of the triphenylamine block, the two biphenyl side groups of MD-Ph are expected, as discussed above, to increase the hole mobility of the corresponding analogue.[76]

2.2.2 Synthesis

Both target compounds (**MD-OMe** and **MD-Ph**) were initially prepared according to the synthetic route depicted in Scheme 2.4. To do so, the direct arylation coupling between BT2F and 4-bromo-N,N-bis(4-methoxyphenyl)aniline was first carried out, and optimized, to afford the arylamine functionalized unsymmetrical 5,6-difluoro-2,1,3-benzothiadiazole derivative **2**.

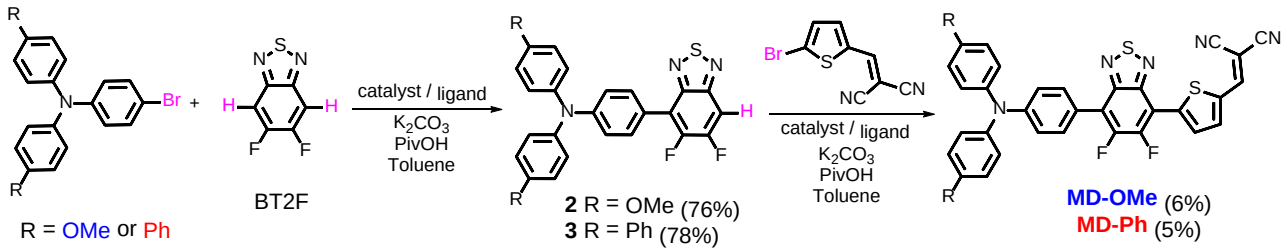

*Scheme 2.4 Synthetic route for **MD-OMe** and **MD-Ph**.*

As shown in Table 2.1, the first attempt was performed in the presence of palladium(II) acetate and tri-tert-butylphosphonium tetrafluoroborate ($P^tBu_3.HBF_4$) in conventional oil bath heating (entry 1). Despite operating in relatively diluted conditions, moderate yields were systematically obtained mainly due to the major formation of the symmetrical arylamine end-capped derivative (**2a**). Following a paper by Marder & all,[82] the number of equivalents of the bromo derivative was reduced by a factor of two resulting, this time in a slight improvement of the conversion yield (entry 2). In parallel, the replacement of the conventional oil bath by microwave irradiations (entry 3) leads to a further slight improvement of the yield while shortening the reaction time. It turned out that one hour of irradiation appeared to be a good compromise between the consumption of the starting material and the formation of the symmetrical by-product (**2a**). Afterward, the initial catalytic system was modified by replacing the tri-tert-butylphosphonium tetrafluoroborate either by the tri(o-tolyl)phosphine (entry 4) or the tricyclohexylphosphine tetrafluoroborate (entry 5). While similar conversion rates were monitored with the neutral ligand (entry 4), a descent synthetic yield reaching almost 80% was achieved with the bulkier and charged analogue (entry 5). Applied to the biphenyl derivative (R = Ph), these conditions led to the target unsymmetrical 5,6-difluoro-2,1,3-benzothiadiazole based analogue **3** in similar yields (*i.e.* 78%). Once isolated, each monoarylated product was then subsequently engaged in another cross-coupling reaction with the 2-bromo-5-(2,2-dicyanovinyl)thiophene.[83]

Table 2.1 Reactions conditions used for the coupling of 4-bromo-N,N-bis(4-methoxyphenyl)aniline and BT2F.

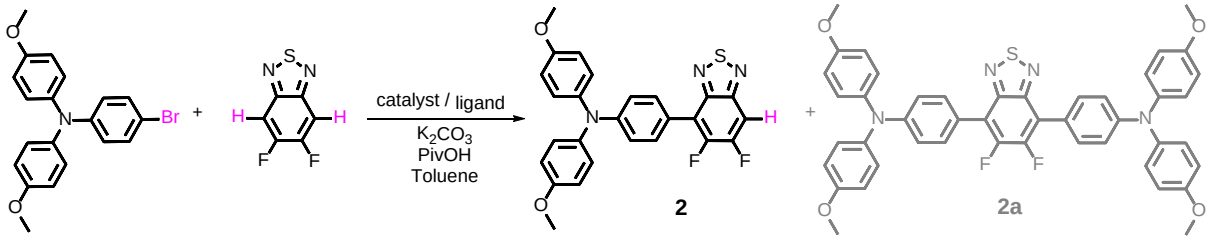

Entry	OMe-Br (eq)	Catalyst	Ligand	Heat source, temp./time	2 (% yield)
1	1.0	$Pd(OAc)_2$	$P^tBu_3.HBF_4$	Oil bath 120°C / 16h	20%
2	0.5	$Pd(OAc)_2$	$P^tBu_3.HBF_4$	Oil bath 120°C / 16h	33%
3	0.5	$Pd(OAc)_2$	$P^tBu_3.HBF_4$	µ-wave 150°C / 1h	36%
4	0.5	$Pd(OAc)_2$	P(*o*-MePh)$_3$	µ-wave 150°C / 1h	40%
5	0.5	$Pd(OAc)_2$	$PCy_3.HBF_4$	µ-wave 150°C / 1h	76%

Even though the unsymmetrical functionalization of the BT2F core by direct arylation was successfully carried out with electron-rich moieties, modest yields were achieved with such electronically deactivated thiophene moiety (Scheme 2.4). Consequently, and as a compromise between reactivity and extra synthetic steps, carbaldehyde functionalized unsymmetrical 5,6-

difluoro-2,1,3 benzothiadiazole derivatives **4** and **5** were prepared by coupling **2** and **3** with the 5-bromo-thiophene-2-carbaldehyde respectively (Scheme 2.5).

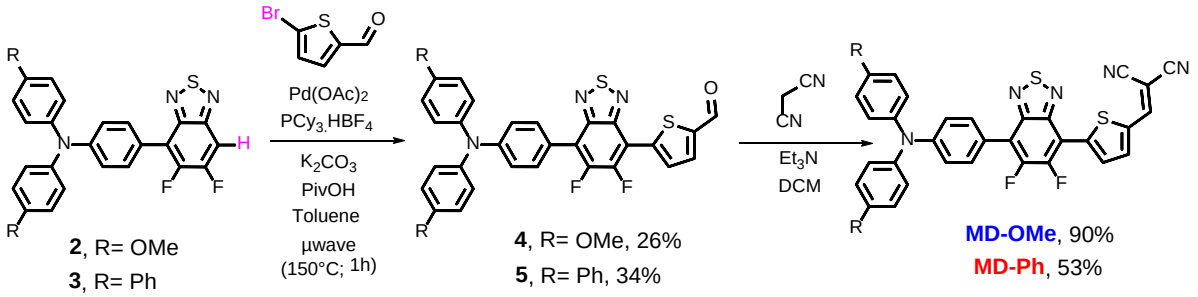

*Scheme 2.5 Second synthetic route considered to **MD-OMe** and **MD-Ph** through a Knoevenagel reaction.*

Though still modest, synthetic yields achieved were nonetheless significantly improved and are in consistency with early reported results.[82] Moreover, as a further step toward simplification, attempts to prepare carbaldehyde derivatives **4** and **5** through a one-pot like strategy were thus considered. Hence, BT2F was first reacted with bromo arylamine before adding the 5-bromo-thiophene-2-carbaldehyde to the reaction mixture. After a second round of microwave

irradiation, carbaldehyde **4** and **5** were successfully isolated with synthetic yields similar to those achieved with the above described two-step procedure (Scheme 2.6).

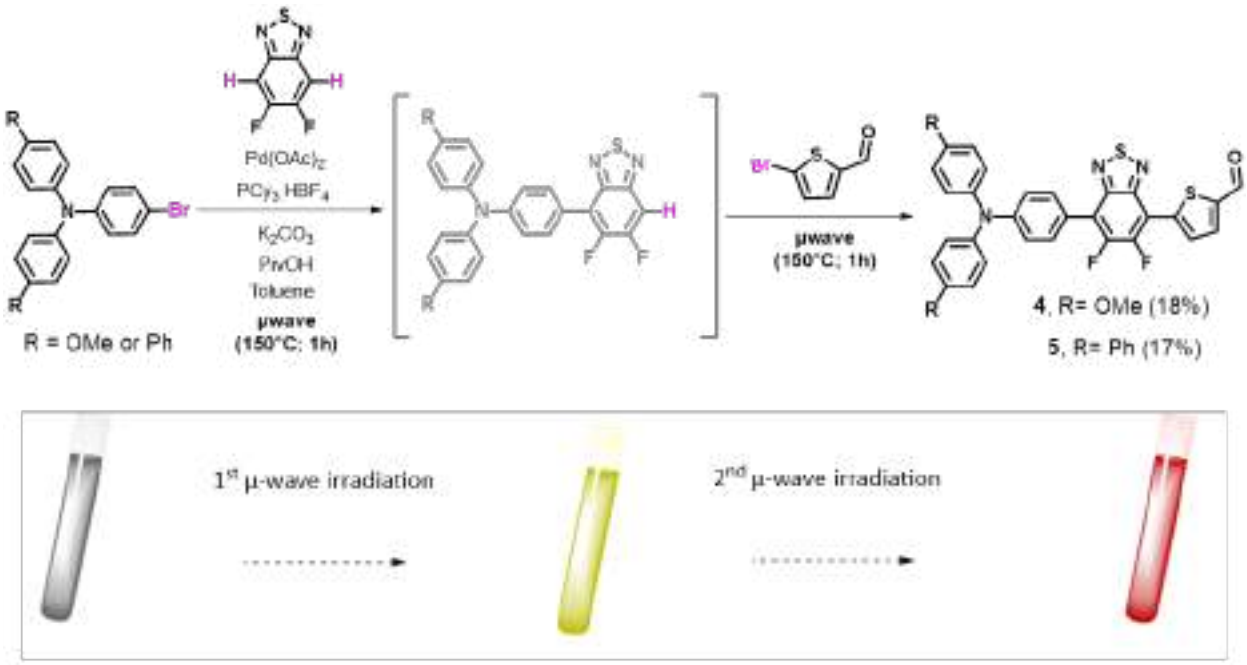

*Scheme 2.6 One-pot reaction to obtain compounds **4** and **5**.*

Finally, the later compounds were engaged in a Knoevenagel reaction with malononitrile to afford the corresponding final push–pull molecules. Despite full conversion confirmed in both cases by TLC, the biphenyl derivative was isolated in lower yield due to a limited solubility at room temperature, limiting its purification by usual technics.

2.2.3 Optoelectronic Properties

Once the identity and purity of the final compounds were confirmed by nuclear magnetic resonance spectroscopy and mass spectrometry, exploration and comparison of their optoelectronic properties were carried out.

2.2.3.1 Electrochemical properties

First, the electrochemical properties of the two molecules were studied by cyclic voltammetry in a 0.5 mM solution in CH_2Cl_2 using tetrabutylammonium hexafluorophosphate ($TBAPF_6$) as supporting electrolyte. The voltammograms of both compounds, plotted in Figure 2.12 show a reversible oxidation wave and an irreversible reduction process.

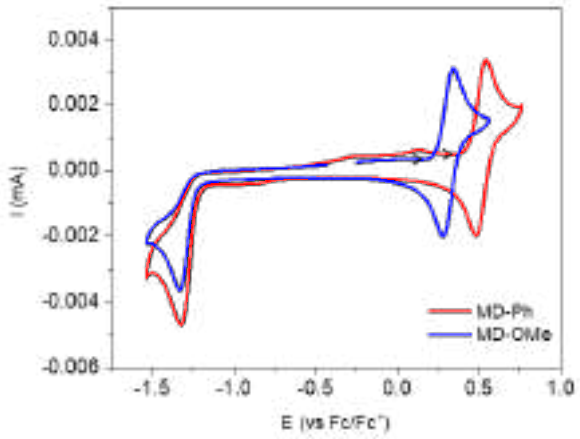

*Figure 2.12 Cyclic voltammograms of **MD-OMe** and **MD-Ph** molecules, 0.5 M in 0.1 M $TBAPF_6$ in CH_2Cl_2 with a scan rate of 100 mV/s.*

While the latter appears at a similar potential of -1.32 V for both molecules, the oxidation wave exhibited a potential of 0.34 V for **MD-OMe** while at higher potential for **MD-Ph** (0.54 V). This difference of $\Delta = 0.20$ V is due to the higher electron donating effect of the methoxy group compared to a phenyl ring.

The HOMO and LUMO energy levels were then deduced from the onset of the oxidation and reduction potentials for both molecules (Table 2.2) through the use of these two equations:[84]

Equation 1: $E_{HOMO}(eV) = -(5.1 + E_{ox/onset}\ Fc/Fc^{+}(V))$

Equation 2: $E_{LUMO}(eV) = -(5.1 + E_{red/onset}\ Fc/Fc^{+}(V))$

*Table 2.2 Electrochemical data of **MD-Ph** and **MD-OMe** molecules.*

Molecule	E_{ox} (V)	$E_{ox/onset}$ (V)	E_{HOMO} (eV)	E_{red} (V)	$E_{red/onset}$ (V)	E_{LUMO} (eV)	ΔE_{elec} (eV)
MD-Ph	0.54	0.43	-5.53	-1.32	-1.22	-3.88	1.65
MD-OMe	0.34	0.23	-5.33	-1.32	-1.22	-3.88	1.45

While the difference in HOMO levels underlines the effect of the methoxy group, the similar LUMO levels suggest a common localization of the electron density on the BT2F-thiophene dicyanovinyl part of the molecules.

2.2.3.2 Optical properties

UV-vis absorption spectra of the two compounds were recorded, as for the cyclic voltammetry, in dichloromethane (DCM) and plotted in Figure 2.13. Spectra show three successive absorption bands with maxima at 332, 413 and 513 nm for the biphenyl compound **MD-Ph** and at 315, 412 and 527 nm for **MD-OMe**.

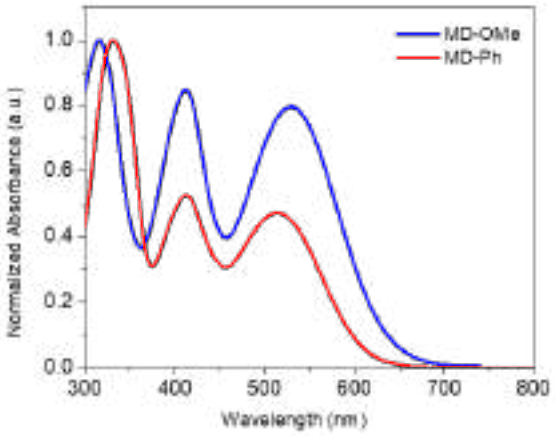

*Figure 2.13 UV-Vis absorption spectra of **MD-OMe** (blue) and **MD-Ph** (red) in DCM.*

As expected, replacing the biphenyl by a methoxy group produces a bathochromic shift of the maxima (*ca* 14 nm), reflecting, in agreement with the electrochemical measurements, the higher electron donating effect of the methoxy group compared to a phenyl ring. Moreover, it turns out that this chemical modification also results in an increase of the molar absorptivity by almost a factor of two for the visible centered absorption bands (Table 2.3).

Table 2.3 Optical Data gathered from DCM solutions and thin films spun cast on glass sheets.

Molecule	λ_{abs}^{max} solution (nm)	ε (M^{-1} cm^{-1})	λ_{abs}^{max} thin film (nm)	E_g^{opt} (eV)[a]	HOMO (eV) [b]	LUMO (eV) [a]
MD-OMe	315 412 527	51800 44100 41100	325 421 571	1.68	-5.43	-3.75
MD-Ph	332 413 513	42900 21900 20200	343 423 552	1.86	-5.64	-3.78

[a] estimated from the low-energy absorption onset of thin films; [b] determined by photoelectron spectroscopy in air (PESA) ; [c] LUMO = HOMO-E_g^{opt}

Considering that the UV-vis absorption patterns of TPA-T-DCV and derivative usually exhibits a single transition in the visible region, attributed to an internal charge transfer (ICT) from the TPA moiety to the DCV group,[85] time-dependent density-functional theory (TD-DFT) calculations were carried to rationalize the presence of a second band around 410 nm (Table 2.4).

*Table 2.4 TD-DFT calculated states and electronic transitions that rule the UV-vis optical absorption of **MD-Ph** and **MD-OMe**.*

Molecular Donor	Wavelength (nm)	Oscillator strength	Major transition	Minor transition
MD-Ph	728	0.524	HOMO->LUMO	-
	469	0.655	HOMO-1->LUMO (62%)	H-1->L+1 (12%), H->L+1 (12%)
	376	0.463	HOMO-1->LUMO+1 (46%)	H-3->L (30%), H->L+2 (26%)
MD-OMe	756	0.529	HOMO->LUMO	-
	471	0.619	HOMO-1->LUMO (67%)	H-1->L+1 (13%), H->L+1 (20%)
	375	0.407	HOMO-1->LUMO+1 (41%)	H-3->L (34%), H->L+2 (25%)

It turned out from these calculations that the latter absorption bands also have a charge-transfer character, such as the low-energy ones (HOMO → LUMO transition), since they predominantly arise from a HOMO-1→ LUMO transition (Figure 2.14).

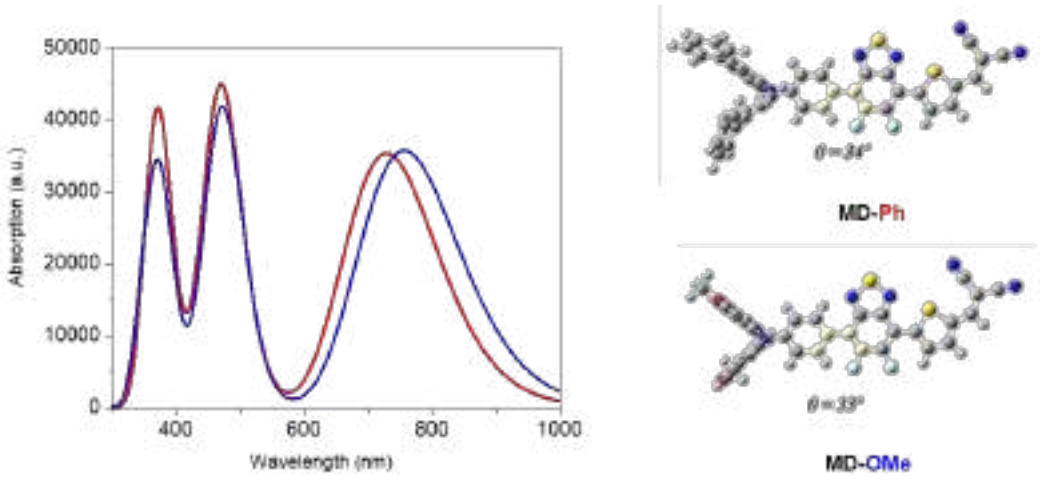

*Figure 2.14 Simulated UV-vis spectra and optimized geometries of **MD-Ph** (red) and **MD-OMe** (blue).*

Moreover, ground-state density-functional theory (DFT) geometry optimizations confirmed the localization of the electron density on the arylamine moiety for the HOMOs and on the benzothiadiazole/thiophene-DCV for LUMOs (Figure 2.15).

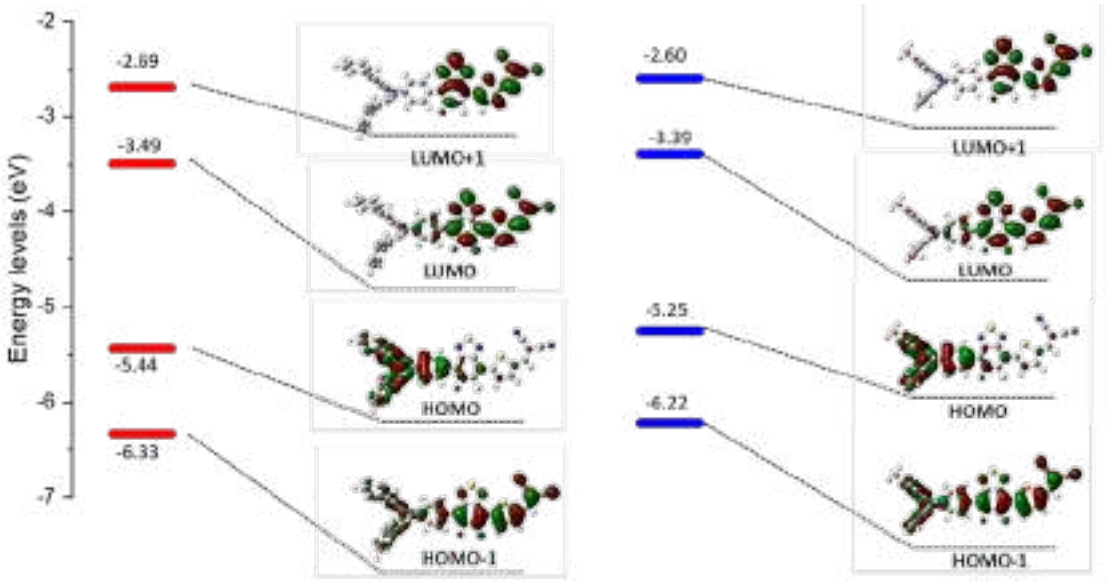

*Figure 2.15 Optimized geometries and computed energy levels of **MD-Ph** (left) and **MD-OMe** (right).*

Also in agreement with the electrochemical and optical characterizations, a reduced band gap was computed for **MD-OMe** that originates from a significant destabilization of the HOMO level, induced by the electron donating methoxy group, exceeding by far that of the LUMO level (Δ_{HOMO} = 0.19 eV vs. Δ_{LUMO} = 0.10 eV). These predictions were subsequently experimentally confirmed at solid state (Figure 2.16).

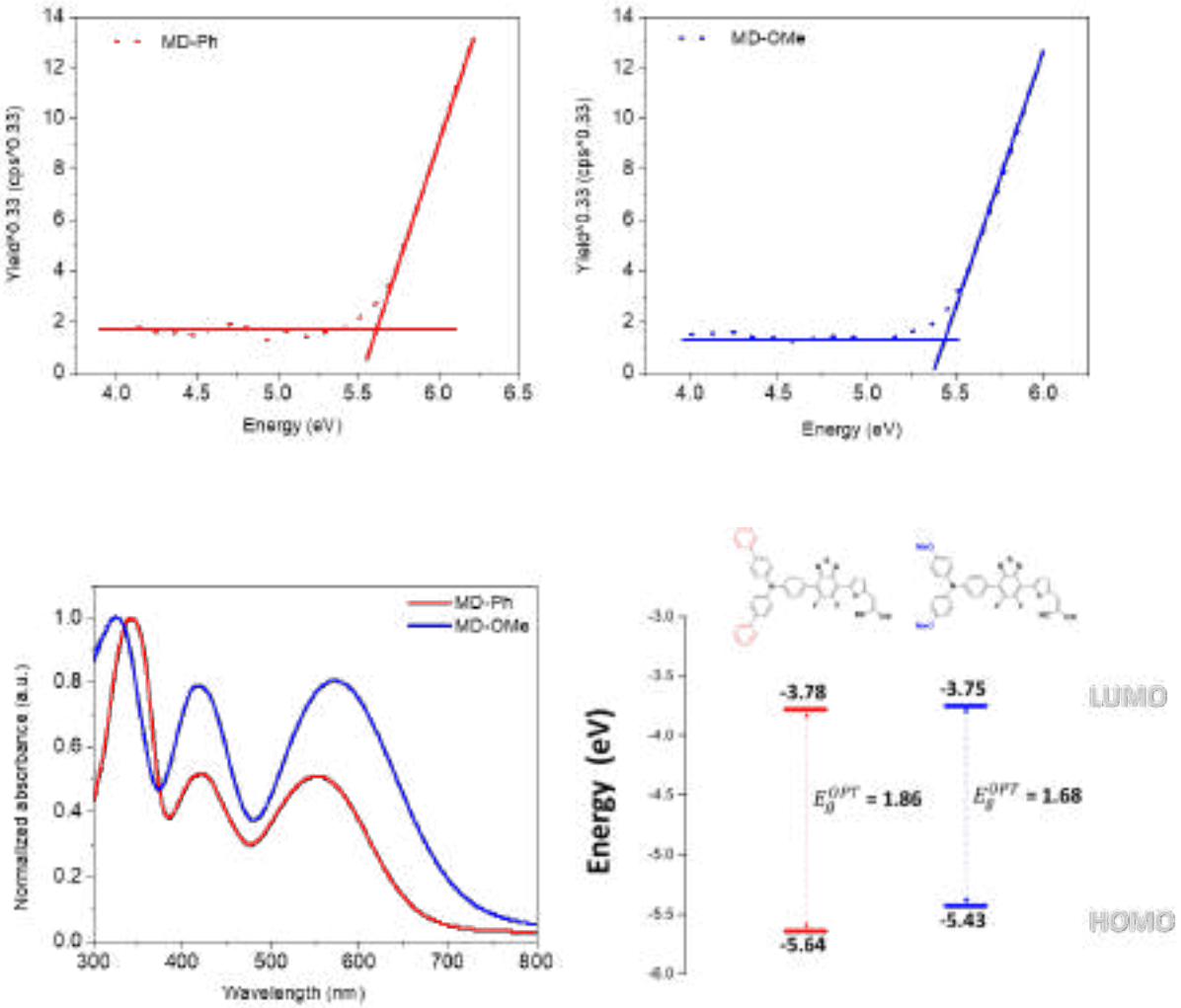

*Figure 2.16. Photoelectron spectroscopy on air (PESA) analysis of **MD-Ph** and **MD-OMe** in thin films (top), UV-visible spectra recorded on thin films, and energetic diagram in solid state.*

Hence, while HOMO levels of -5.43 eV and -5.64 eV were measured by photoelectron spectroscopy in air (PESA) measurements on thin films prepared by spin-casting dichloromethane solutions, optical band gaps of 1.86 to 1.68 eV were calculated from the low-

energy absorption onsets for **MD-OMe** and **MD-Ph** respectively. Once cross-tabulated, LUMO levels were finally resulting in the comparative energy diagram plotted in Figure 2.16. The destabilization of both frontier energy levels was thus confirmed with a major effect on the HOMO level, thus resulting in a reduce gap. Designed as potential donor molecular systems for organic solar cells, such a difference might significantly impact the photovoltaic parameters, particularly the open circuit voltage (V_{oc}).[86]

2.2.4 Evaluation as active materials in Organic Solar Cells

Consequently, simple air-processed bulk heterojunction (BHJ) solar cells using [6,6]phenyl-C_{71}-butyric acid methyl ester ($PC_{71}BM$) as an electron acceptor material were thus fabricated to evaluate, compare, and rationalize the potential of these new push-pull. To do so, active layers with different donor:acceptor (D/A) weight to weight (w/w) ratios were processed, in air, from chloroform solutions with a total concentration of 10 mg/mL, deposited by spin-coating using a speed rate of 1500 rpm, and embedded in devices of architectures: ITO/PEDOT:PSS/active layer/Ca/Al (Figure 2.17).

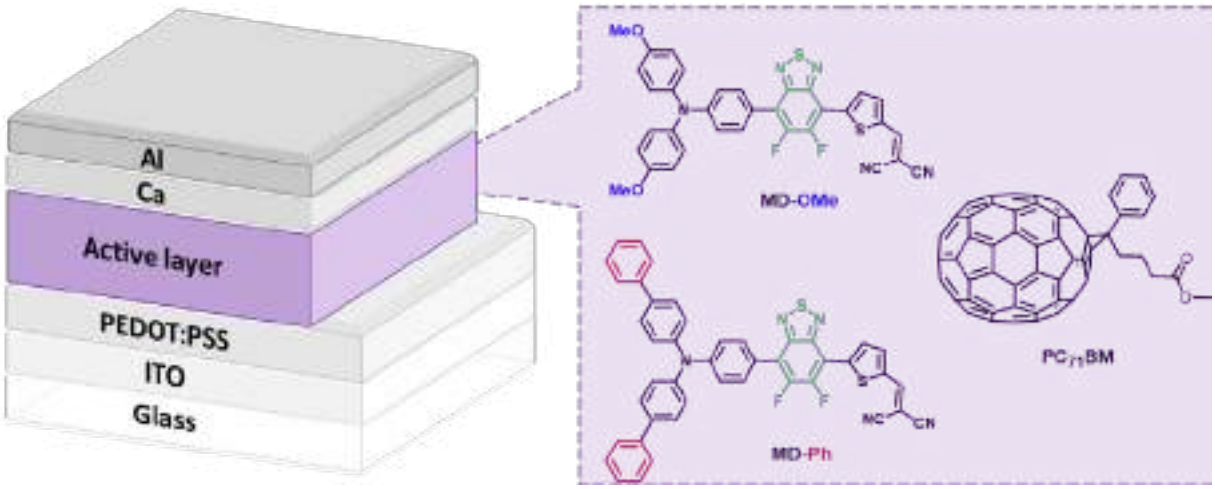

Figure 2.17 Device's architecture with the chemical structures composing the active layer.

The photovoltaic data are gathered in Table 2.5 and the best current density-voltage (J-V) curve plotted in Figure 2.18.

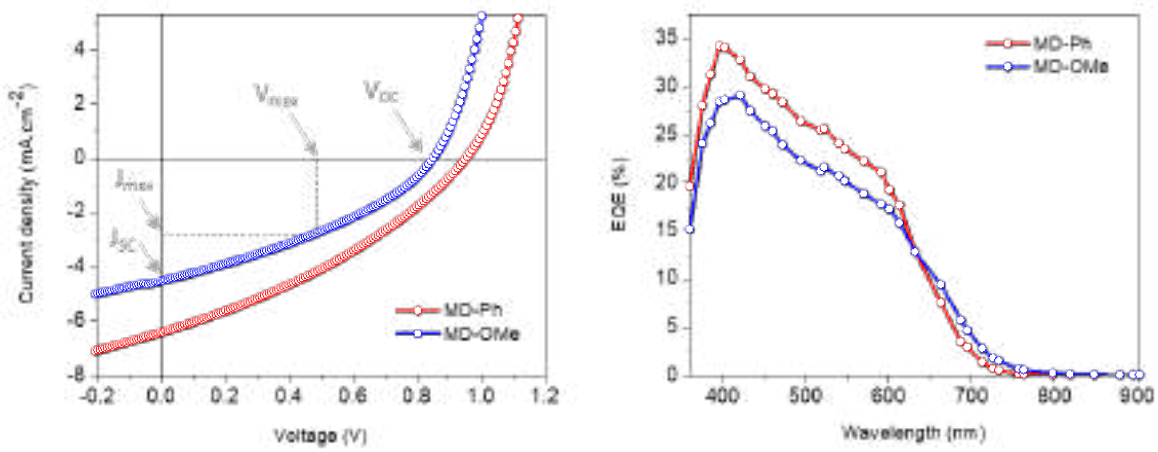

*Figure 2.18 Current density–voltage characteristics and EQE spectra of the best **MD-OMe** (blue) and **MD-Ph** (red) based organic solar cells.*

Different parameters can indeed be extracted from these curves:

i) The open circuit voltage, or $V_{OC,}$ corresponds to the voltage at a neutral current density. Known to be affected by the energy difference between the HOMO of the donor and the LUMO of the acceptor, this parameter is also directly correlated to other factors such as the morphology of the active layer (crystallinity) and/or the thermodynamic and non-radiative recombination (V_{OC} losses).[87]

ii) The short circuit current density, or J_{SC}, is the current measured under illumination when the applied voltage is equal to zero. It depends on several factors related to the active layer, such as its thickness and absorption properties, the mobilities of holes and electrons, and the charges separation capacity.

iii) Then, the fill factor, or FF, is defined as the quotient of the maximum power delivered by the cell by the maximum theoretical power (equation 3).

Equation 3: $$FF = \frac{P_{max}}{V_{OC} \times J_{SC}} = \frac{V_{max} \times J_{max}}{V_{OC} \times J_{SC}}$$

Correlated to the quality of charge extraction and resistivity within the device, many factors can affect this parameter.[88]

iv) And finally, the power conversion efficiency (or PCE), used to benchmark a solar cell, can be directly calculated by dividing the P_{max} by the incident light power (P_i), usually an Air Mass 1.5 Global (AM 1.5 G) of 1000 W.m^{-2} (equation 4).

Equation 4: $$PCE = \frac{P_{max}}{P_i} = \frac{V_{OC} \times J_{SC} \times FF}{P_i}$$

Table 2.5 Photovoltaic data measured on solar cells with 28 mm^2 active area under AM 1.5 simulated solar light illumination at 100 mW·cm^{-2}.

Molecular Donor	D:A ratio (w/w)	V_{oc} (V)	J_{sc} (mA/cm^2)	FF	PCE (%)
MD-OMe	1:1	0.71	-3.18	0.33	0.74
MD-OMe	1:2	0.85	-4.55	0.35	1.35
MD-OMe	1:3	0.77	-4.73	0.33	1.20
MD-Ph	1:1	1.01	-4.56	0.33	1.52
MD-Ph	1:2	1.01	-5.47	0.34	1.88
MD-Ph	1:3	0.96	-6.43	0.34	2.09

Herein, best power conversion efficiencies, of 1.35 % and 2.09 %, were achieved with a 1:2 and 1:3 D/A ratio for **MD-OMe** and **MD-Ph** based devices, respectively. Comparison of their corresponding current density to voltage (J–V) curves revealed that the better efficiencies recorded with **MD-Ph** mainly arise from their higher short circuit current (J_{SC}) and open circuit voltage (V_{OC}) values. While the latter parameter (V_{OC}) can indeed be correlated to the deeper HOMO level of the biphenyl derivative, **MD-OMe** was nonetheless characterized by better absorbing properties in the visible range which was expected to lead to higher J_{SC}. Interestingly and in agreement with the recorded J_{SC} values, external quantum efficiency (EQE) measurements performed on the best devices also highlighted an improved contribution of the

biphenyl derivative to the photocurrent compared to its methoxy counterpart (Figure 2.18). This measurement, also known as the incident photon-to-current conversion efficiency (IPCE), provides the percentage of incident photons converted into electrons at each wavelength, and therefore a direct evaluation of the respective contribution of both constituting materials since generally linked to their absorption profiles.

Hence, in an attempt to rationalize these results, morphologies of the active layers were first probed by atomic force microscopy (AFM). As illustrated in Figure 2.19, smooth surface topographies with similar roughness (RMS) parameters of *ca* 0.6 nm were observed in both cases. Nonetheless, **MD-Ph**/**PC$_{71}$BM** blend exhibits nanodomains of smaller size than those observed with the methoxy derivative which can be the harbinger of a better biphenyl induced self-organization of the donor molecule which can, in turn, be beneficial for the charge transport properties and therefore the J_{SC} parameter.

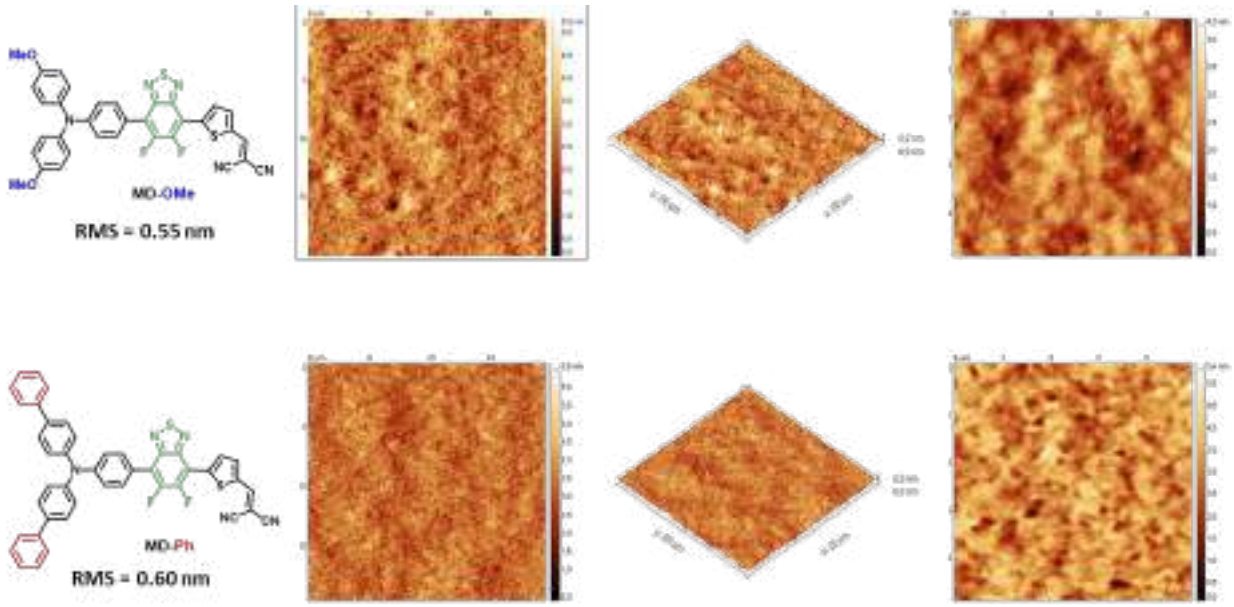

*Figure 2.19 AFM phase images (20 x 20 and 5 x 5 µm) of optimized **MD-OMe** and **MD-Ph** based active layers.*

Consequently, both optimized active layers were subsequently embedded in hole-only devices of architecture ITO/PEDOT:PSS/donor/Au. Through the use of the space charge limited current

(SCLC) method, hole mobilities of ca 7.3×10^{-5} and 8.3×10^{-4} cm^2 $V^{-1}s^{-1}$ were measured for **MD-OMe** and **MD-Ph** respectively (see Figure 2.20).

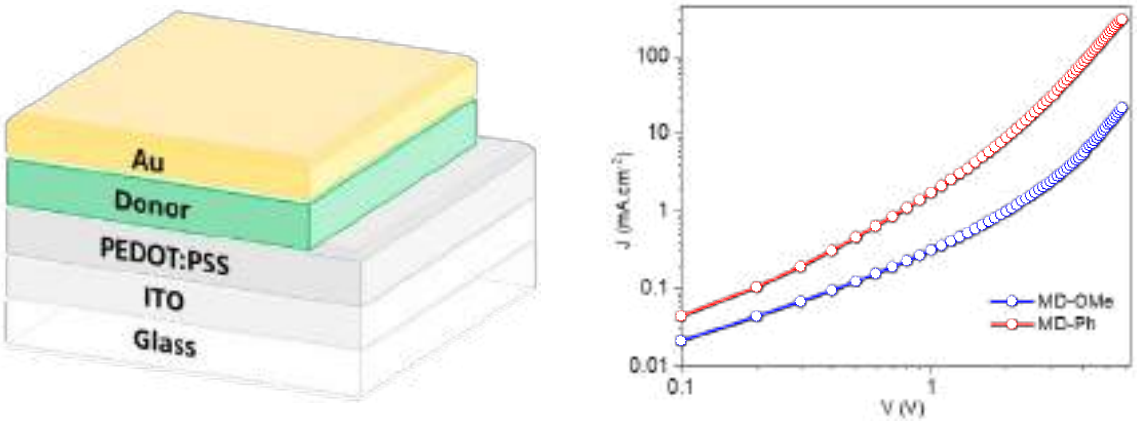

Figure 2.20 Architecture and J-V characteristics of hole only devices.

Hence, this order-of-magnitude difference might compensate for the lower absorbing properties of the active layer and contribute to the higher J_{SC} value delivered by the **MD-Ph**-based devices.

2.2.5 Conclusion

Two new triphenylamine-based push–pull molecules containing, for the first time, the 5,6-difluoro-2,1,3-benzothiadiazole units have been synthesized. In order to simplify the synthesis procedure and limit the formation of potentially toxic by-products, the synthetic route was optimized to mainly use direct (hetero)-arylation conditions. As a step towards simplification, a “one-pot” procedure without modification of the catalytic system nor purification of intermediates was even demonstrated. The analysis of the electronic properties of the two compounds shows, in agreement with theoretical results, that the methoxy derivative presents a red-shifted absorption, a higher molecular absorption coefficient, and leads to a material of a smaller band gap. On the other hand, the photovoltaic properties of the two compounds, used as donor materials, show that in spite of less favorable optical properties, the biphenyl derivative led to better performances due to the conjunction of higher open-circuit voltage and better charge transport properties.

2.3 Perovskite Solar Cells (PSCs)

Beyond the synthetic achievement and demonstration of the use of the BT2F block to prepare unsymmetrical molecules, attempts to valorize side-products was then considered. For instance, the arylamine end-capped **2a** (Figure 2.21), indeed caught our attention since simple architecture with similarities in their design were recently published as promising hole-transporting materials (HTMs) in Perovskite based solar cells (*e.g.* M101 and M102, Figure 2.21).[89-90]

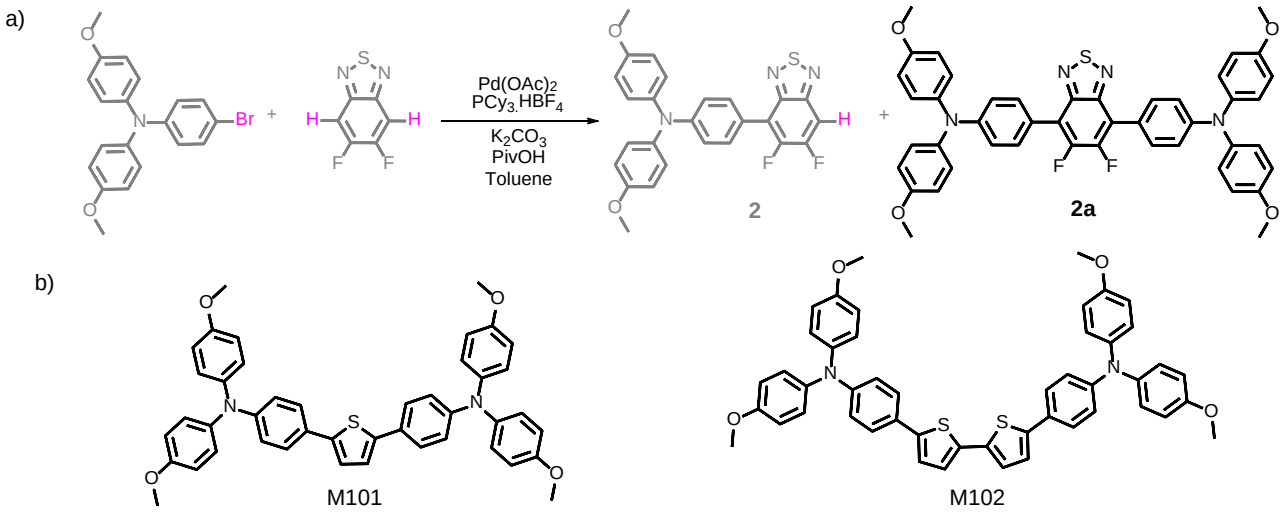

*Figure 2.21 a) Synthesis of **2a** symmetrical molecule, and b) Structure of arylamine end-capped HTMs.*

Interestingly (for us), only limited studies dedicated to developing simple and accessible active compounds by using modern synthetic strategies such as the direct (hetero) arylation were/are reported. In this context, the second part of this chapter will thus focus on such materials and their evaluation in perovskite based solar cells.

2.3.1 Brief History of Perovskites

Organic-inorganic hybrid metal halide perovskite solar cells have been one of the hottest photovoltaic topics in the past decade. Their amazing improvement in a relative short period of time confirmed their huge potential to afford low-cost and high efficient devices.

However, even if recently used for PV, Perovskites are known for more than a century since the first natural Perovskite was found in the Ural Mountains in 1839 by the German mineralogist Gustrav Rose who named it after his Russian colleague Lev Perovsky.[91]

The general chemical formula of a Perovskite is ABX_3, where A and B are cations of different atomic radii (with A being larger than B) and X an anion (see structure in Figure 2.22). In organo-lead halide perovskites, mostly used in solar cells, A is a monovalent cation such as $CH_3NH_3^+$ (methylammonium MA^+) or $(NH_2)_2CH^+$ (formamidinium, FA^+), Cs^+ or Rb^+; X is a monovalent halide anion such as Cl^-, Br^-, or I^- and finally, B is a metallic divalent cation, usually Pb^{2+} or Sn^{2+}.[92]

Amongst all reported studies, the most studied perovskite type is undoubtedly the methyl ammonium lead triiodide, also known as "MAPI" ($CH_3NH_3PbI_3$), due to its excellent optoelectrical properties (broad absorption up to 800 nm associated to an absorption coefficient of 1.5×10^4 cm^{-1} at 550 nm), long electron and hole-diffusion length (up to 1µm), low exciton binding energy (< 10 meV) and a high charge carrier mobility (*ca*. 66 $cm^2V^{-1}s^{-1}$).[93]

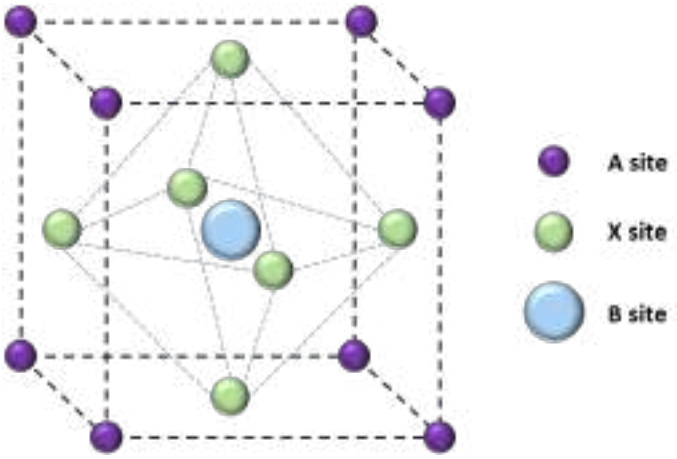

Figure 2.22 Crystal structure of a perovskite material in 3D.

Interestingly, the optical and electrical properties of the perovskites can be further tuned by varying the nature of both the organic cations and halide anions. Consequently, mixed perovskites containing both MA^+ and FA^+ (as organic cations), metal lead cation, with Cl^- and

Br^- anions, have been tested and optimized to afford the current best-performing hybrid devices.[94]

Historically, the incorporation of perovskites in solar cells started in 2009, used instead of an organic molecular dye in dye-sensitized solar cells (DSSCs), reported by Miyasaka and co-workers,[95] an amazing proof of concept that paved the way for decades of research. However, these early devices were unstable and lasted only for a few minutes due to the dissolution of the perovskite materials in the liquid electrolytes. Six years later a major breakthrough occurred, *i.e.*, the replacement of the liquid electrolyte by a solid-state hole-transporting material (HTM).[96-97] This approach encouraged intensified research in the PSCs field from 2012 onwards, focusing on the development and optimization of perovskite materials, device architectures, deposition techniques, and *n*-type and *p*-type charge transporting materials, to keep breaking records.[98]

2.3.2 Device Architectures

PSCs are structurally divided into two categories: mesoporous and planar structures. Since PSCs originated from solid-state DSSCs, the mesoporous structure (FTO/ETM/meso-ETM/perovskite/HTM/Au) used to be dominant during the genesis of this technology. Then, to simplify the fabrication process, mostly to make it compatible with solution-processes, planar PSCs were then developed. Moreover, the ambipolar charge transport properties of the perovskite allows a use in both conventional *n*-*i*-*p* (FTO/ETM/perovskite/HTM/Au) and inverted *p*-*i*-*n* (ITO/HTM/perovskite/ETM/Ag) architectures (see Figure 2.23).[99]

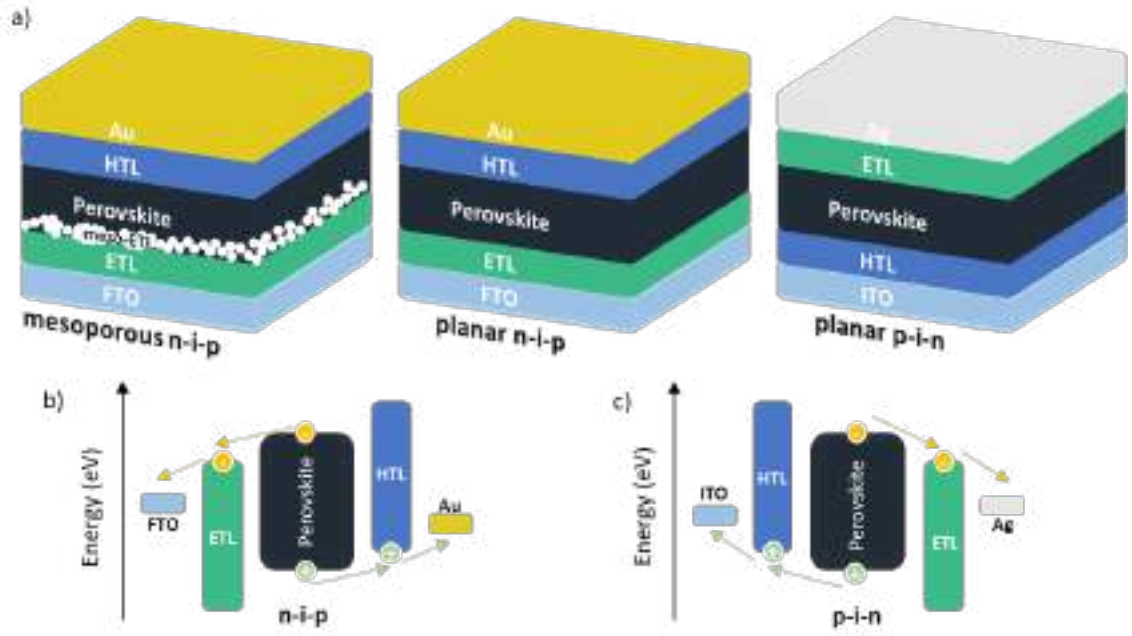

Figure 2.23 a) Device structures of PSCs; energy levels and charge-transfer processes in b) n-i-p and c) p-i-n devices.

Attempts to develop ETL- and/or HTL-free devices have also attracted considerable research efforts, mainly for manufacturing purposes (cost reduction and recyclability), and highly promising results have already been achieved since maximum PCEs of *ca* 16% were demonstrated.[100-102] However, to reach higher PCEs, charge extracting layer are still essential for the development of performing and stable PSCs.

Conscious that inorganic and organic polymer can be used as HTMs, a special emphasis will be put herein on organic molecular systems from the literature to compare/benchmark the potential of the materials developed within the frame of this thesis.

2.3.3 Small Organic HTMs

The major roles of HTMs are basically to optimize the extraction and transport of holes to the cathode. To achieve this, a HTM material should :[93]

(1) Be cost-effective.

(2) Be compatible with solution-processed deposition.

(3) Have suitable and optimized energy level alignment that matches with the perovskite layer: for efficient extraction of holes as well as an effective blocking of electrons.
(4) Show long-term stability: high optical, chemical, water, air, and thermal stability. The glass transition temperature (T_g) should be higher than 120 °C to avoid structural changes in the HTM under continuous sunlight exposure.
(5) Show high hole mobility with values > 10^{-4} $cm^2V^{-1}s^{-1}$.
(6) Achieve pinhole-free layer once processed.

All these requirements can be sum up as the schematic representation depicted in Figure 2.24.

Figure 2.21 Requirements for developing good HTMs.

It is important to mention that some requirements may differ depending on the device's structure. For example, in p-i-n PSCs, the HTMs should be i) insoluble in DMSO and DMF to avoid the dissolution of the perovskite itself and ii) transparent in the visible optical range. In contrast, for n-i-p PSCs, high hydrophobicity is a must since HTMs are coated on perovskite film and should act as a capping layer to protect it from moisture ingress.

Amongst all reported HTMs, small organic molecules have undoubtedly been the most studied category for PSCs. It all started with the use of the spiro-OMeTAD in the first all-solid PSC in 2012.[96] The latter was previously used in solid-state DSSCs architecture.

Spiro-OMeTAD indeed possesses a compatible low lying HOMO level at around -5.1 eV and a wide band gap of 2.98 eV, ensuring a good transparency in the visible range.[103] Moreover, due to its twisted 3D structure, it shows a good solubility in commonly used and orthogonal organic solvents such as chlorobenzene or toluene. From a structural point of view, this HTM consists of a spiro-bifluorene central core end-capped with four diphenylamine units.

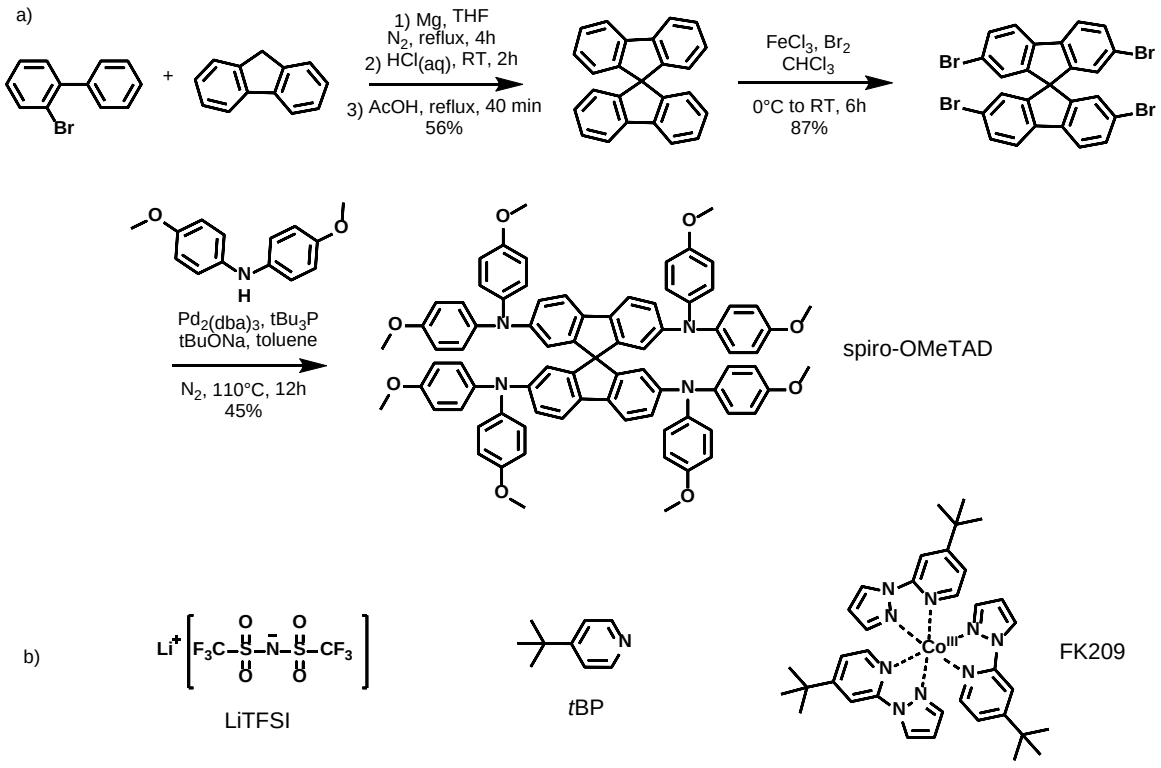

Figure 2.22 a) Synthesis and chemical structure of spiro-OMeTAD; b) Chemical structures of the most used dopants.

With a 5-step synthesis, including the preparation and use of Grignard reagent as well as harsh bromination conditions,[104] (see Figure 2.25) the spiro-core is also known for its touchy purification usually requiring sublimations to achieve high performances. Moreover, it is worth noting that pristine spiro-OMeTAD suffers from moderate hole mobility (~ 10^{-5} $cm^2.V^{-1}s^{-1}$) and

conductivity (10^{-8} $S.cm^{-1}$),[105] consequence of its highly twisted structure that hinders the formation of close π-π stackings, thus requiring the use of chemical dopants added during the deposition process. Indeed, due to the high electron affinity of the p-type dopant, electrons from the HOMO of spiro-OMeTAD molecules are extracted, resulting in an increased hole density and conductivity of the HTM.[106] The structures of the most used dopants are represented in Figure 2.25.

Widely used in combination with spiro-OMeTAD, lithium bis(trifluoromethanesulfonyl)imide (Li-TFSI) is known to oxidize the hole-transporting material (HTM) into a spiro$^{\bullet+}$TFSI$^{\bullet-}$ organic salt but also resulting in the subsequent formation of deleterious and hygroscopic lithium-based byproducts such as Li_xO_y.[107-108] As an alternative, tert-butylpyridine (tBP) was introduced as a potential lithium-free dopant; however, its volatility resulted in an irreversible dedoping and therefore a decrease in the hole extraction of the spiro-OMeTAD based HTL.[109-110] Consequently, understanding, rationalizing, and addressing the instability triggered by these commonly used dopants can be successful milestones for stable and even more efficient PSCs. According to several reports, the full potential of the spiro-OMeTAD based layer indeed might not have been reached in the current systems (*ie*, through doped HTLs). One of the key limits is the slow oxidation processes and low doping efficiency.[111] For instance, Forward *et al.* estimated that only a fraction of Spiro$^{\bullet+}$ was generated by the addition of this lithium salt since 50 mol% of Li-TFSI was required to barely oxidize approximately 7.8±0.5 mol% of spiro-OMeTAD. Moreover, the authors also emphasized that the doping efficiency was far from being quantitative since it was estimated to be approximately 20%,[112] thus requiring a substantial amount of dopants that do not only increase hole transport properties of the spiro-OMeTAD but also severe stability problems.[113-114]

In addition, spiro-OMeTAD is still expensive (506 euros/g at Ossila), mainly due to the multistep synthesis and required sublimation purification, thus the additional doping and oxidation processes further increase the total complexity and cost, making this material currently unsuitable for the large-scale fabrication of efficient and stable PSCs.

For these reasons, intense research efforts were and still are ongoing to find relevant low-cost and efficient HTM alternatives to achieve high performance but, most importantly, stable devices. Based on the spiro-OMeTAD structure, as a general model, variations of the latter were naturally considered. Hence, most of the organic molecules explored are built on a central core

(like 9,9'-spirobifluorene, thiophene derivatives, triphenylamine, silylothiophene, etc.) decorated in the periphery with electron donor units (mostly diphenylamine, triphenylamine, and carbazole derivatives).

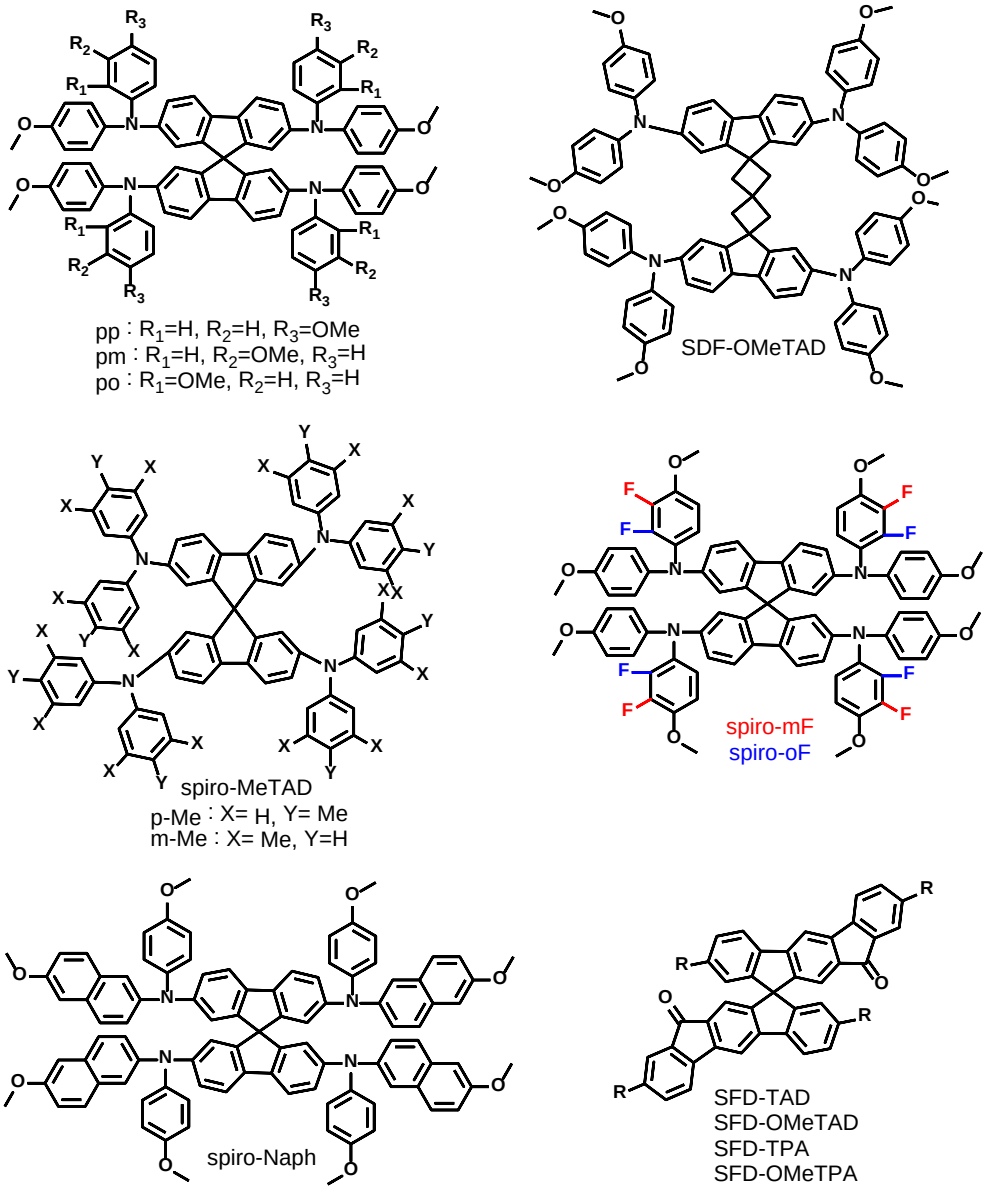

Figure 2.23 Chemical structures of some spiro-like HTMs.

For instance, Seok e*t al.*[103] synthesized in 2014 pp-, pm-, and po-spiro-OMeTAD derivatives, by changing the positions of the two methoxy substituents in each of the quadrants (Figure

2.26). The cell performance was demonstrated to be linked to the positions of the OMe substituents, resulting in a PCE of 16.7% with the o-OMe derivative compared to ~15% for conventional p-OMe substituent, correlated to a lower LUMO of the po-Spiro-OMeTAD that efficiently blocks the electron transport from the perovskite to the Au electrode resulting in an increase of the FF value and thus an enhanced PCE. However, with a similar complex synthesis and purification to that of the conventional Spiro-OMeTAD, and an UV-instability, this approach was limited to the proof of concept and structure/properties investigation. Consequently, in 2017, a low-cost HTM named SDF-OMeTAD was designed and synthesized through a two-step reaction.[115] Its reduced cost and reduced environmental impact compared to other HTMs were highlighted, but the "moderate" efficiency (of 13% compared to the 17% PCE reached, at that time with spiro-OMeTAD) appeared to be a bottleneck. Later, two families of spiro-like molecules were introduced in 2020. First, Sini *et al.*[116] published two spiro-MeTAD compounds that differ from the reference compound only by the presence of methyl substituents as compared to methoxy groups. Despite a reduced glass transition temperature, the lower ionization potentials, and larger hole mobility values obtained, this modification led to promising PCEs of ~17% (*vs* 19% for spiro-OMeTAD). The main take home message of this study was to carefully optimize the perovskite/HTM interface, point that was strongly highlighted by Yang *et al.*[117] who designed two fluorinated isomeric analogs of the spiro-OMeTAD that demonstrated better hydrophobicity (the presence of fluorine atoms inducing a kinetic barriers to slow down O_2 and H_2O intrusion), better mobilities, long-term stability in wet conditions without encapsulation (87% efficiency retention after 500 hours) and better PCE values exceeding 24.8% compared (to 23% with spiro-OMeTAD). Since improved PCE value is still the crux for publication in high impact journals, more tuned and complicated spiro-like structures were developed and reported. For instance, the same group introduced in 2022 the spiro-Naph molecule with asymmetric phenylnaphthylamine edge units.[118] This HTM achieved higher efficiencies (PCE of 24.43%) and stability than that of the reference compound, while showing due to a deeper-lying HOMO, higher hydrophobicity, and tighter molecular packing.

In parallel to these Spiro analogs, several structures and design principles were reported taking into consideration the synthetic accessibility through the use of simpler and accessible building blocks.

Hence, thiophene-based central cores were investigated (Figure 2.27). For instance, five low-cost small organic HTMs were reported by Qiao *et al.* and Wu *et al.* using one, two, three, four

or six thiophene units, as central cores, and end-capped with two TPA-OMe groups.[89, 119] The conductivity was increased with the extension of repeating thiophene number from M101 to HT suggesting that higher conjugation is beneficial to higher conductivity of HTMs. A range of PCEs from 10.74% to 17.69% was thus obtained, the best being with QT molecule that exhibited well-balanced parameters including solvent tolerance, thin film conductivity, and interfacial charge transfer efficiency.

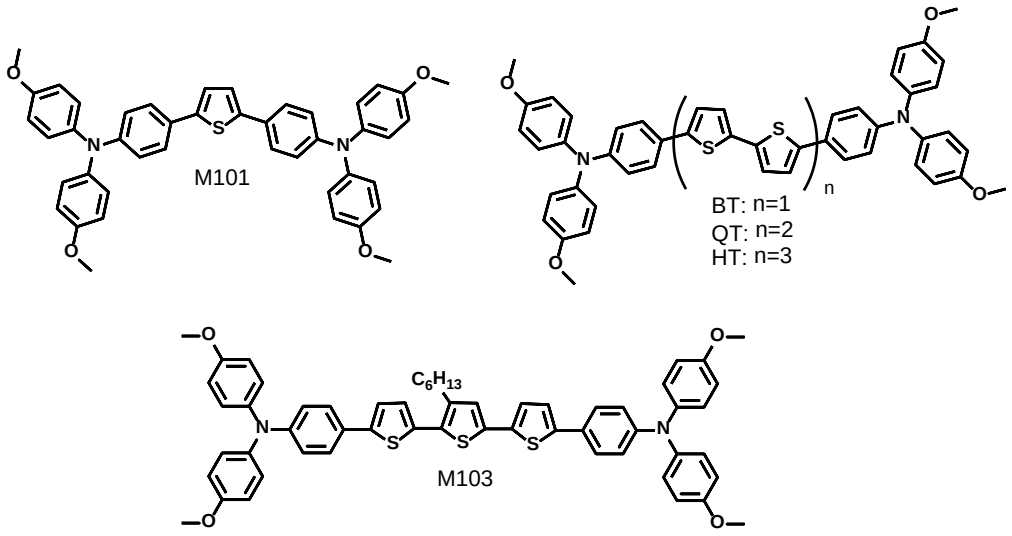

Figure 2.24 Structures of non-fused thiophene-based HTMs.

Adapted from the legacy of OPVs and DSSCs, fused central cores, such as cyclopenta[2,1-b;3,4-b']dithiophene (CPDT) or spiro-[cyclopenta[1,2-b:5,4b′]dithiophene-4,9′-fluorene] (SDTF) (see some structures in Figure 2.28) were also used.

Sun *et al.*[90] indeed compared, in 2019, four extended CPDT-based molecules (CT1-4) . Photoluminescence studies indicated that unsubstituted CPDT (by aliphatic chains, ie, CT1 and CT3) showed highly efficient hole transfer from the perovskite to HTMs. These results demonstrate that a two-dimensional and rigid π-framework facilitate intramolecular π-conjugation and intermolecular π-π stacking, providing both high charge carrier mobility and efficient intermolecular charge transfer resulting in improved device efficiency. As a results and good demonstration, CT1 was able to afford efficient devices (PCE of 17.71%) characterized by long-term stability over 1300 h (86% of the efficiency retained). In 2021,[120] the same authors developed a new class of hole transporting materials by incorporating a dithiolane unit into the CPDT (LYC-1, 2 and 3) and claiming that the electron rich nature of

sulfur and the rigid planar π-conjugated framework can enhance the hole mobility through an intermolecular overlap of π–π clouds in the solid state, alongside to the S···S interaction that is also beneficial to charge transport (due to the electronic softness of the sulfur atoms) and, thus, an increase of effective overlapping. It turned out that the shorter compound (LYC-1) was characterized by higher hole mobility, faster charge collection efficiency, and resulted in more uniform capping layer on top of perovskite, thus leading to a remarkable PCE of 19.07%, that was, at that time significantly higher than those achieved with other analogues and above all with the reference spiro-OMeTAD, under similar conditions.

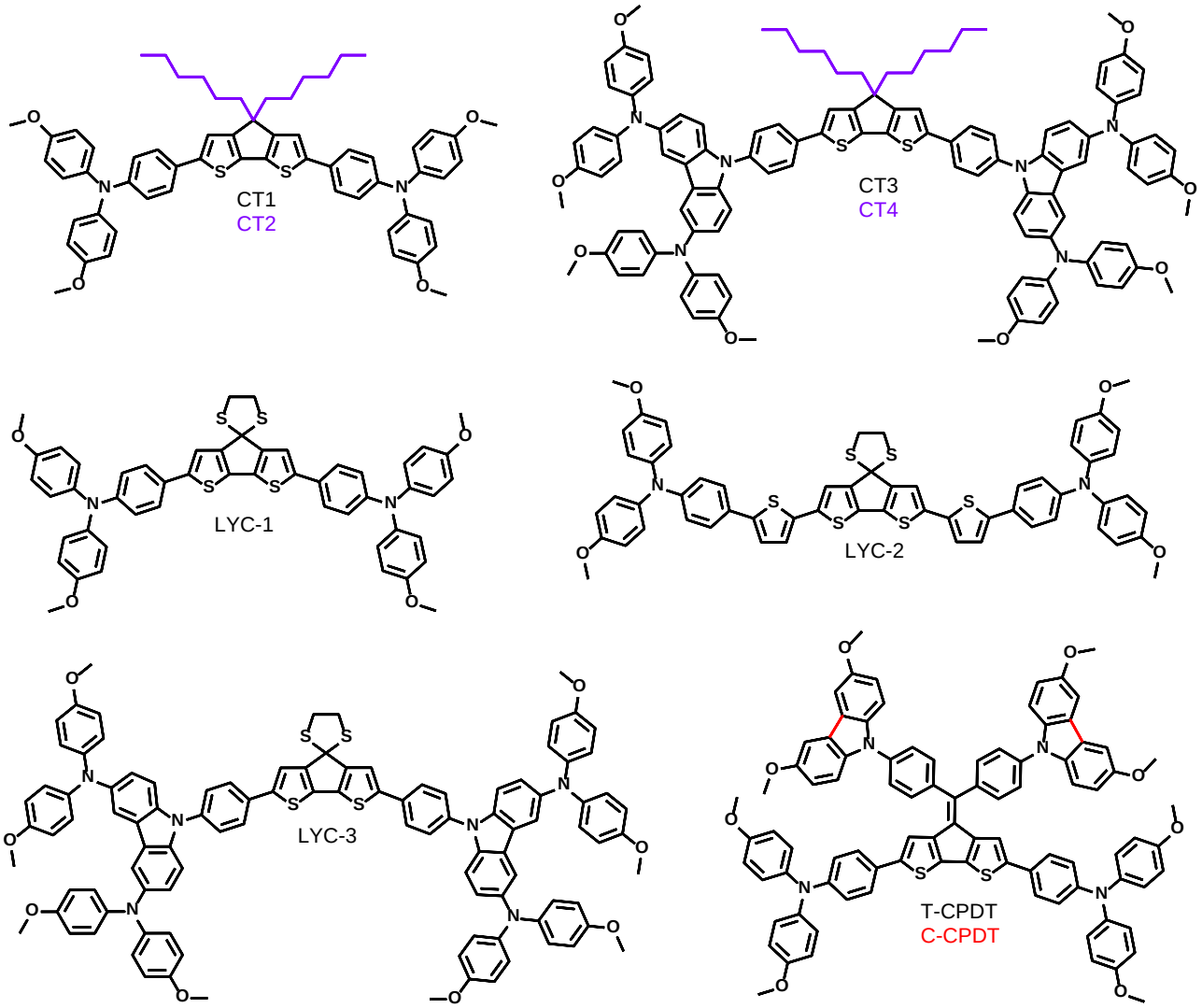

Figure 2.25 Chemical structures of CPDT-based HTMs.

Meanwhile, Lin *et al.*[121] synthesized two new star-shaped HTMs, denoted as T-CPDT and C-CPDT, and based on a central π-extended CPDT core end-capped with four aryl amine moieties. The introduction of the carbazole groups on C-CPDT was found to increase the planarity of the molecule, leading to the formation of a smooth and uniform thin film, with improved hole-transporting capability. More importantly, devices fabricated using the latter compound as dopant-free HTM were able to achieve an impressive PCE of 19.68%, significantly higher than that of the device based on T-CPDT (11.45%).

Other structures, based on the SDTF block as central electron-rich and bulky core, were also designed and reported (see structures in Figure 2.29).

The first one, namely FDT, was published in 2016 by Nazeeruddin *et al.*[122] and was able to directly compete with the reference spiro-OMeTAD in terms of efficiencies since up to 20.2% were demonstrated, with, additionally, a distinct advantage, that it can be dissolved in more environmentally friendly solvents, such as the toluene instead of the traditionally used chlorobenzene.

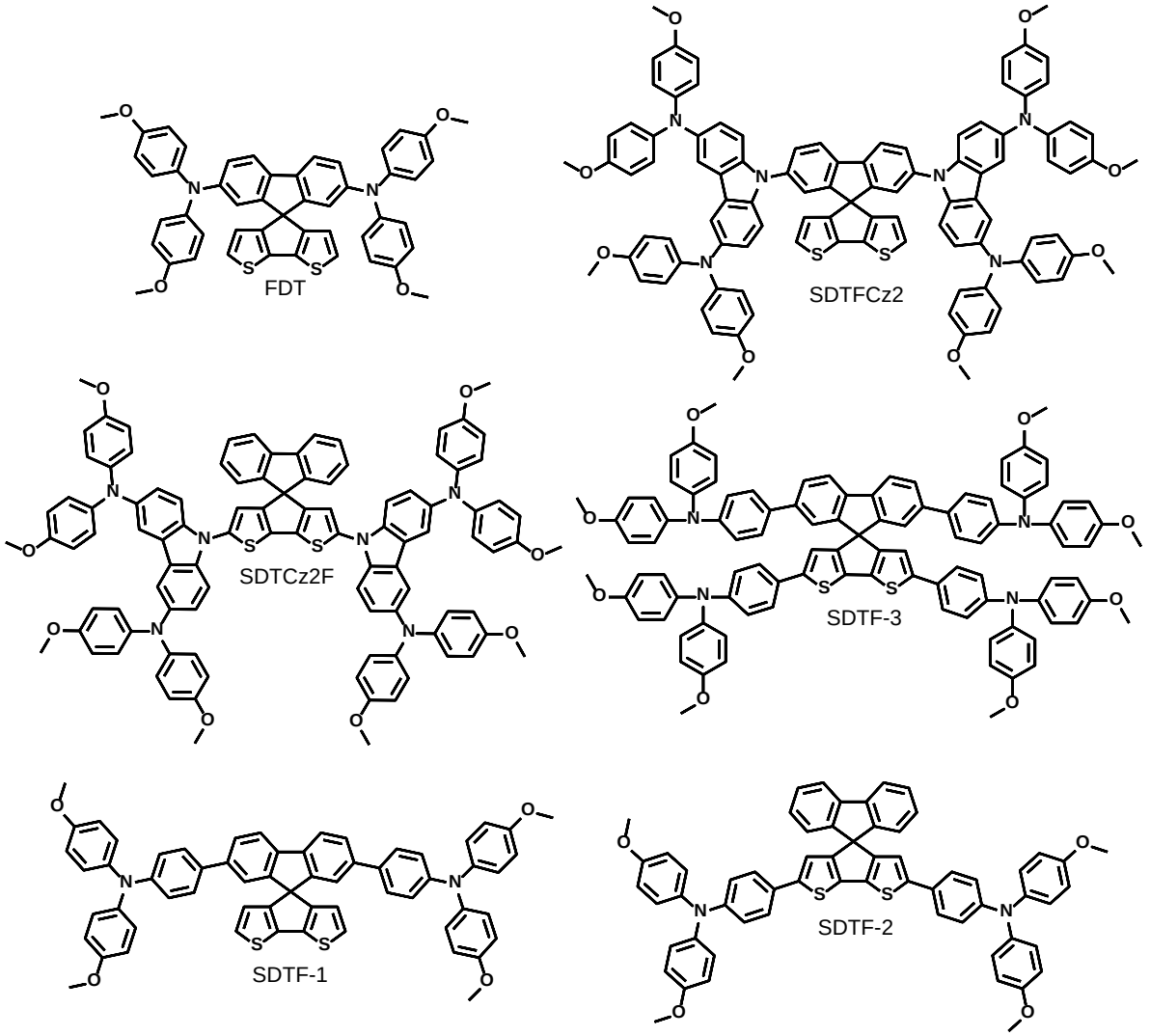

Figure 2.26 Chemical structures of SDTF-based HTMs.

Then, Schmaltz *et al.*[123] reported in 2019 a series of new HTMs based on a SDTF core end-capped with two peripheral 3,6-dimethoxydiphenylaminyl-carbazole (CzDMPA) units on either the fluorene or the cyclopentaditiophene part of the central core (SDTFCz2 and SDTCz2F). As a result, while SDTCz2F was found to display a lower HOMO level (−5.25 eV), a smaller band gap, as well as reduced degradation temperature and hole mobility (8.5×10^{-8} $cm^2\ V^{-1}s^{-1}$), it, nonetheless led to better PCEs (16.4% vs 14.3% PCE for SDTFCz2).

Recently, Gao *et al.*[124] developed another SDTF-based series by varying the grafting position and the number of peripheral triphenylamine (TPA-OMe) moieties (SDTF-1, 2, and 3). PSCs fabricated with SDTF-2, as the HTM, afforded the highest power conversion efficiency (of

19.3% compared to ~14% with the other molecules), in consistency with an optimized HOMO level, band gap, and charge transport capabilities.

Hence, as for the OPV and DSSC, a brief survey of the literature once again reveals that attention is mainly devoted on achieving high efficiencies to reach high impact journal. While few examples really focus on improving/understanding the (lack of) stability of the devices, even scarcest reports provide new design principles or synthetic strategies to accessible materials with industry-compatible and limited synthetic steps. Looking in the literature, only few examples of HTMs synthesized *via* direct (hetero) arylation were found.[125-126] (Note that the majority of these papers have been published by the same group and mainly focus on the use of the EDOT as main building block[126-131]).

2.4 Step-saving routes to simple triarylamine-based HTMs for efficient and stable PSCs

2.4.1 Context and Molecular Design

Obtained as a by-product from the bis-coupling reaction on the BT2F early introduced in this chapter, the TPA-OMe end-capped molecule **2a**, caught our attention since its design principle and structure appeared "familiar" when compared to some efficient yet simple HTMs reported in the literature. However, optoelectronic characterization of the latter by UV-vis spectroscopy and PESA revealed a band gap of 2.16 eV and not really optimized frontier energy levels (HOMO = -5.51 eV and LUMO = -3.35 eV), particularly the LUMO that appeared too shallow to provide sufficient electron blocking ability (Figure 2.30).

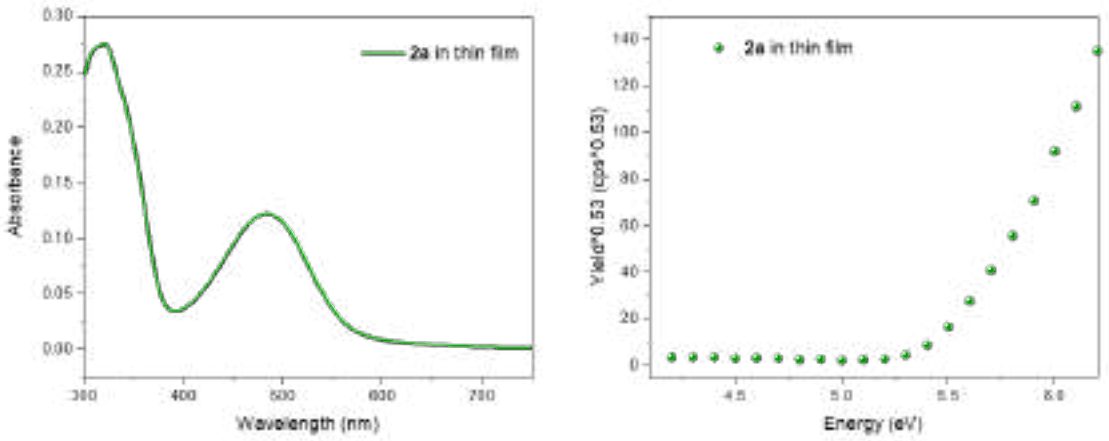

*Figure 2.30 UV-vis and PESA analysis spectra of molecule **2a** in the thin film.*

On the other hand, while thiophene-based materials already showed impressive efficiencies in PSCs, as discussed above, and at the same time they are known for their good reactivity towards direct arylation couplings (acidic H at positions 2 and 2'); three tris(4-methoxyphenyl)amine end-capped materials with different thiophene-based π-conjugated central cores were considered within the frame of this thesis (see structures in Figure 2.31).

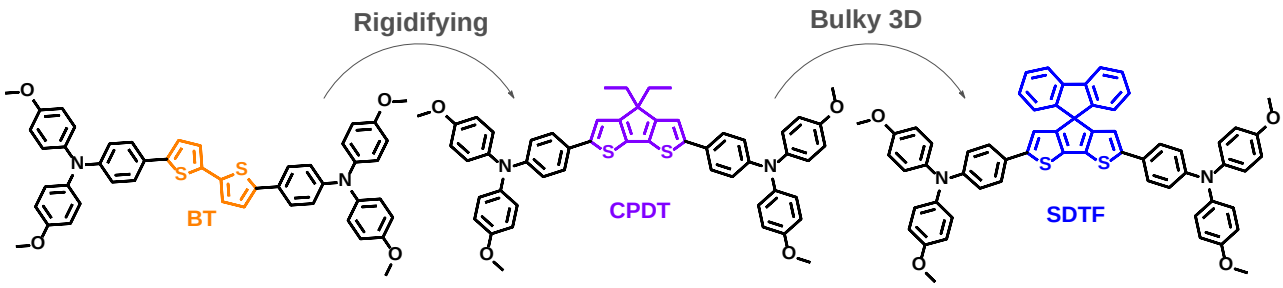

Figure 2.31 Structures of the three target HTMs.

These three central cores were selected for their synthetic accessibility and/or commercial availability as well as their increasing level of steric hindrance, generated through rigidification in the 3,3' position starting from a 2,2'-bithiophene (BT) to the bridged and bulky spiro(cyclopentadithiophene-fluorene) (SDTF) through a diethylcyclopentadithiophene (CPDT). Published separately in different papers from different groups demonstrating their potential, the structure-property relationships between these compounds have thus never been rationalized and their syntheses, solely reported by conventional Stille or Suzuki cross-coupling reactions, have never been optimized and shortened.[119-120, 124]

2.4.2 Synthesis

In the context of simplification, the three target molecules were synthesized following the route depicted in Scheme 2.7. The use of the direct arylation, successfully applied herein, allowed to reduce the number of synthetic steps, by avoiding i) the bromination of all central cores, and ii) the borylation/stannylation of the TPA counterpart.

Moreover and as for the push-pull derivative introduced in the early part of this chapter, conventional homogeneous catalysts were replaced by a silica-supported palladium that is i) tolerant to temperature, ii) stable in air and against moisture iii) recyclable by simple filtration, and iv) avoids any metallic contamination of the final batch.

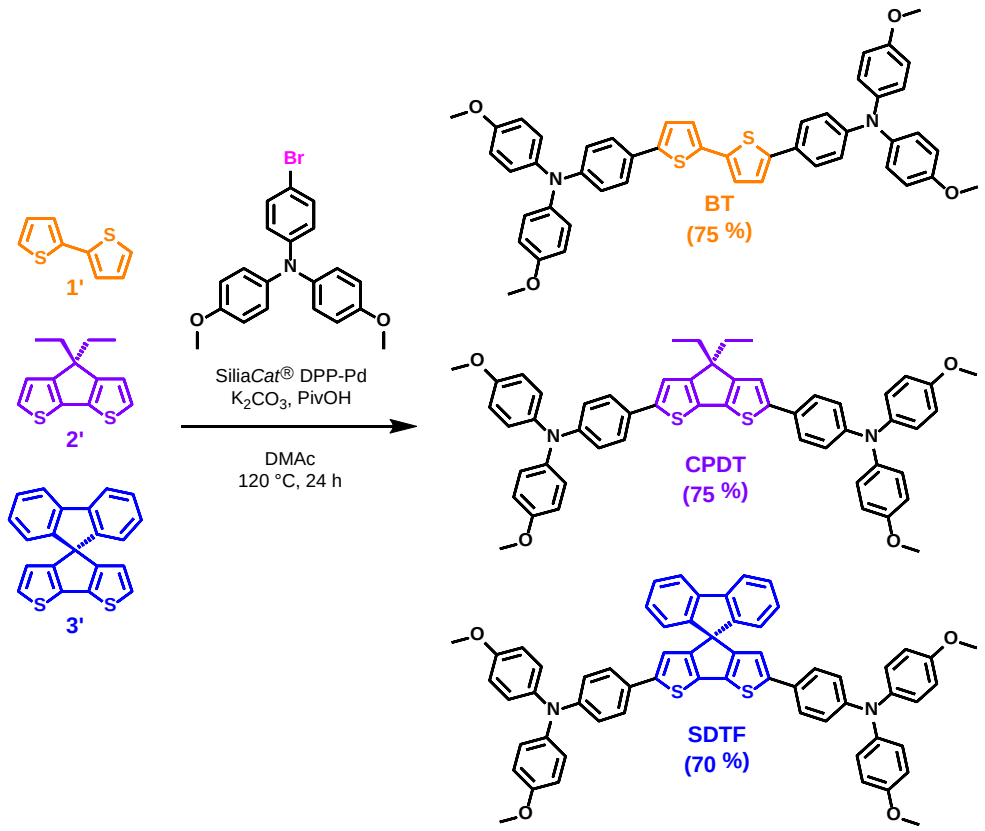

*Scheme 2.7 DHA cross-coupling reactions for the synthesis of **BT**, **CPDT**, and **SDTF** molecules.*

Under these optimized conditions, all the target compounds were obtained in good yields, above 70% after purification on silica gel.[90, 119, 124]

2.4.3 Optoelectronic Properties

Once the identity and purity of the final compounds confirmed by nuclear magnetic resonance spectroscopy and mass spectrometry, exploration and comparison of their optoelectronic properties were investigated to rationalize the impact of the core and evaluate their potential as HTMs for PSCs.

2.4.3.1 Electrochemical properties

First, the electrochemical properties of the three molecules were studied by cyclic voltammetry in a 1 mM solution in DCM using 0.1 M of tetrabutylammonium hexafluorophosphate ($TBAPF_6$) as a supporting electrolyte. The voltammograms of the three compounds, plotted in Figure 2.32, show reversible oxidation waves whose potential values are gathered in Table 2.6.

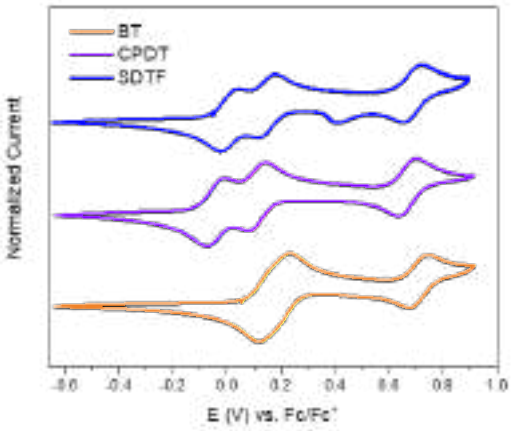

*Figure 2.32 Cyclic voltammograms of **BT**, **CPDT,** and **SDTF** molecules, 1 mM in 0.1 M $TBAPF_6$ in CH_2Cl_2 with a scan rate of 100 mV/s.*

The effect of rigidifying the central core leads to a more conjugated system, which is clearly demonstrated through the electrochemical properties. Compared to **BT**, **CPDT** and **SDTF** molecules can indeed be oxidized at lower potentials with a splitting of the oxidation pattern. The difference, of $\Delta \sim 0.20$ V in the first oxidation, between **BT** and the two other derivatives is due to the increased conjugation upon fusing of the central cores.

Table 2.6 Electrochemical data of the three molecules.

Molecule	E_{ox} (V)	$E_{ox/onset}$ (V)	E_{HOMO} (eV)
BT	0.23 0.74	0.07	-5.17
CPDT	-0.01 0.14 0.70	-0.12	-4.98
SDTF	0.03 0.17 0.71	-0.06	-5.04

The HOMO energy levels were then deduced from the onset of the first oxidation potential for the three molecules (Table 2.6) through the use of Equation 1 mentioned before.

2.4.3.2 Optical properties

Soluble in most commonly used organic solvents, UV-vis absorption spectra of the three compounds were then recorded, as for the cyclic voltammetry, in DCM and plotted in Figure 2.33. Spectra show in all cases, a visible centered absorption band with an internal charge transfer character with maxima at 425, 440, and 444 nm for **BT**, **CPDT,** and **SDTF**, respectively. DFT calculations performed on these systems (see Figure 2.33) indeed emphasize a delocalization of the HOMOs all along the structure while LUMOs appeared mainly localized on the central core and direct vicinal benzene rings in the case of the **SDTF** molecule.

As expected, replacing the non-fused ring (**BT**) with bridged central cores results in a bathochromic shift of the maxima (*ca* 15 to 19 nm for **CPDT** and **SDTF** respectively), reflecting, in agreement with the electrochemical measurements, the increase of the conjugation within the backbone. Moreover, it turns out that this chemical modification also results in an increase in the molar absorptivity for the visible-centered absorption band (Table 2.7).

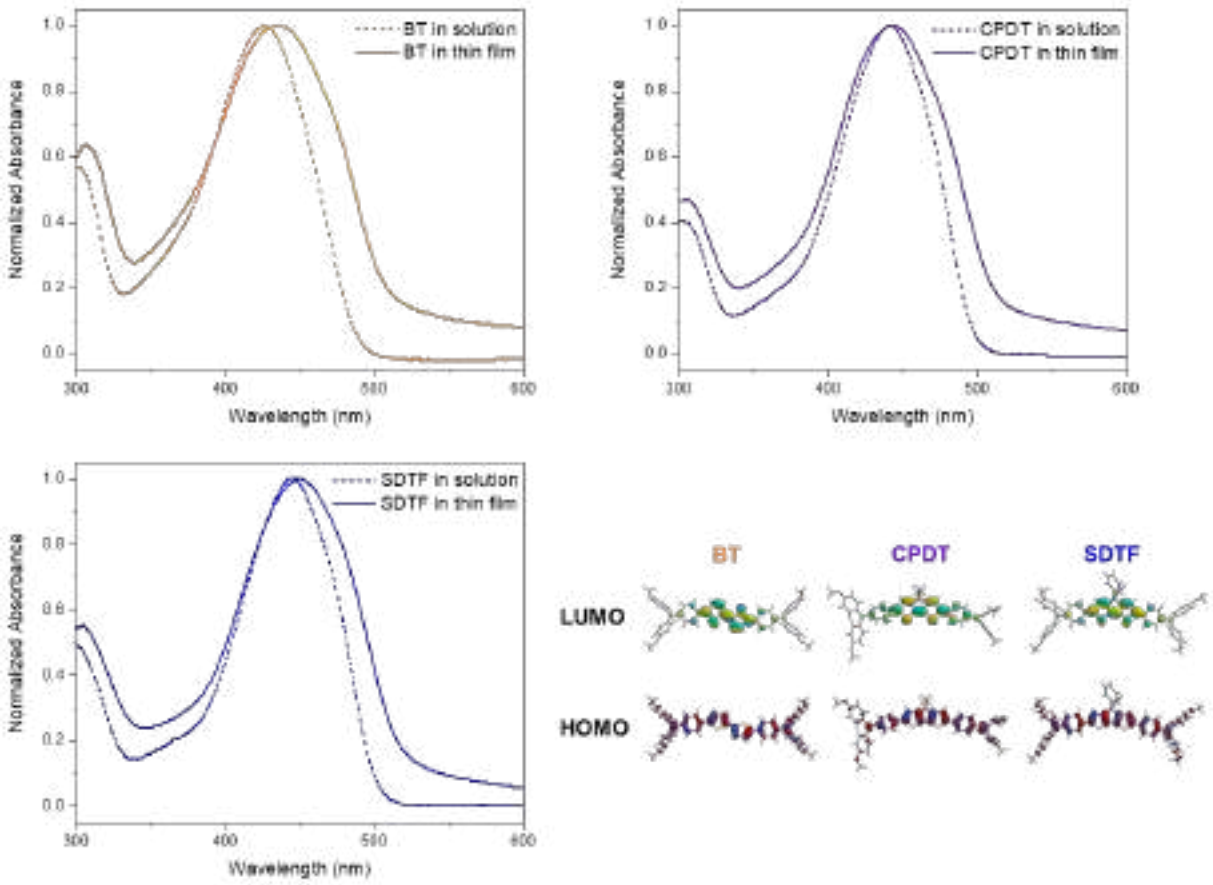

*Figure 2.33 UV-vis spectra in solution and thin film; and computed frontier molecular orbitals of **BT**, **CPDT**, and **SDTF**.*

On the other hand, **BT** molecule shows a more pronounced bathochromic shift from solution to thin film, once spun cast on glass sheet, compared to its bulkier counterparts (11 nm *vs* 2 nm for **CPDT** and 4 nm for **SDTF**). This feature can indeed be correlated to a less sterically hindered structure thus favoring stronger intermolecular π-π stacking at solid state.

Table 2.7 Optical Data gathered from DCM solutions and thin films spun cast on glass sheets.

Molecule	λ_{abs}^{max} solution (nm)	ε (M^{-1} cm^{-1})	λ_{abs}^{max} film (nm)	$\lambda_{threshold}$ (nm)	ΔE^{opt} (eV)
BT	425	55942	435	524	2.53
CPDT	440	70718	443	532	2.48
SDTF	444	67747	450	537	2.46

Analyzed by photoelectron spectroscopy in air (PESA), these thin films were directly used to assess the HOMO energy levels (Figure 2.34).

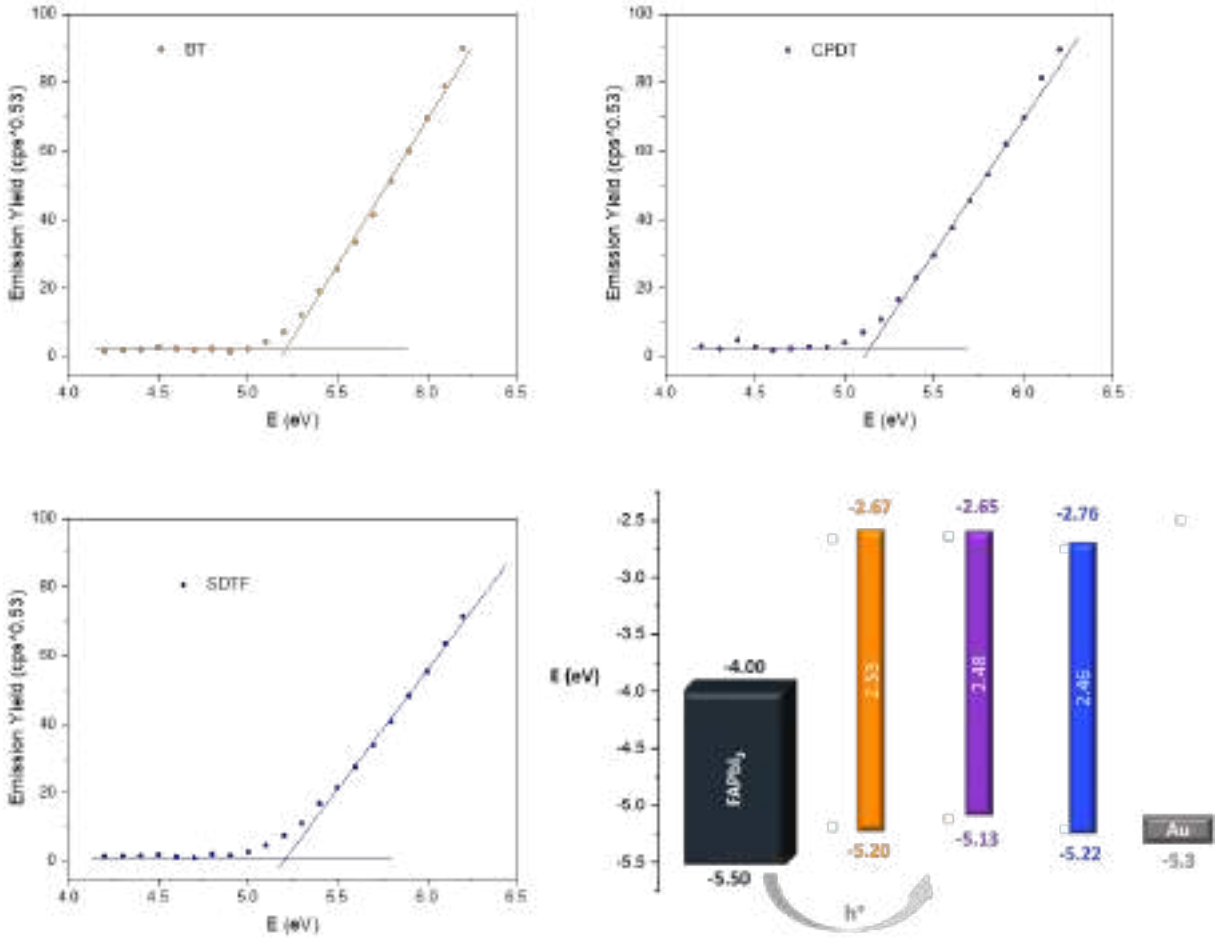

*Figure 2.34 Photoelectron spectroscopy on air (PESA) analysis in thin films, and energetic diagram in solid state of **BT**, **CPDT**, and **SDTF**.*

Hence, while bridging the bithiophene with a spiro barely affect the HOMO levels (-5.20 eV for **BT** *vs* -5.22 eV for **SDTF**), the use of a CPDT core was found to significantly destabilize the latter level since lying around -5.13 eV. These results were then cross tabulated with optical band gaps, determined from the absorption onsets (in thin films), to deduce LUMO levels and afford the comparative energy diagram plotted in Figure 2.34.

Therefore, it turns out that HOMO and LUMO levels of the three molecules are above the valence band maximum (VBM) and the conduction band minimum (CBM) of the conventionally used $FAPbI_3$ perovskite. This band alignment ensures hole transport with sufficient electron blocking ability and thus potential suitability as HTMs for PSC applications.

2.4.4 Evaluation as HTMs in Perovskite Solar Cells

Before the embedment of these potential active layers in devices, their thermal stability was first evaluated by thermogravimetric analyses (TGA, Figure 2.35).

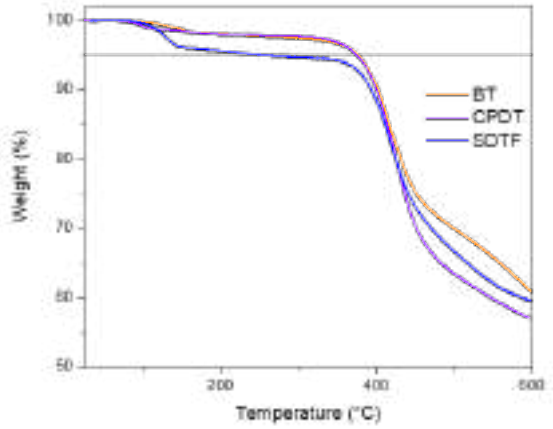

Figure 2.35 Thermogravimetric analysis (TGA) of HTMs at a heating rate of 10 °C/min in N_2.

With a degradation temperature attributed to a loss of 5 weight % (T_{d95}), the spiro(cyclopentadithiophene-fluorene) derivative was found to be more sensitive than the two others with a difference of ca 100°C (T_{d95} 237 °C for **SDTF** vs 376 °C for **BT** and 374 °C for **CPDT)**, in consistency with early reports.[123] However, this range of degradation is still perfectly acceptable for the target application. Other key parameter, contact angle measurements were also conducted to evaluate their moisture resistance, and revealed that both **BT** and **CPDT** exhibit similar affinity to water than the benchmark Spiro-OMeTAD (angles ranging from 74.02° to 76.01°) while, once again, **SDTF** stands out of the crowd with a noticeable higher visualized hydrophobicity (102.36°, Figure 2.36).

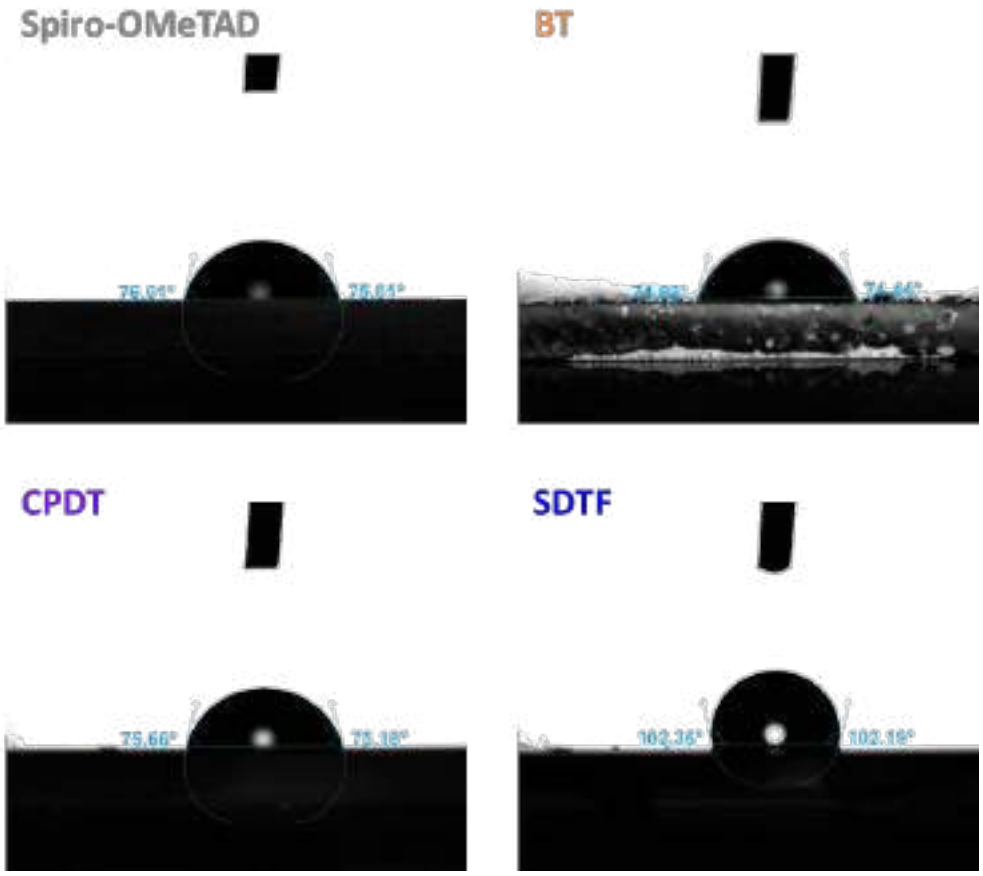

*Figure 2.36 Contact angle measurements of **Spiro-OMeTAD**, **BT**, **CPDT**, and **SDTF**. The films were deposited on ITO glass without dopants.*

Hence, as a logical follow-up, the potential of the three molecules as HTMs was subsequently evaluated and compared in n-i-p type PSCs of architecture: FTO/SnO_2/perovskite/HTM/Au in collaboration with the group of Jong Hyeok Park (Yonsei University). To do so, different dopants such as Li-TFSI, tBP, and FK 209 Co(III) TFSI were used to adjust the Fermi level, hole conductivity, and morphologies of each individual HTM, but still based on the recipe known and applied to the reference Spiro-OMeTAD. It turned out that the best results were still achieved with Li-TFSI and promising maximum efficiencies, *ie* ranging from 18.53% to 20.69%, were demonstrated, almost competing with that of the benchmark Spiro-OMeTAD (PCE = 21.56%).

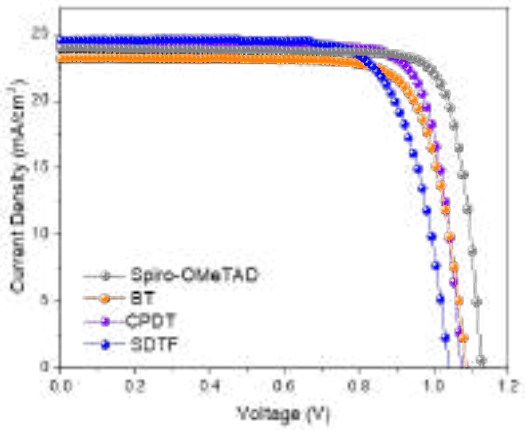

Figure 2.37 J-V curves of perovskite solar cells (PSCs) with individual HTMs.

The best performing J-V curves can be found in Figure 2.37 and the corresponding data extracted in Table 2.8.

Table 2.8 Photovoltaic parameters of PSCs with different HTLs (average of 5 devices each).

Average (Best)	**Spiro-OMeTAD**		**SDTF**		**BT**		**CPDT**	
PCE (%)	21.11	(21.56)	17.39	(18.53)	17.44	(19.27)	19.74	(20.69)
V_{oc} (V)	1.11	(1.12)	1.00	(1.03)	1.06	(1.09)	1.05	(1.07)
J_{sc} (mA/cm^2)	23.84	(24.00)	25.92	(24.26)	22.03	(22.95)	23.58	(23.92)
FF (%)	79.79	(80.24)	72.70	(74.16)	74.69	(77.19)	79.72	(81.36)

Interestingly, **CPDT** was found to slightly outperform its two other counterparts, result correlated to a more uniform and homogenous surface exhibiting an average roughness comparable to that of doped spiro-OMeTAD (Figure 2.38, R_a = 3.234 nm vs R_a = 3.211 nm, respectively), while higher roughness values of 5.585 nm and 6.398 nm were found for **BT** and **SDTF**, respectively.

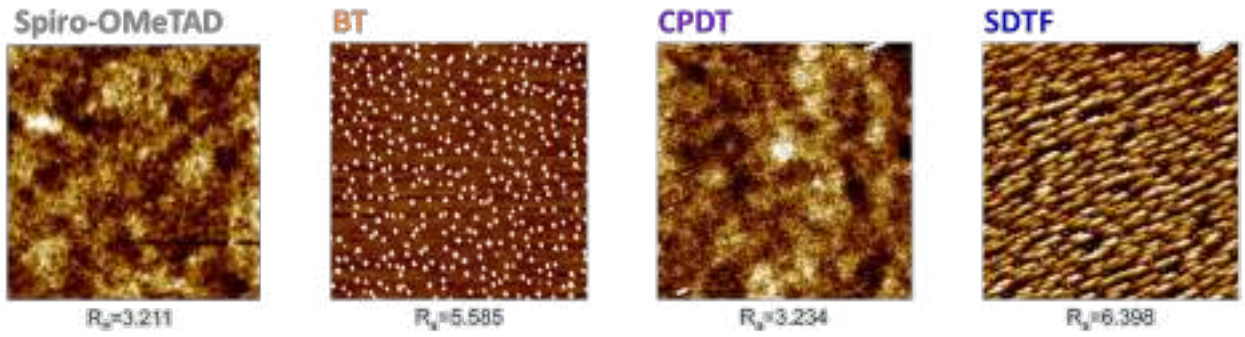

*Figure 2.38 Atomic force microscopy (AFM) images of as-prepared **Spiro-OMeTAD**, **BT**, **CPDT**, and **SDTF** based hole transporting layers (HTLs) with dopants. The samples were prepared on perovskite coated substrate.*

From the morphological similarities between **CPDT** and the reference Spiro-OMeTAD, bicomponent HTMs were then considered to assess the complementarity, compatibility (molecular interactions), and impact of a potential synergetic effect on both the chemical (doping) and electrical properties. Unprecedented (to the best of our knowledge) in the literature, blends with different ratios of HTMs were processed. As a result, efficiencies exceeding those recorded with pristine Spiro-OMeTAD based PSCs were quickly demonstrated with low concentrations of thiophene based molecules since the best results were achieved with only 5 mol% for all three thiophene-based compounds. The champion J-V curves are plotted in Figure 2.39 and data gathered in Table 2.9. To be differentiated from pristine layers, such HTLs will now be referred to as **BT-B**, **CPDT-B** and **SDTF-B** with "B" standing for blends.

Table 2.9 Photovoltaic parameters of PSCs with different blended HTLs.

Average (Best)	**Spiro-OMeTAD**		**SDTF-B**		**BT-B**		**CPDT-B**	
PCE (%)	22.95	(23.72)	23.27	(24.01)	23.12	(24.14)	23.75	(24.49)
V_{oc} (V)	1.14	(1.15)	1.14	(1.14)	1.14	(1.15)	1.15	(1.15)
J_{sc} (mA/cm^2)	24.93	(25.25)	25.36	(25.70)	25.06	(25.31)	25.49	(25.81)
FF (%)	80.74	(81.89)	80.49	(81.61)	80.93	(82.72)	81.02	(82.20)
Hole Mobility (x10^{-3} cm^{2}V^{-1}s^{-1})	3.89		4.71		4.31		5.31	

These higher efficiencies were found to mainly result from the improvement of both the open-circuit voltage (V_{oc}) and the fill factor (FF) correlated to improved shunt resistance and energy band alignment at the HTL/perovskite interface. In particular, an impressive PCE of 24.49%, close to the state of the art (but in a conventional architecture), associated with a FF of 82.20% was indeed achieved with **CPDT-B** based devices.

Beyond pure efficiencies, the key parameter/limitation of the PSCs, which is the overall stability, was naturally explored to confirm the potential of this bi-component strategy. Consequently, best operating devices were subjected to constant illumination under ambient conditions (light illumination was applied using a 150 W Xe lamp solar simulator PEC-L01, PECCELL after 1 sun calibration and active cooling was not applied during the measurement) and without any further encapsulation (Figure 2.39).

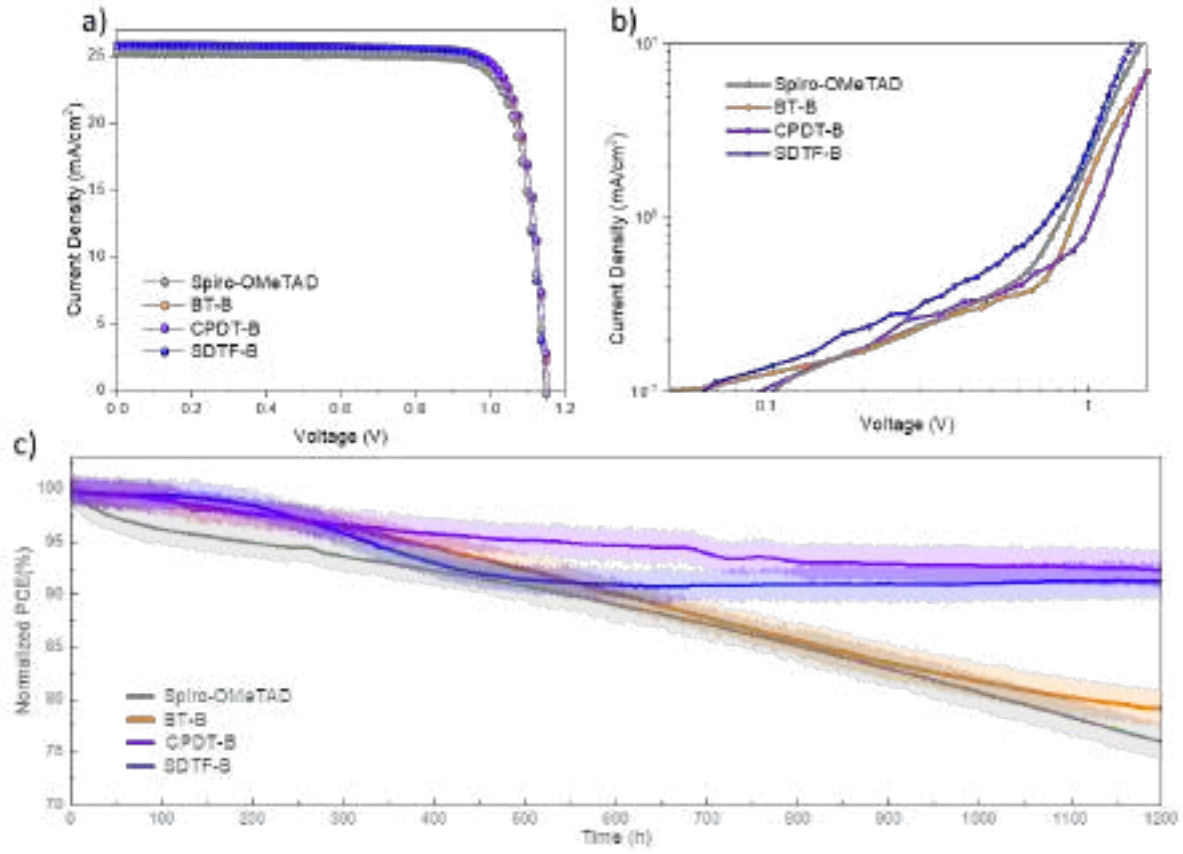

Figure 2.39 (a) J-V curves of perovskite solar cells (PSCs) with blended HTLs. (b) Space charge-limited current (SCLC) measurement of perovskite films with blended HTLs. (c) Operational stability of PSCs with blended HTLs at ambient environment without encapsulation.

It turned out that while a significant drop in efficiency was recorded for both the neat Spiro-OMeTAD and **BT-B** based devices barely reaching 70% of their initial PCE after 1200 hours of constant operation, the **CPDT-B** and **SDTF-B** were able to stabilize the performance above 90% under similar conditions.

Hence, in an attempt to rationalize and elucidate this peculiar increase in efficiencies and stabilities, space charge-limited current (SCLC) measurements were first carried out on the doped blends and directly compared to an optimized Spiro-OMeTAD "only" HTL. From the J-V curves plotted in Figure 2.39 and the application of the Mott-Gurney equation, higher hole mobilities were systematically measured on bicomponent based blends suggesting improved or additional intermolecular π-π stacking interactions, beneficial to charge transport/extraction (see values in Table 2.9).

In parallel, specific attention was drawn to evaluate the degree of oxidized spiro-OMeTAD (into spiro$^{\bullet+}$TFSI$^{\bullet-}$) by the dopant in these HTLs. To do so, UV-vis spectra of optimized doped blends were recorded over a period of 15 days under a dry environment (25 °C, relative humidity (RH) 10%, dark). Starting with the spiro-OMeTAD reference thin films (mono component), two absorption patterns were recorded, at 371 nm (A_{371}) and 520 nm (A_{520}) corresponding to the neutral and TFSI$^-$ stabilized spiro-OMeTAD radical specie (spiro$^{\bullet+}$TFSI$^{\bullet-}$), respectively (Figure 2.40).

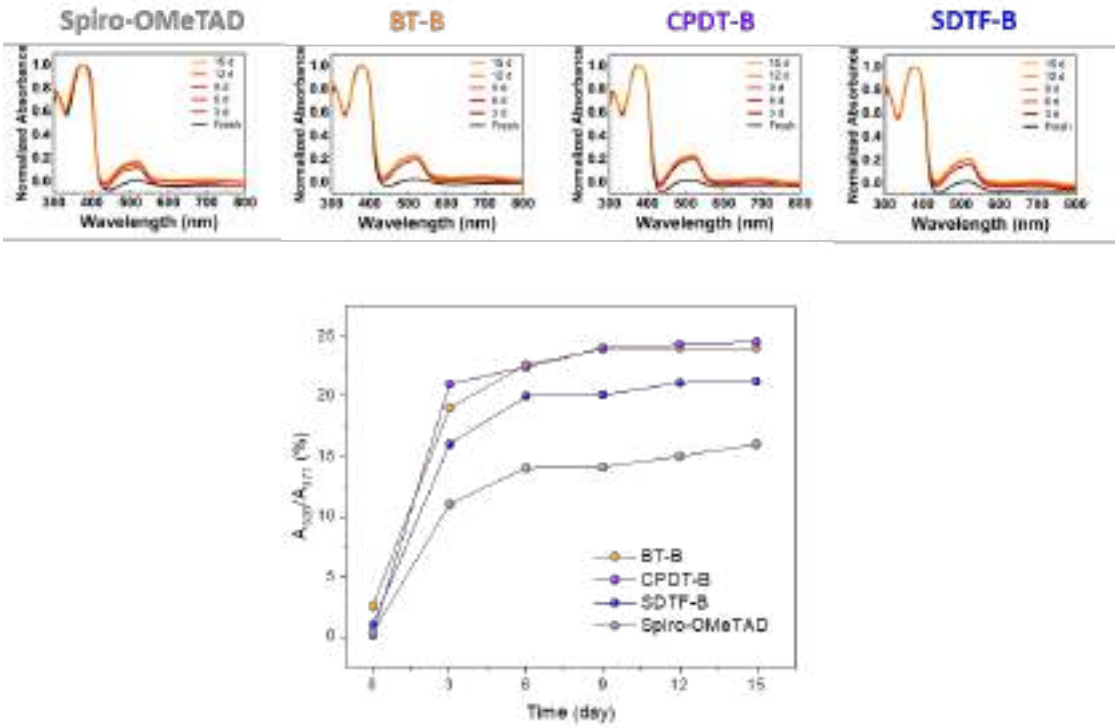

Figure 2.40 UV-vis absorption spectra of pristine spiro-OMeTAD and blended HTLs (5 mol% of each new HTM), and the absorption peak comparison between A_{520} (absorbance at 520 nm) and A_{371} (absorbance at 371 nm) of the samples with different exposure time.

Integration of these patterns (A_{520}/A_{371}) determined ratios that were in turn used to estimate the doping efficiency of Li-TFSI. It thus first appeared that the spiro$^{\bullet+}$TFSI$^{\bullet-}$ was already present in the as-cast and fresh sample, highlighting that the oxidation process already occurs in the solution/ink prior to deposition. Saturation was then reached on aged films after 12 days under this dry and controlled environment with a maxima A_{520}/A_{371} ratio of *ca* 0.15. Interestingly, higher values were calculated in all aged bicomponent systems, reaching almost 0.25 for both

CPDT-B and **SDTF-B** based samples (Figure 2.41) within the same period of time (but with a plateau after only 6 days).

This interesting and unprecedented feature suggests that a similar doping efficiency to that of neat Spiro-OMeTAD can be potentially achieved with a lower amount of dopant, which would have a significant impact on the stability of the device.

In general, the optimized amount of LiTFSI used is 23 µL (from a 1.8M solution in acetonitrile) for a 0.07 mol/L solution of spiro-OMeTAD. Consequently, in consistency with the trend of A_{520}/A_{371} maximum values, the quantity of Li-TFSI was significantly reduced, for both **CPDT-B** and **SDTF-B**, by 22% (from 23 µl to 18 µl) compared to the amount usually used in optimized spiro-OMeTAD only based HTL.

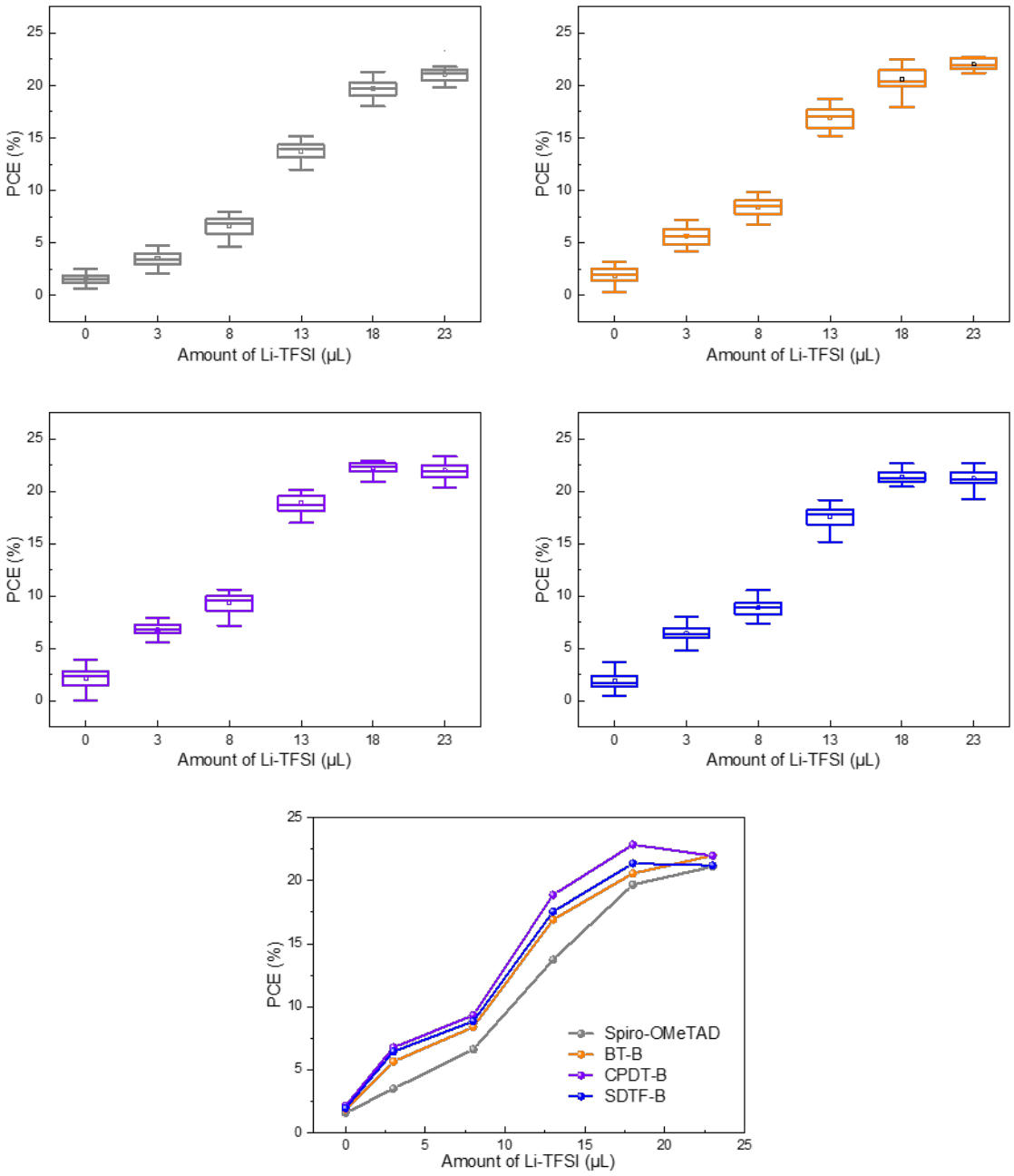

Figure 2.41 Power conversion efficiency (PCE) distribution of the PSCs with different amounts of Li-TFSI (520 mg of Li-TFSI dissolved in 1 mL of acetonitrile) added to the HTL with the corresponding average PCE change of the PSCs.

With suspected improved molecular ordering and interactions within the stacks, grazing incidence wide angle X-ray scattering (GIWAXS) experiments were subsequently performed at the Pohang Light Source (PLS) facilities (Figure 2.42).

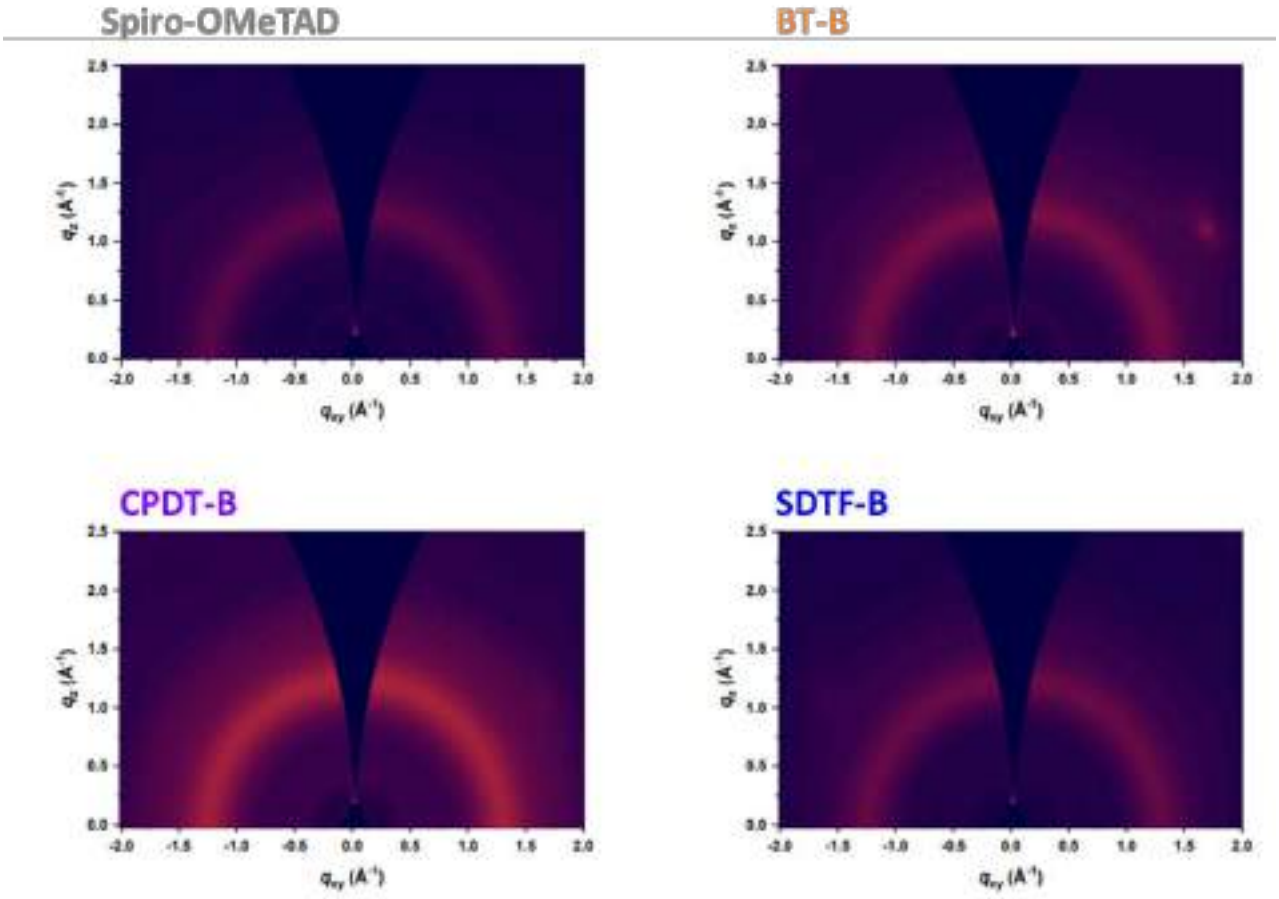

Figure 2.42 Grazing incidence wide angle X-ray scattering (GIWAXS) patterns of as-prepared pristine spiro-OMeTAD and blends. The samples were prepared on silicon substrate and dopants were added.

All samples exhibited broad scattering around q=1.3 $Å^{-1}$ along both the in- and out-of-plane directions. This isotropic ring can be attributed to the amorphous nature of intermolecular π-π stacking (see Figure 2.43 for intensity profiles). In addition, low intensity scattering around q=0.43 $Å^{-1}$ was also observed, which is correlated to the presence of lamellar stacking in the in-plane direction.

The intensities of such interactions were found to be enhanced after molecular blending of the spiro-OMeTAD with one of the three molecules, with a higher degree in the case of **CPDT-B**, thus supporting the role of such bicomponent in enhancing/favoring intermolecular interactions within the films that, in turn, induce efficient intermolecular hole transport. Moreover, it also results in lower quantities of dopant required to generate and stabilize Spiro-OMeTAD radicals. Increasing the number of such species is indeed a cornerstone to minimize V_{OC} losses, as shown

in the J-V curves, and improve energy band alignments between the constituting perovskite layers.

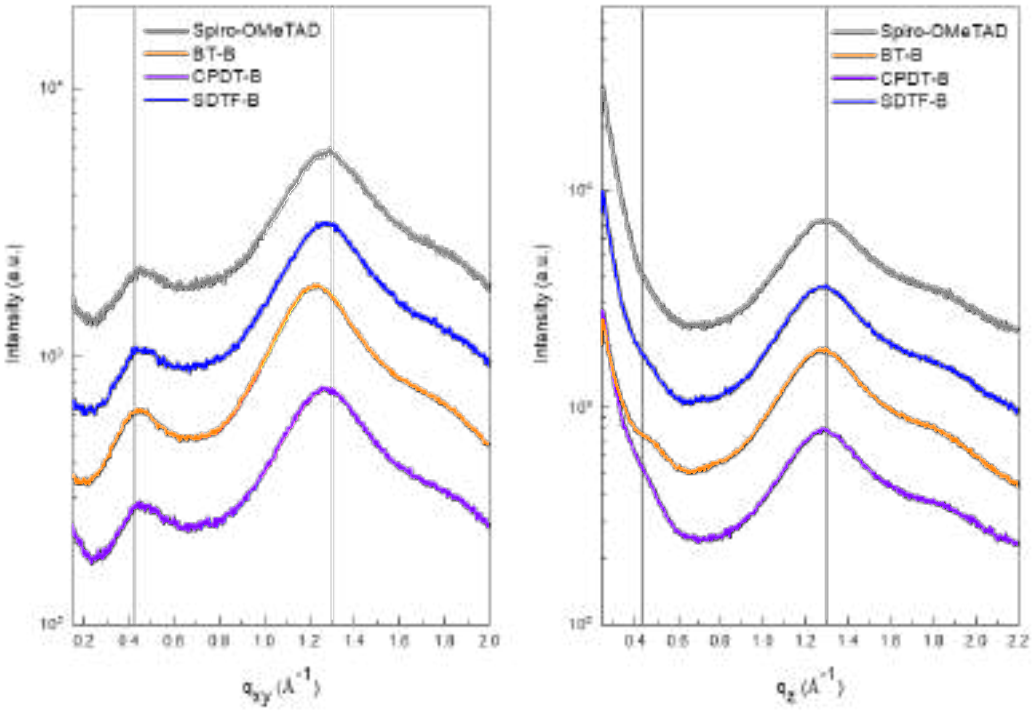

Figure 2.43 The corresponding intensity profiles from GIWAXS patterns of the spiro-OMeTAD and blends along the in-plane (left) and out-of-plane (right) directions.

On the other hand, to rationalize the difference of operation stability, surface analyses were carried out by atomic force microscopy before and after the constant irradiation test (Figure 2.44).

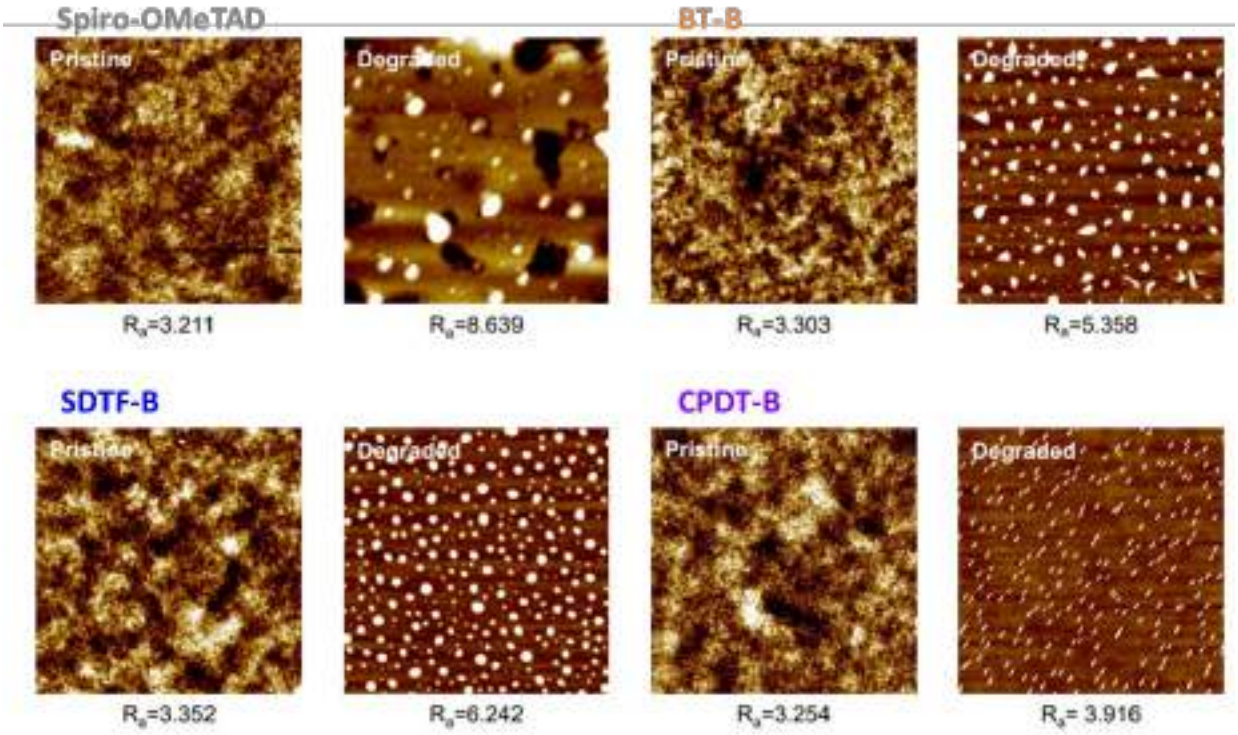

Figure 2.44 Pristine and degraded film analysis using atomic force microscopy (AFM). The morphology analysis of the degraded films was made right after operational stability measurements after 600 h. R_a denotes average roughness of the film. The size of the samples is 5 μm x 5 μm.

Starting with the doped Spiro-OMeTAD only layer, the initial smooth morphology with a R_a of 3.211 nm was found to be significantly affected since irregular aggregates and pinholes with a wide size distribution were probed on the surface, after only 600 hours of operation (90% of the remaining initial PCE). These defects are presumed to be byproducts derived from oxidized spiro-OMeTAD and Li-TFSI (Li aggregation/high hygroscopy was indeed demonstrated to reduce the power output and induce significant morphology changes in the HTL).[97]

Regarding the blends, morphologies scanned on fresh samples appeared almost identical to that of neat Spiro-OMeTAD with R_a under 3.5 nm, considering the low amount of co-HTM (5mol %). After the operation cycle, it was found that the formation of pinholes was somehow inhibited/limited in all three blends, even though aggregates were generated. The latter were relatively uniform and smaller than that observed and generated within the "pure" Spiro-OMeTAD layer, particularly for the best performing and most stable **CPDT-B** based HTL. The feature hence emphasizes a homogeneous distribution of Li-TFSI within the bulk during the

preparation and deposition processes that result in the limited generation of defects induced by the uncontrolled aggregation of Li-TFSI.

2.4.5 Conclusions and Perspectives

To sum up, three HTMs, synthesized by DHA, an eco-friendly cross-coupling reaction, in a simple one-step chemical reaction with a supported catalyst were evaluated in perovskite-based solar cells. Their promising efficiencies, almost competing with that of the reference Spiro-OMeTAD, and fine-tuned/complementary energy levels pushed us to consider and investigate bi-component blends. It turned out that mixing “only” 5 mol% of these molecules with the conventional Spiro-OMeTAD resulted in increased but, above all, more stable PCEs. Considering that dopants are, on one side required to reach high efficiencies, but on the other side, the primary source of limited stabilities, the incorporation of these molecules was found to increase the doping efficiency thus allowing a significant reduction of their needed concentrations within the bulks.

Moreover, these tris(4-methoxyphenyl) amine-based molecules were also found to improve the molecular interactions within the bulk, namely the Spiro-OMeTAD and the dopant, resulting in an improved intermolecular hole transport, shunt resistance, and energy band alignment at the HTL/perovskite interface. With the demonstration of a high PCE of *ca* 24.5% retained over 90% after 1200 hours under constant illumination and without encapsulation, this simple yet original strategy, consisting of blending different complementary and compatible HTMs, will hopefully pave the way to significant future achievements in the field of Perovskite solar cells.

As demonstrated in the push-pull molecule related study, the replacement of the methoxy group by a phenyl on the triphenylamine was found to be an interesting strategy to improve the charge transport characteristics. Consequently, the preparation of the **BT** analog with phenyl moieties on the two triphenylamines could be an easy way to improve its self-assembly and charge transport properties, a study investigated in the following chapter.

Bibliography

[1] A. E. Becquerel, Comptes Rendus Acad. Sci. 1839, 9, 145-149.
[2] A. E. Becquerel, Comptes Rendus Acad. Sci. 1839, 9, 561-567.
[3] D. M. Chapin, C. S. Fuller and G. L. Pearson, Journal of Applied Physics 2004, 25, 676-677.
[4] Photovoltaics Report, Fraunhofer Institute for Solar Energy Systems, ISE, February 2023.
[5] M. Aghaei, A Review on Comparison between Traditional Silicon Solar Cells and Thin-Film CdTe Solar Cells, 2012, p.
[6] O. Vigil-Galán, M. Courel, J. A. Andrade-Arvizu, Y. Sánchez, M. Espíndola-Rodríguez, E. Saucedo, D. Seuret-Jiménez and M. Titsworth, Journal of Materials Science: Materials in Electronics 2015, 26, 5562-5573.
[7] M. A. Green, Journal of Materials Science: Materials in Electronics 2007, 18, 15-19.
[8] M. Grätzel, Journal of Photochemistry and Photobiology C: Photochemistry Reviews 2003, 4, 145-153.
[9] M. K. Nazeeruddin, E. Baranoff and M. Grätzel, Solar Energy 2011, 85, 1172-1178.
[10] K. Prajapat, M. Dhonde, K. Sahu, P. Bhojane, V. V. S. Murty and P. M. Shirage, Journal of Photochemistry and Photobiology C: Photochemistry Reviews 2023, 55, 100586.
[11] D. Kearns and M. Calvin, The Journal of Chemical Physics 1958, 29, 950-951.
[12] G. A. Chamberlain, Solar Cells 1983, 8, 47-83.
[13] A. K. Ghosh, D. L. Morel, T. Feng, R. F. Shaw and C. A. Rowe, Jr., Journal of Applied Physics 2003, 45, 230-236.
[14] C. Tang and A. Albrecht, Nature 1975, 254, 507-509.
[15] V. Y. Merritt and H. J. Hovel, Applied Physics Letters 1976, 29, 414-415.
[16] D. Morel, A. Ghosh, T. Feng, E. Stogryn, P. Purwin, R. Shaw and Fishman, Applied Physics Letters 1978, 32, 495-497.
[17] A. K. Ghosh and T. Feng, Journal of Applied Physics 1978, 49, 5982-5989.
[18] C. W. Tang, Applied Physics Letters 1986, 48, 183-185.
[19] P. Heremans, D. Cheyns and B. P. Rand, Accounts of chemical research 2009, 42, 1740-1747.
[20] J. Halls, C. Walsh, N. C. Greenham, E. Marseglia, R. H. Friend, S. Moratti and A. Holmes, Nature 1995, 376, 498-500.
[21] G. Yu, J. Gao, J. C. Hummelen, F. Wudl and A. J. Heeger, Science 1995, 270, 1789-1791.
[22] M. C. Scharber, D. Mühlbacher, M. Koppe, P. Denk, C. Waldauf, A. J. Heeger and C. J. Brabec, Advanced materials 2006, 18, 789-794.
[23] M. T. Dang, L. Hirsch and G. Wantz in P3HT: PCBM, best seller in polymer photovoltaic research, Vol. Wiley Online Library, 2011.
[24] C. M. Proctor, J. A. Love and T. Q. Nguyen, Advanced Materials 2014, 26, 5957-5961.
[25] I. Ramirez, M. Causa', Y. Zhong, N. Banerji and M. Riede, Advanced energy materials 2018, 8, 1703551.
[26] H. W. Kroto, J. R. Heath, S. C. O'Brien, R. F. Curl and R. E. Smalley, Nature 1985, 318, 162-163.
[27] W. Krätschmer, L. D. Lamb, K. Fostiropoulos and D. R. Huffman, Nature 1990, 347, 354-358.
[28] Q. Xie, E. Perez-Cordero and L. Echegoyen, Journal of the american chemical society 1992, 114, 3978-3980.
[29] M. M. Wienk, J. M. Kroon, W. J. Verhees, J. Knol, J. C. Hummelen, P. A. Van Hal and R. A. Janssen, Angewandte Chemie 2003, 115, 3493-3497.
[30] J. C. Hummelen, B. W. Knight, F. LePeq, F. Wudl, J. Yao and C. L. Wilkins, The Journal of Organic Chemistry 1995, 60, 532-538.

[31] M. Campoy-Quiles, T. Ferenczi, T. Agostinelli, P. Etchegoin, Y. Kim and T. Anthopoulos, Nature Materials 2008, 7, 158-164.
[32] I. Fraga Domínguez, A. Distler and L. Lüer, Advanced Energy Materials 2017, 7, 1601320.
[33] J. Song and Z. Bo, Chinese Chemical Letters 2023, 108163.
[34] H. Liu, T. Dai, J. Zhou, H. Wang, Q. Guo, Q. Guo and E. Zhou, Nano Research 2023.
[35] X. Zhao, Y. Xiong, J. Ma and Z. Yuan, The Journal of Physical Chemistry A 2016, 120, 7554-7560.
[36] J. Feng, W. Jiang and Z. Wang, Chemistry – An Asian Journal 2018, 13, 20-30.
[37] L. Duan, N. K. Elumalai, Y. Zhang and A. Uddin, Solar Energy Materials and Solar Cells 2019, 193, 22-65.
[38] X. Gao, F. Sun, X. Tong, X. Zheng, Y. Wang, C. Xiao, P. Li, R. Yang, X. Wang and Z. Liu, Frontiers of Optoelectronics 2023, 16, 8.
[39] F. Tang, K. Wu, Z. Zhou, G. Wang, B. Zhao and S. Tan, ACS Applied Energy Materials 2019, 2, 3918-3926.
[40] J. D. B. Koenig, M. E. Farahat and G. C. Welch, ChemSusChem 2022, 15, e202200492.
[41] A. Laventure, S. Stanzel, A.-J. Payne, B. H. Lessard and G. C. Welch, Journal of Chemical Technology & Biotechnology 2022, 97, 844-851.
[42] J. Zhang, Y. Li, J. Huang, H. Hu, G. Zhang, T. Ma, P. C. Y. Chow, H. Ade, D. Pan and H. Yan, Journal of the American Chemical Society 2017, 139, 16092-16095.
[43] G. Zhang, J. Feng, X. Xu, W. Ma, Y. Li and Q. Peng, Advanced Functional Materials 2019, 29, 1906587.
[44] K. Ding, T. Shan, J. Xu, M. Li, Y. Wang, Y. Zhang, Z. Xie, Z. Ma, F. Liu and H. Zhong, Chemical Communications 2020, 56, 11433-11436.
[45] S. Chen, D. Meng, J. Huang, N. Liang, Y. Li, F. Liu, H. Yan and Z. Wang, CCS Chemistry 2021, 3, 78-84.
[46] J. Yuan and Y. Zou, Organic Electronics 2022, 102, 106436.
[47] H.-W. Cheng, Y. Zhao and Y. Yang, Advanced Energy Materials 2022, 12, 2102908.
[48] J. Yuan, Y. Zhang, L. Zhou, G. Zhang, H.-L. Yip, T.-K. Lau, X. Lu, C. Zhu, H. Peng, P. A. Johnson, M. Leclerc, Y. Cao, J. Ulanski, Y. Li and Y. Zou, Joule 2019, 3, 1140-1151.
[49] G. Zhang, F. R. Lin, F. Qi, T. Heumüller, A. Distler, H.-J. Egelhaaf, N. Li, P. C. Y. Chow, C. J. Brabec, A. K. Y. Jen and H.-L. Yip, Chemical Reviews 2022.
[50] J.-W. Lee, C. Sun, T. N.-L. Phan, D. C. Lee, Z. Tan, H. Jeon, S. Cho, S.-K. Kwon, Y.-H. Kim and B. Kim, Energy & Environmental Science 2023.
[51] R. Po, G. Bianchi, C. Carbonera and A. Pellegrino, Macromolecules 2015, 48, 453-461.
[52] J. Jin, Q. Wang, K. Ma, W. Shen, L. A. Belfiore, X. Bao and J. Tang, Advanced Functional Materials 2023, 33, 2213324.
[53] L. Yuan, Y. Zhao, J. Zhang, Y. Zhang, L. Zhu, K. Lu, W. Yan and Z. Wei, Advanced Materials 2015, 27, 4229-4233.
[54] M. C.-Y. Hou Fangzhan, Liang Long, Wang Hongyu, Xie Guanghui, Lu Zhengquan, Li Jingjing, Li Wei-Shi, Chinese Journal of Organic Chemistry 2016, 36, 1586-1595.
[55] G. Tarafdar, J. C. Johnson, B. W. Larson and P. C. Ramamurthy, Dyes and Pigments 2020, 177, 108289.
[56] S. Zhang, Y. Qin, J. Zhu and J. Hou, Advanced Materials 2018, 30, 1800868.
[57] X. Chen, C. Liao, M. Deng, X. Xu, L. Yu, R. Li and Q. Peng, Chemical Engineering Journal 2023, 451, 139046.
[58] Q. Peng, X. Liu, D. Su, G. Fu, J. Xu and L. Dai, Advanced Materials 2011, 23, 4554-4558.
[59] C. Sun, F. Pan, H. Bin, J. Zhang, L. Xue, B. Qiu, Z. Wei, Z.-G. Zhang and Y. Li, Nature Communications 2018, 9, 743.

[60] X. Kong, J. Zhang, L. Meng, C. Sun, S. Qin, C. Zhu, J. Zhang, J. Li, Z. Wei and Y. Li, CCS Chemistry 2023, 5, 841-850.
[61] A. Mishra and P. Bäuerle, Angewandte Chemie International Edition 2012, 51, 2020-2067.
[62] V. Malytskyi, J.-J. Simon, L. Patrone and J.-M. Raimundo, RSC Advances 2015, 5, 354-397.
[63] F. Bures, RSC Advances 2014, 4, 58826-58851.
[64] H. Bürckstümmer, E. V. Tulyakova, M. Deppisch, M. R. Lenze, N. M. Kronenberg, M. Gsänger, M. Stolte, K. Meerholz and F. Würthner, Angewandte Chemie International Edition 2011, 50, 11628-11632.
[65] X. Che, Y. Li, Y. Qu and S. R. Forrest, Nature Energy 2018, 3, 422-427.
[66] J. Roncali, P. Leriche and P. Blanchard, Advanced Materials 2014, 26, 3821-3838.
[67] S. Roquet, A. Cravino, P. Leriche, O. Alévêque, P. Frère and J. Roncali, Journal of the American Chemical Society 2006, 128, 3459-3466.
[68] C. Cabanetos, P. Blanchard and J. Roncali, The Chemical Record 2019, 19, 1123-1130.
[69] A. Leliège, C.-H. L. Régent, M. Allain, P. Blanchard and J. Roncali, Chemical Communications 2012, 48, 8907-8909.
[70] P. Blanchard, C. Malacrida, C. Cabanetos, J. Roncali and S. Ludwigs, Polymer International 2019, 68, 589-606.
[71] A. Leliège, J. Grolleau, M. Allain, P. Blanchard, D. Demeter, T. Rousseau and J. Roncali, Chemistry – A European Journal 2013, 19, 9948-9960.
[72] J. W. Choi, C.-H. Kim, J. Pison, A. Oyedele, D. Tondelier, A. Leliège, E. Kirchner, P. Blanchard, J. Roncali and B. Geffroy, RSC Advances 2014, 4, 5236-5242.
[73] Y. Jiang, C. Cabanetos, S. Jungsuttiwong, D. Alberga, C. Adamo and J. Roncali, ChemistrySelect 2017, 2, 6296-6303.
[74] S. Mohamed, D. Demeter, J.-A. Laffitte, P. Blanchard and J. Roncali, Scientific Reports 2015, 5, 9031.
[75] Y. Jiang, C. Cabanetos, M. Allain, P. Liu and J. Roncali, Journal of Materials Chemistry C 2015, 3, 5145-5151.
[76] P. S. Marqués, J. M. Andrés Castán, P. Josse, M. Blais, A. H. Habibi, I. Ramirez, K. Walzer, J. Roncali, P. Blanchard and C. Cabanetos, New Journal of Chemistry 2020, 44, 11441-11447.
[77] M. Riede, D. Spoltore and K. Leo, Advanced Energy Materials 2021, 11, 2002653.
[78] L. Hong, H. Yao, Y. Cui, Z. Ge and J. Hou, APL Materials 2020, 8.
[79] J. Grolleau, F. Gohier, M. Allain, S. Legoupy, C. Cabanetos and P. Frère, Organic Electronics 2017, 42, 322-328.
[80] L.-Y. Lin, Y.-H. Chen, Z.-Y. Huang, H.-W. Lin, S.-H. Chou, F. Lin, C.-W. Chen, Y.-H. Liu and K.-T. Wong, Journal of the American Chemical Society 2011, 133, 15822-15825.
[81] J. Zhang, T. C. Parker, W. Chen, L. Williams, V. N. Khrustalev, E. V. Jucov, S. Barlow, T. V. Timofeeva and S. R. Marder, The Journal of Organic Chemistry 2016, 81, 360-370.
[82] J. Zhang, W. Chen, A. J. Rojas, E. V. Jucov, T. V. Timofeeva, T. C. Parker, S. Barlow and S. R. Marder, Journal of the American Chemical Society 2013, 135, 16376-16379.
[83] L. Zhang, N. S. Colella, B. P. Cherniawski, S. C. B. Mannsfeld and A. L. Briseno, ACS Applied Materials & Interfaces 2014, 6, 5327-5343.
[84] C. M. Cardona, W. Li, A. E. Kaifer, D. Stockdale and G. C. Bazan, Advanced Materials 2011, 23, 2367-2371.
[85] A. Labrunie, Y. Jiang, F. Baert, A. Leliège, J. Roncali, C. Cabanetos and P. Blanchard, RSC Advances 2015, 5, 102550-102554.
[86] L. Chen, G. Wang, P. Yin, C. Weng, S. Tan and P. Shen, Synthetic Metals 2020, 265, 116413.

[87] Q. Liu and K. Vandewal, Advanced Materials 2023, n/a, 2302452.
[88] B. Qi and J. Wang, Physical Chemistry Chemical Physics 2013, 15, 8972-8982.
[89] Y. Wu, Z. Wang, M. Liang, H. Cheng, M. Li, L. Liu, B. Wang, J. Wu, R. Prasad Ghimire, X. Wang, Z. Sun, S. Xue and Q. Qiao, ACS Applied Materials & Interfaces 2018, 10, 17883-17895.
[90] Y.-D. Lin, K.-M. Lee, B.-Y. Ke, K.-S. Chen, H.-C. Cheng, W.-J. Lin, S. H. Chang, C.-G. Wu, M.-C. Kuo, H.-C. Chung, C.-C. Chou, H.-Y. Chen, K.-L. Liau, T. J. Chow and S.-S. Sun, Energy Technology 2019, 7, 307-316.
[91] C. A. Aranda, M. M. Byranvand, S. Essig and M. Saliba, Journal of Materials Chemistry A 2022, 10, 19046-19066.
[92] M. A. Green and A. Ho-Baillie, ACS Energy Letters 2017, 2, 822-830.
[93] L. Calió, S. Kazim, M. Grätzel and S. Ahmad, Angewandte Chemie International Edition 2016, 55, 14522-14545.
[94] A. G. Ricciardulli, S. Yang, J. H. Smet and M. Saliba, Nature Materials 2021, 20, 1325-1336.
[95] A. Kojima, K. Teshima, Y. Shirai and T. Miyasaka, Journal of the American Chemical Society 2009, 131, 6050-6051.
[96] M. M. Lee, J. Teuscher, T. Miyasaka, T. N. Murakami and H. J. Snaith, Science 2012, 338, 643-647.
[97] R. Schölin, M. H. Karlsson, S. K. Eriksson, H. Siegbahn, E. M. J. Johansson and H. Rensmo, The Journal of Physical Chemistry C 2012, 116, 26300-26305.
[98] G.-H. Kim and D. S. Kim, Joule 2021, 5, 1033-1035.
[99] L. P. Lekesi, L. F. Koao, S. V. Motloung, T. E. Motaung and T. Malevu, Applied Sciences 2022, 12, 672.
[100] L. Wang, S. Yang, Q. Han, F. Yu, H. Zhang, X. Cai, C. Zhang, L. Gao and T. Ma, ChemSusChem 2021, 14, 4776-4782.
[101] D. Khan, S. Sajid, S. Khan, J. Park and I. Ullah, Solar Energy 2022, 238, 69-77.
[102] X. Yang, Q. Li, Y. Zheng, D. Luo, Y. Zhang, Y. Tu, L. Zhao, Y. Wang, F. Xu, Q. Gong and R. Zhu, Joule 2022, 6, 1277-1289.
[103] N. J. Jeon, H. G. Lee, Y. C. Kim, J. Seo, J. H. Noh, J. Lee and S. I. Seok, Journal of the American Chemical Society 2014, 136, 7837-7840.
[104] B. A. Kamino, B. Mills, C. Reali, M. J. Gretton, M. A. Brook and T. P. Bender, The Journal of Organic Chemistry 2012, 77, 1663-1674.
[105] Z. Hawash, L. K. Ono and Y. Qi, Advanced Materials Interfaces 2018, 5, 1700623.
[106] L. Nakka, Y. Cheng, A. G. Aberle and F. Lin, Advanced Energy and Sustainability Research 2022, 3, 2200045.
[107] J.-Y. Seo, S. Akin, M. Zalibera, M. A. R. Preciado, H.-S. Kim, S. M. Zakeeruddin, J. V. Milić and M. Grätzel, Advanced Functional Materials 2021, 31, 2102124.
[108] A. K. Jena, M. Ikegami and T. Miyasaka, ACS Energy Letters 2017, 2, 1760-1761.
[109] F. Lamberti, T. Gatti, E. Cescon, R. Sorrentino, A. Rizzo, E. Menna, G. Meneghesso, M. Meneghetti, A. Petrozza and L. Franco, Chem 2019, 5, 1806-1817.
[110] S. Wang, M. Sina, P. Parikh, T. Uekert, B. Shahbazian, A. Devaraj and Y. S. Meng, Nano Letters 2016, 16, 5594-5600.
[111] Z. Li, J. Tinkham, P. Schulz, M. Yang, D. H. Kim, J. Berry, A. Sellinger and K. Zhu, Advanced Energy Materials 2017, 7, 1601451.
[112] R. L. Forward, K. Y. Chen, D. M. Weekes, D. J. Dvorak, Y. Cao and C. P. Berlinguette, ACS Energy Letters 2019, 4, 2547-2551.
[113] G. Tumen-Ulzii, C. Qin, T. Matsushima, M. R. Leyden, U. Balijipalli, D. Klotz and C. Adachi, Solar RRL 2020, 4, 2000305.

[114] N. A. N. Ouedraogo, G. O. Odunmbaku, B. Guo, S. Chen, X. Lin, T. Shumilova and K. Sun, ACS Applied Materials & Interfaces 2022, 14, 34303-34327.
[115] Z. Li, J. Chen, H. Li, Q. Zhang, Z. Chen, X. Zheng, G. Fang, H. wang and Y. Hao, RSC Advances 2017, 7, 41903-41908.
[116] X. Sallenave, M. Shasti, E. H. Anaraki, D. Volyniuk, J. V. Grazulevicius, S. M. Zakeeruddin, A. Mortezaali, M. Grätzel, A. Hagfeldt and G. Sini, Journal of Materials Chemistry A 2020, 8, 8527-8539.
[117] M. Jeong, I. W. Choi, E. M. Go, Y. Cho, M. Kim, B. Lee, S. Jeong, Y. Jo, H. W. Choi, J. Lee, J.-H. Bae, S. K. Kwak, D. S. Kim and C. Yang, Science 2020, 369, 1615-1620.
[118] M. Jeong, I. W. Choi, K. Yim, S. Jeong, M. Kim, S. J. Choi, Y. Cho, J.-H. An, H.-B. Kim, Y. Jo, S.-H. Kang, J.-H. Bae, C.-W. Lee, D. S. Kim and C. Yang, Nature Photonics 2022, 16, 119-125.
[119] E. Li, W. Li, L. Li, H. Zhang, C. Shen, Z. Wu, W. Zhang, X. Xu, H. Tian, W.-H. Zhu and Y. Wu, Science China Chemistry 2019, 62, 767-774.
[120] Y.-D. Lin, K.-M. Lee, S. H. Chang, T.-Y. Tsai, H.-C. Chung, C.-C. Chou, H.-Y. Chen, T. J. Chow and S.-S. Sun, ACS Applied Energy Materials 2021, 4, 4719-4728.
[121] K.-M. Lee, J.-Y. Yang, P.-S. Lai, K.-J. Luo, T.-Y. Yang, K.-L. Liau, S. Y. Abate and Y.-D. Lin, Chemical Communications 2021, 57, 6444-6447.
[122] M. Saliba, S. Orlandi, T. Matsui, S. Aghazada, M. Cavazzini, J.-P. Correa-Baena, P. Gao, R. Scopelliti, E. Mosconi, K.-H. Dahmen, F. De Angelis, A. Abate, A. Hagfeldt, G. Pozzi, M. Graetzel and M. K. Nazeeruddin, Nature Energy 2016, 1, 15017.
[123] R. Nakar, F. J. Ramos, C. Dalinot, P. S. Marques, C. Cabanetos, P. Leriche, L. Sanguinet, M. Kobeissi, P. Blanchard, J. Faure-Vincent, F. Tran-Van, N. Berton, J. Rousset and B. Schmaltz, The Journal of Physical Chemistry C 2019, 123, 22767-22774.
[124] Z. Zhang, W. Li, S. Orlandi, M. Cavazzini, A. M. Asiri, M. K. Nazeeruddin, G. Pozzi, M. Saliba and P. Gao, The Journal of Physical Chemistry C 2022, 126, 18238-18250.
[125] A. Mishra, S. Gupta and A. Patra, Journal of Polymer Science 2022, 60, 975-984.
[126] P.-H. Lin, K.-M. Lee, C.-C. Ting and C.-Y. Liu, Journal of Materials Chemistry A 2019, 7, 5934-5937.
[127] Y.-C. Chang, K.-M. Lee, C.-H. Lai and C.-Y. Liu, Chemistry – An Asian Journal 2018, 13, 1510-1515.
[128] K.-M. Lu, K.-M. Lee, C.-H. Lai, C.-C. Ting and C.-Y. Liu, Chemical Communications 2018, 54, 11495-11498.
[129] Y.-C. Chang, K.-M. Lee, C.-C. Ting and C.-Y. Liu, Materials Chemistry Frontiers 2019, 3, 2041-2045.
[130] J.-H. Chen, K.-M. Lee, C.-C. Ting and C.-Y. Liu, RSC Advances 2021, 11, 8879-8885.
[131] L. Lin, C.-C. Hsu, K.-M. Lee, M.-Y. Lin, Y.-K. Peng and C.-Y. Liu, ChemistrySelect 2022, 7, e20220247

CHAPTER 3
CHAPTER 3

CHAPTER 3

CHAPTER 3
CHAPTER 3
CHAPTER 3

Chapter 3:
Simple Photoluminescent Materials for Organic Electroluminescent Devices

3.1 Organic Light-Emitting Devices

Alongside organic photovoltaics, organic light-emitting devices (OLEDs) are clearly heavy-weight contributors to the development of organic electronics. Cutting-edge technology in display and lighting industries,[1] these devices showed substantial improvement over conventional light and display sources and are nowadays widely used, if not standards in a broad range of "daily" products, including televisions, computers, smartphones, and wearable devices.[2] (Figure 3.1).

Figure 3.1 LG OLED flexible television (left) and foldable Samsung smartphone Galaxy Z Flip 3 (right).

The capacity of OLED technology to generate light directly from the organic layer, as opposed to the conventional backlight required by liquid crystal displays (LCDs), is one of its most important benefits. This characteristic indeed allows OLED displays to achieve "true and deep" blacks with improved contrast ratios, which produce brilliant colors and better image quality.[3] Moreover, organic materials can also be deposited/processed on flexible substrates, enabling the creation of bendable, foldable, and even rollable displays (see examples in Figure 3.1).[4-5-6] Already strongly used in industry, this technology is still expected to keep shaping the way we interact with displays and lighting solutions, enhancing our daily lives with its innovative capabilities.

3.1.1 The different generations of emitters

Photoluminescence is a photophysical process that is initiated by the absorption of a photon by a material thus going from the ground state to an excited state (see Figure 3.2, yellow arrows).[7] According to Frank Condon's principle, this excitation is very fast (of the order of 10^{-15} s) and occurs without geometric modification or spin orientation (or spin multiplicity). Therefore, if the ground state is a singlet state (S_0) then, after excitation, the molecule remains in a singlet excited state (S_n). The excited molecule then rearranges itself into a more stable geometry, during which, the latter loses energy by vibrational relaxation (VR, pink arrows, of the order of 10^{-12} to 10^{-10} s) and/or by internal conversion (IC, purple arrows, of the order of 10^{-11} to 10^{-9} s) to, usually, the first singlet excited state (S_1) followed by several relaxation processes to return to the ground state (S_0). Among them, it can relax i) by internal conversion which is a non-radiative process, ii) by the emission of a photon through the conservation of spin multiplicity, namely the fluorescence (blue arrows, around 10^{-9} to 10^{-7} s) and iii) populating triplet states by inter-system crossing ISC (red arrows, of the order of 10^{-8} to 10^{-3} s). The latter process, slower than internal conversion and fluorescence, requires a change of spin multiplicity (change in spin orientation) leading to a triplet excited state from which the return to the fundamental state can be done by non-radiative processes (inter-system crossings) or by emission of a photon, speaking then of phosphorescence (green arrows, around 10^{-3} to 10^{2} s).[8]

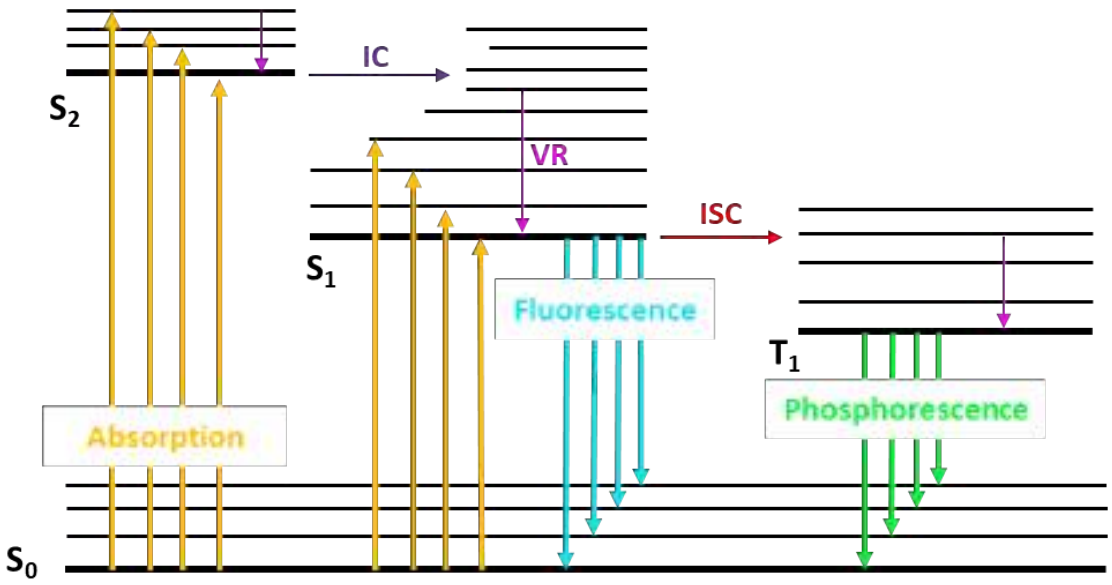

Figure 3.2 Perrin-Jablonski energetic diagram.

In an OLED, π-conjugated molecules or polymers, sandwiched between two electrodes, are excited by applying an external electric field. In this configuration, an electron is injected from the cathode to the LUMO level of the emissive layer (EML), and a hole from the anode to the HOMO level of the EML. After migration, charges can recombine in the (EML) resulting in the formation of an exciton, *i.e.* an electron-hole pair, which will emit light upon the deexcitation pathway (Figure 3.3).

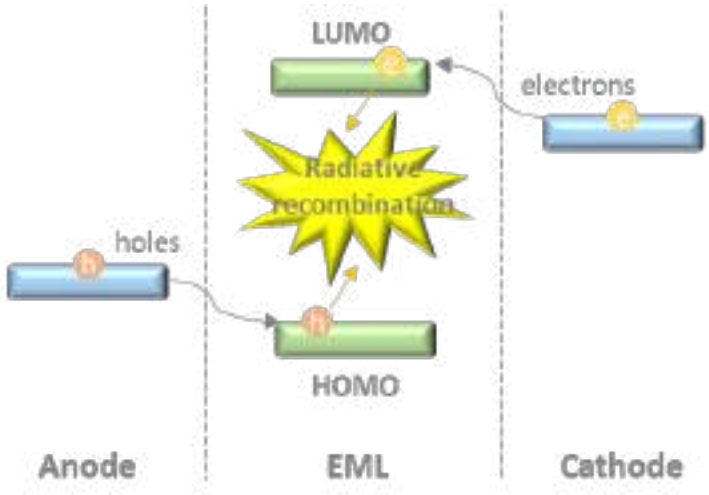

Figure 3.3 Schematic representation of the radiative recombination occurring in OLEDs.

Three generations of OLEDs have already been studied and classified according to the emission properties of the constituting emissive layer. In the case of the 1st generation, also known as fluorescent OLED, part of the singlet excited states leads to fluorescence, and all of the triplet excited states are lost in internal conversions due to the forbidden nature of the $T_1 \rightarrow S_0$ transition, thus reaching a maximum theoretical internal quantum efficiency (IQE) of 25%. After injection of electrons and holes at the respective electrodes and their combination, the generated excitons were indeed demonstrated to result in a statistical distribution between singlet and triplet states with a 1 to 3 ratio (Figure 3.4).[9-10]

In parallel, phosphorescent heavy-metal based complexes have been explored and embedded as emitters resulting in the second generation of OLEDs also known as Ph-OLED, in order to access and use the remaining 75% triplet excitons. Those complexes can accelerate the radiative deactivation through phosphorescence from the lowest-lying triplet state (T_1) to the ground

state (S_0) and also facilitate ISC from the lowest-lying singlet state S_1 to T_1 through an enhanced spin-orbit coupling induced by heavy-metal atoms such as iridium or platinum. In this case, the theoretical IQE can reach a maximum value of 100%.[11-14]

Although this class of emitters have shown great promise and have even been embedded in commercial electroluminescent devices, the cost and environmental/ecological impact of heavy-metal atoms pushed the community to develop alternatives (3rd generation). Among them, the incredibly promising TADF (for Thermally Activated Delayed Fluorescence) materials have attracted considerable research attention. In these molecules, the energy gap (ΔE_{ST}) between the lowest-lying singlet state S_1 and lowest-lying triplet state T_1 is reduced to allow the formally spin-forbidden reverse intersystem crossing (RISC) process by thermal activation, when the lifetime of the T_1 excitons is long enough, resulting in the up-conversion of the triplet excitons into the S_1 state, thus, also leading to a theoretical IQE of 100%.[15-18]

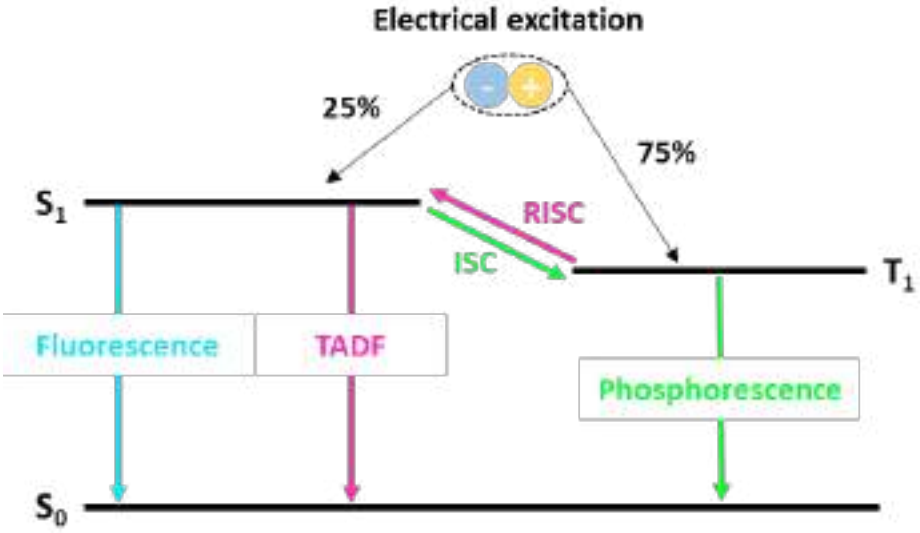

Figure 3.4 The three emission phenomena after electrical excitation.

Even though highly promising results have already been demonstrated with external quantum efficiencies EQE over 30%; [19-21] this third-generation emitter-based devices are clearly in their early stage. As a further key development, the next generation of OLED devices needs to demonstrate good efficiency, color purity, and above all, long lifetimes. Regarding the efficiencies, the latter can be further improved by optimizing the exciton harvesting through

chemical and physical engineering. For instance, hyperfluorescence, which is hailed as the "ultimate solution for OLED displays" refers to the use of cascade-type emissive layers resulting from the combination of a fluorescent dopant and an assistant dopant, usually with TADF properties. The major exciton formation is focused on the dopant molecules by controlling the ratio of complementary compounds promoting up conversion processes by favouring Förster resonance energy transfer (FRET) as depicted in Figure 3.5.[22-23]

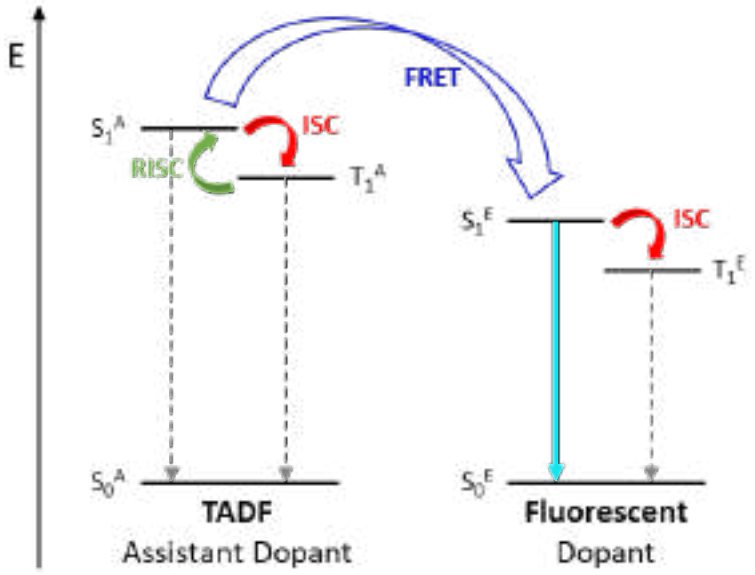

Figure 3.5 Simplified schematic diagram of the main energy transfer and luminescence pathways taking place in hyperfluorescent devices

This concept hence benefits from the fluorescent emitters' excellent stability, narrow emission spectra, and high color purity as well as the effectiveness of RISC process in TADF molecules, thus allowing a theoretical use of all generated excitons.

In this context, chemical structures and device architectures will obviously continue to evolve seeking for record efficiencies; however, as discussed in the previous chapters, related to the photovoltaic conversion, increasing the complexity from both the constituent and the device will still limit their large-scale dissemination and confine their use to academia.

3.1.2 Evolution of organic electroluminescent devices architectures

An OLED device typically consists of several layers of compatible and complementary materials sandwiched between two electrodes.

From the first demonstration reported by Tang et al.,[24] architecture has come a long way to tackle issues of these early OLEDs such as low EQEs and high driving voltages. This was basically achieved by adding layers of functional material to balance charge injection and transport for optimal emissive recombination (Figure 3.6).[2]

From the bottom to the top (following the successive and sequential deposition):

- Substrate: The substrate is the foundational layer of the OLED device. It provides mechanical support for the other layers and can be made of glass, plastic, or other transparent materials that can also be flexible.
- Anode (Transparent Electrode): The anode is a transparent, conductive layer that sits on top of the substrate. As for OPV, indium Tin Oxide (ITO) is a commonly used and reference material. It serves as a positive electrode for the injection of holes (positively charged carriers) into the organic layers.
- Hole Injection Layer (HIL): The layer aims at helping the injection of holes from the anode to the hole transport layer.
- Hole Transport Layer (HTL): The latter is usually made of an organic material that facilitates the percolation of positive charges (holes) from the anode toward the emissive layer. It ensures efficient charge transport.
- Electron Blocking Layer (EBL): It blocks the electron transport from the cathode to the anode to favour charge recombination in the emissive layer.
- Emissive Layer (EML): The emissive layer is the heart of the OLED device. It consists of organic materials (organic electroluminescent materials) that will generate the light from the recombination of injected charges.
- Hole Blocking Layer (HBL): It blocks the hole transport from the anode to the cathode to favour charge recombination in the emissive layer.
- Electron Transport Layer (ETL): As for the hole transport layer, ETL is made of organic materials and aims at facilitating the movement of electrons from the cathode toward the emissive layer.

- Electron Injection Layer (EIL): The electron injection layer is incorporated between the cathode and the electron transport layer to facilitate and help the injection of electrons from the cathode.
- Cathode: The cathode is the back electrode, typically made of metals with low work functions, such as calcium, silver, or aluminum. The cathode serves as the negative electrode for the injection of electrons into the organic layers.
- Encapsulation Layer: OLED devices are sensitive to moisture and oxygen, which can degrade their performance over time. To protect theses organic layers from environmental factors, an encapsulation layer is thus finally processed.

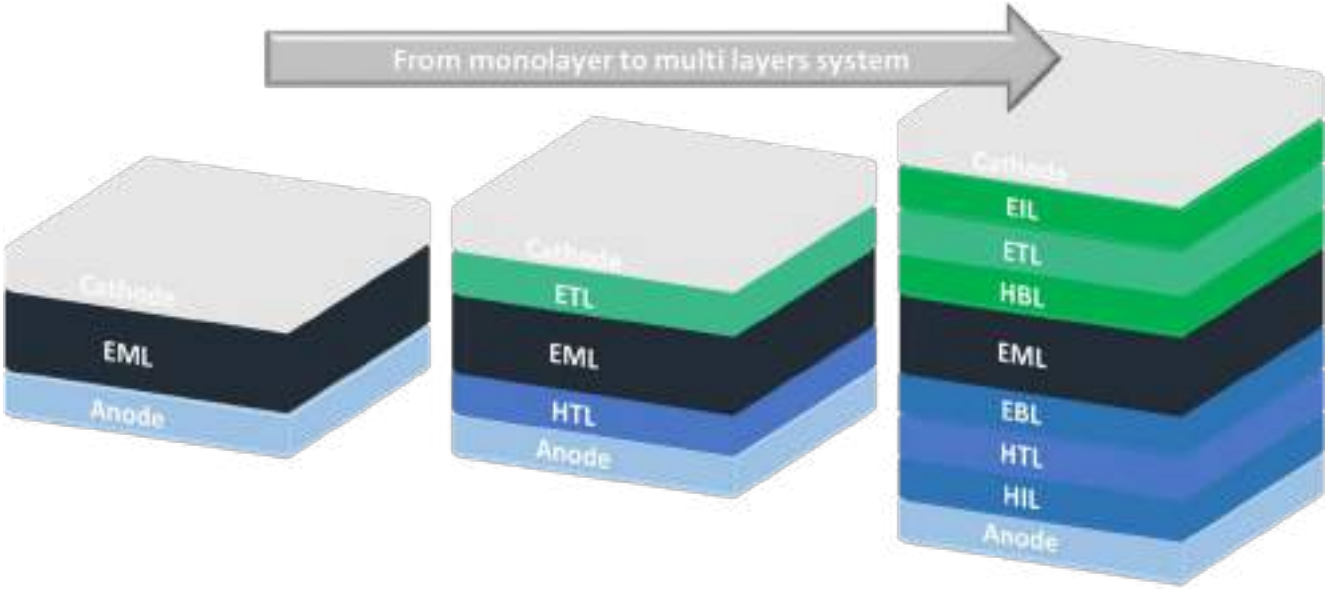

Figure 3.6 Evolution of the architectures of OLED devices from initial monolayer to "conventional" state of the art multi layers system.

The fabrication of these devices requires a non-negligible production time and above all a high standards of chemical and physical engineering to *i)* successfully process a large number of layers without altering/degrading the previous ones and ii) limit as much as possible the defects at the interfaces to improve lifetime and stability. Moreover, the multiplication of layers automatically generates high production costs and environmental impact since more organic

compatible and complementary materials have to be synthesized, purified, processed, and recycled.

In this context and as an attempt to simplify these structures, light-emitting electrochemical cells (LECs) were developed and introduced in 1995 by Pei et al.[25] For this demonstration polyphenylene vinylene was used as the emissive polymer as for the first polymer-based OLED introduced five years earlier.[26] Also sandwiched between an ITO anode and an aluminum cathode, the main difference with their OLED cousins relies on the incorporation of mobile ions within the emitting layers. When a voltage is applied between the electrodes, several anions and cations migrate to accumulate close to the positive anode and negative cathode, respectively, resulting in the generation of two injection layers (electric double layers).

Migration of remaining ions will then take place to electrostatically compensate the first injected holes and electrons thus defining an n-type transport layer next to the cathode and a p-type transport layer at the anode. Injected holes and electrons can thus recombine between the latter layers in the so-called p-n junction (Figure 3.7).

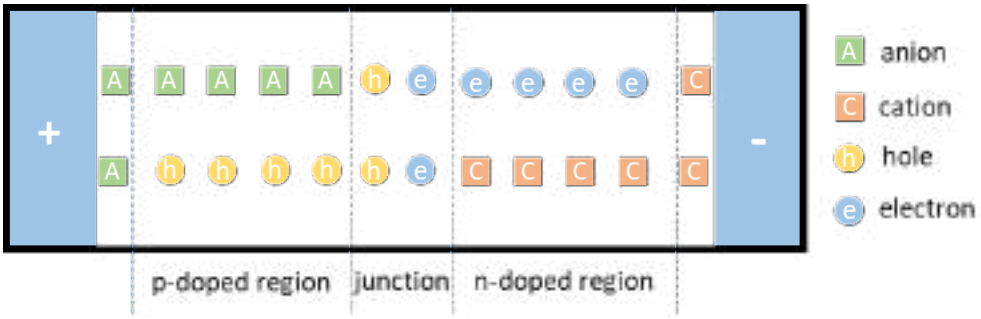

Figure 3.7 Illustration of the light emitting mechanism occurring in a LEC.

Known and reported as a “simplified version” of an OLED, the development of LECs took a different path since mainly focused on understanding the operating mechanism rather than increasing complexity to improve the performances.

However, even if different from a mechanistic and operating point of views, OLEDs and LECs are both characterized by key parameters related to the quantification of light emitted by these devices:

- The luminance (L in cd/m²) defines the intensity of the light emitted in a given direction per unit area; with the candela (cd) being the luminous intensity in lumen/steradian, formerly defined by the emission of a candle.
- The (injected) current density (J, expressed in mA/cm²) is the ratio of the current injected by the diode area
- Luminous Current Efficiency (CE in cd/A), which is the ratio between the emission of the diode and the current, or in other words, the relationship between the luminance and the current density.
- Luminous Power Efficiency (PE in lm/W) takes into account the CE and the applied voltage to the diode; the lumen (lm), which measures the luminous flux, is calibrated with respect to the detection of the human eye.
- The turn-on voltage (V_{on} in V), is the voltage value from which the diode starts emitting light, usually determined at L = 0.1 cd/m². It reflects the effectiveness of the injection of charges from the electrodes (in other words, the lower it is, the better it is).
- The internal quantum efficiency (IQE) is defined by the equation:

$$IQE = \frac{Nbr\ of\ emitted\ photons}{Nbr\ of\ injected\ charges} = \beta\ .\rho\ .\eta_{PL}$$

  In the latter, β represents the charge recombination efficiency, i.e. the exciton formation efficiency, ρ represents the proportion of excitons that can emit light (0.25 for fluorescent emitters and 1 for phosphorescent emitters) and η_{PL} is the photoluminescence quantum yield of the chromophore which assume there is only one emitter in the OLED.
- The external quantum efficiency (EQE) defined by the equation, $EQE = IQE\ .\ \eta_{opt}$ where η_{opt} represents the optical yield, i.e. the proportion of photons “trapped” or absorbed by the OLED compared to those emitted in the EML (out coupled photons per injected charge). This parameter evolves greatly depending on the structure of the device and the

refractive index (η) of the constituting layers. Experimentally, the EQE is measured directly in making the ratio of the photons emitted by the charges consumed.

- Finally, the chromaticity coordinates, defined by the International Commission of Illumination (also known as the CIE from its French title, the "Commission Internationale d'Eclairage") provide information on the color of the emission. They are reported on a two-dimensional x and y diagram as depicted in Figure 3.8.

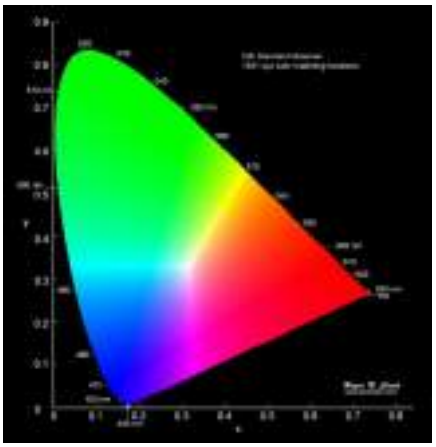

Figure 3.8 Chromaticity diagram defined by the CIE. Copyright Roger N Clark, clarkvision.com

Besides this amazing achievement from lab to customers, high-performing OLEDs are, to date and as stated above, built on a multi-layer (ML) stack, which ensures that holes and electrons are properly injected, transported, and recombined in the EML.[27-30] These devices nevertheless impact the production costs and limit the scope of use (mainly to "high tech" end product) and also the recyclability. Indeed, for large and daily dissemination, such as simple packaging, road signs, advertising, etc.: the simpler, the better (for the price and recycling).

Consequently, researchers started putting efforts into "re"simplifying the device's architectures and improve the originally reported single-layer OLED (SL-OLED).[31-35] Consequently through chemical engineering, the EML has to play the role of all intermediate functional layers. To maximize exciton recombination within the center of the EML and prevent leaks through the electrodes, such a material must: (*i*) show high and balanced mobilities of electrons and holes; (*ii*) have HOMO and LUMO levels aligned with the Fermi levels of the anode and the cathode

to maximize hole and electron injection, respectively; and (*iii*) exhibit good thermal and morphological stabilities to maximise OLED lifetimes.[36-39]

With all these criteria, this field is challenging and has not yet attracted the attention it deserves. Examples from the literature are still rare and usually deal with complex molecular structures prepared from multi-step syntheses to finally achieve modest results compared to ML-OLEDs. Some examples are depicted in Figure 3.9.[40-43]

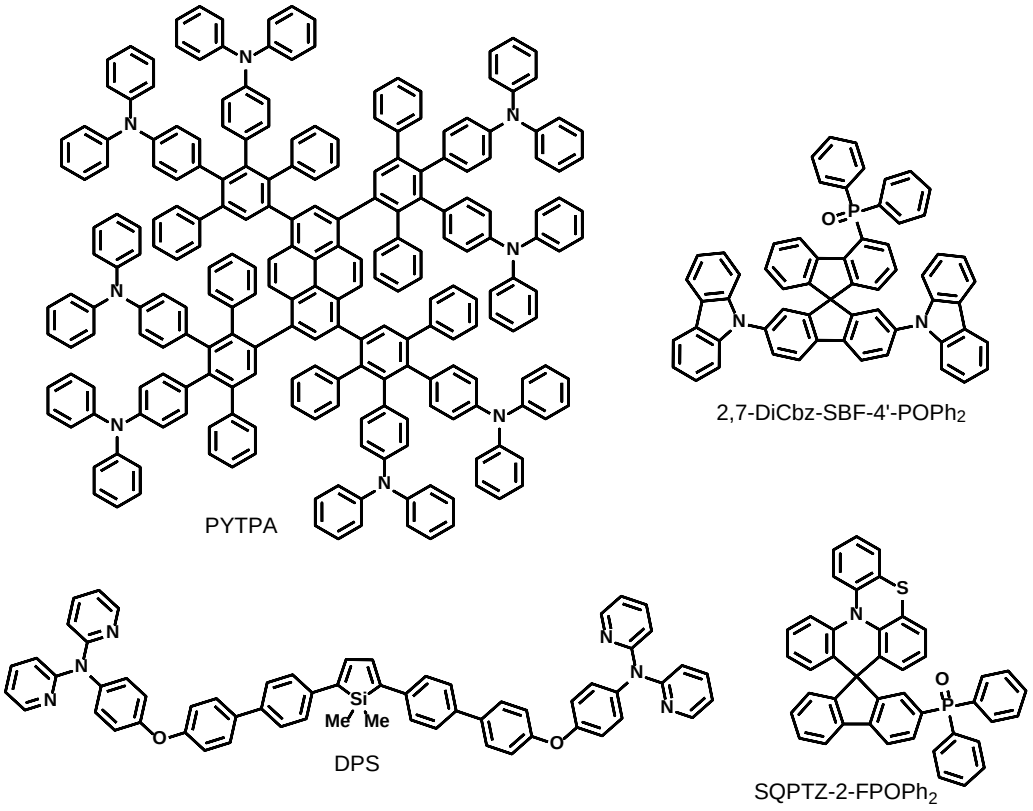

Figure 3.9 Chemical structures of some EML for SL-OLEDs.

Ideally, together with the device simplification, accessible emitting materials should be designed and evaluated to reduce both the environmental footprint and production cost.[35, 44] Their syntheses should be carried out in a minimum of steps, in high yields, and from accessible and commercially available blocks to be easily transposed to large scale production. With an

ultra-low cost and recyclable device, stability and performance can thus be easily revised downwards.

3.2 TPA-BP end-capped thiophene-based moieties as simple light-emitting materials

3.2.1 Context and synthesis

As stated in the perspective section of the photoconversion related chapter (chapter 2), the replacement of the methoxy group by a phenyl moiety on the triphenylamine of **BT** molecule was carried out to improve the self-assembly and charge transport property (Figure 3.10).

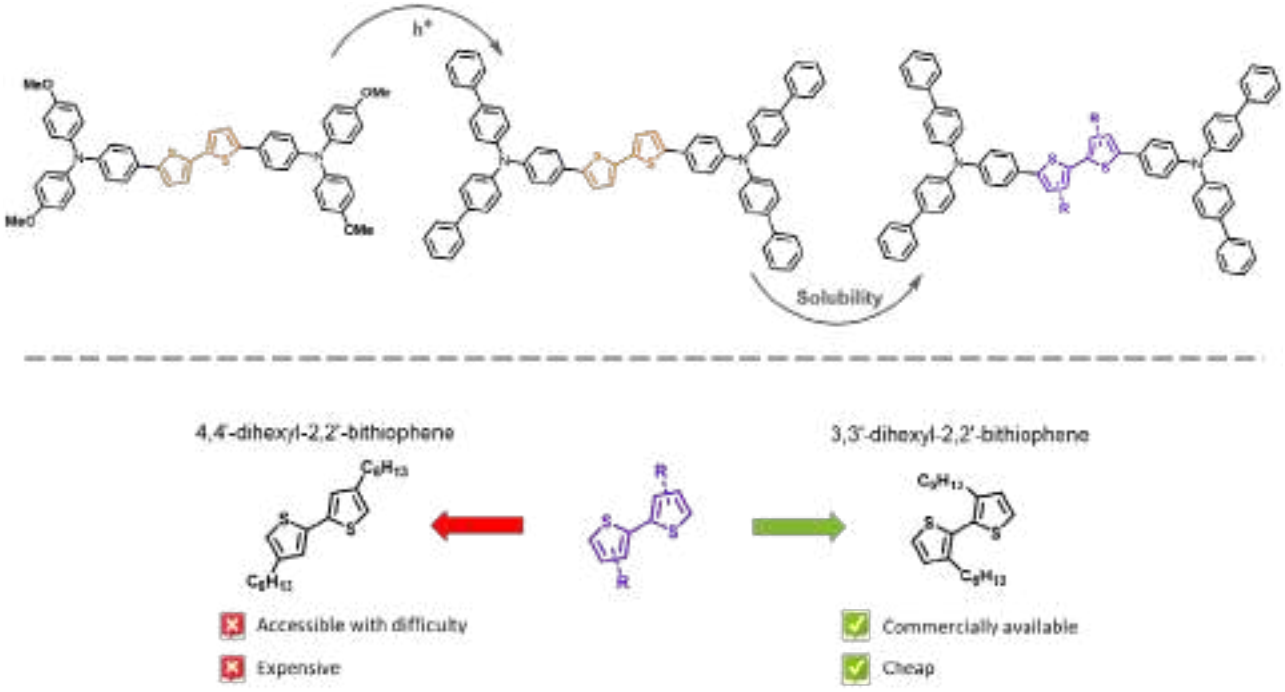

Figure 3.10 Origin of the design and structure of the BT1 studied herein

However, due to low solubility, insertion of aliphatic chains was then considered. Following our philosophy based on accessibility, we found out that the 2,2'-bithiophene functionalized by hexyl chains on positions 3 and 3' was available from common chemical suppliers and affordable unlike its 4,4'-dihexyl-functionalized analogue (expensive and from start-up like companies).

Consequently, even if the distortion induced by the two hexyl chains might affect the solid state aggregation and conjugation along the backbone, **BT$_1$** was synthesized by direct (hetero)arylation, in only one step, from these cheap commercially available building blocks (Scheme 3.1).

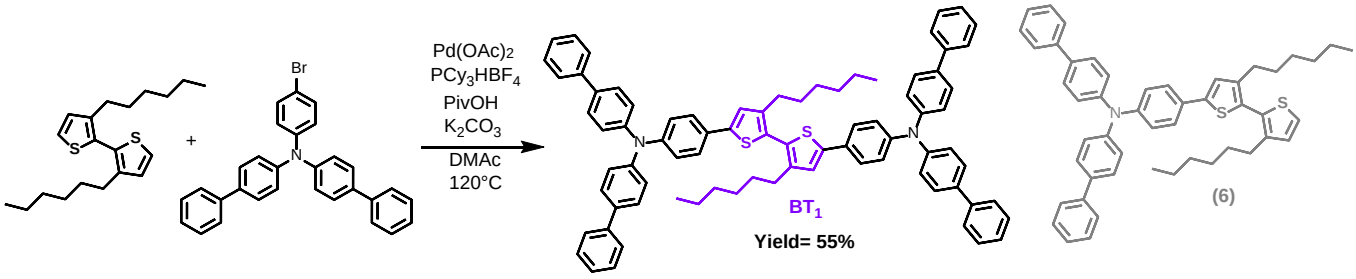

Scheme 3.1 Synthesis of BT1.

Once purified and isolated, the target compound showed, at first sight, intriguing emission properties in both solution and as thin film guiding us towards its potential use in light-emitting devices. Single crystals of **BT$_1$** were grown by slow evaporation of a chloroform solution. Its X-ray structure, represented in Figure 3.11, shows that the two thiophene rings adopt a “syn” conformation with a dihedral torsion angle of 60 ° induced by the hindering hexyl chains.

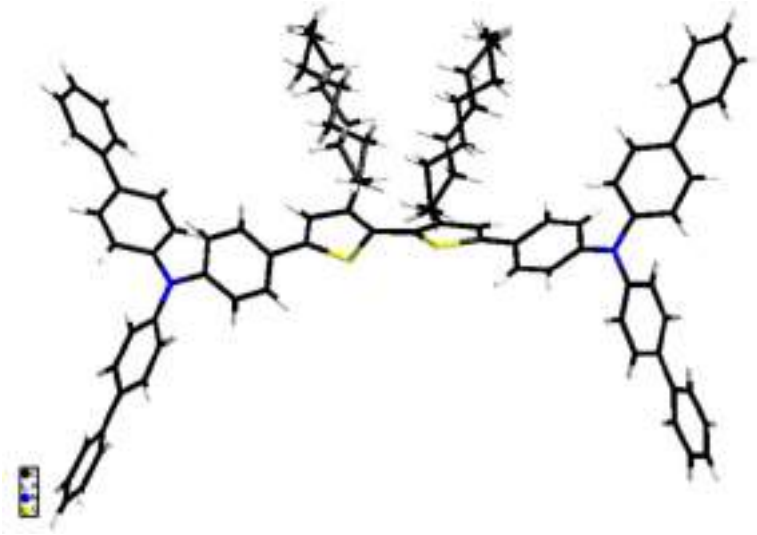

*Figure 3.11 X-ray structure of the **BT$_1$** compound.*

The latter was obtained in modest yields (55%), because compound **(6)**, resulting from the monocoupling reaction, was found to be the major side product. From this feature, it was decided to use it for the preparation of two other derivatives, namely **BT2** and **BT3**, which were designed and prepared to rationalize the impact of the length of the bi-thiophene based connector on the optoelectronic properties (Scheme 3.2).

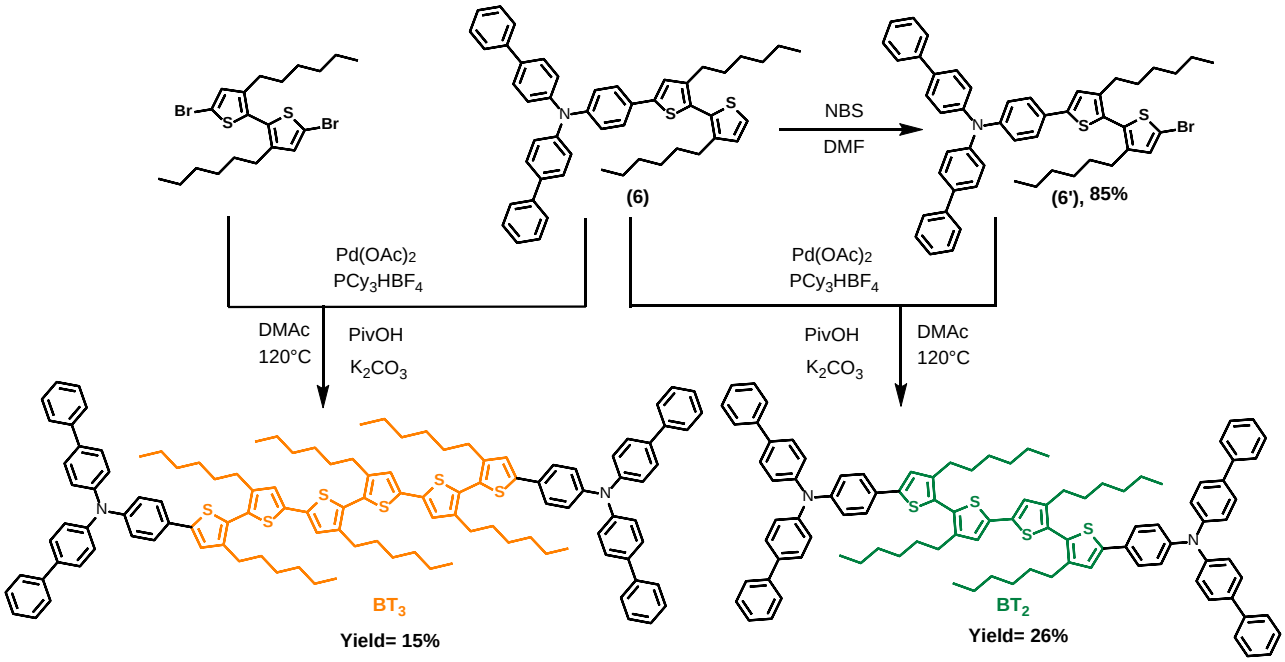

*Scheme 3.2 Synthetic route to **BT2** and **BT3** from compound **(6)**.*

To do so, bromination reactions were first carried out using N-bromosuccinimide (NBS) in DMF to afford both the 5,5'-dibromo-3,3'-dimethyl-2,2'-bithiophene and **6'** in good yields that were finally combined and engaged in two direct (hetero)arylation reactions.

3.2.2 Optoelectronic properties

Once the identity and the purity of the three final compounds were confirmed by nuclear magnetic resonance spectroscopy (NMR) and mass spectrometry (MS and HRMS), exploration and comparison of their optical and electrochemical properties were then carried out.

3.2.2.1 Electrochemical properties

First, the electrochemical properties of the three molecules were studied by cyclic voltammetry in a 0.5 mM solution in DCM using 0.1 M of tetrabutylammonium hexafluorophosphate ($TBAPF_6$) as a supporting electrolyte. As illustrated in Figure 3.12, reversible oxidation processes were recorded for all **BT** derivatives.

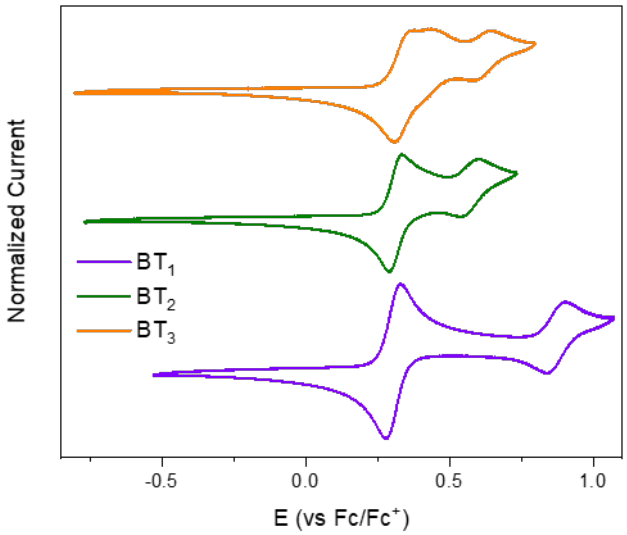

*Figure 3.12 Cyclic voltammograms of **BT₁**, **BT₂**, and **BT₃** molecules, 0.5 mM in 0.1 M $TBAPF_6$ in CH_2Cl_2 with a scan rate of 100 mV/s.*

While the first intense and reversible oxidation waves of the BT series occurring at relatively close potentials can be attributed to the concomitant one-electron oxidation of the two end-capping aryl amine groups which behave independently due to the highly distorted oligothiophene central cores, as suggested by the X-ray structure of **BT₁**. On the other hand, the effect of the length of the connector was directly monitored and assessed by the significant shift of the second oxidation wave toward lower potentials (from *ca* 0.87 V for **BT₁** to 0.56 V and 0.43 V for **BT₂** and **BT₃** respectively). Moreover, it is noteworthy that a third oxidation wave at 0.57 V was even recorded for **BT₃** demonstrating the stabilization and ease of generating multi-charged species up to a tetracations through the increase of the length of the connector.

Table 3.1 Electrochemical data of the three molecules ($E_{HOMO}(eV) = -(5.1 + E_{ox/onset})$).

Molecule	E_{ox} (V)	$E_{ox/onset}$ (V)	E_{HOMO} (eV)
BT_1	0.30 0.87	0.21	**-5.31**
BT_2	0.31 0.56	0.23	**-5.33**
BT_3	0.33 0.43 0.57	0.25	**-5.35**

Hence, with almost similar onsets values recorded from the first oxidation wave, close HOMO energy levels were then deduced emphasizing a localization of the electron density on the arylamine moieties and the first connected thiophene unit (Table 3.1).

3.2.2.2 Optical properties

Soluble in most commonly used organic solvents, UV-vis absorption spectra of the three compounds were thereafter recorded in DCM and plotted in Figure 3.13.

Comparison of their spectra shows in all cases, an intense UV-visible absorption band centered in the 300-450 nm region with maxima at 356, 358, and 360 nm for **BT_1**, **BT_2**, and **BT_3**, respectively. Interestingly, such a minor bathochromic shift confirms the significant impact of the position of the aliphatic side chains leading to a weak increase of π-conjugation with extension of the thiophene backbone.

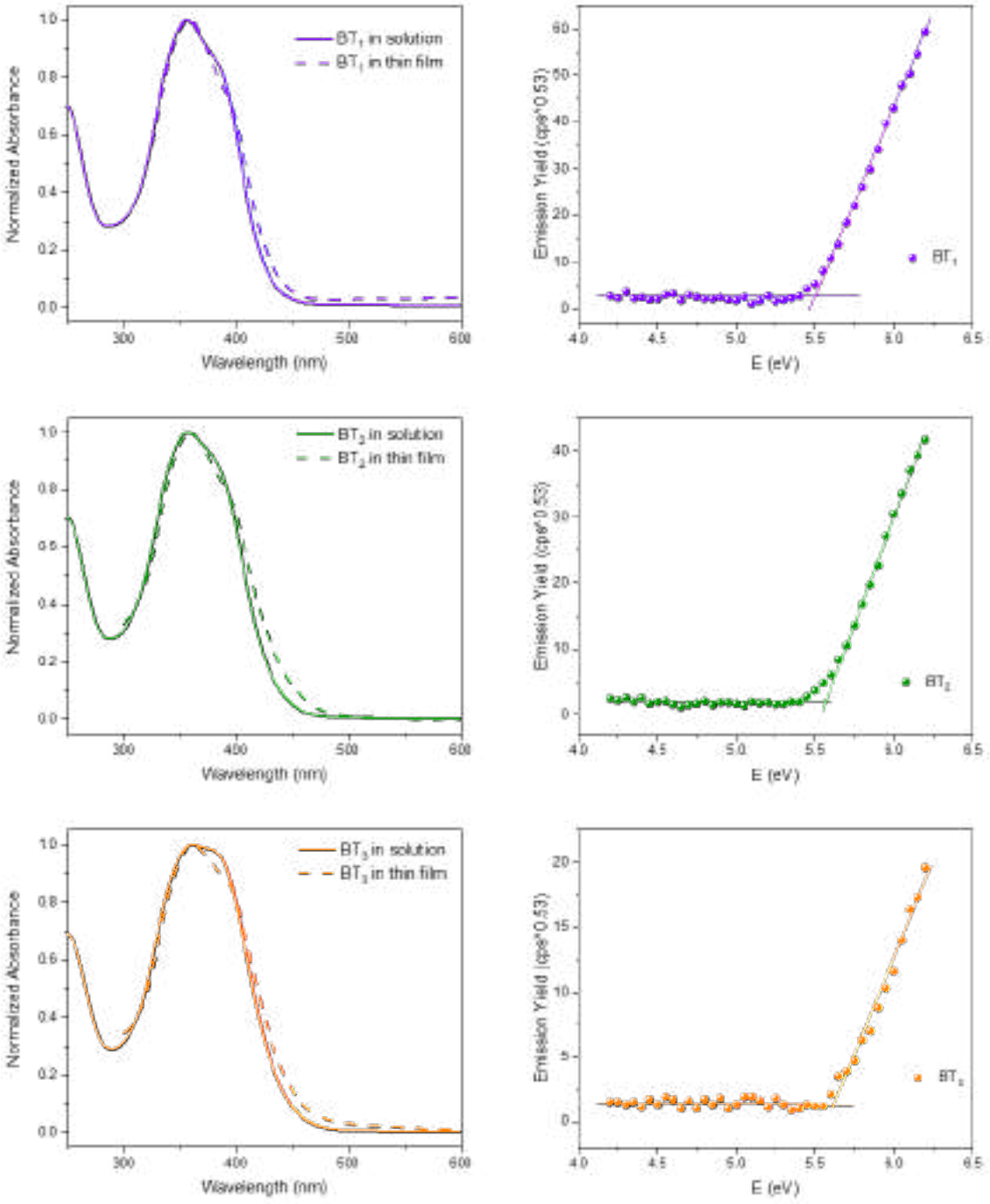

Figure 3.13 UV-vis spectra of solutions and thin films and photoelectron spectroscopy in air (PESA) analysis of thin films of ***BT₁****,* ***BT₂****, and* ***BT₃*** *molecules.*

Moreover, once spun cast on glass sheets, a similar feature was observed with almost negligible shifts toward the lowest energies (ca 3 nm for **BT₁** and only 1 nm for **BT₂** and **BT₃**) highlighting

the limited intermolecular π–π stacking resulting from the steric hindrance generated by the hexyl chain. Nonetheless, from the low-energy absorption onset of these films, optical band gaps were estimated and found to be 2.79 eV for **BT$_1$** and 2.70 eV for **BT$_2$** and **BT$_3$**. These results were finally combined with photoelectron spectroscopy in air (PESA) measurements to further determine and compare the frontier orbital energies (Table 3.2).

Table 3.2 Optical data gathered from DCM solutions and thin films spun cast on glass sheets.

Molecule	λ_{abs}^{max} solution (nm)	ε (M^{-1} cm^{-1})	λ_{abs}^{max} thin film (nm)	E_g^{opt} (eV)	HOMO (eV)	LUMO (eV)
BT$_1$	356	69315	359	2.79	-5.49	-2.70
BT$_2$	358	83630	359	2.70	-5.53	-2.83
BT$_3$	360	93180	361	2.70	-5.64	-2.94

Following the trend observed in solution by cyclic voltammetry, increasing the length of the connector slightly stabilized the HOMO. In addition, the LUMO is also slightly stabilized without drastically reducing the bandgap.

Regarding their emissive properties, spectra recorded at room temperature also in DCM exhibit emission bands with maxima at 483, 519, and 528 nm for **BT$_1$**, **BT$_2$**, and **BT$_3$**, respectively with a common excitation at 356 nm (Figure 3.14).

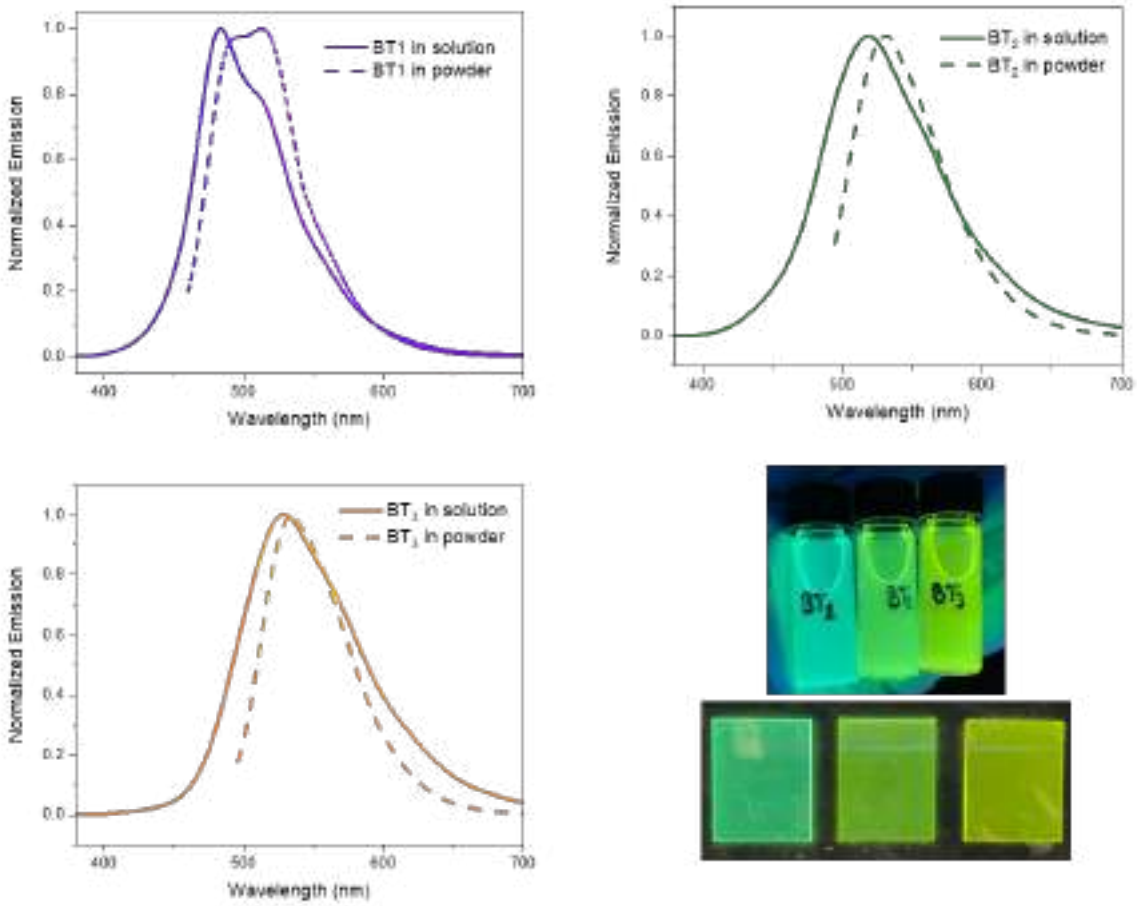

Figure 3.14 Normalized fluorescence emission spectra in solution and powder state and a picture of ***BT₁***, ***BT₂****, and* ***BT₃*** *molecules in solutions (DCM) and thin films under UV lamp irradiation at 254 nm.*

The gradual and larger Stokes shift recorded from **BT₁** to **BT₃** might be correlated to conformational differences between ground (aromatic) and excited (quinoid) states.

Unlike the absorption profile, this trend was maintained in the solid state (Table 3.3).

Table 3.3 Emission data gathered from DCM solutions and powder materials.

Molecule	Solution λ_{emi}^{max} (nm)	Powder λ_{emi}^{max} (nm)	Solution QY (%)	Powder QY (%)
BT_1	483	492 - 513	24	17
BT_2	519	530	21	12
BT_3	528	535	25	13

Regarding their emission quantum yields recorded using an integrated sphere, all molecule show similar/close QY in both solution and solid state (powder) with nonetheless a slight decrease once aggregated. However, while the deformation/twisting of the backbone, induced by the hexyl chains, limits the π-π stacking, it, on the other hand, prevents strong aggregation caused quenching (ACQ) phenomenon usually observed with such π-platforms.

3.2.3 Evaluation as light-emitting materials in OLEDs

As a logical follow-up, the evaluation of the three above-synthesized molecules as potential emitters was subsequently carried out in collaboration with the group of Gregory Welch (University of Calgary). Demonstration and first round of optimization were performed with **BT_1** since sent in much more quantities due to its synthetical accessibility (obtained in only one step). Hence, the first device prepared from **BT_1** was of architecture: ITO/PEDOT:PSS/PVK/BT_1/PFN/Ag (Figure 3.15). In which PFN, (Poly [(9,9bis(3'-(N,N dimethylamino)propyl)-2,7-fluorene)-alt-2,7-(9,9–dioctylfluorene)]), is used as an ETL.

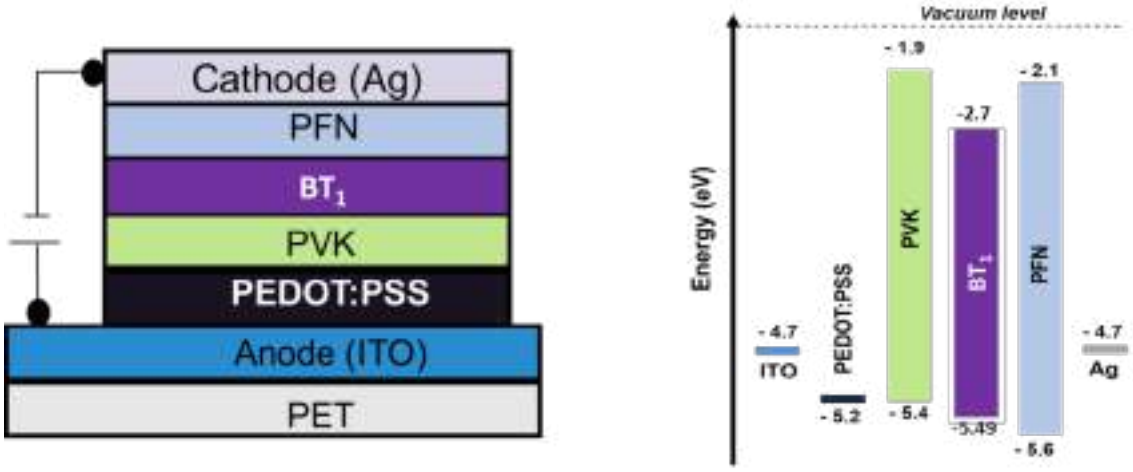

Figure 3.15 Architecture and energetic diagram of the first OLED device tested.

While a cyan emission was monitored, the poor (non-homogenous) quality of the EML (poly(9-vinylcarbazole) PVK then **BT$_1$** made the characterization of these devices almost impossible. Consequently, it was considered, as the first optimization, to blend the emitter (**BT$_1$**) with the poly(9,9-di-n-octylfluorenyl-2,7-diyl), also known as PFO, and used as a host material to improve film-forming ability and charge transport within the active layer. Interestingly the impact of the latter was also evaluated, in parallel, through the preparation of an EML solely constituted of **BT$_1$** directly deposited on PEDOT-PSS. Much more stable, compared to the PVK-based OLEDs, characteristics graphs of these operating devices are plotted in Figure 3.16 and their corresponding data, gathered in Table 3.4.

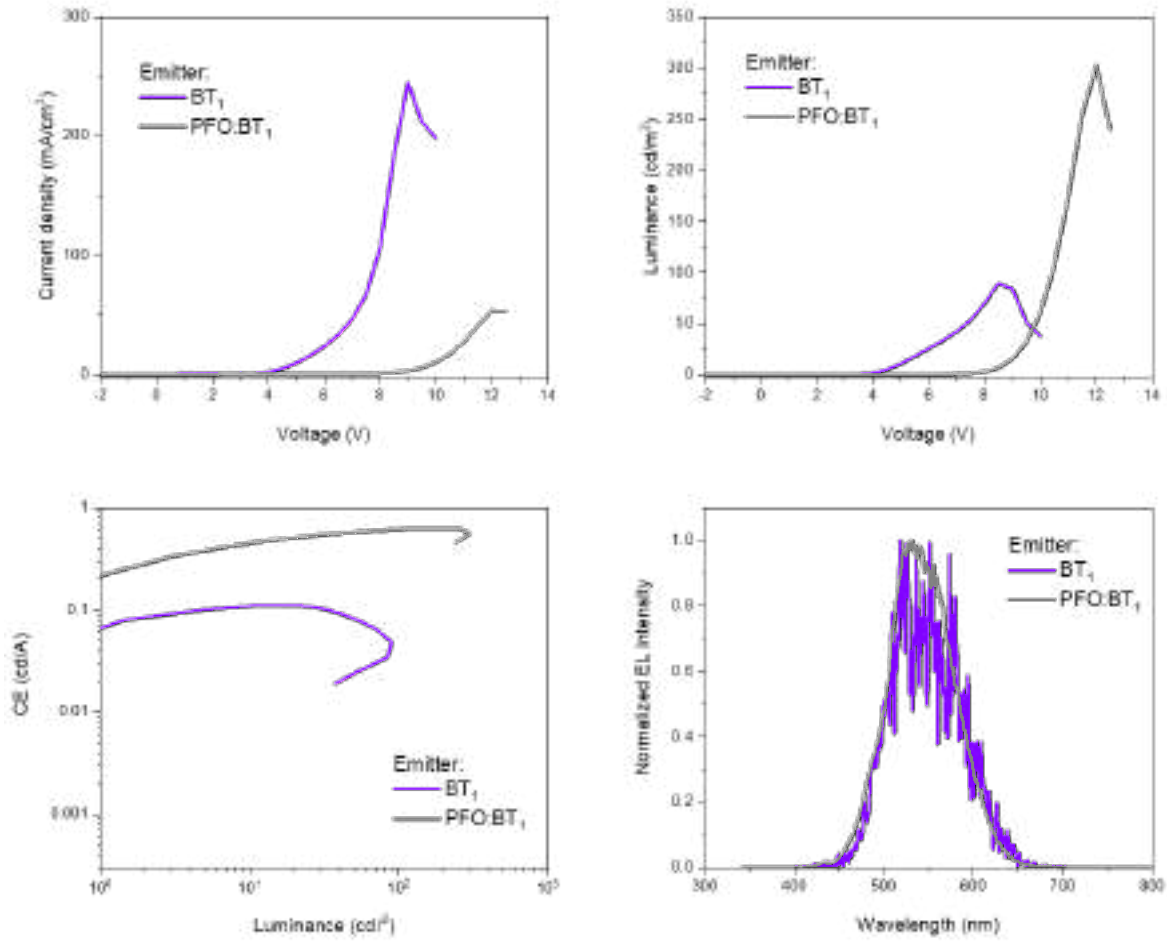

Figure 3.16 Current density, luminance, current efficiency, and normalized electroluminescence intensity spectra of ***BT₁*** *and* ***PFO:BT₁*** *OLED devices.*

The incorporation of PFO in a 19:1 ratio (PFO:BT_1) was found to significantly increase the luminance, current, and power efficiency of the devices. However, that goes along with a higher turn-on voltage since a difference of ca 3.5 V was recorded with the PFO-free device. On the other hand, this comparative study revealed that **BT_1** can directly be used as the EML, by itself, which considerably simplifies the structure and fabrication of the device.

Table 3.4 Performances of OLEDs incorporating ***BT$_1$ and PFO:BT$_1$*** *as emitters. (Average from over 5 devices each).*

Emitter	Turn-on voltage (V)	Max. luminance (cd/m^2)	Max. CE (cd/A)	Max. PE (lm/W)
PFO:BT$_1$	7.5	302.3	0.63	0.18
BT$_1$	4.0	89.42	0.11	0.07

With the aim of simplicity and potentially ultra low-cost, it was decided to evaluate the series in such conditions, i.e. in solution-processed devices of architecture: ITO/PEDOT:PSS/**BT$_x$**/PFN/Ag (Figure 3.17). [45]

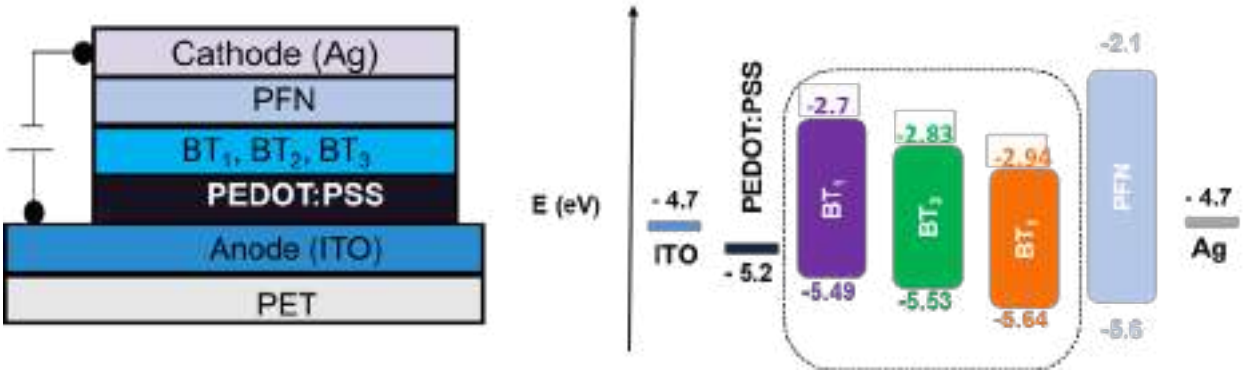

Figure 3.17 Architecture and energetic diagram of OLED devices.

All the characteristic values of these single-component EML OLEDs are gathered in Table 3.5 and the associated graph plotted in Figure 3.18.

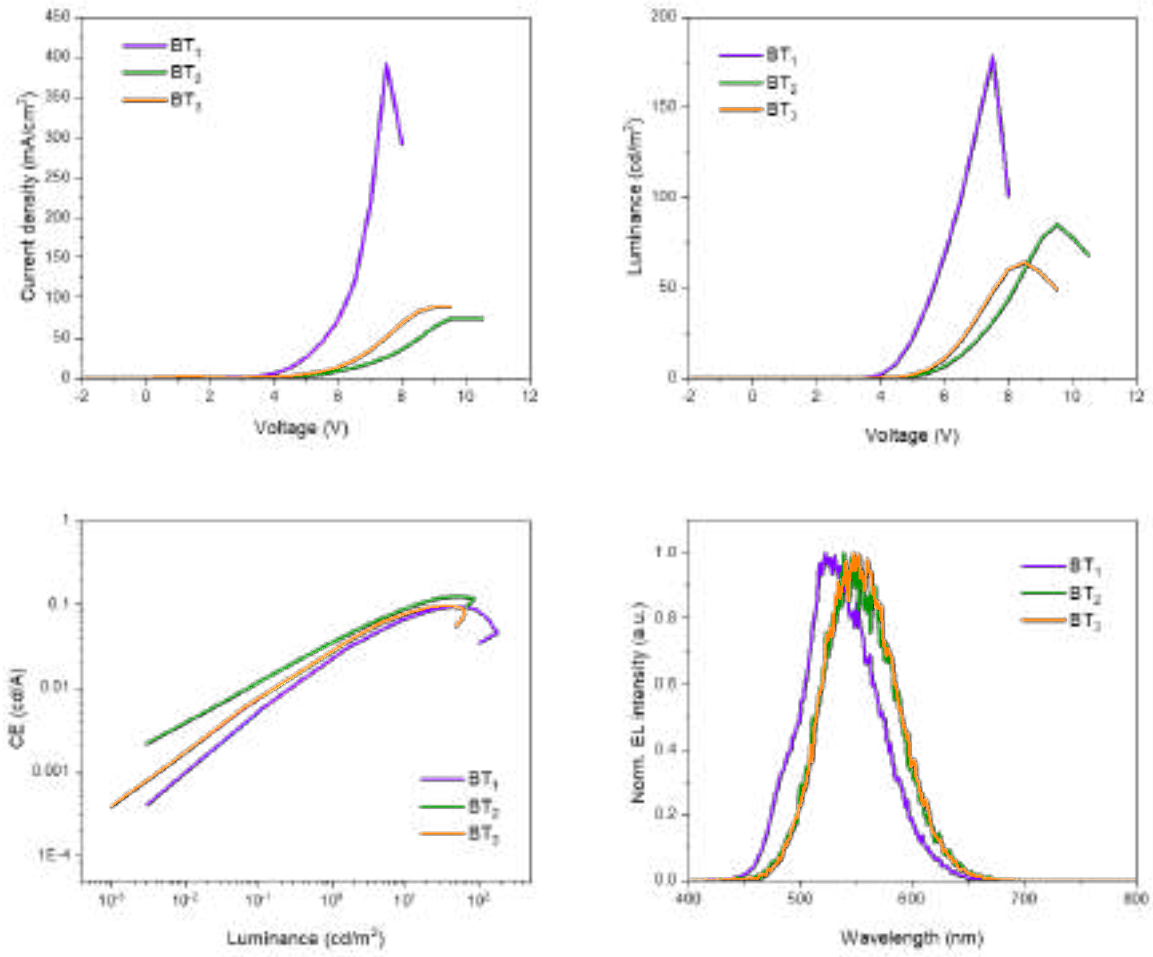

Figure 3.18 Current density, luminance, current efficiency, and normalized electroluminescence intensity spectra of ***BT₁***, ***BT₂***, *and* ***BT₃*** *OLED devices. (Substrate size: 15×15 mm²; Active area: 2×7 mm² = 14 mm²)*

First devices prepared from **BT₁** exhibit the lowest turn-on voltage (V_{on}= 4 V vs 5 V for both **BT₂** and **BT₃**) which can be correlated to the relatively lower energy barrier for hole injection from the PEDOT:PSS layer. Then, the highest luminance and current density were also reached with **BT₁** based devices which might be due to higher hole mobility (transport) as compared with devices embedding either **BT₂** or **BT₃**.

*Table 3.5 Performances of OLEDs incorporating **BT₁**, **BT₂**, and **BT₃** as emitters. (Average from over 5 devices each).*

Emitter	Turn-on voltage (V)	Max. luminance (cd/m^2)	Max. CE (cd/A)	Max. PE (lm/W)
BT_1	4.0 ± 0.5	178.3 ± 19.2	0.09 ± 0.03	0.053± 0.03
BT_2	5.0 ± 0.5	85.4 ± 5.8	0.12 ± 0.01	0.050± 0.01
BT_3	5.0 ± 0.5	63.9 ± 7.0	0.10 ± 0.05	0.043± 0.05

Regarding the CE and PE, values within the same range were obtained for all compounds. Finally, while **BT₁** based devices were characterized by a blue-cyan emission (maximum at 525 nm) corresponding to CIE coordinates located at (x, y) = (0.23, 0.42), the colour emitted by both **BT₂** and **BT₃** appeared greener, in consistency with the electroluminescent properties discussed above (maximum at 550 nm, see Figure 3.19).

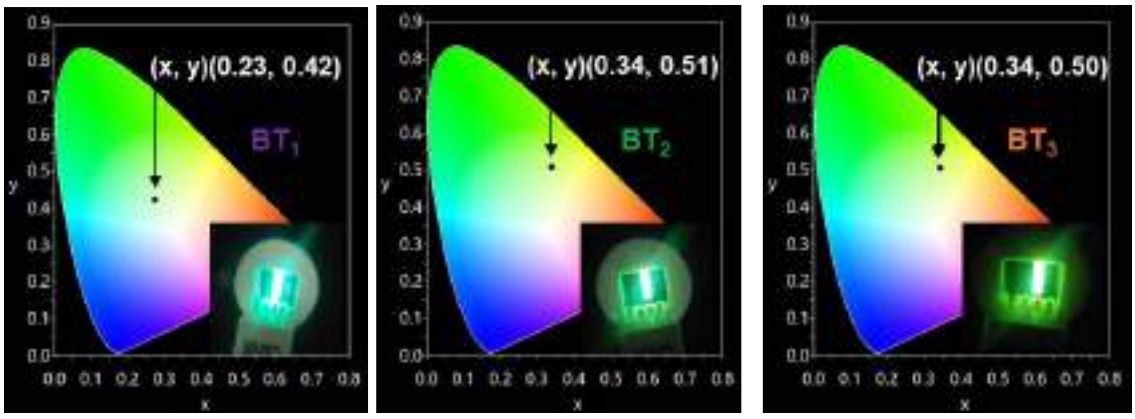

*Figure 3.19 CIE coordinates of **BT₁**, **BT₂**, and **BT₃** OLED devices.*

Even if these devices show modest efficiencies compared to the state-of-the-art high performing ones,[27-28, 34] simple operating single layer-based OLEDs were demonstrated with synthetically accessible emitters. Consequently, attempts to print large surfaces by slot-die coating technique were naturally and subsequently considered. Compatibility with roll-to-roll techniques used to process organic and inorganic layers is indeed an important parameter for the potential large-scale development and dissemination of ultra low-cost devices. In this context, a FOM Nano Roll Coater (slot-die head with 13 mm shim width) was used to print the PEDOT:PSS interlayer, the EML, and the PFN onto a ITO pre coated flexible substrate (see Figure 3.20).

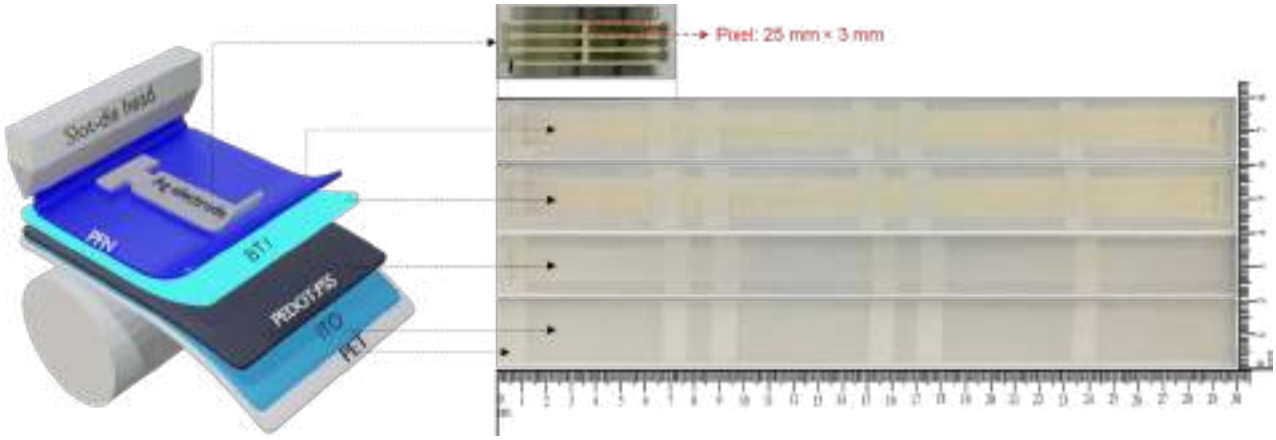

*Figure 3.20 Flexible device architecture prepared from **BT₁** as emitting layer.*

Solubility and pre-printing tests were first carried out in different non-halogenated and green solvents (compatible with industrial processes) revealing that only **BT₁** can achieve sufficient film qualities (but still not ideal) and thus be used in this very next step. As a result, flexible devices of large area with an EML processed from o-xylene were successfully prepared (Figure 3.21).

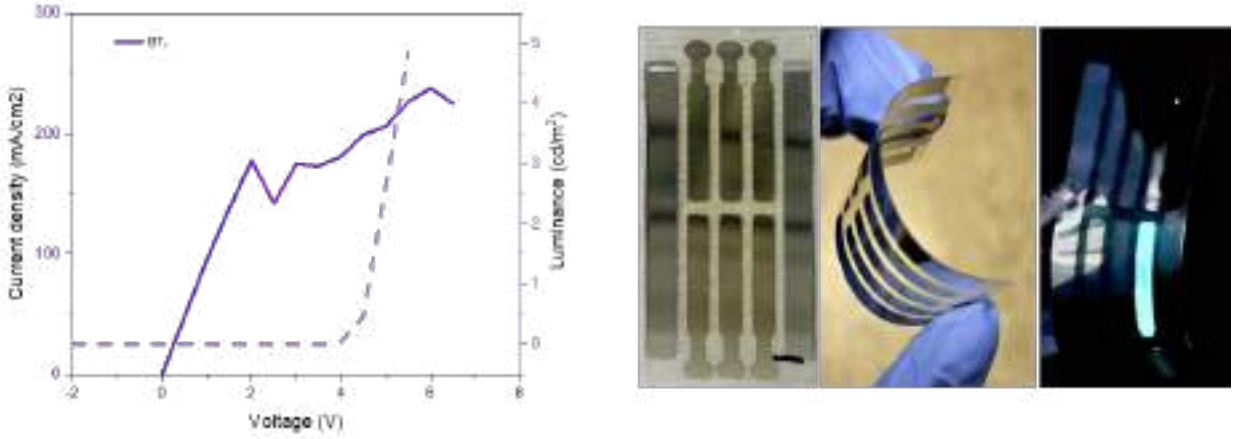

Figure 3.21 Current density (dashed line) and Luminance (solid line) vs voltage curves of flexible ***BT₁****-based OLEDs (left) and related pictures (right).*

Although uniform emission was demonstrated, modest performances were achieved compared to the above reported and conventional chloroform processed devices (Table 3.6).

Table 3.6 Summary of the device performance of slot-die coating OLED based on ***BT₁*** *films.*

Emitter	Turn-on voltage (V)	Max. luminance (cd/m^2)	Max. CE (cd/A)	Max. PE (lm/W)
BT_1	5.0 ± 0.5	4.8	0.00214	0.00122

The main reason might be rooted to the need of pre-heating the solution in *o*-xylene prior to deposition, resulting in poor films quality upon cooling with apparition of aggregates in the layer that in turn cause high current leakage points. Consequently, screening of other and more compatible processing solvents might lead to significant improvement in both efficiency and stability.

3.2.4 Conclusion

A series of simple and accessible oligothiophene based molecules, end-capped with TPA-BP moieties, was successfully synthesized using the step-saving direct-arylation reaction. Characterized by promising optoelectronic properties the latter were embedded as emitters in single layer OLED devices. Structure-property relationship rationalization revealed that increasing the length of the bi-thiophene based connector has a minor effect due to the deformation of the backbone induced by the steric hindrance generated by the aliphatic chains. Moreover, best efficiencies and film forming capabilities were achieved with **BT_1**, the less synthetically demanding derivative since prepared in only one step. Transposed from conventional lab scale processed with halogenated solvent, operating printed large area demonstrator were even fabricated from industry friendly o-xylene solutions. Even if optimizations are nonetheless still required, these promising results open doors to ultra low-cost large area and light weight devices where efficiency and stability are no longer discriminating factors.

3.3 Replacement of the oligothiophene central cores by the BTI dye: towards red emitters

3.3.1 Context and Molecular Design

The main advantage of organic compounds is, from a chemist's point of view, the amazing versatility in tuning the optoelectronic properties through synthetic modifications. Red, the one of the three primary colors, is essential for white-light lighting and full-color displays.[46-47] In addition to their significant applicability in optoelectronic devices, red emitters are also attractive fluorometric probes in the biological field due to their strong tissue penetration capacity, and low photo-damage to bio-substrates.[48-50] Hence, since the strategy aiming at increasing the length of the oligothiophene in the BT derivatives did not induce a sufficient red shift of the emission, the latter were subsequently and "simply" replaced by a dye.

Flagship of our group, the benzothioxanthene imide (**BTI**) molecule (see structure in Figure 3.22) was naturally selected for its i) synthetic accessibility (initially prepared at tone scale for textile industry), ii) ease of functionalization (pioneered by our group)[51-57] and iii) optical properties (λ_{em}^{max} = 502 nm with 99% solution QY).[58]

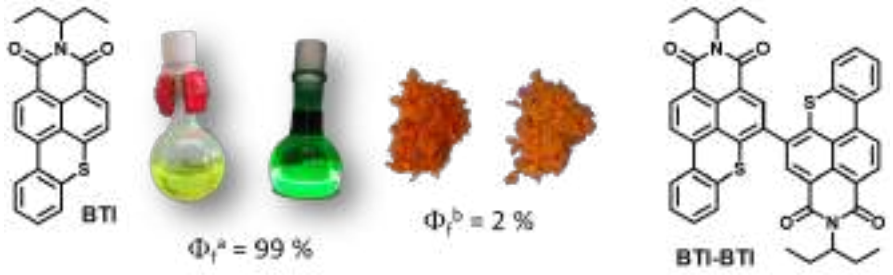

*Figure 3.22 Chemical structures of **BTI** (with pictures of solutions in DCM and powders) and **BTI-BTI**.*

Last but not least, our group recently demonstrated the potential of this dye as an emitter in light-emitting devices with the preparation and evaluation of the BTI-BTI dimer whose

structure is illustrated in Figure 3.22). Prepared by copper-catalyzed Ullmann reaction from the brominated BTI, the large dihedral angle between the two rylenes (ca 76°) was found to significantly improve the solubility and thus film forming capabilities but limits the π-conjugation resulting in minor bathochromic shifts compared to the BTI itself.[59]

In this context, by cross-tabulating our experience in functionalizing this dye with the results gathered from the BT series, two new potential red emitters were considered, namely **BTI-TPA$_2$** and **BTI-TPA$_3$** (Figure 3.23).

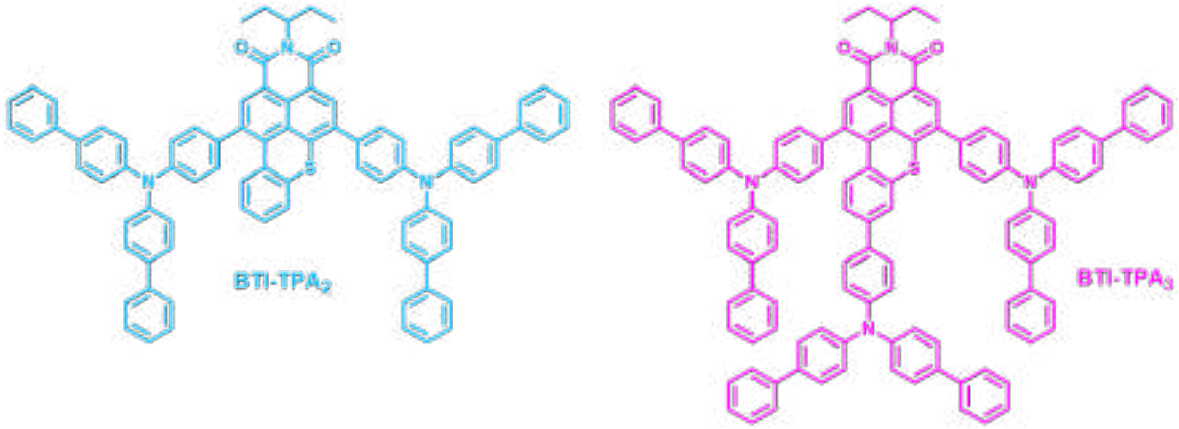

*Figure 3.23 Structures of the target molecules **BTI-TPA$_2$** and **BTI-TPA$_3$**.*

3.3.2 Synthesis and Characterization

Recently, our group reported an updated and modernized synthetic procedure to afford **BTI** molecule in large quantities and in a minimum of time.[60] That was successfully transposed to the preparation of **BTI-N-Br**. Hence, the two steps successive "one-pot-like" reactions between the brominated naphthalene imide derivative and either the 2-aminobenzenethiol or the 2-amino-5-bromobenzenthiol were carried out in 2-ethoxyethanol. (Scheme 3.3).

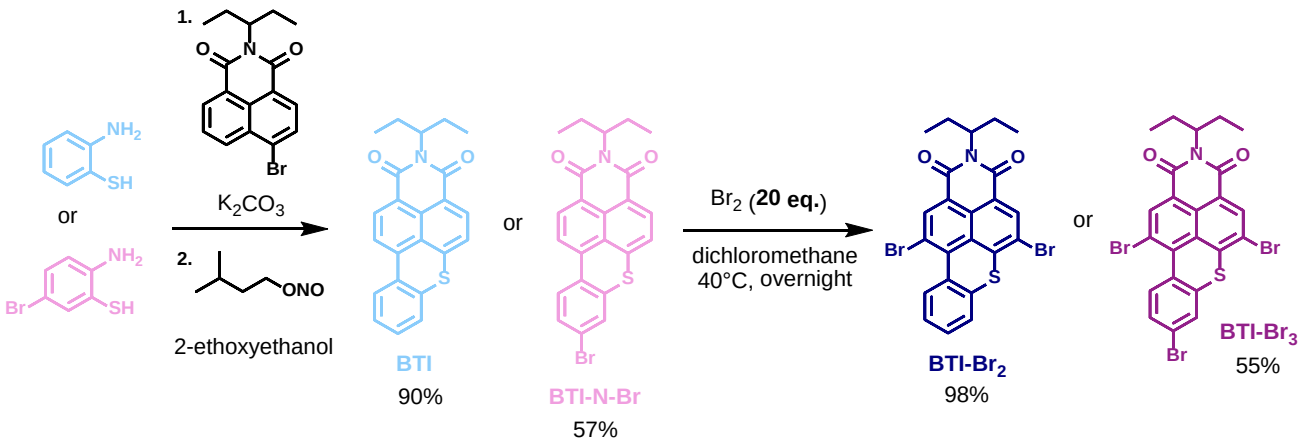

Scheme 3.3 Schematic representation of the formation and bromination of BTI molecules.

Starting with a nucleophilic aromatic substitution (S_NAr), isoamyl nitrite was directly added to the media resulting in a Pschorr cyclization and preparation of the target dyes. Isolated for the first time (and not yet reported in the literature), the structure of **BTI-N-Br** was, in parallel, confirmed by X-ray diffraction carried out on single crystals successfully grown by slow evaporation technique (see structure in Figure 3.24).

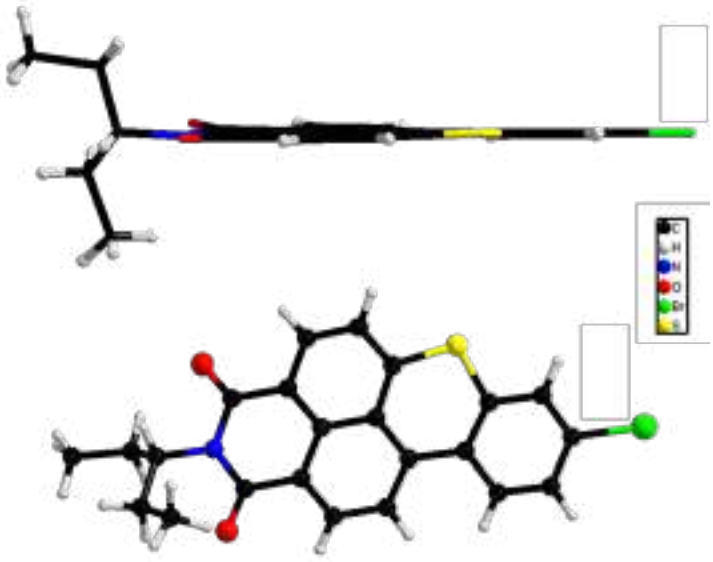

*Figure 3.24 X-ray planar structure of **BTI-N-Br**.*

Then, the double bromination of the naphthyl moiety was carried out by reacting the dyes with 20 eq of Br_2 at reflux in dichloromethane. Assigned NMR spectra of the target **BTI-Br$_2$**, and **BTI-Br$_3$** are depicted in Figure 3.25 and compared to those of their early intermediates, namely the **BTI** and **BTI-N-Br**, to confirm the substitution and position of the bromine atoms.

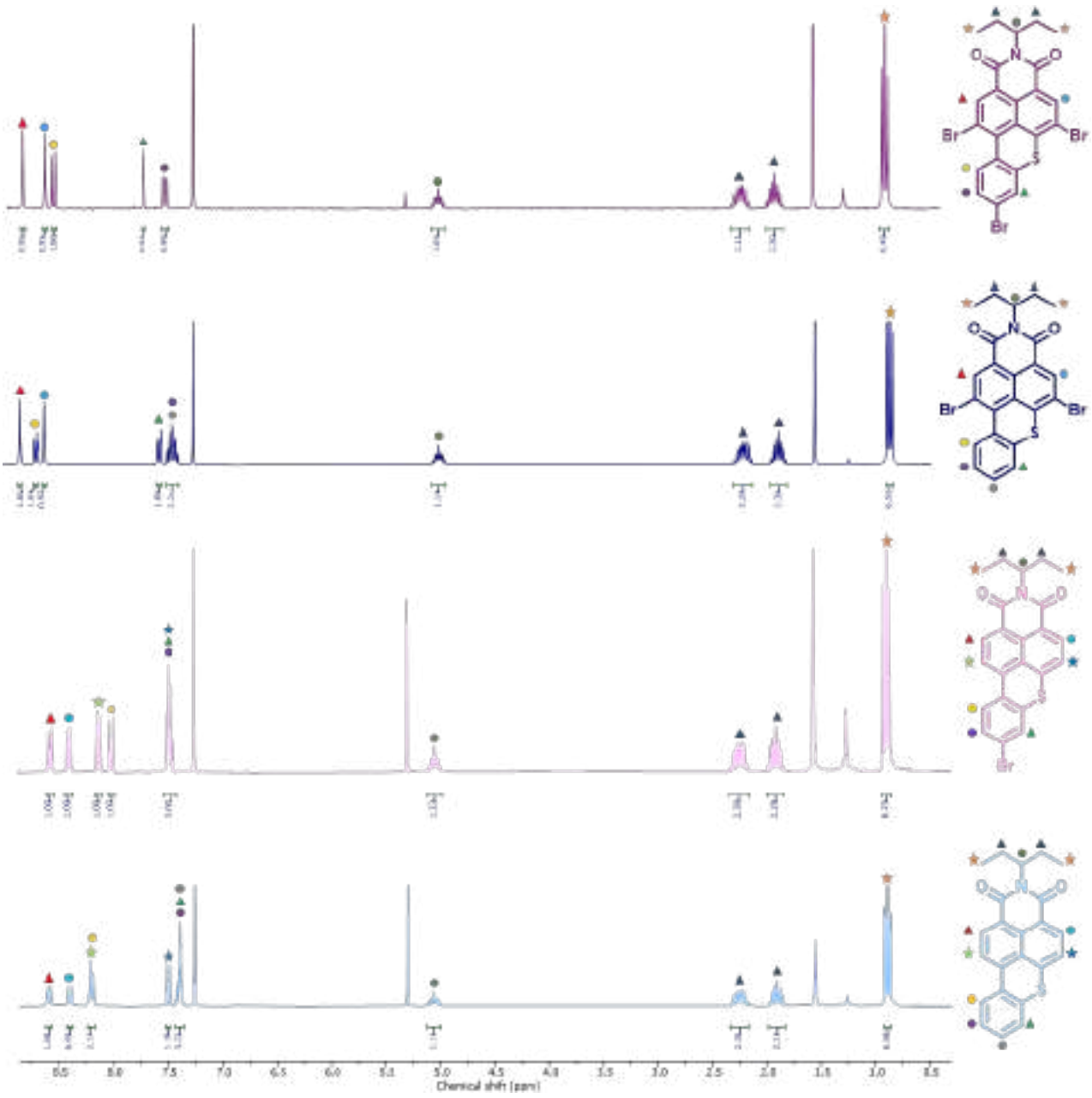

*Figure 3.25 300 MHz NMR spectra of **BTI**, **BTI-N-Br**, **BTI-Br$_2$**, and **BTI-Br$_3$** in $CDCl_3$ with signals attributions.*

Finally, **BTI-Br$_2$** and **BTI-Br$_3$** were engaged in Suzuki coupling reactions with the commercially available N-([1,1'-biphenyl]-4-yl)-N-(4-(4,4,5,5-tetramethyl-1,3,2-dioxaborolan-2-yl)phenyl)-[1,1'-biphenyl]-4-amine (Scheme 3.4).

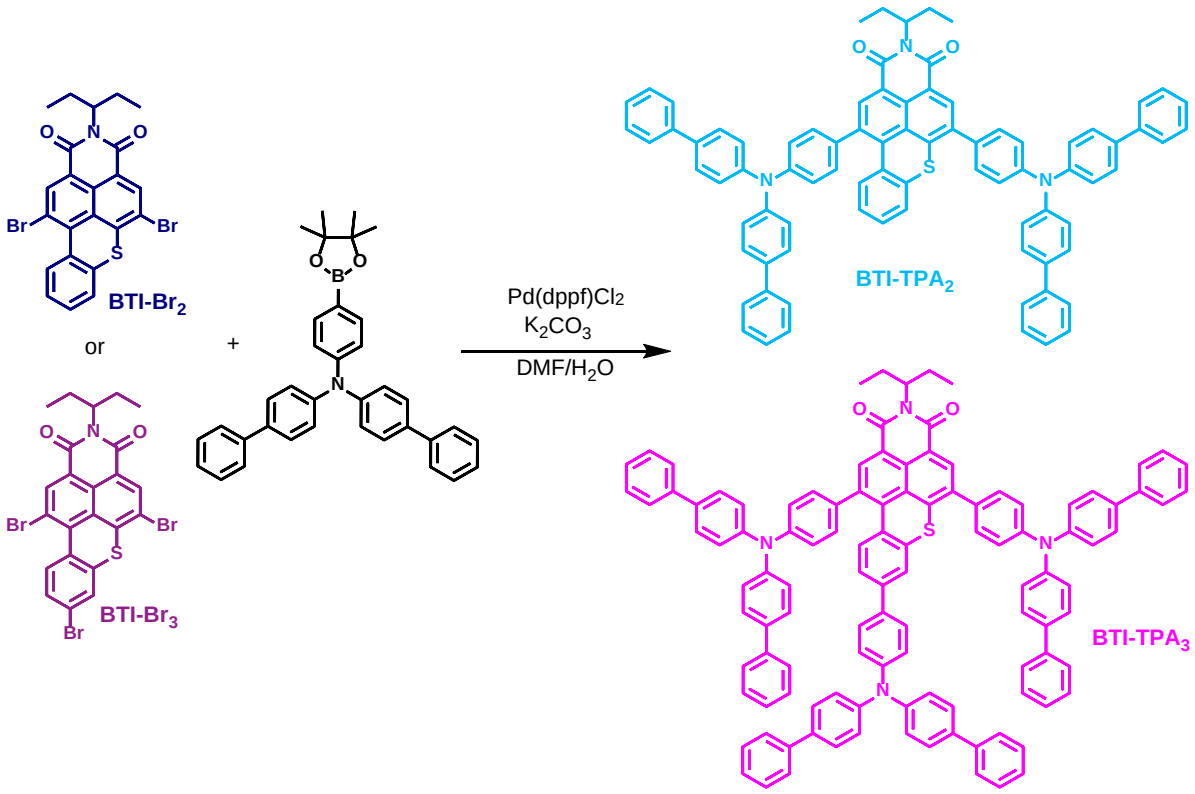

Scheme 3.4 Suzuki couplings for the formation of the two target compounds.

Obtained in 70% and 35% yields, respectively, identity and the purity of the two final compounds, namely **BTI-TPA$_2$** and **BTI-TPA$_3$**, were confirmed by nuclear magnetic resonance spectroscopy (NMR) and mass spectrometry (MS and HRMS) before investigating their optoelectronic properties.

3.3.3 Optoelectronic properties

Exhibiting good solubility in common organic solvents despite minimal aliphatic side chains, the optical properties of both molecules were first studied by UV-vis spectroscopy in chloroform solutions (see Figure 3.26 and Table 3.7).

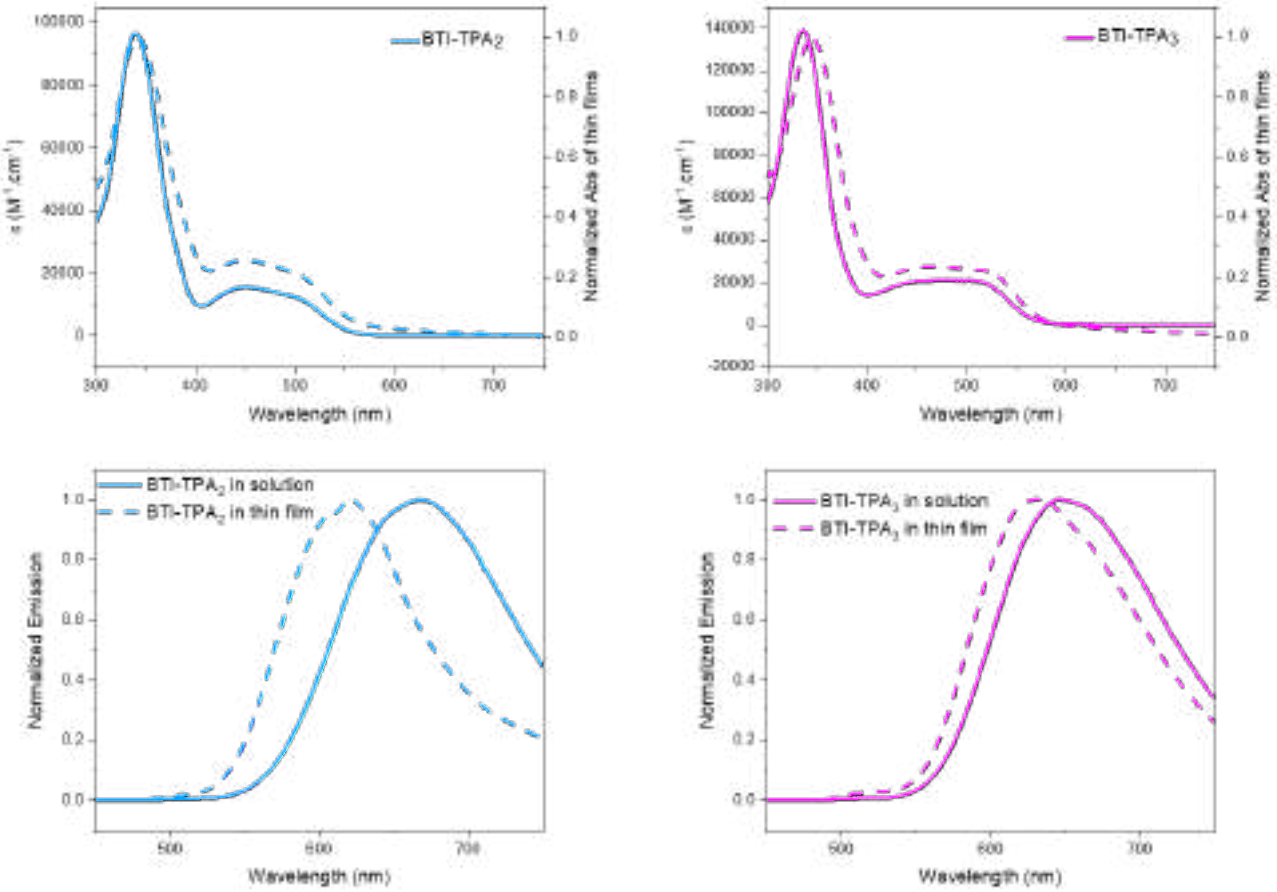

*Figure 3.26 Absorption and emission spectra of **BTI-TPA₂** (in blue) and **BTI-TPA₃** (in pink) in solution (solid lines) and thin films (dashed lines).*

Their absorbance spectra show a well-defined band in the UV region at 339 nm for **BTI-TPA₂** and 335 nm for **BTI-TPA₃** attributed to the arylamine groups and a large absorbance band in the visible range (from 400 to 550 nm approximatively) with maxima at 440 nm and 515 nm for **BTI-TPA₂** and **BTI-TPA₃**, respectively. Hence, functionalization of the lower phenyl ring

of the BTI with a triphenylamine results in increasing the charge transfer character of the band and thus in a non-negligible bathochromic shift of ca 75 nm.

In solid state optical signals slightly broaden and red shift, a typical signature of π–π interactions. However, the latter are clearly limited, according to the modest amplitude of these shift (of *ca* 6nm), thus reflecting the impact of sterical hindrance generated by the bulky propeller-shaped arylamine on the self-assembly properties.

Table 3.7 Absorption and emission data gathered from solutions, thin films, and powder materials.

Molecule	λ_{abs}^{max} solution (nm)	ε (M^{-1} cm^{-1})	λ_{abs}^{max} thin film (nm)	E_g^{opt} (eV)	HOMO (eV)	λ_{emi}^{max} solution (nm)	λ_{emi}^{max} thin film (nm)	Solution QY (%)	Powder QY (%)
BTI-TPA$_2$	339 440	96500 15500	340 446	2.21	-5.61	667	620	30	28
BTI-TPA$_3$	335 515	139000 20500	344 523	2.13	-5.77	647	630	31	30

Regarding their emission properties, significant Stokes shifts were recorded of ca 227 and 132 nm for **BTI-TPA$_2$** and **BTI-TPA$_3$** respectively. Interestingly emission band of the di-functionalized molecule appeared more shifted towards the longer wavelengths than that of its tris-TPA based counterpart (of ca 20 nm), a feature that might be correlated to a higher degree of deformation from ground to excited state. More interestingly these maxima appear blue-shifted in thin films compared to solutions, with a less important Stokes shift in the solid state suggesting that the aggregation of the molecules induces less conformational changes. Consequently, quantum yields estimated in solution (ca 30%) are preserved in the solid state, highlighting the effectiveness of this hindrance to avoid aggregation caused quenching (ACQ) phenomena.[61-62]

Finally, from the optical band gap determined from the absorption onsets and PESA measurements performed on the latter, frontier orbital energy levels were estimated and plotted in the diagram illustrated in Figure 3.27.

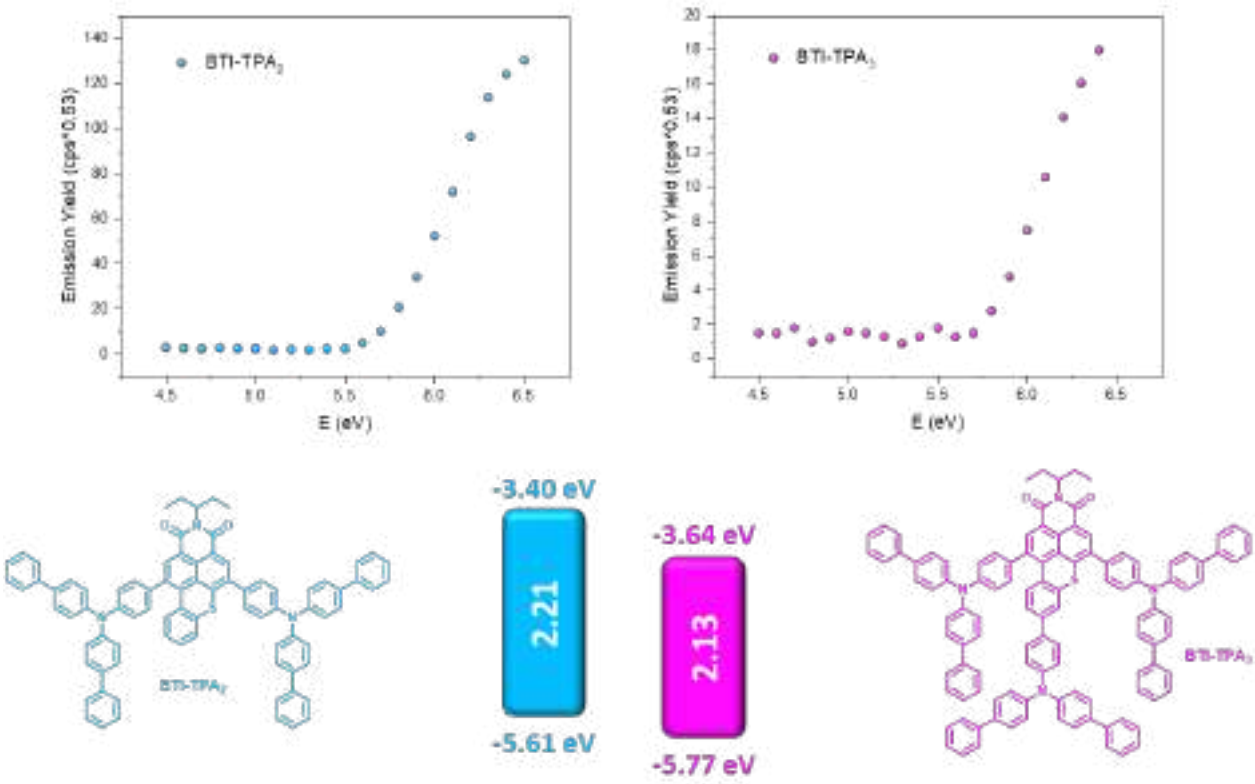

*Figure 3.27 Photoelectron spectroscopy in air (PESA) analysis of **BTI-TPA$_2$** and **BTI-TPA$_3$** in thin films.*

It appears that the HOMO and LUMO levels are both stabilized after the addition of the third TPA on the BTI core. In general, the addition of a donor moiety should destabilize the HOMO level of a molecule, however in this example, the steric hindrance induced by the third TPA leads probably to a weaker conjugation between the two other TPAs and the BTI central core, thus limiting their donor effect.

3.3.4 Evaluation as light-emitting materials in OLEDs

With great solubility in toluene and film-forming capabilities from this solvent, our collaborator (Gregory Welch, University of Calgary) has directly decided to evaluate the potential of these two compounds in printed devices. Hence, solvent-resistance tests were first performed to find proper orthogonal conditions to sequentially process all successive layers. Avoiding the degradation and/or intermixing of functional layers in multilayer devices is indeed critical to achieving homogeneous deposition and therefore high performance and stability in all solution-processed and fully printed/coated OLEDs.

To do so, very thin films were processed by slot-die coating from toluene solutions at only 5 mg mL^{-1} onto glass substrates and "washed" with different solvent used for the deposition of the top electron transporting layer (PFN). Comparison of the absorption spectra recorded before and after this step, plotted in Figure 3.28, revealed that while EtOAc causes a total dissolution of the films, a good solvent resistance to MeOH was monitored for both compounds. On the other hand, it is noteworthy that unlike **BTI-TPA$_2$**, **BTI-TPA$_3$** also showed promising results toward heptane.

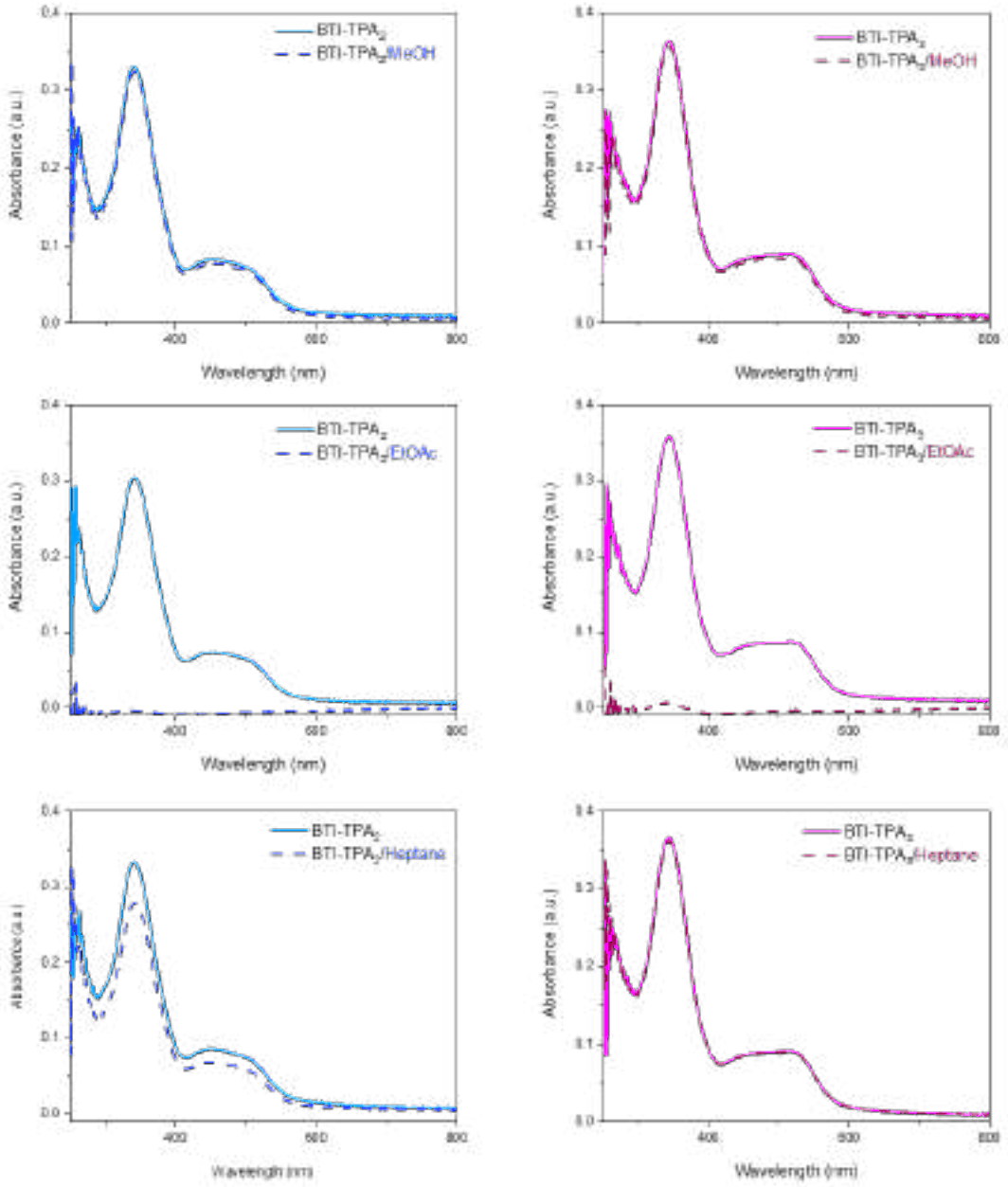

*Figure 3.28 Solvent resistance of thin-films of **BTI-TPA$_2$** and **BTI-TPA$_3$** studied by UV-vis spectroscopy.*

Hence, to standardize the fabrication, MeOH was thus selected for the deposition of the PFN layer. As for the previously discussed BT series, the PFO polymer was used as host in the EML in order to improve the overall device performances and also the film forming properties to achieve large-area uniform slot-die coated films (Figure 3.29).[58]

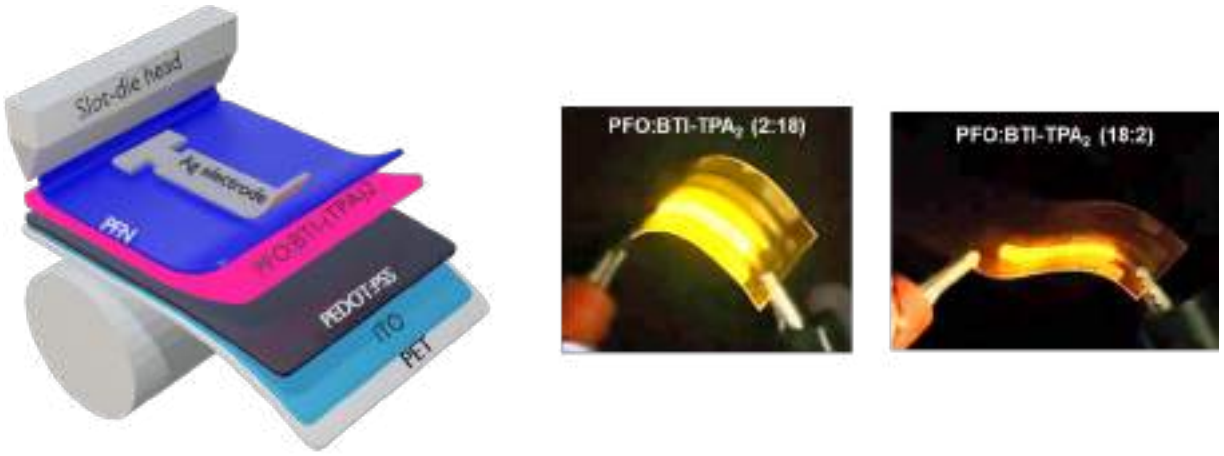

Figure 3.29 Architecture and pictures of the flexible OLED devices.

Prepared in higher quantities, **BTI-TPA$_2$** and two different ratios of host:guest (**PFO:BTI-TPA$_2$**) were used to fabricate and evaluate first devices. Except for the silver back electrode that was thermally evaporated, all layers, namely the PEDOT:PSS, PFO:BTI-TPA$_2$ blend (EML), and PFN were sequentially slot-die coated from water, toluene, and methanol solutions, respectively.

Remarkably, and in contrast with the BT based series, highly homogenous films were prepared leading to a uniform emission of the devices which directly reflects their performances (Table 3.8 and Figure 3.30).

Table 3.8 Summary of the devices performances of slot-die coated OLEDs based on ***PFO:BTI-TPA$_2$*** *(2:18) and (18:2).*

Emitter	Turn-on voltage (V)	Max. luminance (cd/m^2)	Max. CE (cd/A)	Max. PE (lm/W)
PFO:BTI-TPA$_2$ **(2:18)**	6.0 ± 0.5	23.6 ± 5.2	0.036 ± 0.02	0.011 ± 0.02
PFO:BTI-TPA$_2$ **(18:2)**	7.5 ± 0.5	146.3 ± 5.8	0.235 ± 0.001	0.064 ± 0.001

The significant differences recorded between these demonstrators clearly highlight the key role of the host and the importance of controlling its ratio in the EML. Devices made with larger amount of PFO than that of emitter (18 to 2) indeed simply outperform, at all levels, those prepared with the opposite ratio (PFO:BTI-TPA$_2$ = 2:18).

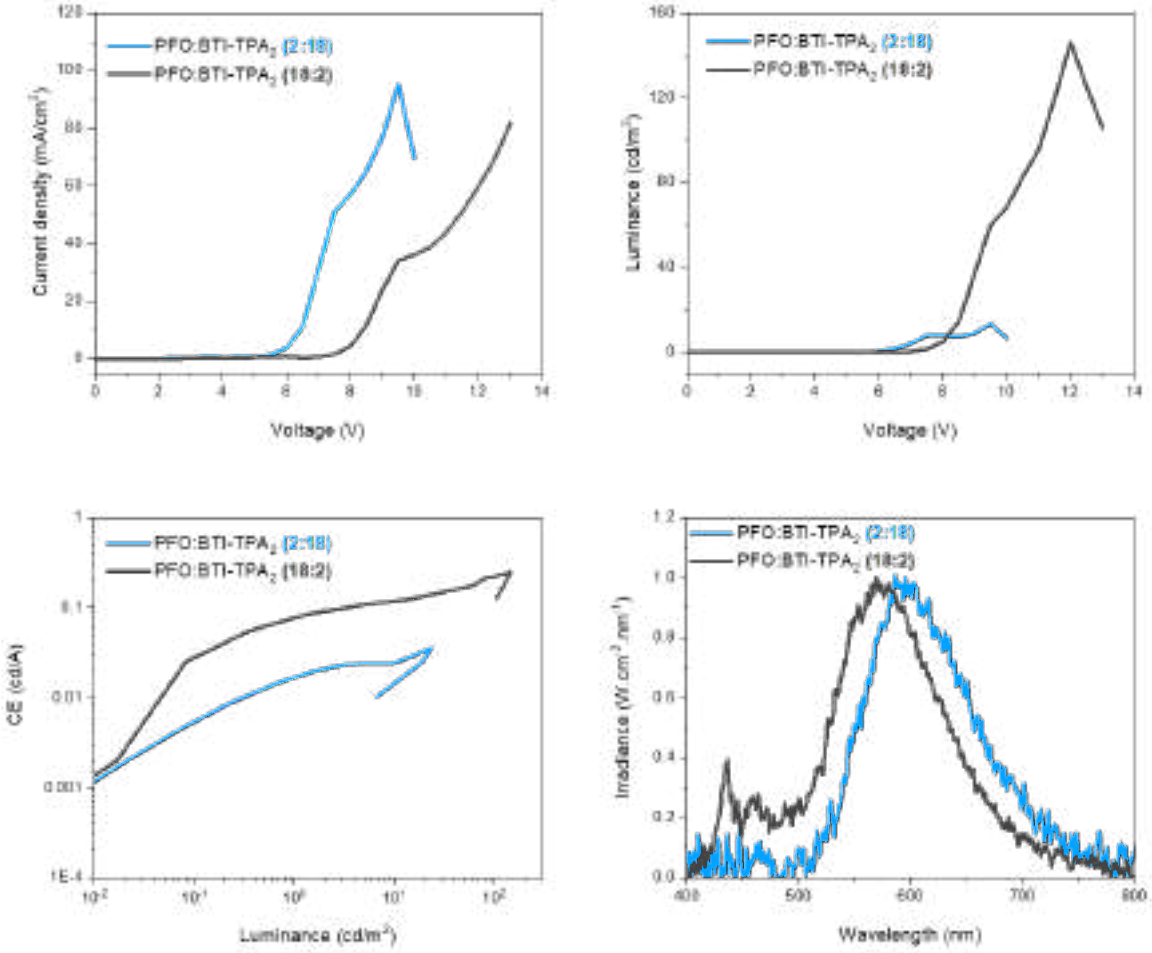

Figure 3.30 Characteristics of OLEDs based on ***PFO:BTI-TPA₂*** *with a 2:18 (blue line) and 18:2 ratio (black line).*

With a higher turn on voltage, the devices based on PFO:BTI-TPA_2 (18:2) indeed show higher luminance and improved CE and PE. However, the only "limitation", if low energy wavelength are precisely targeted is that high concentration of PFO induces a slight hypsochromic shift of the emission (*of* ca 25 nm) which is clearly noticeable from the CIE diagrams (Figure 3.31).

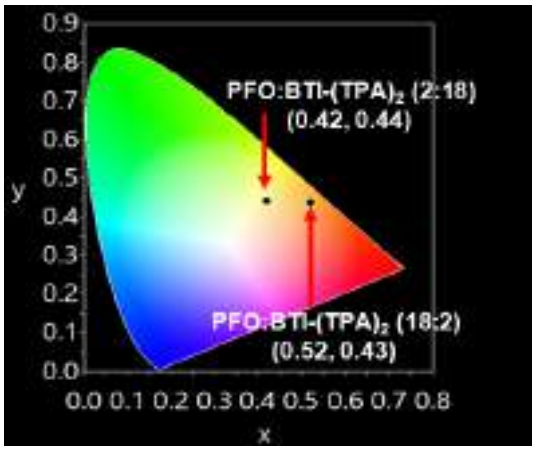

*Figure 3.31 CIE coordinates of OLEDs based on **PFO:BTI-TPA$_2$** with a 2:18 or 18:2 ratio.*

Further optimizations and, above all, evaluation of **BTI-TPA$_3$**, currently undertaken in parallel of the writing of this thesis manuscript, is thus highly expected to assess and rationalize the impact of the third arylamine group on the processing and device performances.

3.3.5 Conclusion

To summarize, we have demonstrated through the preparation of a tris-functionalized BTI the selective bromination of the lower benzene ring which was, to date unreported. In addition to this synthetic achievement, and based on the expertise of the group, two new BTI derivatives functionalized by either two or three extended triphenylamine were successfully prepared and characterized. This strategy was demonstrated to be efficient in preventing ACQ phenomenon but also for the film forming properties once blended with the PFO polymer. As a result, promising flexible and large area printed OLEDs with orange emission have already been demonstrated with **BTI-TPA$_2$**. From these preliminary yet highly promising results, it is undeniable that other will follow.

3.4 Upcycling of the Isoviolanthrone Vat Dye

3.4.1 Context and Molecular Design

In recent years, our group has devoted considerable research attention to the highly promising BTI. Initially prepared for textile industry, we pioneered i) the functionalization of its π-conjugated core and ii) the demonstration of its use in OPV, OLEDs, OFET and even for photodynamic therapy.[52-53, 57-59, 63] In other word, we "upcycled" this dye.

However, BTI is also only one "exotic" dye amongst so many others. For instance, amazing overlooked structures can be found in vat dyes catalogues, that are, once again produced in enormous quantities for textile coloring, ie, available in large quantities and thus potential new candidate for upcycling. Moreover, the latter are also disastrous for the environment since mostly discarded without post-treatment as waste water (more than 200,000 tons per year).[64-66] Consequently, strategies to recycle and/or purify these dye-contaminated water wastes should be a priority focus of research development.[67]

Moreover, from a chemical point of view, these platforms usually possess highly conjugated sp^2 carbon networks, resulting in interesting optical properties and thus making them appealing building blocks for potential low-cost organic based electronics. Other noteworthy benefits include their high environmental, thermal, and chemical stability, the ability to undergo chemical transformations to change their properties due to the presence of functional groups like ketones, halogens, and amines, and their extremely low cost when purchased due to the few, inexpensive synthetic steps required to prepare them.[68]

In this context, couple of vat dyes have already been functionalized and embedded in organic field-effect transistors (**OFETs**), light-emitting devices (**OLEDs**), wearable electronics, and for battery applications.[69-73] Major names and associated structures of such early reported upcycled vat dyes are depicted in Figure 3.32.

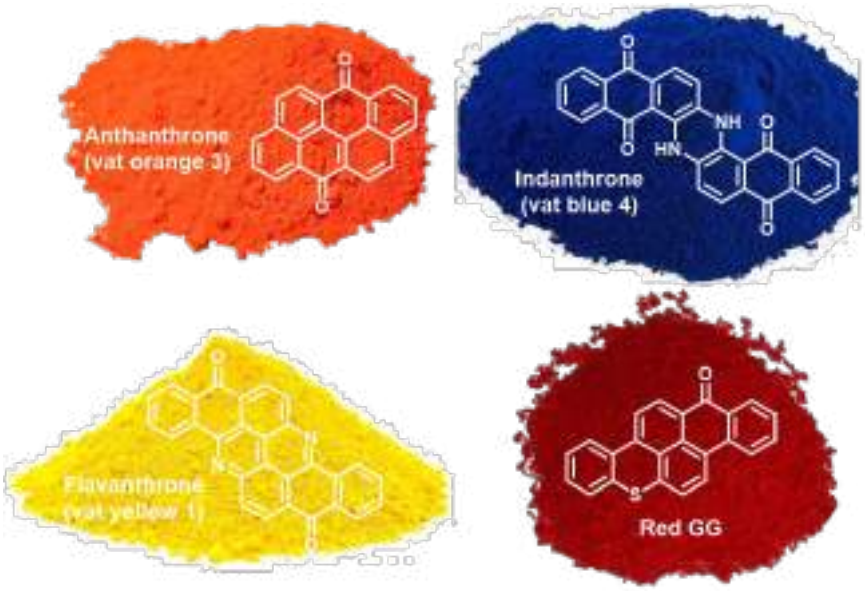

Figure 3.32 Chemical structures, names, and colors of some vat dyes used in organic electronics.

In this context, and in parallel to the substantial work carried out on the BTI, the potential of a nine-ring aromatic diketone compound was explored within the frame of this thesis, namely the Isoviolanthrone also known as vat violet 10. Through chemical engineering, it is expected to improve the solubility of this naturally insoluble dye to rationalize its properties and finally use it in a suitable application (Figure 3.33).

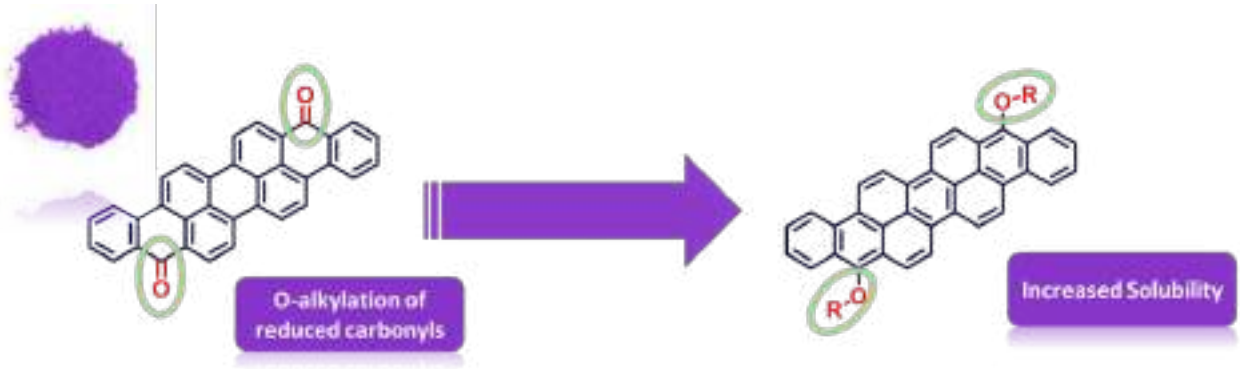

Figure 3.33 Structure of the Isoviolanthrone vat dye and potential target O-alkylated "soluble" compounds.

3.4.2 Synthesis

During the dyeing process, insoluble vat dyes are usually treated by reducing agents such as sodium dithionite ($Na_2S_2O_4$) thus allowing the dye to become water-soluble. Once soaked in these "leuco" dye solutions, textiles are exposed to air in order to re-oxidize the dyes into their neutral and therefore insoluble form. With a modest "dyeing" yield, these "leuco" baths are usually reused and then directly discarded as wastewater. Considering that most of the textile-producing countries do not have strict regulations on water treatment, vat dyes are thus considered as major pollutants.

Consequently, we have decided to use the "leuco" form of the Isoviolanthrone as a precursor for further functionalization. Hence the commercially available dye was first reduced in the presence of sodium dithionite in basic conditions (Scheme 3.5).

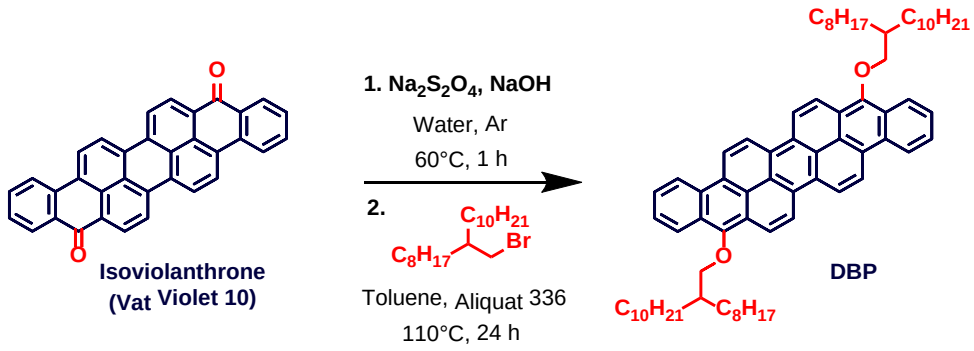

*Scheme 3.5 One-pot reaction for the preparation of the **DBP** molecule.*

Then, through a one-pot sequential procedure, 9-(bromomethyl)nonadecane was added to the mixture with toluene and *Aliquat 336*, a quaternary ammonium salt, used as the phase transfer catalyst to form an alkylated derivative of Isoviolanthrone.

The 9,18-dialkoxylated 1.2,8.9-dibenzoperopyrene (**DBP**) was isolated with 35% yield and characterized by nuclear magnetic resonance spectroscopy (^1H and ^{13}C) and mass spectrometry (MS and HRMS). Soluble in common organic solvent owing to the successful double O-alkylation, its optoelectronic properties were subsequently investigated.

3.4.3 Optoelectronic properties

3.4.3.1 Electrochemical properties

Starting with the cyclic voltammetry, measurements were carried out in THF solutions using tetrabutylammonium perchlorate as the electrolyte (0.1 M), glassy carbon as the working electrode, platinum as the counter electrode, Ag/AgCl as the reference electrode, at a scan rate of 100 mV/s (Figure 3.34).

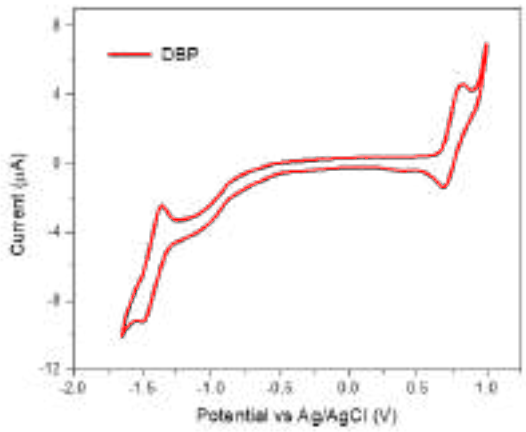

*Figure 3.34 Cyclic voltammogram of **DBP** (1 mM) in degassed THF solution containing 0.1 M of tetrabutylammonium perchlorate with a scan rate of 100 mV/s.*

It turned out that a quasi-reversible wave in both anodic and cathodic regions peaking at E_{ox} = +0.80 V and E_{red} = -1.49 V respectively were monitored, highlighting “dual redox” properties.

Moreover, from the onset potential of these redox processes, frontier orbital energy levels were estimated at -5.45 eV and -3.47 eV for the HOMO and the LUMO energy levels, respectively (Table 3.9).

*Table 3.9 Electrochemical data of **DBP**.*

Molecule	E_{ox} (V)	E_{red} (V)	E_{HOMO} (eV)	E_{LUMO} (eV)
DBP	0.80	-1.49	-5.45	-3.47

3.4.3.2 Optical properties

Even with limited solubilities, the optical properties of both the commercial Isoviolanthrone vat dye and its alkylated derivative **DBP** were investigated and compared (Figure 3.35).

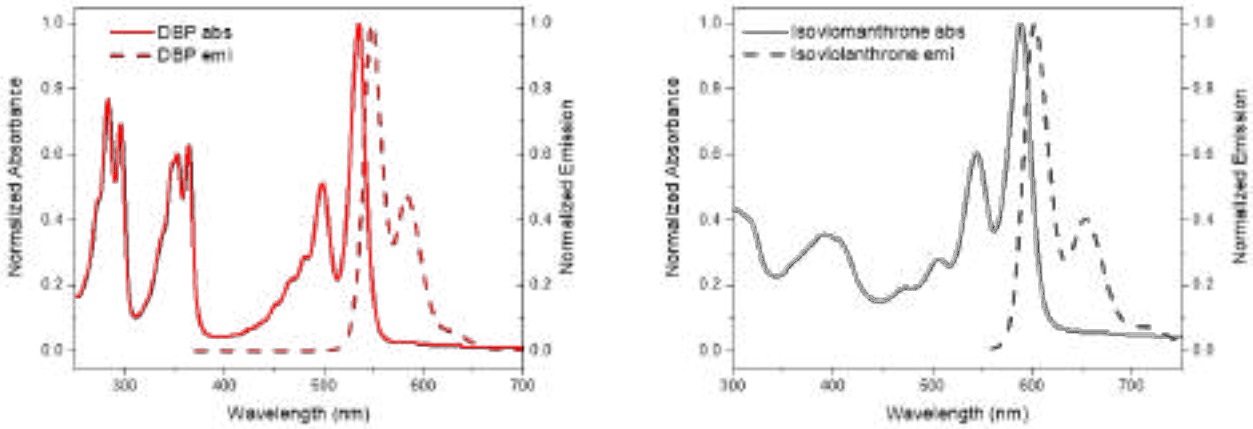

Figure 3.35 Normalized absorption and emission spectra of DBP and Isoviolanthrone in $CHCl_3$.

Highly structured, spectra of the **DBP** appears significantly blue-shifted compared to the ketone-based starting material. While the latter indeed exhibits two prominent and well-defined absorption bands in the visible range at 543 and 588 nm, those of **DBP** were monitored around 500 and 534 nm. Attributed to the allowed π–π* transitions, these absorption bands were also characterized by impressive extinction coefficients of 120000 and 62000 $M^{-1}{\cdot}cm^{-1}$, respectively.

From the emission point of view, **DBP** shows a significant greenish-yellow emission associated with emission maxima at 548 and 583 nm together with a photoluminescent quantum yield (PLQY) in solution of *ca.* 80% (Table 3.10).

*Table 3.10 Optical data of **DBP** and Isoviolanthrone.*

Molecule	λ_{abs}^{max} solution (nm)	ε (M^{-1} cm^{-1})	λ_{em}^{max} solution (nm)	HOMO (eV)
DBP	500 534	62000 120000	548 583	-5.26
Isoviolanthrone	543 588	-	602 653	-5.70

While the modest solubility of its parent compound limited its characterization in solution, PESA measurements were carried out on powders to determine their respective HOMO levels (Figure 3.36).

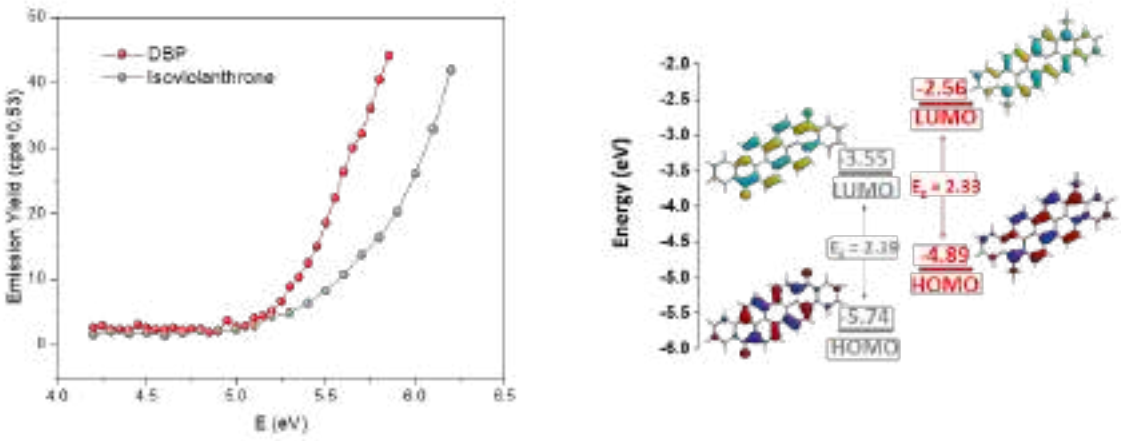

*Figure 3.36 PESA spectra recorded on **DBP** (red) and Isoviolanthrone (gray) powders (left) and optimized geometries and computed energy diagram for Isoviolanthrone (gray) and **DBP** (red) (right).*

As a result, the O-alkylation was found to significantly destabilize the HOMO and LUMO levels since lying at -5.26 eV vs -5.70 eV for the Isoviolanthrone. This feature, investigated by quantum chemical simulations, was correlated to i) a better conjugation along the π-conjugated backbone (improved delocalization of both frontier energy levels beyond the central pyrene core) (see diagram in Figure 3.36) and ii) the replacement of electron-withdrawing ketones (inductive and resonance effects) by mesomeric alkoxy donor groups.

3.4.4 Evaluation as light-emitting materials in LECs

With such high QY, integration in thin film-based light-emitting devices was subsequently targeted to demonstrate the upcycling potential of **DBP**. In coherence with the synthetic accessibility of the dye and also its dual redox behavior, light-emitting electrochemical cells (LECs) were considered herein for their simplicity and ease of fabrication.[74]

Prepared in collaboration with the group of Eunkyoung Kim at Yonsei University, active layers consisting of **DBP**, 4′-bis(N-carbazolyl)-1,1′-biphenyl (CBP), and tetrahexylammonium benzoate (THAB) ionic liquid, used as guest (emitter), host, and supporting electrolyte, respectively, were processed on PEDOT-PSS pre-coated indium tin oxide (ITO) substrates before being covered by a thermally evaporated aluminum back electrode.

First attempts were carried out with 18 weight percentage of **DBP**. While operating devices were demonstrated with promising turn-on voltages of ca 6.1 V under direct current-voltage-luminance (IVL) mode (increase of 0.1 V per second), a very low luminescence was nonetheless recorded (ca 1.2 $cd.m^{-2}$ @ 561 nm). Even if functionalized by long and bulky alkyl chains, these modest emission values might have originated from the aggregation-caused quenching (ACQ) effect induced by the large π-conjugated scaffold of **DBP**.

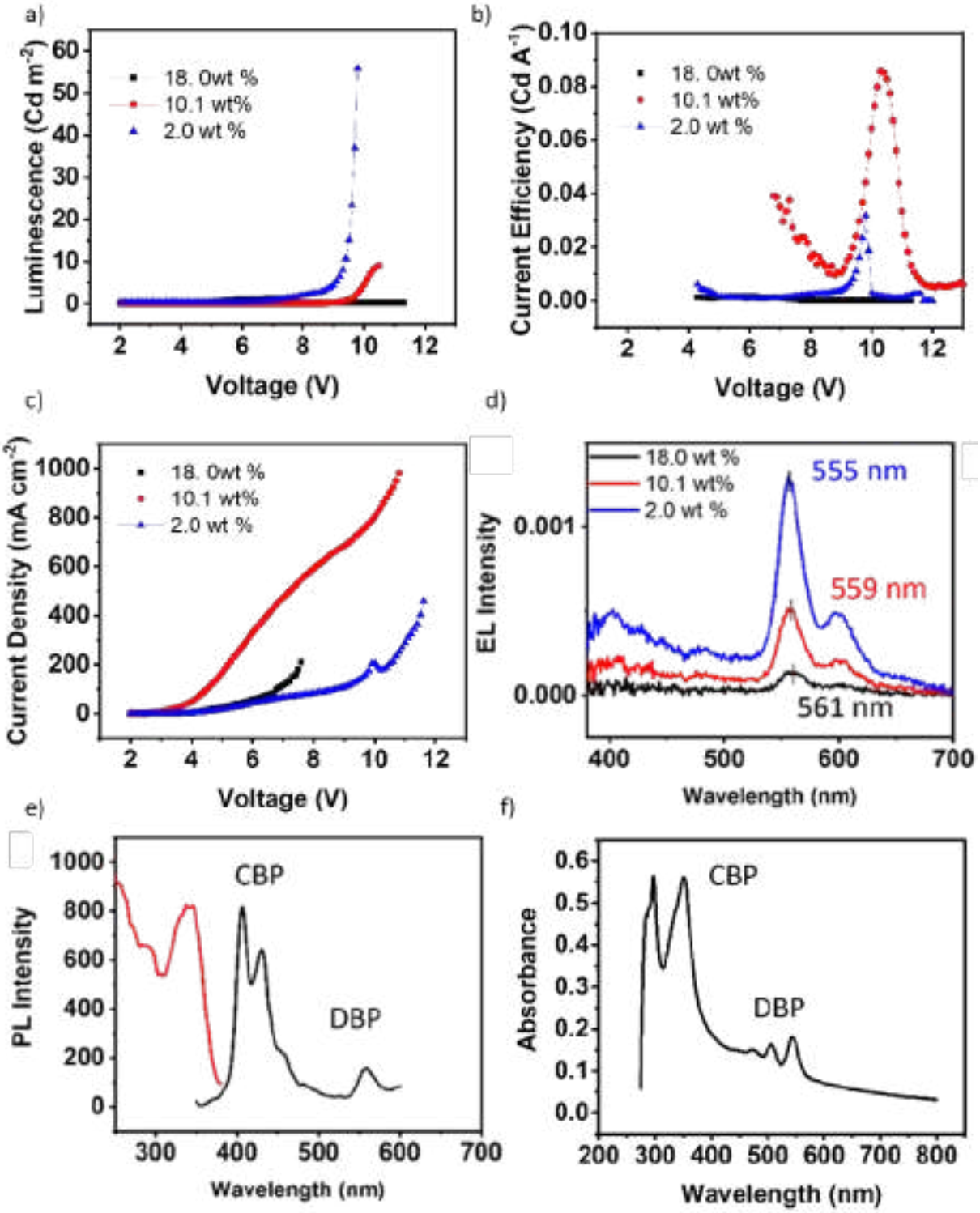

*Figure 3.37 Luminescence (a), current efficiency (b), current density (c), and electroluminescence (d) of the **DBP/CBP** devices at different concentrations of **DBP** (18, 10.1, and 2.0 wt %); photoluminescence intensity (f) and absorption (e) of the best performing LEC (2.0 wt %).*

Consequently, the guest weight percentage was therefore reduced to limit this ACQ effect to 10.1 and then 2 weight % resulting in a significant increase of luminescence from 9.1 $cd.m^{-2}$ to 55.9 $cd.m^{-2}$ respectively (Figure 3.37) along with a shift of the **DBP** characteristic EL peak from 559 nm (10.1 wt %) to 555 nm (2.0 wt %, Figure 3.37 d). While PL experiments performed on the best operating device revealed a strong and major contribution at 406 nm attributed to the CBP, the EL spectra showed intense luminescence of the **DBP**, thus emphasizing a good transfer from the host to the guest under EL conditions.

Finally, to improve the device performance, the driving method was changed from IVL mode to pulsed current-voltage mode (Table 3.11, Figure 3.38 a).[75-77]

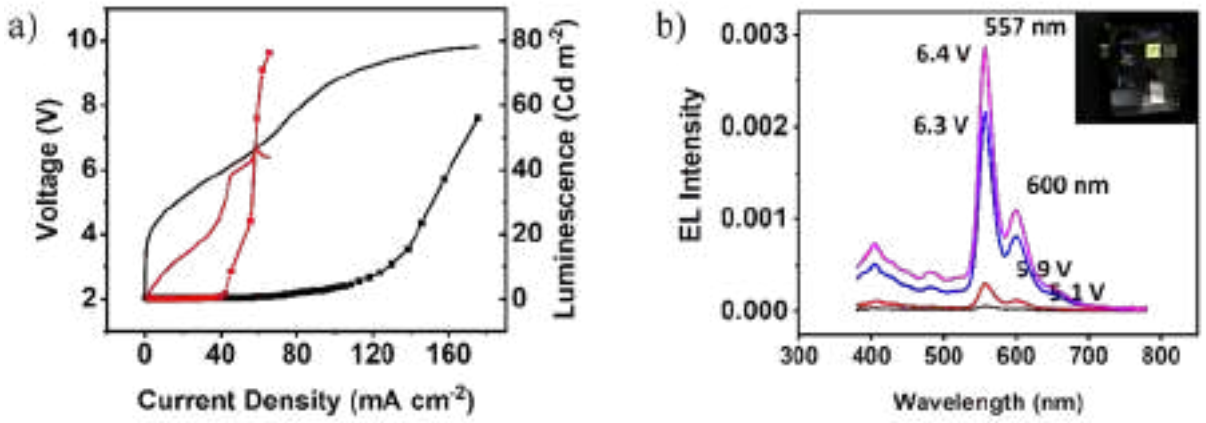

*Figure 3.38 a) The luminescence (square) and voltage (solid line) changes with increasing current density under different driving conditions of IVL (black) and pulse current mode (red) (b). EL spectra for pulse current-driven **DBP/CBP** LEC devices.*

As expected, both the turn-on and peak voltage were reduced (Table 3.11) while the luminescence was significantly increased (+36%) with maximum intensity reached at 557 nm (Figure 3.38 b).

Table 3.11 Comparison of the best device performances recorded under ILV and pulse current mode [a]Turn-on voltage above 1Cd m^{-2}. [b]Voltage at peak luminescence.

Driving current	Turn-on Voltage[a] (V)	Peak Luminescence (Cd m^{-2})	Peak Voltage[b] (V)	Current Efficiency (Cd A^{-1})	Current Density (mA cm^{-2})
IVL	7.3	55.9	9.8	0.0027	175.2
Pulse	5.1	76.1	6.4	0.11	65.6

Almost negligible, the ca 2-nm redshift of the maximum EL peak recorded under pulsed conditions (vs. 555 nm for direct IVL) yet still has a noticeable effect on the respective Commission Internationale de l'Eclairage (CIE) coordinates (Figure 3.39).

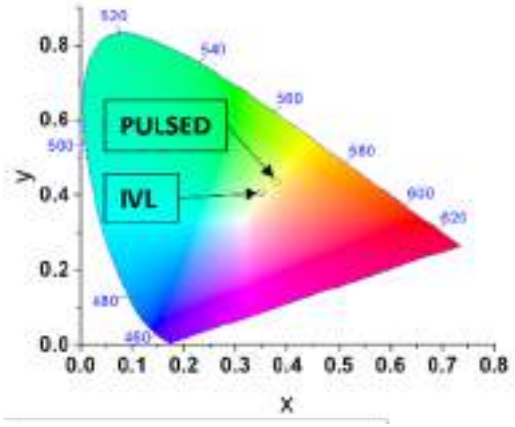

*Figure 3.39 CIE chromaticity diagram of the **DBP** LEC device under IVL and pulse current mode.*

Choice of driving conditions hence appears to be a method of choice to fine-tune the emitting and thus perceived color of the device.

3.4.5 Conclusion

Initially synthesized for textile coloring, we report through this last part of this chapter a successful example of upcycling of another overlooked dye. Through a one-pot sequential functionalization, soluble version of the vat violet 10 was indeed successfully embedded in light-emitting electrochemical cells. Hence, considering i) the simplicity of this reaction to provide processable active material, ii) the large amount of wastewater still full of reactive anionic precursors generated and discarded by the textile industry, iii) the successful fabrication/demonstration of low-cost operating devices, and iv) the tremendous variety of ton-scale-produced and commercially available vat dyes, this exploratory and preliminary contribution highlights the huge potential of upcycling these building blocks for both value-added applications and environmental purposes. Even if conversion yields are somehow moderate, as well as device performances in terms of pure efficiencies, we demonstrate that dye-contaminated wastewater can still be valorized with a minor effort. In the current context of ecological transition, it is indeed vital to develop simple research guidelines aiming at transposing our recycling/upcycling household routines to laboratories, and above all, industries.

Bibliography

[1] G. Hong, X. Gan, C. Leonhardt, Z. Zhang, J. Seibert, J. M. Busch and S. Bräse, Advanced Materials 2021, 33, 2005630.
[2] J. Bauri, R. B. Choudhary and G. Mandal, Journal of Materials Science 2021, 56, 18837-18866.
[3] N. Sain, D. Sharma and P. Choudhary, Int. J. Eng. Appl. Sci. Technol 2020, 4, 587-591.
[4] H. Wen, Highlights in Science, Engineering and Technology 2022, 27, 716-722.
[5] LG.com https://www.lg.com/fr/televiseurs/lg-42lx3q6la-oled-tv-flex-4k?cmpid=2023HQSEM_OLED-TV_FS_Google_Lifestyle-Screens_Brand-NA_Broad_Flex_k2023051115069_pc_NPI_tROAS&utm_content=Lifestyle-Screens&utm_term=Brand&gad=1&gclid=CjwKCAjwu4WoBhBkEiwAojNdXtU1j0I-jE5j94AZmuNJ15bKDX1iL2qCR-TMuozjwCjufqf6Vw4LVRoCGEwQAvD_BwE&gclsrc=aw.ds.
[6] Samsung.com https://www.samsung.com/fr/smartphones/galaxy-z-flip5/buy/?modelCode=SM-F731BZYHEUB&cid=fr_pd_ppc_google_f2h23-b5-brand-exact_launch_shop-im_text_none_none&&&gclid=CjwKCAjwu4WoBhBkEiwAojNdXqOgCuTAOMxCciakJN3OkFEJ2PXuF30YQXTLLXuRteVCD6Cs-KsKqxoC3mEQAvD_BwE&gclsrc=aw.ds.
[7] D. Frackowiak, Journal of Photochemistry and Photobiology B: Biology 1988, 2, 399.
[8] B. Valeur and M. N. Berberan-Santos, Journal of Chemical Education 2011, 88, 731-738.
[9] H. Liu, J. Chen, Y. Fu, Z. Zhao and B. Z. Tang, Advanced Functional Materials 2021, 31, 2103273.
[10] X.-H. Zhu, J. Peng, Y. Cao and J. Roncali, Chemical Society Reviews 2011, 40, 3509-3524.
[11] X. Xu, X. Yang, J. Zhao, G. Zhou and W.-Y. Wong, Asian Journal of Organic Chemistry 2015, 4, 394-429.
[12] J. Zhang, F. Zhao, X. Zhu, W.-K. Wong, D. Ma and W.-Y. Wong, Journal of Materials Chemistry 2012, 22, 16448-16457.
[13] S.-W. Kang, E.-J. Bae, Y.-W. Park and B.-K. Ju, Nanomaterials 2023, 13, 2357.
[14] Q. Li, H. Liu, X. Li and S. Wang, Journal of Materials Chemistry C 2023, 11, 7833-7840.
[15] Z. Xie, C. Cao, Y. Zou, X. Cao, C. Zhou, J. He, C.-S. Lee and C. Yang, Advanced Functional Materials 2022, 32, 2112881.
[16] T. Zhang, Y. Xiao, H. Wang, S. Kong, R. Huang, V. Ka-Man Au, T. Yu and W. Huang, Angewandte Chemie International Edition n/a, e202301896.
[17] Y.-L. Zhang, Q. Ran, Q. Wang, Y. Liu, C. Hänisch, S. Reineke, J. Fan and L.-S. Liao, Advanced Materials 2019, 31, 1902368.
[18] N. B. Kotadiya, P. W. M. Blom and G.-J. A. H. Wetzelaer, Nature Photonics 2019, 13, 765-769.
[19] H. Chen, J. Zeng, R. Huang, J. Wang, J. He, H. Liu, D. Yang, D. Ma, Z. Zhao and B. Z. Tang, Aggregate 2023, 4, e244.
[20] G. Li, J. Pu, Z. Yang, H. Deng, Y. Liu, Z. Mao, J. Zhao, S.-J. Su and Z. Chi, Aggregate 2023, n/a, e382.
[21] Y. Liu, J. Yang, Z. Mao, D. Ma, Y. Wang, J. Zhao, S.-J. Su and Z. Chi, Advanced Optical Materials 2023, 11, 2201695.
[22] H. Abroshan, V. Coropceanu and J.-L. Brédas, ACS Materials Letters 2020, 2, 1412-1418.
[23] E. Cho, M. Hong, Y. S. Yang, Y. J. Cho, V. Coropceanu and J.-L. Brédas, Journal of Materials Chemistry C 2022, 10, 4629-4636.

[24] C. W. Tang and S. A. VanSlyke, Applied Physics Letters 1987, 51, 913-915.
[25] Q. Pei, G. Yu, C. Zhang, Y. Yang and A. J. Heeger, Science 1995, 269, 1086-1088.
[26] J. H. Burroughes, D. D. C. Bradley, A. R. Brown, R. N. Marks, K. Mackay, R. H. Friend, P. L. Burns and A. B. Holmes, Nature 1990, 347, 539-541.
[27] Y. Zhang, J. Wei, L. Wang, T. Huang, G. Meng, X. Wang, X. Zeng, M. Du, T. Fan, C. Yin, D. Zhang and L. Duan, Advanced Materials 2023, 35, 2209396.
[28] W. Yang, J. Miao, F. Hu, Y. Zou, C. Zhong, S. Gong and C. Yang, Advanced Functional Materials 2023, 33, 2213056.
[29] L. Wang, J. Miao, Y. Zhang, C. Wu, H. Huang, X. Wang and C. Yang, Advanced Materials 2023, 35, 2303066.
[30] W. Zhu, M. Hu, R. Yao and H. Tian, Journal of Photochemistry and Photobiology A: Chemistry 2003, 154, 169-177.
[31] C. Poriel and J. Rault-Berthelot, Accounts of Materials Research 2023.
[32] J. Y. Xue, T. Izumi, A. Yoshii, K. Ikemoto, T. Koretsune, R. Akashi, R. Arita, H. Taka, H. Kita, S. Sato and H. Isobe, Chemical Science 2016, 7, 896-904.
[33] Z. M. Hudson, Z. Wang, M. G. Helander, Z.-H. Lu and S. Wang, Advanced Materials 2012, 24, 2922-2928.
[34] O. Sachnik, Y. Li, X. Tan, J. J. Michels, P. W. M. Blom and G.-J. A. H. Wetzelaer, Advanced Materials 2023, 35, 2300574.
[35] C. Poriel and J. Rault-Berthelot, Advanced Functional Materials 2020, 30, 1910040.
[36] H. Movla, Optik 2015, 126, 5237-5240.
[37] S. Negi, P. Mittal and B. Kumar, Microsystem Technologies 2018, 24, 4981-4989.
[38] X. J. Feng, S. F. Chen, Y. Ni, M. S. Wong, M. M. K. Lam, K. W. Cheah and G. Q. Lai, Organic Electronics 2014, 15, 57-64.
[39] P. Wang, S. Fan, J. Liang, L. Ying, J. You, S. Wang and X. Li, Dyes and Pigments 2017, 142, 175-182.
[40] F. Lucas, C. Brouillac, S. Fall, N. Zimmerman, D. Tondelier, B. Geffroy, N. Leclerc, T. Heiser, C. Lebreton, E. Jacques, C. Quinton, J. Rault-Berthelot and C. Poriel, Chemistry of Materials 2022, 34, 8345-8355.
[41] S. Thiery, D. Tondelier, B. Geffroy, E. Jacques, M. Robin, R. Métivier, O. Jeannin, J. Rault-Berthelot and C. Poriel, Organic Letters 2015, 17, 4682-4685.
[42] L. Aubouy, P. Gerbier, C. Guérin, N. Huby, L. Hirsch and L. Vignau, Synthetic Metals 2007, 157, 91-97.
[43] G. Zhang, M. Baumgarten, M. Auer, R. Trattnig, E. J. W. List-Kratochvil and K. Müllen, Macromolecular Rapid Communications 2014, 35, 1931-1936.
[44] C. Poriel and J. Rault-Berthelot, Advanced Functional Materials 2021, 31, 2010547.
[45] A. C, D. K. Dubey, M. Pahlevani and G. C. Welch, Advanced Materials Technologies 2021, 6, 2100264.
[46] L. Hua, Y. Liu, B. Liu, Z. Zhao, L. Zhang, S. Yan and Z. Ren, Nature Communications 2022, 13, 7828.
[47] J. Liu, J. Liu, H. Li, Z. Bin and J. You, Angewandte Chemie International Edition 2023, 62, e202306471.
[48] Y. Huang, J. Mei and X. Ma, Dyes and Pigments 2019, 165, 499-507.
[49] W. Qiao, P. Yao, Y. Chen, Q. Xiao, L. Zhang and Z. a. Li, Materials Chemistry Frontiers 2020, 4, 2688-2696.
[50] H. Sun, J. Jin, Q. Wang, S. Wang, W. Na, Z. Li, B. Yao, P. Sun, L. Dong and X.-C. Hang, Dyes and Pigments 2022, 200, 110169.

[51] P. Josse, S. Li, S. Dayneko, D. Joly, A. Labrunie, S. Dabos-Seignon, M. Allain, B. Siegler, R. Demadrille, G. C. Welch, C. Risko, P. Blanchard and C. Cabanetos, Journal of Materials Chemistry C 2018, 6, 761-766.
[52] A.-J. Payne, N. A. Rice, S. M. McAfee, S. Li, P. Josse, C. Cabanetos, C. Risko, B. H. Lessard and G. C. Welch, ACS Applied Energy Materials 2018, 1, 4906-4916.
[53] S. V. Dayneko, A. D. Hendsbee, J. R. Cann, C. Cabanetos and G. C. Welch, New Journal of Chemistry 2019, 43, 10442-10448.
[54] J. M. Andrés Castán, L. Abad Galán, S. Li, C. Dalinot, P. Simón Marqués, M. Allain, C. Risko, C. Monnereau, O. Maury, P. Blanchard and C. Cabanetos, New Journal of Chemistry 2020, 44, 900-905.
[55] C. Dalinot, P. Simón Marqués, J. M. Andrés Castán, P. Josse, M. Allain, L. Abad Galán, C. Monnereau, O. Maury, P. Blanchard and C. Cabanetos, European Journal of Organic Chemistry 2020, 2020, 2140-2145.
[56] P. Simon Marques, J. M. Andres Castan, L. A. Galan, M. Allain, O. Maury, T. Le Bahers, P. Blanchard and C. Cabanetos, J Org Chem 2021, 86, 5901-5907.
[57] J. M. Andrés Castán, S. Abidi, T. Ghanem, S. Touihri, P. Blanchard, G. C. Welch, Y. Zagranyarski, J. Boixel, B. Walker, P. Josse and C. Cabanetos, Colorants 2023, 2, 22-30.
[58] J. M. A. Castán, C. Amruth, P. Josse, L. A. Galan, P. S. Marqués, M. Allain, O. Maury, T. Le Bahers, P. Blanchard, C. Monnereau, G. C. Welch and C. Cabanetos, Materials Chemistry Frontiers 2022, 6, 1912-1919.
[59] J. M. Andrés Castán, C. Dalinot, S. Dayneko, L. Abad Galan, P. Simón Marqués, O. Alévêque, M. Allain, O. Maury, L. Favereau, P. Blanchard, G. C. Welch and C. Cabanetos, Chemical Communications 2020, 56, 10131-10134.
[60] P. Josse, K. Morice, D. Puchán Sánchez, T. Ghanem, J. Boixel, P. Blanchard and C. Cabanetos, New Journal of Chemistry 2022, 46, 8393-8397.
[61] Y. Liu, Y. Zhang, X. Wu, Q. Lan, C. Chen, S. Liu, Z. Chi, L. Jiang, X. Chen and J. Xu, Journal of Materials Chemistry C 2014, 2, 1068-1075.
[62] O. Younis, M. S. Tolba, E. A. Orabi, A. M. Kamal, R. Hassanien, O. Tsutsumi and M. Ahmed, Journal of Photochemistry and Photobiology A: Chemistry 2020, 400, 112642.
[63] M. Deiana, José M. Andrés Castán, P. Josse, A. Kahsay, Darío P. Sánchez, K. Morice, N. Gillet, R. Ravindranath, Ankit K. Patel, P. Sengupta, I. Obi, E. Rodriguez-Marquez, L. Khrouz, E. Dumont, L. Abad Galán, M. Allain, B. Walker, H. S. Ahn, O. Maury, P. Blanchard, T. Le Bahers, D. Öhlund, J. von Hofsten, C. Monnereau, C. Cabanetos and N. Sabouri, Nucleic Acids Research 2023.
[64] B. Lellis, C. Z. Fávaro-Polonio, J. A. Pamphile and J. C. Polonio, Biotechnology Research and Innovation 2019, 3, 275-290.
[65] Z. Wang, G. W. Walker, D. C. G. Muir and K. Nagatani-Yoshida, Environmental Science & Technology 2020, 54, 2575-2584.
[66] A. Sweetman, Front. Environ. Chem. 2020, 1.
[67] S. Haslinger, Y. Wang, M. Rissanen, M. B. Lossa, M. Tanttu, E. Ilen, M. Määttänen, A. Harlin, M. Hummel and H. Sixta, Green Chemistry 2019, 21, 5598-5610.
[68] J.-F. Morin, Journal of Materials Chemistry C 2017, 5, 12298-12307.
[69] J.-B. Giguère, Q. Verolet and J.-F. Morin, Chemistry – A European Journal 2013, 19, 372-381.
[70] K. Kotwica, P. Bujak, D. Wamil, M. Materna, L. Skorka, P. A. Gunka, R. Nowakowski, B. Golec, B. Luszczynska, M. Zagorska and A. Pron, Chemical Communications 2014, 50, 11543-11546.

[71] K. Kotwica, P. Bujak, P. Data, W. Krzywiec, D. Wamil, P. A. Gunka, L. Skorka, T. Jaroch, R. Nowakowski, A. Pron and A. Monkman, Chemistry – A European Journal 2016, 22, 7978-7986.
[72] O. A. Melville, T. M. Grant, N. A. Rice, B. Wang, P. Josse and B. H. Lessard, New Journal of Chemistry 2020, 44, 845-851.
[73] M. R. Chetyrkina, F. S. Talalaev, L. V. Kameneva, S. V. Kostyuk and P. A. Troshin, Journal of Materials Chemistry C 2022, 10, 3224-3231.
[74] K. Schlingman, Y. Chen, R. S. Carmichael and T. B. Carmichael, Advanced Materials 2021, 33, 2006863.
[75] A. Pertegás, D. Tordera, J. J. Serrano-Pérez, E. Ortí and H. J. Bolink, Journal of the American Chemical Society 2013, 135, 18008-18011.
[76] N. M. Shavaleev, R. Scopelliti, M. Grätzel, M. K. Nazeeruddin, A. Pertegás, C. Roldán-Carmona, D. Tordera and H. J. Bolink, Journal of Materials Chemistry C 2013, 1, 2241-2248.
[77] M. Rémond, J. Hwang, J. Kim, S. Kim, D. Kim, C. Bucher, Y. Bretonnière, C. Andraud and E. Kim, Advanced Functional Materials 2020, 30, 2004831.

General Conclusions

GENERAL CONCLUSIONS

Over the last three years, this PhD was mainly devoted to the development of more efficient and sustainable synthetic routes to provide new and accessible π-conjugated materials for organic electronics applications. Beyond performances, the main criteria sought by most research groups, accessibility and cost-effectiveness should be of major concerns to truly bridge the gap between academia and industry. Hence, as a contribution from a chemistry point of view to achieve a greener and more sustainable future for the electronics industry, the development of synthetic methods that consume fewer resources, produce less waste, and have a smaller environmental impact indeed appears crucial. It is therefore in this context that this PhD thesis was carried out.

Following a general introduction on organic electronics to set the scene, scope, and limitations in the field, the second chapter describes the preparation of active compounds, by the direct (hetero)arylation reaction for solar cell applications. Separated into two parts, two different triphenylamine-based push-pull molecules were first introduced and used as donor materials for OSCs. Prepared *via* an optimized "one-pot" procedure (without modification of the catalytic system nor purification of intermediates), the latter were then successfully embedded in solution-processed bulk-heterojunction OSCs. Beyond the demonstration, investigation of their structural properties rationalized the better efficiencies achieved with the biphenyl derivative **MD-Ph** (compared to its methoxy counterpart **MD-OMe**) due to a higher open-circuit voltage (energetics) and better charge transport properties (design principle).

Then, in a second sub-chapter, the use of the direct arylation reaction was demonstrated to prepare simple but efficient hole-transporting materials (HTMs) for Perovskite-based solar cells. Hence, three tris(4-methoxyphenyl)amine end-capped molecules with different thiophene-based central cores were successfully synthesized through step-saving routes. Tested in *n-i-p* type PSCs highly promising power conversion efficiencies, ranging from 18 to 20%, were achieved, almost competing with those of the reference Spiro-OMeTAD. Moreover, it turned out that mixing 5 mol% of the synthesized HTMs with the latter Spiro-OMeTAD, resulted in i) an increase of the efficiencies of the photovoltaic devices, ii) a reduction of the dopants concentration, iii) improved intermolecular hole transport, and iv) stabilized PCEs over time. As a result, a high PCE of 24.5% retained over 90% after 1200 hours under constant illumination and without encapsulation was achieved with one of the synthesized compounds.

GENERAL CONCLUSIONS

Alongside organic/hybrid photovoltaics, organic light-emitting devices are also great contributors, if not THE contributors, to the development and success of organic electronics. Therefore, chapter 3 was dedicated to the development of simple and accessible photoluminescent materials and evaluation in light-emitting devices.

Starting with thiophene-based molecules end-capped with triarylamine moieties, three emissive compounds with different π-conjugated central cores were prepared, once again, by direct arylation coupling reactions. Through their optoelectronic characterization, the twisting of the backbone, induced by the hexyl chains in the 3,3' positions of the thiophene rings, was confirmed to prevent the ACQ phenomenon but on the other hand, limit the intramolecular π-electronic delocalization through the backbone. Embedded as emitters in single-layer OLED devices, the best efficiencies and film-forming capabilities were achieved with the shorter and less synthetically demanding derivative. Indeed prepared in one step from commercial and affordable starting materials, the latter was finally used for the preparation of operating printed flexible large-area blue emitting demonstrators processed from industry-friendly o-xylene solutions.

Then, to shift the emissions toward higher wavelengths, the bithiophene central core was replaced by the BTI dye. Hence, two molecules, bearing two or three extended arylamine groups, were successfully synthesized and characterized highlighting promising optoelectronic properties. Embedded in flexible and large-area printed OLEDs, **BTI-TPA$_2$** has already demonstrated promising orange emission.

Finally, in the last part of chapter 3, the upcycling of a vat dye, namely the Isoviolanthrone, was investigated. Through a one-pot sequential functionalization, a soluble version was isolated and successfully embedded in light-emitting electrochemical cells. Even though conversion yields and device efficiencies were somehow moderate, this study demonstrated, with minor synthetic efforts, that wastewater from the textile industry, *ie* containing unreacted dyes, can still be valorized for both value-added applications and environmental purposes.

Consequently, the work performed during this PhD thesis demonstrates that great results and perspectives can be achieved with well-designed, accessible, and even simple molecules. As quoted by Da Vinci, "*Simplicity is the ultimate sophistication*".

Exp Section

Exp Section

Exp Section

Exp Section

Exp Section

Experimental Section

1. General methods

All reagents and solvents were purchased from commercial sources and used without further purification unless otherwise stated. Reactions were carried out under an argon atmosphere unless otherwise stated. Microwave assisted reactions were performed using a Biotage initiator system. Flash chromatography was performed with analytical-grade solvents using Aldrich silica gel (technical grade, pore size 60 Å, 230–400 mesh particle size). Flexible plates ALUGRAM® XtraSIL G UV254 from MACHEREY-NAGEL were used for TLC. Compounds were detected by UV irradiation (Bioblock Scientific) unless stated otherwise. ^{1}H and ^{13}C NMR were recorded on a Bruker AVANCE III 300 (^{1}H, 300 MHz; ^{13}C, 75 MHz) or a Bruker AVANCE DRX500 (^{1}H, 500 MHz; ^{13}C, 125 MHz). Chemical shifts are given in parts per million (ppm) relative to TMS and coupling constants J in Hertz (Hz). High resolution mass spectrometry (HRMS) was performed with a JEOL JMS-700 B/E.

UV-visible absorption spectra were recorded with a Shimadzu UV-1800 spectrometer. Emission spectra were recorded with a Shimadzu RF-6000 or a Jasco FP-8500. Luminescence quantum yields were measured in diluted solutions with an absorbance lower than 0.1 or in powder state using an ILF-835 100 mm Integrating Sphere from Jasco. Electrochemical measurements were performed with a Biologic SP-150 potentiostat with positive feedback compensation using a conventional single-compartment three-electrode cell. The working electrode was a platinum electrode. The auxiliary was a platinum wire and the pseudo-reference electrode was a silver wire calibrated with the ferrocene potential. The supporting electrolyte was 0.1 M Bu_4NPF_6 (tetrabutylammonium hexafluorophosphate) in dichloromethane (DCM) and solutions were purged with argon prior to each experiment. All potentials are quoted relative to Fc/Fc^+. In all the experiments, the scan rate was 100 mV/s. Photoelectron spectroscopy in air (PESA) measurements were recorded using a Riken Keiki PESA spectrometer (Model AC-2). Thermogravimetric analyses (TGA) were performed with TA Instruments Q500 under nitrogen at a heating rate of 5°C/min.

X-ray single-crystal diffraction data were collected on a Rigaku Oxford Diffraction SuperNova diffractometer equipped with Atlas CCD detector and micro-focus Cu-Kα radiation (1.54184 Å). The structures were solved by direct methods and refined on F2 by full matrix least-squares techniques using SHELX programs (G. M. Sheldrick, 2018). All non-H atoms were refined anisotropically and multiscan empirical absorption was corrected using

CrysAlisPro program (CrysAlisPro, Agilent Technologies, V 1.171.40.45a, 2019). The H atoms were included in the calculation without refinement.

General procedure for purification with recycling preparative size exclusion HPLC:

Crude compounds were solubilized in HPLC grade chloroform (stabilized with ethanol, 5 mL). Prior to injection, the solution was filtered through a 0.45 μm PTFE filter (VWR 25 mm syringe filter w/ 0.45 μm membrane). Purification was performed on a LC-9160NEXT system from the Japan Analytical Industry Co., Ltd. (JAI) equipped with coupled UV-vis 4Ch NEXT and RI-700 II detectors at room temperature through a set of two JAIGEL-2H and 2.5H columns at an elution rate of 10 $mL.min^{-1}$.

2. Synthetic procedures

The following molecules were described and published in “Synthesis of push–pull triarylamine dyes containing 5,6-difluoro-2,1,3-benzothiadiazole units by direct arylation and their evaluation as active material for organic photovoltaics. Materials Advances 2021, 2 (22), 7456-7462” with the corresponding supporting information.

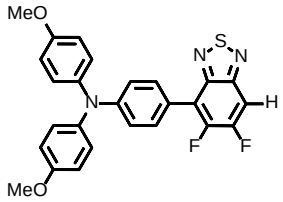

4-Methoxy-N-(4-methoxyphenyl)-N-(4-(5,6-difluorobenzo[c][1,2,5]thiadiazol-4-yl) phenyl)aniline (2): General procedure: To an oven-dried round bottom flask or microwave tube containing a stirring bar, difluorobenzothiadiazole (DFBT) (100 mg, 0.58 mmol) and 4-bromo-4',4''-dimethoxytriphenylamine (1 or 0.5 eq.), the palladium source (0.058 mmol), the ligand (0.12 mmol), pivalic acid (59 mg, 0.58 mmol) and potassium carbonate (240 mg, 1.7 mmol) were sequentially added before a septum-cap was crimped on the vial/flask to form a seal. Solids were degassed 3 times by vacuum-argon filling cycles. Dry toluene (4 mL) was then added to the reaction mixture before being heated with a conventional oil bath or under microwave assisted conditions. The resulting mixture was cooled to room temperature, concentrated under reduced pressure and the residue was purified by column chromatography on silica gel (eluent: DCM/Petroleum Ether (PE) with 4/1 ratio) affording the corresponding **(2)** and the bi-substituted **(2a)** products as orange solids.

Optimized synthesis: To an oven-dried microwave tube containing a stirring bar, difluorobenzothiadiazole (DFBT) (100 mg, 0.58 mmol) and 4-bromo-4',4''-dimethoxytriphenylamine (111 mg, 0.29 mmol, 0.5 eq.), palladium acetate (13 mg, 0.058 mmol), tricyclohexylphosphinetetrafluoroborate (43 mg, 0.12 mmol), pivalic acid (59 mg, 0.58 mmol) and potassium carbonate (240 mg, 1.7 mmol) were sequentially added before a septum-cap was crimped on the vial to seal it. Solids were degassed 3 times by vacuum-argon filling cycles. Anhydrous toluene (4 mL) was then added before exposing the reaction mixture to microwave irradiation for 1 hour at 150 °C. The resulting mixture was cooled to room temperature, concentrated under reduced pressure and the residue was purified by column chromatography on silica gel (eluent: DCM/PE with 4/1 ratio) affording the corresponding product as an orange solid (105 mg, 76%).

^{1}H NMR (300 MHz, Chloroform-d) δ 7.69 – 7.58 (m, 3H), 7.22 – 7.13 (m, 4H), 7.04 (d, J = 8.8 Hz, 2H), 6.88 (d, J = 7.1 Hz, 4H), 3.81 (s, 6H).

^{13}C NMR (75 MHz, Chloroform-d) δ 156.63, 151.08, 150.98, 150.82, 149.68, 140.27, 131.35, 131.31, 127.61, 121.05, 118.69, 115.01, 55.67.

HRMS (MALDI-TOF) m/z: Calculated for $C_{26}H_{19}F_2N_3O_2S$ (M+), 475.1166; Found, 475.1170 (Δ = 1.91 ppm).

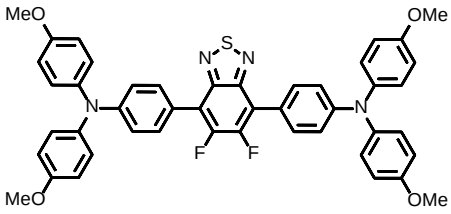

4,4'-(5,6-Difluorobenzo[c][1,2,5]thiadiazole-4,7-diyl)bis(N,N-bis(4-methoxyphenyl)aniline) (2a):

^{1}H NMR (500 MHz, Chloroform-d) δ 7.68 – 7.64 (m, 4H), 7.19 – 7.14 (m, 8H), 7.06 – 7.02 (m, 4H), 6.90 – 6.86 (m, 8H), 3.82 (s, 12H).

^{13}C NMR (125 MHz, Chloroform-d) δ 156.52, 151.22, 150.87, 149.40, 149.18, 140.35, 131.30, 127.52, 121.44, 118.82, 117.81, 114.96, 55.63.

HRMS (MALDI-TOF) m/z: Calculated for $C_{46}H_{36}F_2N_4O_4S$ (M+) 778.2425; Found 778.2427 (Δ = 0.91 ppm).

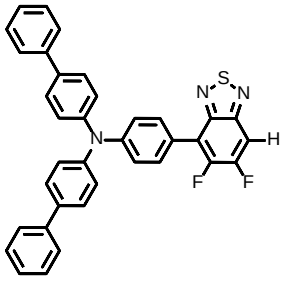

4-Phenyl-N-(4-biphenylyl)-N-(4-(5,6-difluorobenzo[c][1,2,5]thiadiazol-4-yl)phenyl)aniline (3): To an oven-dried microwave tube containing a stirring bar, DFBT (100 mg, 0.58 mmol) and N,N-bis(4-biphenylyl)-N-(4-bromophenyl)amine (138 mg, 0.29 mmol, 0.5 eq.), palladium acetate (13 mg, 0.058 mmol), tricyclohexylphosphinetetrafluoroborate (43 mg, 0.12 mmol), pivalic acid (59 mg, 0.58 mmol) and potassium carbonate (240 mg, 1.7 mmol), were sequentially added and a septum-cap was crimped on the vial to form a seal. The solids were degassed 3 times under vacuum followed by a flow of argon. Anhydrous toluene (4 mL) was added and the reaction mixture was heated under microwave irradiation at 150 °C for 1 hour. The resulting

mixture was cooled to room temperature, concentrated under reduced pressure and the residue was purified by column chromatography on silica gel (eluent: DCM/PE with 4/1 ratio) affording the corresponding product as a yellowish solid (130 mg, 78%).

^{1}H NMR (500 MHz, Chloroform-d) δ 7.75 (d, J = 7.9 Hz, 2H), 7.69 (dd, J = 9.0, 7.7 Hz, 1H), 7.63 – 7.55 (m, 8H), 7.45 (t, J = 7.6 Hz, 4H), 7.36 – 7.29 (m, 8H).

^{13}C NMR (125 MHz, Chloroform-d) δ 150.91, 150.84, 150.81, 148.49, 146.50, 140.62, 136.57, 131.62, 131.60, 128.93, 128.22, 127.18, 126.90, 125.44, 123.60, 122.49, 104.30, 104.14.

HRMS (MALDI-TOF) m/z: Calculated for $C_{36}H_{23}F_2N_3S$ (M+), 567.1581; Found, 567.1577 (Δ = 0.30 ppm).

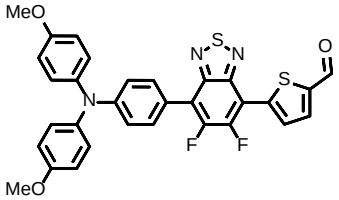

5-(7-(4-(Bis(4-methoxyphenyl)amino)phenyl)-5,6-difluorobenzo[c][1,2,5]thiadiazol-4-yl) thiophene-2-carbaldehyde (4): To an oven-dried microwave tube containing a stirring bar and compound **2** (110 mg, 0.23 mmol), palladium acetate (4.2 mg, 0.023 mmol), tricyclohexylphosphinetetrafluoroborate (17 mg, 0.046 mmol), pivalic acid (23.5 mg, 0.23 mmol) and potassium carbonate (96 mg, 0.69 mmol) were added under a flow of argon and a septum-cap was crimped on the vial to form a seal. Anhydrous toluene (4 mL) and 5-bromo-2-thiophenecarboxaldehyde (53 mg, 0.28 mmol, 1.2 eq.) were added and the resulting mixture was heated under microwave irradiation at 150 °C for 1 hour. The resulting mixture was cooled to room temperature, concentrated under reduced pressure and the residue was purified by column chromatography on silica gel (eluent: DCM) affording the corresponding product as a dark orange solid (35 mg, 26%).

^{1}H NMR (300 MHz, Chloroform-d) δ 10.02 (s, 1H), 8.31 (d, J = 4.1 Hz, 1H), 7.86 (dd, J = 4.2, 1.1 Hz, 1H), 7.68 (d, J = 7.0 Hz, 2H), 7.17 (d, J = 8.4 Hz, 4H), 7.02 (d, J = 8.5 Hz, 2H), 6.91 – 6.84 (m, 4H), 3.82 (s, 6H).

^{13}C NMR (125 MHz, Chloroform-d) δ 183.20, 156.64, 150.45, 150.38, 149.82, 148.73, 144.58, 144.54, 139.88, 135.74, 131.44, 131.00, 130.92, 127.59, 120.36, 120.12, 118.27, 114.92, 110.02, 55.52.

HRMS (MALDI-TOF) m/z: Calculated for $C_{31}H_{21}F_2N_3O_3S_2$ (M+), 585.0992; Found, 585.0986 (Δ = -0.23 ppm).

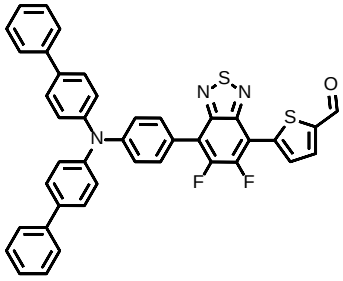

5-(7-(4-(Bis(4-biphenylyl)amino)phenyl)-5,6-difluorobenzo[c][1,2,5]thiadiazol-4-yl) thiophene-2-carbaldehyde (5): To an oven-dried microwave tube containing a stirring bar and compound **3** (145 mg, 0.25 mmol), palladium acetate (5.7 mg, 0.025 mmol), tricyclohexylphosphinetetrafluoroborate (18.8 mg, 0.051 mmol), pivalic acid (26 mg, 0.25 mmol) and potassium carbonate (106 mg, 0.76 mmol) were added under a flow of argon and a septum-cap was crimped on the vial to form a seal. Anhydrous toluene (4 mL) and 5-bromo-2-thiophenecarboxaldehyde (58.5 mg, 0.31 mmol) were added and the resulting mixture was heated under microwave irradiation at 150 °C for 1 hour. The resulting mixture was cooled to room temperature, concentrated under reduced pressure and the residue was purified by column chromatography on silica gel (eluent: DCM) affording the corresponding product as a red solid (60 mg, 34%).

^{1}H NMR (300 MHz, Chloroform-d) δ 10.05 (s, 1H), 8.36 (d, J = 3.9 Hz, 1H), 7.90 (d, J = 4.0 Hz, 1H), 7.80 (d, J = 7.8 Hz, 2H), 7.64 – 7.56 (m, 8H), 7.48 – 7.42 (m, 4H), 7.38 – 7.28 (m, 8H).

^{13}C NMR (125 MHz, Chloroform-d) δ 183.39, 148.84, 146.36, 140.61, 136.83, 135.88, 131.79, 131.76, 131.36, 131.28, 128.97, 128.29, 127.25, 126.94, 125.64, 123.08, 122.18, 77.16.

HRMS (MALDI-TOF) m/z: Calculated for $C_{41}H_{25}F_2N_3OS_2$ (M+), 677.1407; Found, 677.1407 (Δ = 0.73 ppm).

General procedure for the preparation of (4) and (5) through a "one-pot" reaction: To an oven-dried microwave tube containing a stirring bar, DFBT (1 eq.) and 4-bromo-4',4''-dimethoxytriphenylamine or N,N-bis(4-biphenylyl)-N-(4-bromophenyl)amine (0.5 eq.), palladium acetate (0.1 eq.), tricyclohexylphosphinetetrafluoroborate (0.2 eq.), pivalic acid (1 eq.) and potassium carbonate (3 eq.) were sequentially added before a septum-cap was crimped on the vial to seal it. Solids were degassed 3 times by vacuum-argon filling cycles. Anhydrous toluene (4 mL) was then added before exposing the reaction mixture to microwave irradiation

for 1 hour at 150 °C. Then, 5-bromo-2-thiophenecarboxaldehyde (1.2 eq.) was directly added to the reaction mixture through the septum and the tube was re-heated at 150°C for 30 minutes. The resulting mixture was cooled to room temperature, concentrated under reduced pressure and the residue was purified by column chromatography on silica gel (eluent: DCM/PE with 4/1 ratio) affording the corresponding products, namely **4** (18%) or **5** (17%).

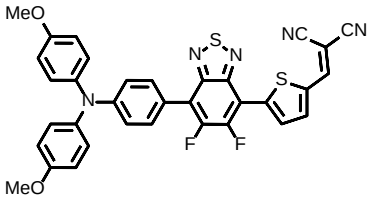

Synthesis of 2-((5-(7-(4-(bis (4methoxyphenyl) amino) phenyl)-5,6-difluorobenzo[c][1,2,5]thiadiazol-4-yl) thiophen-2-yl)methylene)malononitrile (MD-OMe): From (**2**) by DHA cross-coupling reaction: To an oven-dried microwave tube containing a stirring bar, compound **2** (40 mg, 0.08 mmol) and 5-bromo-2-dicyanovinylthiophene (40 mg, 0.17 mmol), palladium acetate (1.9 mg, 0.008 mmol), tricyclohexylphosphinetetrafluoroborate (6.2 mg, 0.016 mmol), pivalic acid (8.6 mg, 0.08 mmol) and potassium carbonate (35 mg, 0.25 mmol), were sequentially added before a septum-cap was crimped on the vial to seal it. Solids were degassed 3 times by vacuum-argon filling cycles. Anhydrous toluene (4 mL) was then added before exposing the reaction mixture to microwave irradiation for 1 hour at 150 °C. The resulting mixture was cooled to room temperature, concentrated under reduced pressure and the residue was purified by column chromatography on silica gel (eluent: DCM/PE with 4/1 ratio) affording the corresponding product as a dark purple solid (3.5 mg, 6%).

From (**4**) by a Knoevenagel reaction: Five drops of triethylamine were added to a mixture of **4** (50 mg, 0.075 mmol) and malononitrile (10.3 mg, 0.16 mmol) in $CHCl_3$ (4 mL). The reaction mixture was stirred under air at room temperature. After TLC analysis showed completion of the reaction, the desired product was obtained by precipitation in hexane as a dark purple solid (47 mg, 90%).

^{1}H NMR (300 MHz, Chloroform-d) δ 8.38 (d, J = 4.3 Hz, 1H), 7.96 (d, J = 4.4 Hz, 1H), 7.88 (s, 1H), 7.71 (dd, J = 8.9, 1.7 Hz, 2H), 7.21 – 7.14 (m, 4H), 7.02 (d, J = 8.9 Hz, 2H), 6.92 – 6.85 (m, 4H), 3.82 (s, 6H).

^{13}C NMR (125 MHz, Chloroform-d) δ 156.72, 150.43, 150.37, 150.20, 150.03, 143.20, 139.78, 137.55, 136.69, 136.63, 131.53, 131.50, 131.43, 131.34, 127.64, 120.99, 120.18, 118.17, 114.93, 114.04, 113.23, 109.43, 109.34, 55.52, 30.94.

^{19}F NMR (283 MHz, Chloroform-d) δ -123.01 (d, J = 16.3 Hz), -134.60 (d, J = 16.3 Hz).

HRMS (MALDI-TOF) m/z: Calculated for $C_{34}H_{21}F_2N_5O_2S_2$ (M+), 633.1105; Found, 633.1098 (Δ = -0.22 ppm).

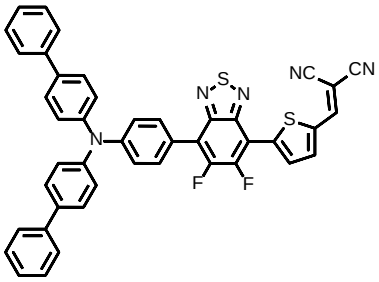

Synthesis of 2-((5-(7-(4-(bis(4-biphenylyl) amino) phenyl) -5,6-difluorobenzo[c] [1,2,5] thiadiazol-4-yl) thiophen-2-yl)methylene)malononitrile (MD-Ph): From (**3**) by DHA cross-coupling reaction: To an oven-dried microwave tube containing a stirring bar, compound **3** (40 mg, 0.07 mmol) and 5-bromo-2-dicyanovinylthiophene (33 mg, 0.14 mmol), palladium acetate (1.6 mg, 0.007 mmol), tricyclohexylphosphinetetrafluoroborate (5.2 mg, 0.014 mmol), pivalic acid (7.2 mg, 0.07 mmol) and potassium carbonate (29 mg, 0.21 mmol) were sequentially added before a septum-cap was crimped on the vial to seal it. Solids were degassed 3 times by vacuum-argon filling cycles. Anhydrous toluene (4 mL) was then added before exposing the reaction mixture to microwave irradiation for 1 hour at 150 °C. The resulting mixture was cooled to room temperature, concentrated under reduced pressure and the residue was purified by column chromatography on silica gel (eluent: DCM/PE with 4/1 ratio) affording the corresponding product as a purple solid (2.6 mg, 5%).

From (**5**) by a Knoevenagel reaction: Five drops of triethylamine were added to a mixture of **5** (23 mg, 0.034 mmol) and malononitrile (4.7 mg, 0.071 mmol) in $CHCl_3$ (4 mL). The reaction mixture was stirred under air at room temperature. After TLC analysis showed completion of the reaction, the desired product was obtained by precipitation in hexane as a purple solid (13 mg, 53%).

^{1}H NMR (300 MHz, Chloroform-d) δ 8.40 (d, J = 4.2 Hz, 1H), 7.97 (d, J = 4.1 Hz, 1H), 7.90 (s, 1H), 7.81 (dd, J = 10.3 Hz, 2H), 7.64 – 7.54 (m, 8H), 7.50 – 7.41 (m, 4H), 7.38 – 7.29 (m, 8H).

^{13}C NMR (125 MHz, Chloroform-d) δ 150.35, 149.02, 148.66, 148.59, 146.26, 140.57, 137.68, 136.95, 131.86, 131.83, 131.73, 131.65, 128.97, 128.31, 127.28, 126.94, 125.72, 122.01, 114.12, 113.33, 78.67.

^{19}F NMR (283 MHz, Chloroform-d) δ -122.95 (d, J = 16.3 Hz), -133.85 (d, J = 16.3 Hz).

HRMS (MALDI-TOF) m/z: Calculated for $C_{44}H_{25}F_2N_5S_2$ (M+), 725.1519; Found, 725.1509 (Δ = -0.70 ppm).

The following molecules were described and published in "Enhancing Intermolecular Interaction of Spiro-OMeTAD for Stable Perovskite Solar Cells with Efficiencies over 24%. ACS Energy Letters 2023, 3895-3901" with the corresponding supporting information.

General procedure for the synthesis of BT, CPDT and SDTF: One of the three thiophene-based central core **1', 2' or 3'** (1 eq), 4-bromo-N,N-bis(4-methoxyphenyl)aniline (2.1 eq), Silia*Cat*® DPP-Pd (0.25 mmol Pd/g, 0.05 eq), pivalic acid (0.3 eq), and potassium carbonate (4.5 eq) were charged with a stir bar into a 5 mL pressure vial that was sealed with a Teflon® cap under an argon atmosphere. After addition of anhydrous and degassed *N*,*N*-dimethylacetamide (4 mL), the reaction mixture was heated to 120 °C in a Lab Armor™ beads bath for 24 hours. After cooling down to room temperature, the reaction mixture was diluted with dichloromethane and the organic phase was washed with water and brine before being dried over $MgSO_4$. After evaporation of the solvent, the crude was purified by column chromatography on silica gel (eluent: DCM:PE with 3:2 V:V ratio) affording the corresponding compounds **BT, CPDT** and **SDTF**.

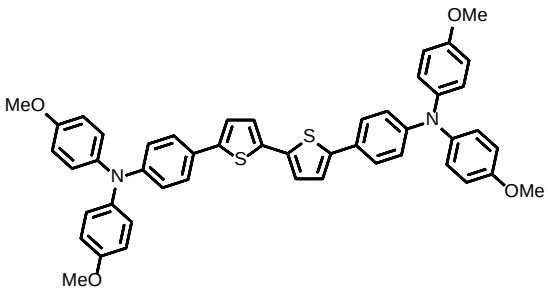

4,4'-([2,2'-Bithiophene]-5,5'-diyl)bis(N,N-bis(4-methoxyphenyl) aniline) (BT): Bright orange powder (300 mg, 75% yield).

^{1}H NMR (500 MHz, Chloroform-d) δ 7.39 (d, *J* = 8.5 Hz, 4H), 7.08 (d, *J* = 8.6 Hz, 12H), 6.92 (d, *J* = 8.3 Hz, 4H), 6.84 (d, *J* = 8.8 Hz, 8H), 3.81 (s, 12H).

^{13}C NMR (125 MHz, Chloroform-d) δ 156.16, 148.40, 143.23, 140.76, 135.73, 126.82, 126.35, 124.25, 122.44, 120.62, 114.88, 55.64.

HRMS (MALDI-TOF) m/z: Calculated for $C_{48}H_{40}N_2O_4S_2$ (M+), 772.2429; Found, 772.2440 (Δ = 2.13 ppm).

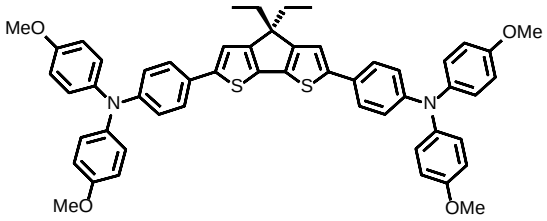

4,4'-(4,4-Diethyl-4H-cyclopenta[2,1-b:3,4-b']dithiophene-2,6-diyl) bis(N,N-bis(4-methoxyphenyl)aniline) (CPDT): Dark orange powder (270 mg, 75% yield).

^{1}H NMR (300 MHz, $CDCl_3$) δ 7.20 – 6.73 (m, 26H), 3.81 (s, 12H), 1.92 (d, J = 6.4 Hz, 4H), 0.65 (t, J = 7.3 Hz, 6H).

^{13}C NMR (76 MHz, CD_2Cl_2) δ 156.55, 148.34, 141.21, 127.04, 127.01, 125.98, 121.01, 115.08, 55.87, 55.83, 30.65, 9.30.

HRMS (MALDI-TOF) m/z: Calculated for $C_{53}H_{48}N_2O_4S_2$ (M+), 840.3055; Found, 840.3038 (Δ = 1.38 ppm).

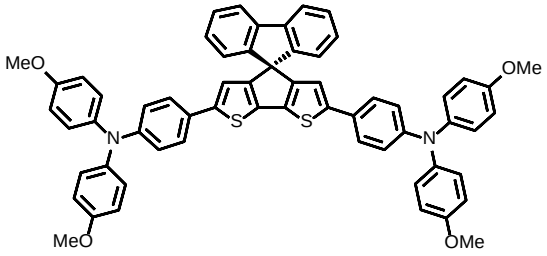

4,4'-(Spiro[cyclopenta[2,1-b:3,4-b']dithiophene-4,9'-fluorene]-2,6-diyl)bis(N,N-bis(4-methoxyphenyl)aniline) (SDTF): Dark orange powder (250 mg, 70% yield).

^{1}H NMR (300 MHz, $CDCl_3$) δ 7.84 (d, *J* = 7.6 Hz, 2H), 7.38 (t, *J* = 7.5 Hz, 2H), 7.32 – 7.20 (m, 3H), 7.15 (t, *J* = 7.5 Hz, 3H), 7.03 (d, *J* = 8.7 Hz, 8H), 6.96 (d, *J* = 7.6 Hz, 2H), 6.83 (t, *J* = 6.2 Hz, 12H), 6.53 (s, 2H), 3.79 (s, 12H).

^{13}C NMR (76 MHz, CD_2Cl_2) δ 145.83, 145.77, 145.70, 142.05, 128.46, 128.45, 128.28, 128.13, 124.05, 120.55, 115.33, 115.18, 114.79, 55.82, 55.80.

HRMS (MALDI-TOF) m/z: Calculated for $C_{61}H_{46}N_2O_4S_2$ (M+), 934.2899; Found, 934.2903 (Δ = 1 ppm).

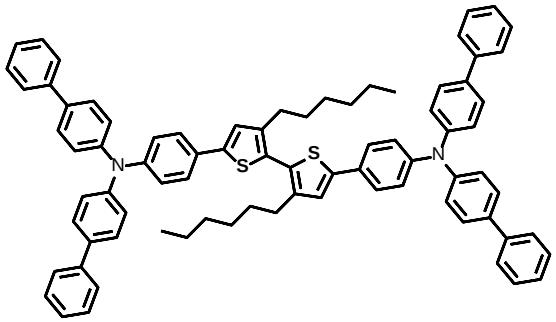

N,N'-((3,3'-dihexyl-[2,2'-bithiophene]-5,5'-diyl)bis(4,1-phenylene))bis(N-([1,1'-biphenyl]-4-yl)-[1,1'-biphenyl]-4-amine) (BT_1): To an oven-dried Schlenk tube containing a stirring bar, 3,3'-dihexyl-2,2'-bithiophene (200 mg, 0.60 mmol) and N,N-bis(4-biphenylyl)-N-(4-bromophenyl)amine (626 mg, 1.32 mmol, 2.2 eq.), palladium acetate (6.7 mg, 0.029 mmol), tricyclohexylphosphinetetrafluoroborate (22 mg, 0.06 mmol), pivalic acid (18.3 mg, 0.18 mmol) and potassium carbonate (207 mg, 1.5 mmol), were sequentially added. The solids were degassed 3 times under vacuum followed by a flow of argon. After addition of anhydrous and degassed *N*,*N*-dimethylacetamide (10 mL), the reaction mixture was heated at 120 °C in a Lab Armor™ beads bath for 20 hours. The resulting mixture was cooled to room temperature, concentrated under reduced pressure and the residue was purified by column chromatography on silica gel (eluent: DCM:PE with 1:1 V:V ratio) affording the corresponding product as a light-yellow powder (370 mg, 55%).

^{1}H NMR (300 MHz, Chloroform-d) δ 7.63 – 7.57 (m, 8H), 7.56 – 7.49 (m, 12H), 7.48 – 7.40 (m, 8H), 7.36 – 7.29 (m, 4H), 7.25 – 7.20 (m, 8H), 7.20 – 7.15 (m, 4H), 7.14 (s, 2H), 2.63 – 2.52 (m, 4H), 1.68 – 1.55 (m, 4H), 1.35 – 1.24 (m, 12H), 0.88 – 0.84 (m, 6H).

^{13}C NMR (76 MHz, Chloroform-d) δ 147.03, 146.83, 143.61, 143.50, 140.73, 135.95, 129.13, 128.93, 128.09, 127.86, 127.09, 126.87, 126.64, 124.62, 124.49, 124.22, 31.85, 30.87, 29.31, 22.76, 14.24.

HRMS (MALDI-TOF) m/z: Calculated for $C_{80}H_{72}N_2S_2$ (M+), 1124.5137; Found, 1124.5112 (Δ = 1.76 ppm).

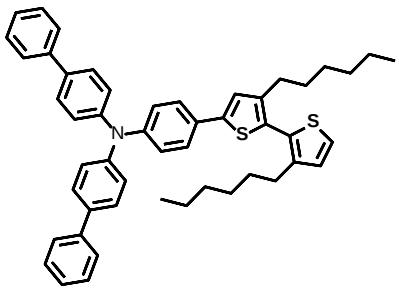

N-([1,1'-biphenyl]-4-yl)-N-(4-(3,3'-dihexyl-[2,2'-bithiophen]-5-yl)phenyl)-[1,1'-biphenyl]-4-amine (6): Same procedure as BT_1, affording the corresponding product from the mono-coupling as a yellowish solid (180 mg, 41%).

^{1}H NMR (300 MHz, Chloroform-d) δ 7.66 – 7.59 (m, 4H), 7.59 – 7.50 (m, 6H), 7.46 (m, 4H), 7.40 – 7.30 (m, 3H), 7.30 – 7.22 (m, 5H), 7.22 – 7.14 (m, 2H), 7.00 (d, *J* = 5.2 Hz, 1H), 2.61 – 2.49 (m, 4H), 1.62 – 1.56 (m, 4H), 1.32 – 1.26 (m, 12H), 0.91 – 0.85 (m, 6H).

^{13}C NMR (76 MHz, Chloroform-d) δ 146.97, 146.80, 143.55, 143.44, 142.53, 140.70, 135.89, 129.12, 128.92, 128.77, 128.07, 127.07, 126.85, 126.60, 125.41, 124.59, 124.47, 124.10, 31.81, 30.87, 30.84, 29.28, 29.26, 29.19, 29.04, 22.74, 14.23.

HRMS (MALDI-TOF) m/z: Calculated for $C_{50}H_{51}NS_2$ (M+), 729.3463; Found, 729.3458 (Δ = 0.13 ppm).

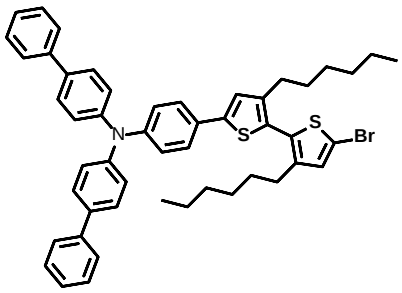

N-([1,1'-biphenyl]-4-yl)-N-(4-(5'-bromo-3,3'-dihexyl-[2,2'-bithiophen]-5-yl)phenyl)-[1,1'-biphenyl]-4-amine (6'): To a solution of compound **6** (160 mg, 0.22 mmol) in DMF (5 mL) was added slowly at 0°C, 49 mg of NBS (1.05 eq). The reaction mixture was stirred at RT overnight in the dark. DMF was evaporated, then DCM was added and the organic phase was washed with water and brine. Once dried over $MgSO_4$, the solvent was removed by rotary evaporation and the crude was subsequently subjected to silica gel column chromatography (eluent: DCM:PE with 4:1 V:V ratio) to give the target compound as a yellow solid (150 mg, 85%).

^{1}H NMR (300 MHz, Chloroform-d) δ 7.63 – 7.56 (m, 5H), 7.56 – 7.47 (m, 7H), 7.47 – 7.40 (m, 4H), 7.36 – 7.27 (m, 3H), 7.25 – 7.19 (m, 5H), 7.19 – 7.14 (m, 2H), 7.11 (s, 1H), 6.93 (s, 1H), 2.54 – 2.46 (m, 4H), 1.25 (m, 12H), 0.88 – 0.83 (m, 6H).

^{13}C NMR (76 MHz, Chloroform-d) δ 146.76, 144.09, 143.40, 140.70, 136.00, 131.58, 130.67, 128.93, 128.09, 127.11, 126.87, 126.66, 124.66, 124.37, 123.92, 31.81, 31.76, 30.83, 30.70, 29.25, 29.18, 29.00, 22.74, 22.71, 14.23.

HRMS (MALDI-TOF) m/z: Calculated for $C_{50}H_{50}BrNS_2$ (M+), 807.2568; Found 807.2545 (Δ = 0.15 ppm).

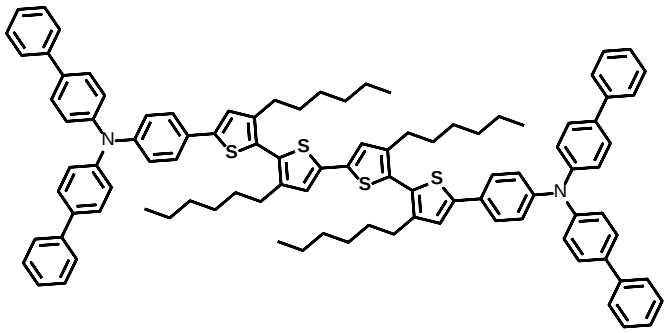

N,N'-((3,3',3''',4''-tetrahexyl-[2,2':5',2'':5'',2'''-quaterthiophene] -5,5'''-diyl) bis(4,1-phenylene))bis(N-([1,1'-biphenyl] -4-yl)-[1,1'-biphenyl]-4-amine) (BT_2): To an oven-dried Schlenk tube containing a stirring bar, compound **6** (95 mg, 0.129 mmol) and **6'** (105 mg, 0.129 mmol), palladium acetate (1.5 mg, 0.0064 mmol), tricyclohexylphosphinetetrafluoroborate (4.7 mg, 0.013 mmol), pivalic acid (4 mg, 0.039 mmol) and potassium carbonate (45 mg, 0.322 mmol), were sequentially added. The solids were degassed 3 times under vacuum followed by a flow of argon. After addition of anhydrous and degassed *N*,*N*-dimethylacetamide (4 mL), the reaction mixture was heated at 120 °C in a Lab Armor™ beads bath for 20 hours. The resulting mixture was cooled to room temperature, concentrated under reduced pressure and then filtered on a plug of silica gel using DCM, before being injected in the preparative HPLC to give the product as a yellow powder (50 mg, 26%).

^{1}H NMR (300 MHz, Chloroform-d) δ 7.63 – 7.59 (m, 8H), 7.57 – 7.50 (m, 12H), 7.48 – 7.41 (m, 8H), 7.38 – 7.31 (m, 4H), 7.31 – 7.27 (m, 1H), 7.25 – 7.21 (m, 7H), 7.21 – 7.16 (m, 4H), 7.15 (s, 2H), 7.06 (s, 2H), 2.62 – 2.50 (m, 8H), 1.64 – 1.58 (m, 8H), 1.33 – 1.24 (m, 24H), 0.91 – 0.85 (m, 12H).

^{13}C NMR (76 MHz, CD_2Cl_2) δ 147.48, 147.16, 144.30, 144.00, 143.91, 140.95, 137.20, 136.26, 129.24, 128.32, 128.27, 127.60, 127.41, 127.05, 126.86, 125.64, 125.03, 124.80, 124.64, 32.11, 31.11, 31.04, 29.57, 29.50, 23.05, 14.29.

HRMS (MALDI-TOF) m/z: Calculated for $C_{100}H_{100}N_2S_4$ (M+), 1456.6769; Found 1456.6740 (Δ = 1.65 ppm).

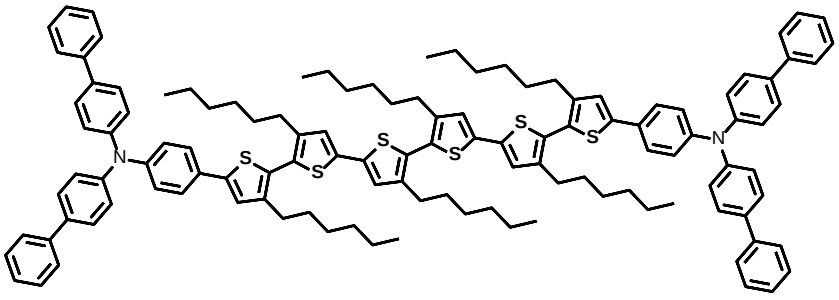

N,N'-((3,3',3''',3''''',4'',4''''-hexahexyl-[2, 2' : 5', 2'': 5'',2''':5''',2'''':5'''',2''''':5''''',2'''''-sexithiophene]-5,5''''' -diyl) bis (4,1 -phenylene)) bis(N-([1,1'-biphenyl]- 4-yl)- [1,1'-biphenyl] -4-amine) (BT_3): To an oven dried Schlenk tube containing a stirring bar, 5,5'-dibromo-3,3'-dihexyl-2,2'-bithiophene (30 mg, 0.061 mmol), compound **6** (90 mg, 0.123 mmol), palladium acetate (2.7 mg, 0.012 mmol), tricyclohexylphosphinetetrafluoroborate (9 mg, 0.024 mmol), pivalic acid (3.7 mg, 0.036 mmol) and potassium carbonate (25 mg, 0.183 mmol), were sequentially added. The solids were degassed 3 times under vacuum followed by a flow of argon. After addition of anhydrous and degassed *N*,*N*-dimethylacetamide (4 mL), the reaction mixture was heated at 120 °C in a Lab Armor™ beads bath for 20 hours. The resulting mixture was cooled to room temperature, concentrated under reduced pressure and then filtered on a plug of silica gel using DCM, before being injected in the preparative recycling HPLC to give the product as a yellow powder (17 mg, 15%).

^{1}H NMR (300 MHz, Chloroform-d) δ 7.64 – 7.57 (m, 8H), 7.56 – 7.50 (m, 12H), 7.48 – 7.40 (m, 8H), 7.35 (t, *J* = 1.3 Hz, 1H), 7.33 (t, *J* = 2.1 Hz, 2H), 7.30 (t, *J* = 1.3 Hz, 1H), 7.26 – 7.21 (m, 8H), 7.20 – 7.16 (m, 4H), 7.14 (s, 2H), 7.05 (d, *J* = 1.0 Hz, 4H), 2.62 – 2.48 (m, 12H), 1.67 – 1.56 (m, 12H), 1.30 – 1.26 (m, 36H), 0.90 – 0.85 (m, 18H).

^{13}C NMR (76 MHz, Chloroform-d) δ 147.10, 146.82, 143.78, 143.73, 143.58, 143.43, 140.74, 137.21, 136.94, 135.98, 129.05, 128.93, 128.10, 128.04, 127.52, 127.41, 127.10, 126.87, 126.66, 125.28, 125.23, 124.65, 124.46, 124.22, 31.84, 31.81, 30.78, 29.86, 29.28, 29.23, 22.75, 14.23.

HRMS (MALDI-TOF) m/z: Calculated for $C_{120}H_{128}N_2S_6$ (M+) 1788.8402; Found 1788.8419 (Δ = 1.30 ppm).

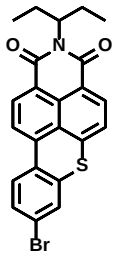

8-Bromo-2-(pentan-3-yl)-1H-thioxantheno[2,1,9-def]isoquinoline-1,3(2H)-dione (BTI-N-Br): 6-bromo-2-(pentan-3-yl)-1H-benzo[de]isoquinoline-1,3(2H)-dione (600 mg, 1eq), 2-amino-5-bromobenzenethiol (460 mg, 1.3 eq) and K_2CO_3 (144 mg, 0.6 eq) were refluxed in 15 mL of 2-ethoxyethanol for 15 h. Then, isoamyl nitrite (0.7 mL, 3eq) was added and the reaction mixture was refluxed for another 15 h. The mixture was cooled down before being diluted with DCM. The organic phase was washed twice with water and once with brine, then dried over $MgSO_4$ and finally filtered. After removal of the solvent by rotary evaporation, the crude was subjected to a silica gel column chromatography using DCM as eluent to afford **BTI-N-Br** as a yellowish orange powder (450mg, 57%).

^{1}H NMR (300 MHz, Chloroform-d) δ 8.58 (d, *J* = 8.1 Hz, 1H), 8.40 (d, *J* = 7.9 Hz, 1H), 8.13 (d, *J* = 8.3 Hz, 1H), 8.02 (d, *J* = 8.7 Hz, 1H), 7.52 – 7.44 (m, 3H), 5.10 – 4.98 (m, 1H), 2.33 – 2.15 (m, 2H), 1.98 – 1.82 (m, 2H), 0.89 (t, *J* = 7.5 Hz, 6H).

^{13}C NMR (76 MHz, Chloroform-d) δ 139.09, 135.77, 133.77, 130.86, 130.68, 128.87, 127.57, 127.31, 125.53, 124.46, 120.71, 119.44, 57.57, 25.06, 11.46.

HRMS (MALDI-TOF) m/z: Calculated for $C_{23}H_{18}BrNO_2S$ (M+) 451.0242; Found 451.0229 (Δ= –1.68).

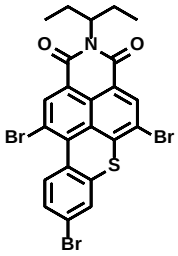

5,8,11-Tribromo-2-(pentan-3-yl)-1H-thioxantheno[2,1,9-def]isoquinoline-1,3(2H)-dione (BTI-N-Br$_3$): To a solution of BTI-N-Br (200 mg, 0.44 mmol) in CH_2Cl_2 (100 mL) was added dropwise a solution of bromine (20 eq, 1 M, 8.8 mL) in CH_2Cl_2. The reaction mixture was heated overnight at 40°C before being subsequently washed with a saturated aqueous solution of $Na_2S_2O_3$, water and brine. Once dried over $MgSO_4$, the solvent was removed by rotary evaporation and the crude was subsequently subjected to silica gel column chromatography using CH_2Cl_2 as eluent to give the target compound as an orange solid (150 mg, 55%).

^{1}H NMR (300 MHz, Chloroform-d) δ 8.83 (s, 1H), 8.62 (s, 1H), 8.55 (d, *J* = 8.9 Hz, 1H), 7.72 (d, *J* = 2.1 Hz, 1H), 7.52 (dd, *J* = 8.9, 2.1 Hz, 1H), 5.06 – 4.93 (m, 1H), 2.31 – 2.11 (m, 2H), 1.97 – 1.81 (m, 2H), 0.87 (t, *J* = 7.4 Hz, 6H).

^{13}C NMR (125 MHz, Chloroform-d) δ 138.19, 135.98, 135.11, 132.23, 130.56, 130.12, 129.50, 127.27, 127.23, 124.70, 117.95, 116.36, 58.08, 24.97, 11.38.

HRMS (MALDI-TOF) m/z: Calculated for $C_{23}H_{16}Br_3NO_2S$ (M+) 606.8452; Found 606.8453 (Δ= −0.77 ppm).

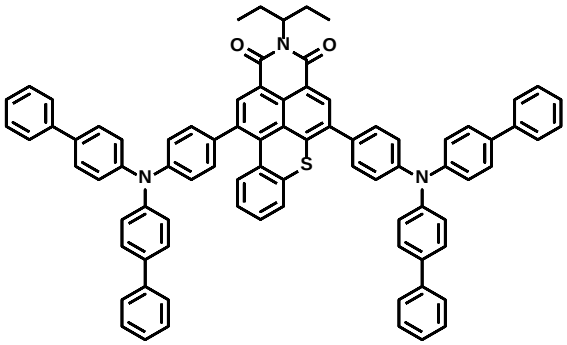

5,11-Bis(4-(di([1,1'-biphenyl]-4-yl)amino)phenyl)-2-(pentan-3-yl)-1H-thioxantheno[2,1,9-def]isoquinoline-1,3(2H)-dione (BTI-TPA$_2$): To an oven dried Schlenk tube containing a stirring bar, BTI-Br_2 (100mg, 0.188 mmol, 1eq), N-([1,1'-biphenyl]-4-yl)-N-(4-(4,4,5,5- tetramethyl-1,3,2-dioxaborolan-2-yl)phenyl)-[1,1'-biphenyl]-4-amine (216 mg, 0.414 mmol, 2.2 eq), Pd(dppf)Cl_2 (20 mg, 0.028 mmol, 0.15 eq) and K_2CO_3 (65 mg, 0.470 mmol, 2.5eq) were sequentially added. The solids were degassed 3 times under vacuum followed by a flow of argon. After addition of degassed DMF and water (10:1 V:V ratio) the reaction mixture was heated at 110 °C in a Lab Armor™ beads bath for 24 hours. DMF was evaporated under reduced pressure, then the reaction mixture was diluted with dichloromethane and the organic phase was washed with water and brine before being dried over $MgSO_4$. After evaporation of the solvent, the crude was filtered on a plug of silica gel using $CHCl_3$ as eluent to be injected in the preparative recycling HPLC affording, after purification, the corresponding compound (155 mg, 70%).

^{1}H NMR (300 MHz, Chloroform-d) δ 8.71 (s, 1H), 8.42 (s, 1H), 7.64 – 7.52 (m, 17H), 7.51 – 7.39 (m, 14H), 7.37 – 7.29 (m, 11H), 7.24 – 7.17 (m, 5H), 7.00 (t, *J* = 7.8 Hz, 1H), 5.15 – 5.03 (m, 1H), 2.36 – 2.20 (m, 2H), 1.98 – 1.83 (m, 2H), 0.91 (t, *J* = 7.4 Hz, 6H).

^{13}C NMR (76 MHz, Chloroform-d) δ 147.92, 147.30, 146.75, 146.69, 140.68, 140.65, 137.57, 137.17, 136.28, 136.11, 135.78, 134.93, 133.58, 133.03, 132.83, 130.63, 130.24, 129.87, 129.67, 128.93, 128.79, 128.20, 128.14, 127.14, 126.90, 126.87, 125.97, 125.12, 124.75, 124.51, 124.31, 123.48, 57.51, 31.07, 25.11, 11.43.

HRMS (MALDI-TOF) m/z: Calculated for $C_{83}H_{61}N_3O_2S$ (M+) 1163.4484; Found 1163.4470 (Δ = -0.76 ppm).

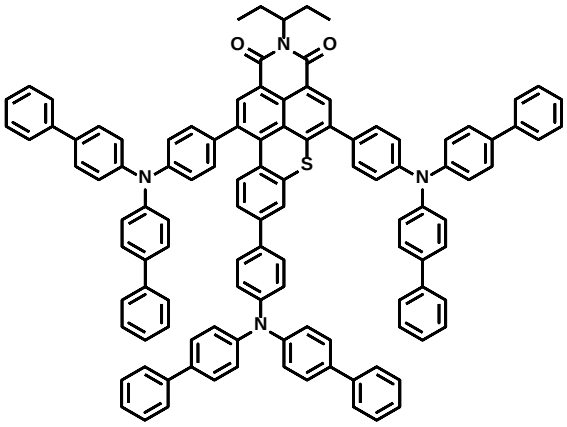

5,8,11-Tris(4-(di([1,1'-biphenyl]-4-yl)amino)phenyl)-2-(pentan-3-yl)-1H-thioxantheno[2,1,9-def]isoquinoline-1,3(2H)-dione (BTI-N-TPA$_3$): To an oven dried Schlenk tube containing a stirring bar, BTI-Br_3 (90 mg, 0.147 mmol, 1 eq), N-([1,1'-biphenyl]-4-yl)-N-(4-(4,4,5,5- tetramethyl-1,3,2-dioxaborolan-2-yl)phenyl)-[1,1'-biphenyl]-4-amine (255 mg, 0.486 mmol, 3.3 eq), Pd(dppf)Cl_2 (27 mg, 0.037 mmol, 0.15 eq) and K_2CO_3 (61 mg, 0.442 mmol, 3 eq) were sequentially added. The solids were degassed 3 times under vacuum followed by a flow of argon. After addition of degassed DMF and water (10:1 V:V ratio) the reaction mixture was heated to 110 °C in a Lab Armor™ beads bath for 48 hours. DMF was evaporated under reduced pressure, then the reaction mixture was diluted with dichloromethane and the organic phase was washed with water and brine before being dried over $MgSO_4$. After evaporation of the solvent, the crude was filtered on a plug of silica gel using $CHCl_3$ as eluent to be injected in the HPLC affording, after purification, the corresponding red compound (80 mg, 35%).

^{1}H NMR (300 MHz, Chloroform-d) δ 8.72 (s, 1H), 8.43 (s, 1H), 7.64 – 7.50 (m, 30H), 7.47 – 7.39 (m, 15H), 7.38 – 7.34 (m, 3H), 7.34 – 7.30 (m, 8H), 7.29 – 7.26 (m, 3H), 7.25 – 7.20 (m, 10H), 5.17 – 5.04 (m, 1H), 2.39 – 2.21 (m, 2H), 2.00 – 1.84 (m, 2H), 0.93 (t, *J* = 7.4 Hz, 6H).

^{13}C NMR (125 MHz, Chloroform-d) δ 148.02, 147.93, 147.33, 146.75, 146.70, 146.62, 140.72, 140.65, 140.59, 140.58, 137.33, 137.31, 136.26, 136.06, 135.78, 134.97, 134.25, 133.17, 133.06, 132.68, 130.67, 130.28, 129.69, 128.93, 128.19, 128.15, 128.12, 127.97, 127.80, 127.17, 127.13, 126.88, 126.86, 126.82, 125.10, 124.95, 124.71, 124.31, 124.28, 124.09, 123.89, 123.53, 57.51, 29.85, 25.13, 11.45.

HRMS (MALDI-TOF) m/z: Calculated for $C_{113}H_{82}N_4O_2S$ (M+) 1558.6158; Found 1558.6133 (Δ = -1.25 ppm).

The following molecule was described and published in "From Textile Coloring to Light-emitting Electrochemical Devices: Upcycling of the Isoviolanthrone Vat Dye. Chemistry – An Asian Journal 2023, 18, e202300014" with the corresponding supporting information.

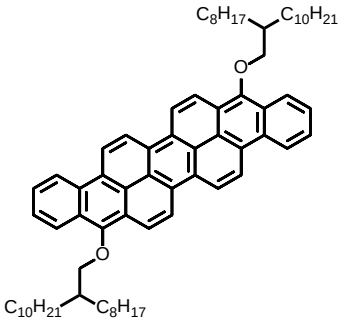

9,18-Dialkoxylated 1.2,8.9-dibenzoperopyrene (DBP): A 250 mL three-necked flask was charged with an aqueous solution of NaOH (1.6 M, 35 mL) and, subsequently, the whole system was purged with argon (15 min). The solution was then heated to 60°C whereupon 190 mg (1.10 mmol) of sodium dithionite and 500 mg (1.10 mmol) of isoviolanthrone were added. The resulting mixture was stirred for 1 h, and then 25 mL of toluene and ~2.5 mL of Aliquat 336 were added. The mixture was then heated to 110°C and subsequently 2 mL (5.48 mmol) of 9-(bromomethyl)nonadecane were added. It was kept at this temperature for 24 h and then allowed to cool down to RT and neutralized by drop-wise addition of HCl solution. The organic phase was extracted with DCM and concentrated. The crude was filtered on a plug of basic alumina using DCM as eluent and then precipitated in hexane to give a red solid (390 mg, 35%).

^{1}H NMR (300 MHz, Chloroform-d) δ 9.09 – 8.76 (m, 8H), 8.64 – 8.33 (m, 4H), 7.88 – 7.63 (m, 4H), 4.16 (d, J = 5.4 Hz, 4H), 2.31 – 2.04 (m, 2H), 1.93 – 1.78 (m, 4H), 1.75 – 1.64 (m, 4H), 1.54 – 1.24 (m, 56H), 0.97 – 0.81 (m, 12H).

^{13}C NMR (76 MHz, Chloroform-d) δ 150.15, 128.91, 125.97, 125.83, 125.46, 125.06, 124.25, 123.83, 123.51, 122.85, 122.73, 122.07, 121.96, 121.85, 121.57, 79.28, 39.88, 32.15, 31.57, 30.42, 30.00, 29.62, 27.33, 22.90, 14.32.

HRMS (MALDI-TOF) m/z: Calculated for $C_{74}H_{98}O_2$ (M+) 1018.7567; Found 1018.7540 (Δ = -2.06 ppm).

3. Devices fabrication and measurements

3.1 Organic Solar Cells (OSCs)

Fabrication: Indium tin oxide (ITO) pre-coated glass slides of 24×25×1.1 mm with a sheet resistance of RS = 7 Ω/sq were purchased from Visiontek Systems LTD. The substrates were washed with a diluted Deconex® 12 PA-x solution (2% in water) and scrubbed using dishwashing soap before being cleaned by a series of ultrasonic treatments in distilled water, acetone, and isopropanol for 15 min each. Once dried under a steam of nitrogen, a UV-ozone plasma treatment (UV/Ozone ProCleaner Plus, Bioforce Nanosciences) was performed for 15 min. An aqueous solution of poly(3,4-ethylenedioxy-thiophene):poly(styrenesulfonate) (PEDOT:PSS; Ossila), filtered through a 0.45 µm RC membrane (Millex®), was spun-casted onto the patterned ITO surface at 6000 rpm for 40 s before being baked at 140 °C for 30 min. Then, blends of MD-OMe or MD-Ph and $PC_{71}BM$ at different weight-to-weight ratios were dissolved in chloroform at a total concentration of 10 $mg.mL^{-1}$, stirred at 30 °C for 30 minutes, and spuncasted on the PEDOT:PSS layer. Finally, devices were completed by the successive thermal deposition of Ca (7 nm) and aluminum (100 nm) at a pressure of 1.5×10^{-6} Torr through a shadow mask defining six cells of 27 mm^2 each (13.5 mm x 2 mm).

Device Characterization: J-V curves were recorded using a Keithley 236 source-measure unit and a homemade acquisition program. The light source was an AM1.5 Solar Constant 575 PV simulator (Steuernagel Lichttecknik, equipped with a metal halogen lamp). The light intensity was measured by a broadband power meter (13PEM001, Melles Griot). EQEs were measured under an ambient atmosphere using a halogen lamp (Orsam) with an Action Spectra Pro 150 monochromator, a lock-in amplifier (Perkin-Elmer 7225) and a S2281 photodiode (Hamamatsu).

AFM: Atomic Force Microscopy (AFM) experiments were performed using the Nano-Observer microscope from CS Instrument. The topographic images were obtained in tapping mode. Images were processed using Gwyddion SPM data analysis software. Optimized blends were spun cast on the above-described PEDOT:PSS modified ITO substrates.

Hole-only devices (SCLC devices and measurements): Gold electrodes (100 nm) were subsequently and thermally evaporated under a vacuum of 1.5 x 10^{-5} Torr, through a shadow mask defining active areas of 10 mm^2, 5 mm^2, 1.5 mm^2 and 0.8 mm^2 per substrate. Hole

mobilities μ_h were evaluated using the Mott-Gurney law, ie, $J_{SCLC} = (9/8)\varepsilon_0\varepsilon_r\mu_h(V^2/d^3)$ where ε_r is the static dielectric constant of the medium ($\varepsilon_r = 3$) and d, the thickness of the active layer.

3.2 Perovskite Solar Cells (PSCs)

Materials: Isopropanol (IPA; anhydrous, 99.5%), $SnCl_2.2H_2O$ (≥ 99.995%), PbI_2 (99.999%), CsI (99.999% trace metal basis), N,N-dimethylformamide (DMF; anhydrous, 99.8%), dimethylsulfoxide (DMSO; anhydrous, 99.9%), lithium bis(trifluoromethanesulfonyl)imide (Li-TFSI; anhydrous, 99.99% trace metal basis), acetonitrile (anhydrous, 99.8%), 4-tertbutylpyridine (tBP; 98%), and chlorobenzene (anhydrous, 99.8%) were purchased from Sigma–Aldrich. FAI (≥ 99.99%), MABr (≥ 99.99%), MACl (≥ 99.99%), and 4-methoxyphenethylammonium iodide (MeO-PEAI) were purchased from GreatCell Solar. $PbBr_2$ (>98%) was purchased from TCI. Diethyl ether (99% extra pure) was purchased from Duksan. 2,2',7,7'Tetrakis-(N,N-di-p-methoxyphenylamine)-9,9'-spirobifluorene (spiro-OMeTAD; > 99.5%) and tris(2-(1H-pyrazol-1-yl)-4-tert-butylpyridine)cobalt(III)tris(bis(trifluoromethylsulfonyl)imide) (FK 209 Co(III) TFSI, > 99%) were purchased from Lumtec.

Fabrication: Partially etched fluorine-doped tin oxide (FTO, Asahi glass, ~7 Ω sq^{-1}) glass substrates were cleaned with detergent solution, acetone, and ethanol for 20 min sequentially. After 20 min of ultraviolet (UV)-O_3 treatment, a 75 mM $SnCl_2.2H_2O$ solution dissolved in IPA was spin-coated on the substrate at a speed of 3000 rpm for 30 s and annealed at 200 ℃ for 30 min. Oxygen vacancy passivation in the SnO_{2-x} layer was performed. Otherwise, chemical bath deposition was used to coat smooth SnO_2 on FTO glass. Prior to perovskite film deposition, 15 min of UV-O_3 treatment was applied. The perovskite precursor solution was prepared by mixing 1.4 M FAI, 1.4 M PbI_2, 0.023 M MABr, 0.023 M $PbBr_2$, 0.023 M CsI, and 0.5 M MACl in a mixed solvent of DMF and DMSO at a ratio of 85:15 (v:v). The precursor solution was spin-coated in a two-step process (1st: 1000 rpm for 10 sec, 2nd: 5000 rpm for 20 sec). 1 ml of diethyl ether was poured 5 sec before the end of the spin coating process. Subsequently, the sample was annealed at 150 ℃ for 15 min and 100 ℃ for 10 min. For perovskite passivation, 10 mM MeO-PEAI solution dissolved in IPA was spin-coated at 5000 rpm for 30 s immediately after loading 150 μL of the solution on the substrate. For the spiro-OMeTAD hole transport layer (HTL), 90 mg of spiro-OMeTAD was dissolved in 1 mL of CB. Then, 23 μL of Li-TFSI solution (520 mg mL^{-1} in acetonitrile), 10 μL of FK209 Co(III) TFSI solution, and 39 μL of tBP

were added to the spiro-OMeTAD solution as additives. For the new HTLs, 60 mg of each compound was dissolved in 1 mL of CB. Additives for the new HTLs were equal in molar ratio to the spiro-OMeTAD system. For the intermolecular interaction enhanced HTL, blended systems, 5 mol% of each compound was added to the spiroOMeTAD system. The solution was spin-coated onto the perovskite surface at 3000 rpm for 30 s. Finally, 120 nm of Au counter electrode was deposited by a thermal evaporator in a high vacuum chamber below 10^{-6} Torr at a rate between 0.8 and 1.2 Å s^{-1}.

Device Characterization: The photocurrent density-voltage (J-V) curves were measured using a solar simulator (Newport, Oriel Sol3A Class AAA Solar Simulator) with a source meter (Keithley 2400) under AM 1.5 G irradiation with a power density of 100 mW cm^{-2}. The light was calibrated using a standard Si solar cell (VLSI standards, Oriel P/N 91150V). The J-V curves were measured by applying reverse (1.2 V to -0.1 V) or forward (0.1 V to 1.2 V) scans. The step voltage and scan speed were fixed at 13 mV and 130 mV s^{-1}, respectively. The device was measured in a dry room (RH below 15%). The devices were measured with a metal aperture with an area of 7.6 mm^2. Grazing incidence wide-angle X-ray scattering (GIWAXS) was performed at the 9A U-SAXS beamline of the Pohang Light Source. The GIWAXS images were recorded with a 2D CCD (Rayonix MX170-HS). The diffraction angles were calibrated by a pre-calibrated sucrose solution (Monoclinic, P21, a = 10.8631 Å, b = 8.7044 Å, c = 7.7624 Å and β = 102.938°). The sample-to-detector distance was 221 mm. The topography of the HTLs was measured by atomic force microscopy (AFM; NX-10, Park Systems).

Stability measurements: For operational stability measurements, 0.9 V biasing was applied to the encapsulated perovskite solar cell using a potentiostat (CHI 660, CH instruments), and light illumination was applied using a 150 W Xe lamp solar simulator (PEC-L01, PECCELL) after 1 sun calibration. Active cooling was not applied during the measurement.

3.3 Organic Light Emitting Diodes (OLEDs)

Materials: Poly(9,9-di-n-octylfluorenyl-2,7-diyl) (PFO), PVK with an average Mn of 25,000-50,000 g/mol, o-xylene, methanol, and ITO-coated PET with a sheet resistance of 20-50 $\Omega \cdot sq^{-1}$ were obtained from Millipore-Sigma. (Poly [(9,9bis(3'-(N,N dimethylamino)propyl)-2,7-fluorene)-alt-2,7-(9,9–dioctylfluorene)]) (PFN) was purchased from Ossila Ltd. (Sheffield, UK). PEDOT:PSS dissolved in water (CLEVIOS™ P VP AI 4083) was supplied from Heraeus (Hanau, Germany). Silver pellets with a purity of 99.99% and tungsten boat sources were

acquired from RD Mathis. FOM nanoroll coater (from FOM Technologies, Copenhagen S., Denmark), a roll slot-die coater, was used for coating OLEDs layers on flexible PET substrates. Spin-coater from Osilla Ltd., Sheffield, UK, was used to form spin-coated OLED layers. The top silver layer as a cathode was deposited using a Covap system supplied by Angstrom Engineering.

Fabrication of spin-coated devices: OLED devices were fabricated on ITO-coated glass substrates (sheet resistance of 10 Ohm Sq^{-1}), which were first cleaned by sequentially ultrasonicating detergent, and de-ionized water, acetone, and isopropanol before use. Glass/ITO substrates were first pretreated under UV-ozone for 30 minutes. PEDOT:PSS aqueous suspension was spin-coated onto the ITO-coated glass substrates at 4000 rpm for 60 s and annealed in air at 140°C for 20 min. The PEDOT:PSS solution was filtered with a 0.45 μm pore size PVDF filter before spin coating. PVK, if used, was dissolved in 1,4-dioxane (10 mg/mL) spin-coated at 3000 rpm for 60 s and baked at 120 °C for 10 min. For deposition of the emitting layer, the solutions or blend solutions (with PFO, if used) were spin-cast at 2000 rpm for 60 s and annealed in air at 100°C for 10 min. PFN was processed from MeOH (2 mg/mL + 2 μL/mL acetic acid) at 4000 rpm for 60 s. Finally, the Ag (100 nm) electrode was deposited using a thermal evaporation system through a shadow mask under a base pressure of $\sim 2 \times 10^{-6}$ torr. The device area was 14 mm^2 as defined by the overlapping area of the ITO films and top electrodes.

Ink formulation: PEDOT:PSS inks were warmed up to room temperature from a storage temperature of +4°C. PEDOT:PSS dispersion is subjected to filtration using a 0.45 μm polyvinylidene fluoride (PVDF) filter to remove any particles or impurities. In addition, a PVK solution is prepared by dissolving PVK in 1,4-dioxane at a concentration of 10 mg/mL. For the PFN solution, PFN is dissolved in MeOH at a concentration of 2 mg/mL, with the addition of 2 μL/mL of acetic acid. The PFN solution is stirred at room temperature for a minimum of 2 hours to ensure proper dissolution. Prior to use, the PVK, and PFN solutions undergo filtration through a 0.45 μm polytetrafluoroethylene (PTFE) filter to remove any impurities or particles that may be present in the solutions.

Fabrication of slot-die-coated devices: Prior to the coating of functional layers, the PET/ITO substrates underwent a cleaning process in an ultrasonic bath with water and isopropanol for 10 minutes, followed by a 30-minute UV-ozone treatment to enhance the surface energy. The

PEDOT:PSS ink was applied at a speed of 0.5 m/min with a flow rate of 20 μL/min, while maintaining a substrate temperature of 60 °C. The coated substrates were subsequently annealed at 100 °C for 60 minutes in ambient air. **BT_1** dissolved in o-xylene (15 mg/mL) or **PFO:BTI-$(TPA)_2$** dissolved in toluene (15 mg/mL) were deposited at a speed rate of 0.5 m/min, with a flow rate of 60 μL/min, and a substrate temperature of 35 °C. The resulting films were heat-treated at 90 °C for 30 minutes to remove any residual solvent. PFN was coated on top of the emissive layer at a speed of 0.3 m/min, with a flow rate of 20 μL/min, under ambient conditions (20-25 °C, relative humidity 50%), and then dried at 100 °C for 15 minutes. Finally, a 200 nm thick Ag cathode was deposited using thermal evaporation. The deposition process was conducted at a power of 20 W, a pressure of 2×10^{-6} mbar, and a total deposition time of 20 minutes.

Device Characterization: The *J–V* characteristics of the OLED devices were measured using a Keithley Source meter (Model: 2612B) provided by Tektronix, Inc., based in Beaverton, USA. The luminance of the OLEDs was measured using a luminance meter (Model: LS 150) supplied by Konica Minolta, Inc. in Tokyo, Japan. UV-absorption spectra were obtained using a Cary 60 spectrometer from Agilent Technologies, Inc. in Santa Clara, CA, USA. To measure the electroluminescent (EL) spectrum, a preconfigured LED measurement system with an integrating receptor (Stellarnet, 2 × 2 × 2 in. with a 5/8 in. input port) and a Black-Comet spectrometer for UV-vis (190-850 nm) coupled with an F600-VISNIR fiber optic cable from StellarNet were employed. Film thickness was determined using KLA-Tencor's probe profilometer (D-500 Stylus Profilometer).

3.4 Light-Emitting Electrochemical Cells (LECs)

Materials: THAB was used as received from Sigma Aldrich. 4,4'-bis(9H-carbazol-9-yl) biphenyl (CBP) was purchased from TCI and used as received. Chlorobenzene was HPLC grade [Aldrich, >99% purity]. PEDOT: PSS and pattered ITO glass were purchased from Ossila and Wooyang GMS, respectively.

Fabrication: Solutions of the active layer were prepared by dissolving dye **DBP** at three different concentrations of 5.25 mg/mL, 2.65 mg/mL, and 0.5 mg/mL with CBP, PFO, and THAB in chlorobenzene, with a weight ratio of CBP/guest/electrolyte = 61:18.3:20.6, 67.2:10.1:22.6 and 73.2:2.1:24.7. Patterned ITO glass substrates were cleaned by a 20 min ultrasonic bath in 500 mL of DI water and 5 mL of Hellmanex™ III, followed by 20 min in DI

water and finally 20 min in acetone. The substrates were then dried in an oven at 80 °C for 1 h to remove any solvent residues before undergoing a UV-ozone treatment for 20 min. PEDOT:PSS (35 nm) was spin-coated on the substrates at 4000 rpm for 60 s before baking at 110 °C for 1 h. The substrates were then transferred into a dry N2-filled glovebox. The active layers were then spin-coated at 2000 rpm for 60 s and annealed for 1 h at 40 °C. Finally, a set of four Al (100 nm) electrodes was added on top of the active material by thermal evaporation under high vacuum (1.5×10^{-5} Pa) through a shadow mask.

Device Characterization: The LECs were driven by a pulsed current mode (235 Hz, 50 % duty cycle) generated by a Keithley 2400 sourcemeter controlled by a MATLAB code. The voltage and luminescence of the LEC were measured upon application of a current ramp. Absorption and fluorescence spectra of thin films were measured on a Perkin-Elmer lambda 750 spectrophotometer and a Konica Minolta CS-2000 spectroradiometer, respectively (with excitation at 365 nm from a UV lamp).

4. Crystallographic data

*Table S1 Crystal data collection and refinement parameters of **BT_1** and **BTI-N-Br**.*

Molecule	**BT_1**	**BTI-N-Br**
Empirical formula	$C_{80}H_{72}N_2S_2$	$C_{23}H_{18}BrNO_2S$
Formula weight	1304.56	452.35
Temperature (K)	230.0(1)	200.0(1)
Wavelength(Å)	1.54184	1.54184
Crystal system, space group	Orthorhombic, P b c n	Triclinic, P-1
a(Å)	30.808(16)	7.0658(3)
b(Å)	23.598(11)	9.3475(4)
c(Å)	10.040(2)	15.0577(7)
α(deg)	90	79.341(4)
β(deg)	90	83.234(4)
γ(deg)	90	74.547(4)
Z	4	2
Volume ($Å^3$)	7299(5)	939.56(8)
Calculated density (Mg/m^3)	1.187	1.599
Absorption coefficient (mm^{-1})	2.507	4.179
θ range (deg)	2.358 to 72.679	2.994 to 73.893
Completeness to θ = 70.000	97.8%	98.2%
GOF	1.030	0.861
Largest diff. peak & hole ($e/Å^3$)	0.264 and -0.399	1.479 and -0.848

List of publications

- Lee, J. H.; **Ghanem, T.**; Sánchez, D. J. P.; Josse, P.; Blanchard, P.; Ahn, H.; Lungerich, D.; Park, N.-G.; Cabanetos, C.; Park, J. H., Enhancing Intermolecular Interaction of Spiro-OMeTAD for Stable Perovskite Solar Cells with Efficiencies over 24%. *ACS Energy Letters* **2023**, 3895-3901.

- **Ghanem, T.**; Leong, K. K.; Jang, H.; Hardouin, A.; Blanchard, P.; Lungerich, D.; Josse, P.; Kim, E.; Cabanetos, C., From Textile Coloring to Light-emitting Electrochemical Devices: Upcycling of the Isoviolanthrone Vat Dye. Chemistry – An Asian Journal **2023**, 18, e202300014.

- Andrés Castán, J. M.; Abidi, S.; **Ghanem, T.**; Touihri, S.; Blanchard, P.; Welch, G. C.; Zagranyarski, Y.; Boixel, J.; Walker, B.; Josse, P.; Cabanetos, C., N-Annulation of the BTI Rylene Imide Organic Building Block: Impact on the Optoelectronic Properties of pi-Extended Molecular Structures. Colorants **2023**, 2 (1), 22-30.

- Josse, P.; Morice, K.; Puchán Sánchez, D.; **Ghanem, T.**; Boixel, J.; Blanchard, P.; Cabanetos, C., Revisiting the synthesis of the benzothioxanthene imide five decades later. New Journal of Chemistry **2022**, 46 (18), 8393-8397.

- Nicolas, C.; **Ghanem, T.**; Canevet, D.; Sallé, M.; Nicol, E.; Gautier, C.; Levillain, E.; Niepceron, F.; Colombani, O., Oxidation-Sensitive Supramolecular Polymer Nanocylinders. Macromolecules **2022**.

- **Ghanem, T**.; Vincendeau, T.; Marqués, P. S.; Habibi, A. H.; Abidi, S.; Yassin, A.; Dabos-Seignon, S.; Roncali, J.; Blanchard, P.; Cabanetos, C., Synthesis of push–pull triarylamine dyes containing 5,6-difluoro-2,1,3-benzothiadiazole units by direct arylation and their evaluation as active material for organic photovoltaics. Materials Advances **2021**, 2 (22), 7456-7462.

COLLEGE DOCTORAL PAYS DE LA LOIRE
ED MATIERE, MOLECULES MATERIAUX ET GEOSCIENCES

université angers

Synthèse, Caractérisation, et Utilisation de Systèmes π-conjugués Accessibles pour l'Electronique Organique

Mots clés : Synthèse organique, arylation directe, l'électronique organique, photovoltaïque organique, cellules solaires pérovskites, dispositifs organiques électroluminescents.

Résumé : Les matériaux semi-conducteurs organiques constituent sans aucun doute une révolution technologique vers des dispositifs écologiques, peu coûteux et flexibles pour une variété d'applications à haut potentiel technologique. Cependant, une vision critique des publications souligne qu'efficacité va généralement avec complexité synthétique des matériaux et des processus de fabrication. De plus, à quelques exceptions près, les synthèses multi-étapes de la plupart des structures conjuguées font également appel à des réactions de couplage croisé C-C catalysées par des métaux de transition impliquant l'utilisation de précurseurs fonctionnalisés par des groupes organométalliques, entraînant une augmentation du nombre global d'étapes, impactant le coût de synthèse et imposant des contraintes liées aux traitement des déchets. Dans ce contexte, ce travail de thèse visait à concevoir de nouvelles structures π-conjuguées accessibles par des voies de synthèse minimisant le nombre d'étapes et surtout plus écoresponsables. Par conséquent, la réaction d'arylation directe a été sélectionnée pour la préparation de la plupart des composés présentés dans ce manuscrit. Puis, en fonction de leurs propriétés optoélectroniques, ils ont été intégrés, avec succès, dans différents dispositifs pour l'électronique organique Ainsi, après une introduction générale (chapitre 1), le chapitre 2 se concentre sur l'étude de composés moléculaire actifs pour le photovoltaïque organique et hybride (Pérovskite). Finalement dans un dernier chapitre (3), de nouveaux matériaux aux propriétés optiques prometteuses ont été évaluées dans des dispositifs émissifs type OLED et LECs.

Synthesis, Characterization, and Use of Accessible π-conjugated Structures for Organic Electronics

Keywords : Organic synthesis, direct heteroarylation reaction, organic electronics, organic photovoltaic, perovskite solar cells, organic light emitting devices.

Abstract : Organic semiconducting materials have undoubtedly paved the way to a technological revolution towards eco-friendly, low-cost, and flexible devices for a variety of optoelectronic or electronic applications. However, a critical vision of the state-of-the-art reports from the literature highlights that the highest efficiencies generally go along with a significant rise in the synthetic complexity of the materials but also the device fabrication processes. Moreover, with only a few exceptions, the synthesis of most of these active conjugated structures relies on transition-metal-catalyzed C-C cross-coupling reactions. This strategy usually implies the halogenation and functionalization of complementary building blocks by organometallic functional groups, leading to an increase in the overall number of steps and therefore impacting the costs and waste treatments. In this context, the main objective of this thesis aimed at designing new accessible π-conjugated structures through step-saving and eco-friendly synthetic routes. Hence, the direct heteroarylation reaction was selected as a method of choice to prepare most of the compounds reported in this manuscript. Then, depending on their optoelectronic properties, the latter were subsequently embedded in different types of organic electronic devices. Thus, after a general introduction, the second chapter focuses on the preparation of molecular structures for both organic and hybrid photovoltaics. Then, in the third chapter, new structures exhibiting promising optical properties were evaluated as active compounds in organic and electrochemical light-emitting devices.